UNIVERSIDADE FEDERAL DO RIO GRANDE DO SUL
INSTITUTO DE FÍSICA
DEPARTAMENTO DE ASTRONOMIA
PROGRAMA DE PÓS-GRADUAÇÃO EM FÍSICA

Star Formation and Chemical Properties in Nearby Metal-Poor Low-Mass Galaxies: The cases of SDSS J0205-0814 and ESO 400-43[†]

(*Formação estelar e propriedades químicas de galáxias locais com baixas massa e metalicidade: Os casos de SDSS J0205-0814 e ESO 400-43*)

Augusto Eduardo Lassen

Porto Alegre, RS

2024

[†]**Trabalho financiado pelos órgãos de fomento à pesquisa e educação CNPq e CAPES**

Augusto Eduardo Lassen

STAR FORMATION AND CHEMICAL PROPERTIES IN NEARBY METAL-POOR LOW-MASS GALAXIES: THE CASES OF SDSS J0205-0814 AND ESO 400-43 (*FORMAÇÃO ESTELAR E PROPRIEDADES QUÍMICAS DE GALÁXIAS LOCAIS COM BAIXAS MASSA E METALICIDADE: OS CASOS DE SDSS J0205-0814 E ESO 400-43)*

Tese de doutorado, realizada sob orientação dos professores Dr. Rogério Riffel e Dra. Ana Leonor Chies Santiago Santos e submetida ao Programa de Pós-Graduação em Física da Universidade Federal do Rio Grande do Sul como requisito parcial para obtenção do título de Doutor em Ciências.

Supervisor: Prof. Dr. Rogério Riffel

Co-supervisor: Profa. Dra. Ana Leonor Chies Santiago Santos

Porto Alegre, RS

26 de Julho de 2024

Agradecimentos

Agradeço à minha mãe pelo apoio e amor incondicionais, representando para mim mais do que um porto seguro, mas também um exemplo de resiliência e amor ao próximo que carregarei comigo por toda vida. Agradeço ao meu pai pela insistência em me fazer entender que existe muito mais a ser conquistado do que os caminhos mais óbvios da vida nos reservam, e que não podemos nos definir por aquilo que os outros esperam de nós. Agradeço à minha esposa Gabriella pelo amor, confiança, cumplicidade, apoio e por estar sempre disposta a sacrificar dias e horas do nosso tempo juntos na esperança de que, cedo ou tarde, todo trabalho duro seria recompensado. Quero continuar celebrando e dividindo contigo cada conquista. A todos os numerosos membros de minha família a quem amo profundamente, que sempre me desejaram o melhor e cujo carinho aquece meu coração constantamente, deixo meus agradecimentos.

Gostaria de agradecer a todos professores que tive, desde o jardim de infância à pós-graduação, no desejo de expressar minha admiração por aqueles que dão mais do que recebem, exercendo a profissão pela paixão de ensinar e que pavimentaram o caminho da minha formação como profissional e cidadão. Em especial, gostaria de agradecer aos meus orientadores Dr. Rogério Riffel e Dra. Ana Chies Santos, que me guiaram com muita paciência e sabedoria nessa jornada altamente desafiadora. Agradeço também pela hospitalidade com que fui recebido pela Dra. Angela Adamo e pelo Dr. Arjan Bik durante minha estadia em Estocolmo. Sou extremamente grato pelas excelentes discussões científicas que tivemos, e pela confiança depositada em mim para trabalhar com dados de tão alta qualidade. Agradeço aos alunos de pós-graduação, pós-doutorandos e demais professores da Universidade de Estocolmo por terem feito eu me sentir completamente integrado. Fiz amizades incríveis e, embora curto, o período que passei em Estocolmo encontra-se cristalizado em minha memória. Por fim, deixo o mais sincero agradecimento àqueles que contribuíram para minha formação como pesquisador e que não tiveram seus nomes citados aqui.

Agradeço a absolutamente todos os meus amigos, em especial a Fábio, Luan e Ramon. Dividimos momentos de diversão que facilitaram muitíssimo os períodos de dificuldade da graduação. Ter conhecido vocês me mudou para melhor, e suas contribuições individuais para que eu chegasse até aqui são inestimáveis.

Agradeço ao Programa de Pós-Graduação em Física da UFRGS e aos órgãos de fomento à pesquisa e educação no Brasil, Conselho Nacional de Desenvolvimento Científico e Tecnológico (CNPq) e Coordenação de Aperfeiçoamento de Pessoal de Nível Superior (CAPES), pelo apoio financeiro que tornou esse trabalho possível.

This thesis includes text partially revised using OpenAI's GPT-4/GPT-3.5, a large-scale language-generation model. AI language model was used restrictively to correct grammar according to English (USA) conventions and minor adjustments as needed, upon the provision of detailed input drafts. The author reviewed, edited, and revised the text and takes ultimate responsibility for the content of this thesis.

"The history of astronomy is a history of receding horizons."
(The Realm of the Nebulae, Edwin Hubble, 1936)

Resumo

Considerando o modelo cosmológico ΛCDM, halos de matéria escura de baixa massa formam-se primeiro, crescendo hierarquicamente através de sucessivas fusões. Assim, espera-se que o Universo Primordial tenha sido populado por galáxias anãs de baixa metalicidade, principais candidatas a terem reionizado o Universo. A fração de galáxias com morfologias *clumpy* no UV e Hα atinge seu pico em torno de $z \approx 2$, com evolução cósmica semelhante à densidade de formação estelar. Os gatilhos de formação estelar *clumpy* e sua menor ocorrência no Universo local permanecem em debate. A acreção de gás frio pode gerar instabilidades em discos marginalmente estáveis, formando *clumps* "in situ". Fusões entre galáxias podem levar à formação de clumps "ex situ", seja gerando instabilidades locais ou os sistemas incorporados tornando-se os próprios *clumps*. Em termos de evolução química, diversas galáxias a $z \gtrsim 2$ exibem gradientes de metalicidade invertidos, sugerindo a acreção de gás pouco metálico. Gradientes planos podem originar-se de fusões ou de outros processos em grande escala eficientes na mistura e redistribuição do gás. As propriedades de galáxias anãs próximas com formação estelar (baixas $M_\star$, altas $f_{\rm gas}$, baixas $Z_{\rm gas}$) as tornam excelentes laboratórios para estudar a evolução química e os processos de formação estelar em alta resolução espacial. Esse trabalho apresenta análises espacialmente resolvidas das propriedades físicas e químicas do gás ionizado em duas galáxias anãs ($\sim 10^9\,M_\odot$) próximas com meio interestelar (ISM) pouco metálico. Usando espectroscopia de campo integrado do VLT/MUSE, caracterizamos a anã irregular SDSS J0205-0814 ($z = 0.04025$). Combinando dados do VLT/MUSE–AO com fotometria multibanda do HST, estudamos aglomerados estelares e seu *feedback* no ISM da galáxia azul compacta ESO 400-43 ($z = 0.01965$) através das propriedades do gás ionizado e da população de aglomerados. Para SDSS J0205-0814, encontramos $M_\star \approx 3{\times}10^9\,M_\odot$ e uma taxa de formação estelar (SFR) total de $\approx 0.7 M_\odot\,{\rm yr}^{-1}$. Modelos cinemáticos sugerem interação ao prever o alinhamento entre o gás na galáxia anã e o campo de velocidades estelares em Mrk 1172. Os *clumps* residem na componente em rotação, apoiando a hipótese de formação "in situ". O ISM é sub-solar e apresenta gradientes planos, em contraste com os gradientes invertidos e a anticorrelação entre $Z_{\rm gas}$ e SFR esperada em caso de acreção de gás de baixa metalicidade. No entanto, reforçamos que, dadas as escalas espaciais envolvidas, inomogeneidades na metalicidade podem ser diluídas, mimetizando gradientes planos. Em ESO 400-43 , $\sim$5% dos aglomerados estelares são jovens ($t \leqslant 5\,{\rm Myr}$) e massivos ($M_\star \geqslant 10^5\,M_\odot$), potencialmente abrigando estrelas Wolf-Rayet (WR). Os aglomerados correlacionam-se espacialmente com os picos de He II λ4686, onde componentes largas e estreitas são observadas. Diagramas de diagnóstico indicam regiões da galáxia candidatas a ionização por choques radiativos, com um ramo enriquecido em N próximo ao pico de emissão em He II. Observamos inclinação negativa na relação N/O vs. O/H e anticorrelação entre $Z_{\rm gas}$ e SFR, sugerindo enriquecimento localizado de N pela ejeção de material sintetizado em estrelas WR e surto de formação estelar causado pela injeção de gás pouco metálico, respectivamente. O enriquecimento de N no ISM devido a estrelas WR tem sido proposto para explicar os níveis elevados de N/O recentemente estimados em algumas galáxias distantes observadas com o JWST. Com um espalhamento de $\sim$1 dex nos valores de $Z_{\rm gas}$ e padrões erráticos na morfologia e velocidade do gás, discutimos a possibilidade de um evento de fusão no passado como mecanismo de gatilho para o surto de formação estelar observado em ESO 400-43 .

Palavras-Chave: Galáxias: Anãs – Galáxias: Abundâncias – Galáxias: ISM – Galáxias: Interações

Abstract

In the ΛCDM cosmological paradigm, low-mass dark matter halos form first, growing hierarchically through successive mergers. Thus, we expect the Early Universe to be populated mostly by very metal-poor low-mass galaxies, likely the major contributors to cosmic reionization. The fraction of galaxies with clumpy rest-frame UV and Hα morphologies peaks around $z \approx 2$, roughly following the Star Formation Rate Density evolution. The triggers of clumpy star formation and why clumps become less common at low z remain subjects of debate. Cold gas accretion can drive instabilities in marginally stable disks, forming clumps "in situ". Major/minor mergers can lead to "ex situ" clump formation by generating local gravitational instabilities or by accreted galaxies themselves becoming clumps. In terms of chemical evolution, several $z \gtrsim 2$ galaxies show inverted metallicity gradients, favoring accretion of metal-poor gas. Flat metallicity gradients can result from mergers or other efficient galactic-scale mechanisms of gas mixing/redistribution. The properties of local star-forming dwarf galaxies (low $M_\star$, high $f_{\rm gas}$, low $Z_{\rm gas}$) make them excellent laboratories to study chemical evolution and star-formation processes at high spatial resolutions. This work presents a spatially resolved analysis of the ionized gas physical and chemical properties of two local star-forming metal-poor $\sim 10^9\,M_\odot$ galaxies. Using VLT/MUSE Integral Field Spectroscopy, we characterize the irregular galaxy SDSS J0205-0814 at $z = 0.04025$. Combining VLT/MUSE – AO data with Hubble Space Telescope (HST) multiband photometry, we examine star cluster feedback into the Interstellar Medium (ISM) of ESO 400-43 ($z = 0.01965$) through the properties of the ionized gas and cluster population. For SDSS J0205-0814, we find $M_\star \approx 3{\times}10^9\,M_\odot$ and a total "instantaneous" Star Formation Rate (SFR) of $\approx 0.7 M_\odot\,{\rm yr}^{-1}$. Kinematic models show an alignment between the gas (dwarf) and stellar velocity field of its companion (Mrk 1172), suggesting interaction. The kpc-sized clumps reside in the rotating component of SDSS J0205-0814, supporting the hypothesis of clumpy formation via violent disk instability. The ISM shows a sub-solar, flat metallicity gradient, in contrast to the inverted gradients and the anti-correlation between $Z_{\rm gas}$ and SFR that would be expected if clumps were formed through accretion of metal-poor gas. However, at the spatial scales analyzed, we stress that chemical inhomogeneities might be diluted. In ESO 400-43 , $\sim$5% of the star cluster population is found to be young ($t \leqslant 5\,$Myr) and massive ($M_\star \geqslant 10^5\,M_\odot$), potentially hosting Wolf-Rayet (WR) stars. These clusters spatially correlate with regions of increased He II λ4686 flux, where both broad and narrow He II λ4686 components are detected. Emission line diagnostic diagrams show galaxy regions overlapping with fast radiative shock grids, with a N-enriched branch emerging around the He II emission peak. A negative slope in the N/O vs. O/H relation and an anti-correlation between $Z_{\rm gas}$ and SFR suggest localized N enrichment possibly originating from WR ejecta and starburst triggered by metal-poor gas infall, respectively. A similar ISM chemical enrichment process has been proposed for a few high-z galaxies recently observed with the James Webb Space Telescope, for which enhanced N/O values are reported. With an estimated $\sim$1 dex metallicity spread and erratic gas morphology/velocity patterns, we also debate a past merger event as the trigger of starburst in ESO 400-43 .

Keywords: Galaxies: Dwarfs – Galaxies: Abundances – Galaxies: ISM – Galaxies: Interactions

Abbreviations

AGN – Active Galactic Nuclei.

AO – Adaptive Optics.

BCD – Blue Compact Dwarf.

BCG – Blue Compact Galaxy.

CCD – Charged-Coupled Device.

CEEL – Collisionally Excited Emission Line.

DECaLS – Dark Energy Camera Legacy Survey.

DIG – Diffuse Ionized Gas.

DM – Dark Matter.

EELG – Extreme Emission Line Galaxy.

ETG – Early-Type Galaxy.

FoV – Field of View.

FWHM – Full Width at Half Maximum.

GALEX – Galaxy Evolution Explorer.

GeMS – Gemini Multi-conjugate adaptive optics System.

GMC – Giant Molecular Cloud.

GSAOI – Gemini South Adaptive Optics Imager.

HST – Hubble Space Telescope.

ICF – Ionization Correction Factor.

IFS – Integral Field Spectroscopy.

IGM – Intergalactic Medium.

IMF – Initial Mass Function.

ISM – Interstellar Medium.

JWST – James Webb Space Telescope.

LOSVD – Line-Of-Sight Velocity Distribution.

LSF – Line Spread Function.

MZR – Mass-Metallicity Relation.

NIR – Near Infrared.

NUV – Near Ultra-Violet.

PSF – Point Spread Function.

SDSS – Sloan Digital Sky Survey.

SED – Spectral Energy Distribution.

SFDG – Star-Forming Dwarf Galaxies.

SFH – Star Formation History.

SFR – Star Formation Rate.

SFRD – Star Formation Rate Density.

SMBH – Supermassive Black Hole.

SPS – Stellar Population Synthesis.

sSFR – Specific Star Formation Rate.

SSP – Simple Stellar Population.

UFD – Ultra Faint Dwarf.

UV – Ultra-Violet.

VDI – Violent Disk Instability.

VLT – Very Large Telescope.

WCS – World Coordinate System.

WMAP – Wilkinson Microwave Anisotropy Probe.

XMD – Extremely Metal-Deficient.

XMP – Extremely Metal-Poor.

YSC – Young Star Cluster.

List of Figures

List of Tables

Contents

1 Introduction

1.1 The big picture: A cosmological background

Understanding how the Universe was formed and its subsequent evolution is, perhaps, the main goal of modern astronomy and astrophysics. Several unanswered questions (e.g., the nature of dark matter and dark energy), incomplete theoretical models and observational limitations pose strong challenges to this ambitious task (Caldwell; Kamionkowski, 2009). The definitions of time and spatial scales of the Universe are intrinsically related to the frontiers of human knowledge. An episode that illustrates this well is the Shapley-Curtis discussion (often called the "Great debate") that occurred between Harlow Shapley and Heber D. Curtis in 1920 (Shapley; Curtis, 1921; Berendzen; Hart; Seeley, 1976). While Shapley argued that the Milky Way was itself the entire Universe and "nebular" sources like Andromeda were simply gas clouds contained within our Galaxy, Curtis claimed that the Milky Way was just one among many similar systems ("Island Universes"). The debate ended in 1924, when Edwin Hubble used the largest telescope of that epoch[1], a 100-inch Hooker Telescope at Mount Wilson, to derive the light curve of a Cepheid variable star located in M31 and infer its distance, conclusively determining it was well beyond the Milky Way (Sharov; Novikov, 1993). Edwin Hubble's discovery marked the birth of the extragalactic astronomy research field, and his remarkable observations are just about to reach the 100-year milestone.

Telescope instrumentation improved drastically since then, allowing galaxies to be observed across cosmological timescales. The physical phenomena driving their formation and evolution provide invaluable insights into the history and initial conditions of our Universe. Currently, cosmological models consider our Universe to be composed of baryonic matter, Dark Matter (DM) and dark energy, with the latter two comprising approximately 95% of the total energy density (Planck Collaboration et al., 2016; Euclid Collaboration et al., 2020). Variations in the relative contributions of each component lead to different cosmological models, as well as changes in the assumptions about the properties of dark energy and DM particles.

Nowadays, the standard cosmological model is the Λ Cold Dark Matter (ΛCDM) model, which predicts a flat[2] Universe with cold[3] DM particles. In this cosmological

[1] https://www.mtwilson.edu/100-telescope-observing/

[2] The geometry of the Universe is indicated by the curvature of space-time. Light rays travel along geodesics (the shortest path between two locations), making them excellent tracers of the space-time curvature. In a flat Universe, two parallel light rays in vacuum will never meet, in accordance with the principles of Euclidean geometry (Ryden, 2003).

[3] The temperature here refers to the Maxwell-Boltzmann distribution of velocities for the DM particles

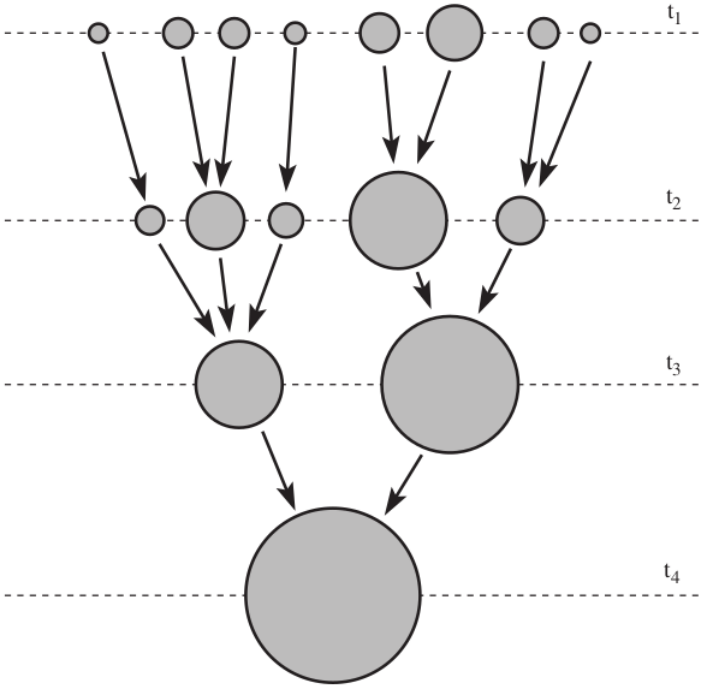

Figure 1 – Illustration of the hierarchical growth ("bottom-up" scenario) of DM halos predicted by ΛCDM cosmological framework. Larger halo sizes correspond to higher masses, and the dashed lines indicate four different epochs. The lower-mass DM halos (on top of the figure, epoch t_1) are formed first from the primordial density fluctuations, and the larger DM halos are formed through accretion of the smaller progenitors. Credit: Mo, van den Bosch and White (2010).

framework, the lower-mass DM halos are the first to originate from the primordial density fluctuations, as their amplitudes are larger on smaller scales (Mo; van den Bosch; White, 2010; Ishiyama, 2014), and larger halos form subsequently through successive mergers (White; Rees, 1978; Peebles, 1980; White; Frenk, 1991; De Lucia; Blaizot, 2007; Annibali; Tosi, 2022). The hierarchical growth of DM halos creates a merger tree that is illustrated in Fig. 1.

Semi-analytical models support the hierarchical scenario by highlighting the large contribution to the ionizing power at $z \gtrsim 6$ from $10^9\,M_\odot$ DM halos harboring primarily metal-free stars (Choudhury; Ferrara, 2006; Choudhury; Ferrara, 2007; Choudhury; Ferrara; Gallerani, 2008). Additional support is provided by observations of $z \gtrsim 4$ galaxies with the Hubble Ultra Deep Field in the Near Infrared (NIR), which extrapolated the faint end of the Luminosity Function (LF) and found UV ionizing fluxes suggesting star-forming galaxies as the predominant agents of the reionization of neutral Hydrogen in the Universe (Bouwens et al., 2012a; Bouwens et al., 2015) that is thought to have occurred in the redshift range $6 \lesssim z \lesssim 11$ (Ouchi et al., 2009; Komatsu et al., 2011). Although star-forming galaxies residing in low-mass DM halos are well established as the main candidates for the cosmic reionization (Atek et al., 2015; Finkelstein et al., 2015), alternative candidates are

in the earlier stages of Universe formation. Cold DM particles were non-relativistic at the time they decoupled from the other components of the universe (Ryden, 2003).

still a matter of debate (Robertson, 2022). For instance, some models claim that quasars and other types of Active Galactic Nuclei (AGN) with high escape fractions of ionizing photons could alone drive the cosmic reionization around 600 – 800 Myr after the Big Bang (Madau; Haardt, 2015; Mitra; Choudhury; Ferrara, 2018). However, recent observations from the James Webb Space Telescope (JWST) have gathered further evidence of the contribution from faint high-z star-forming galaxies to the cosmic reionization. For instance, eight ultra-faint ($-17 \lesssim M_{\rm UV}\,[\rm AB] \lesssim -15$) $z \gtrsim 6$ dwarf galaxies gravitationally lensed were analyzed spectroscopically with JWST / NIRSpec (Atek et al., 2024), and 677 galaxies from the JWST Advanced Deep Extragalactic Survey (JADES) in the redshift range $4 \lesssim z \lesssim 9$ were observed with JWST / NIRCam (Simmonds et al., 2024). Both samples presented elevated production of ionizing photons, and if these galaxies are assumed to be representative of the star-forming dwarf galaxy population at this redshift range, the ionization efficiency would be more than sufficient to account for the cosmic reionization (Atek et al., 2024).

1.2 Global properties of dwarf galaxies

Dwarf galaxies are the most abundant class of galaxies in the Universe and can be found in a wide variety of environments, from dense galaxy clusters and groups to isolated regions (Staveley-Smith; Davies; Kinman, 1992; Karachentsev et al., 2004; Karachentsev; Makarov; Kaisina, 2013; Lelli, 2022). In terms of mass, dwarfs are considered to have baryonic masses of $\lesssim 10^9\,M_\odot$ (Annibali; Tosi, 2022; Thornton et al., 2023). Traditionally, dwarf galaxies are classified based either on their morphology (e.g., dwarf irregulars, dwarf spheroidals, ultra-compact dwarfs), brightness (e.g., low surface brightness dwarfs), or on their recent star formation activity, with quenched/quiescent and Star-Forming Dwarf Galaxies (SFDGs). While quenched dwarf galaxies exhibit little to no evidence of recent ($\lesssim 10\,$Myr) star formation activity and lack a cool gas reservoir to fuel further star formation, SFDGs have large gas fractions[4], lying in the interval $0.25 \lesssim f_{\rm gas} \lesssim 0.95$ (Calabrò et al., 2017; Lelli, 2022).

SFDGs can be found in the outskirts of galaxy clusters, in galaxy groups or in isolation (Binggeli; Tarenghi; Sandage, 1990; Kovač; Oosterloo; van der Hulst, 2009). Quenched dwarfs, on the other hand, are frequently found in galaxy clusters or orbiting high-mass galaxies (Binggeli; Tarenghi; Sandage, 1990; Ferguson; Binggeli, 1994; Putman et al., 2021), but are rarely found in isolation (Binggeli; Tarenghi; Sandage, 1990; Geha et al., 2012; Lelli, 2022). In contrast to the continuous Star Formation History (SFH) often observed in higher-mass galaxies, theoretical models (Hopkins et al., 2014) and observations (Guo et al., 2016) indicate that star formation in dwarfs is typically bursty. The star formation in these episodic bursts is efficient when compared to the extrapolation of the

[4] $f_{\rm gas} \equiv M_{\rm gas}/(M_{\rm gas} + M_\star)$

galaxy main sequence of star formation (Brinchmann et al., 2004; Daddi et al., 2007; Noeske et al., 2007) to the low stellar mass regime (Amorín et al., 2015; Calabrò et al., 2017). Classifying dwarfs solely based on their optical appearance, without further examination of their SFHs, might lead to misinterpretations. For instance, earlier studies suggested that metal-poor SFDGs could be currently experiencing their first episode of star formation (Sargent; Searle, 1970; Kunth; Maurogordato; Vigroux, 1988). However, deeper optical and NIR photometry (Telles, 1995; Papaderos et al., 1996; Bergvall; Östlin, 2002; Noeske et al., 2005) revealed that, at least for the vast majority of Blue Compact Dwarf (BCD) galaxies, these bursts are superimposed on a low surface brightness ($\mu_{\rm B} \gtrsim 24\,{\rm mag\,arcsec^{-2}}$) stellar host with evolved stellar populations (Amorín et al., 2007; Amorín et al., 2009) that exhibits moderate and continuous star-forming activity (Tolstoy; Hill; Tosi, 2009). This raises questions related to the connections between the quiescent and star-forming dwarf galaxies, leading to suggestions of a scenario where SFDGs may evolve into quenched dwarfs due to the gas consumption and/or environmental effects (e.g., ram pressure stripping) that remove the the cool gas supply necessary to sustain star formation (Efstathiou, 1992; Tolstoy; Hill; Tosi, 2009; Gallart et al., 2015; Vulcani et al., 2020).

Galaxy size is also an important observable in the study of galaxy formation and evolution, as alterations in size are linked to the mechanisms of galaxy growth and galaxy mass assembly over cosmic time (Oesch et al., 2010; Yang et al., 2022). For instance, while in disk galaxies the size is mainly controlled by the transfer of angular momentum from the DM halo to the disk (Fall; Efstathiou, 1980; Mo; Mao; White, 1998; Wechsler; Tinker, 2018), in Early-Type Galaxies (ETGs) major mergers and feedback from central Supermassive Black Hole (SMBH) act as the main agents shaping galaxy size (López-Sanjuan et al., 2012; Choi et al., 2018). Considering the hierarchical scenario of galaxy formation illustrated in Fig. 1, the successive accretion of lower-mass systems produces larger masses and can also increase the luminosity of the resulting galaxy. Therefore, both parameters (size and luminosity) are expected to reflect the underlying processes of galaxy mass assembly that are intimately governed by galaxy evolution (Kormendy, 1977; Trujillo et al., 2004; Danieli; van Dokkum, 2019).

These physical processes result in the size-luminosity relation (Kormendy, 1977; Binggeli; Sandage; Tarenghi, 1984; Kormendy, 1985; McConnachie, 2012; Simon, 2019; Revaz, 2023), a scaling relation between size, usually parameterized by the effective radius (also called half-light radius, as it is defined to contain half of the galaxy luminosity) $r_{\rm eff}$, and luminosity in a given band (usually the V band). To illustrate, in Fig. 2 we show the luminosity relation for samples of dwarf galaxies, extended to the faint end of galaxy luminosity function to include Ultra Faint Dwarf (UFD) galaxy candidates (gray squares) from Revaz (2023). The UFDs are the faintest galaxies known in the Universe, with V band luminosities below $10^5\,L_\odot$ (Simon, 2019; Revaz, 2023). They are hard to detect due to their faintness, with the majority of the confirmed UFDs being satellites of the Milky

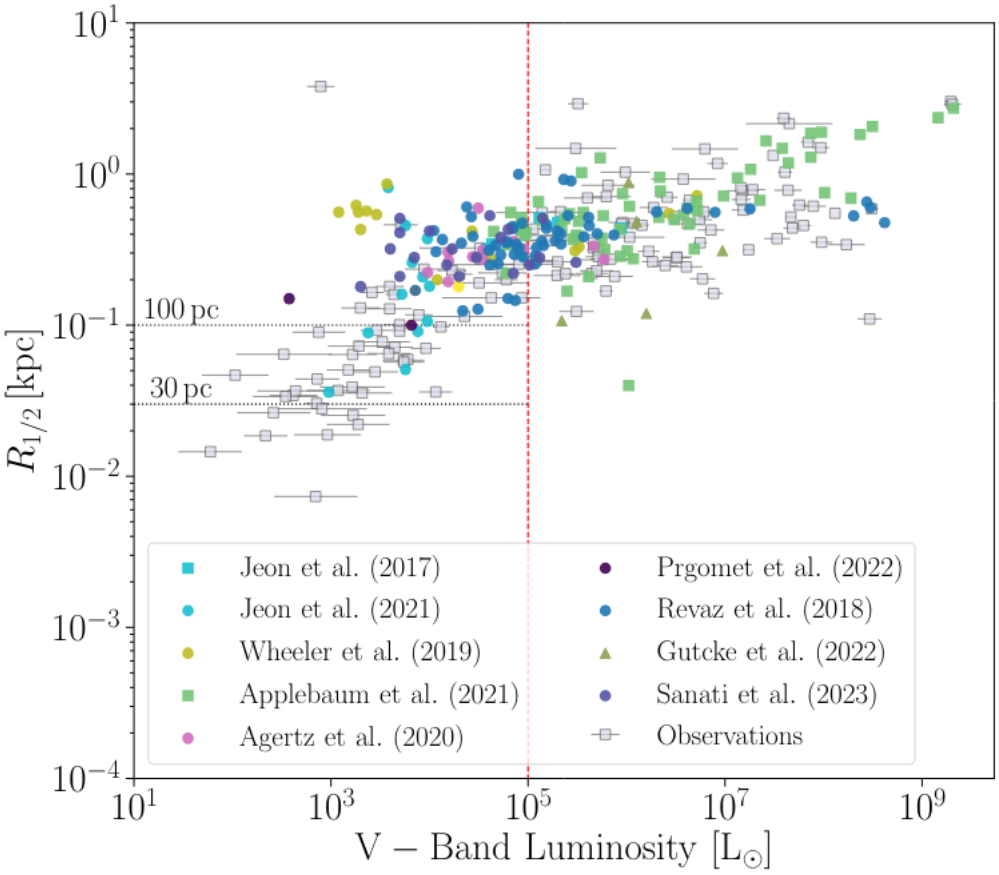

Figure 2 – Luminosity-size relation for samples of dwarf galaxies in the literature (References are indicated in the label, coded by symbols and colors), including UFD galaxy candidates (gray squares). The vertical line indicates the V band luminosity threshold ($L_V < 10^5\,L_\odot$) for UFDs (Simon, 2019). $R_{1/2}$ corresponds to the half-light radius, i.e. the radius enclosing half of the galaxy luminosity. Credit: Revaz (2023).

Way. These galaxies appear to be generally very compact, with sizes below 100 pc, but their true sizes have been matter of debate in the recent literature, with studies suggesting the presence of extended faint stellar halos in UFDs (Vivas; Martínez-Vázquez; Walker, 2020; Qi et al., 2022; Sestito et al., 2023; Tau; Vivas; Martínez-Vázquez, 2024).

Throughout this work, we will analyze the galaxy Interstellar Medium (ISM) by investigating the physical conditions of the ionized gas. Therefore, we are mostly focused on SFDGs, meaning that throughout this work, unless explicitly stated otherwise, we may use the term dwarf to refer to SFDGs exclusively.

1.3 The chemical composition of star-forming dwarf galaxies

One of the most important parameters for studying galaxy evolution is metallicity. In astrophysics, metals are considered to be any atomic nuclei heavier than H and He. Besides the aforementioned properties used to investigate the formation and evolution of dwarf galaxies, the chemical composition of a galaxy (whether in the stellar or gas phases),

measured from the relative abundances of heavy elements with respect to hydrogen, offers invaluable insights into galaxy chemical evolution. The chemical evolution, in its turn, is intrinsically related to past star formation processes and, consequently, to galaxy evolution itself (Matteucci, 2012). Less massive stars remain longer on the main sequence and tend to retain the chemical composition of the molecular gas cloud they were formed from, as suggested by the typically low (∼0.02 dex) chemical inhomogeneities exhibited among F, G, K and red giant stars observed in open clusters (De Silva et al., 2006; Liu et al., 2016; Casamiquela et al., 2020; Johnson et al., 2023). Massive stars, on the other hand, have shorter lifetimes and produce heavier atomic nuclei in their interior, polluting the galaxy ISM with their enriched nucleosynthesized products during and after advanced stellar evolutionary stages (López-Sánchez; Esteban, 2010; Kobayashi; Ferrara, 2024; Rivera-Thorsen et al., 2024). This enriched material can supply future star formation, resulting in more metallic stellar generations and subsequently increasing the metallicities as the galaxy evolves.

Even with the new generation 8-10 m telescopes, determining the metallicity of individual stars becomes impossible for distances greater than 1 Mpc (Annibali; Tosi, 2022). As a consequence, the analysis of the chemical composition of extragalactic SFDs is usually based on the composition of their ionized gas (Kirby et al., 2013; Annibali; Tosi, 2022; Taibi et al., 2022). In practice, the metallicity of the gas phase is typically quantified using the Oxygen abundance relative to H. Oxygen is a convenient and reliable choice for abundance determination because it exhibits many bright emission lines in the optical and most of its ionization stages can be observed (Kunth; Östlin, 2000, a deeper discussion on this topic is provided in §3.4).

The determination of gas-phase metallicity in SFDs is facilitated by their characteristic optical spectra, often presenting strong nebular emission lines superimposed on a blue stellar continuum (Kunth; Östlin, 2000). For instance, abundance determinations from H II regions in dwarf irregulars within the Local Group, M81 and Sculptor, show metallicities ranging from $1/3\,Z_\odot$ to $1/50\,Z_\odot$ (Mateo, 1998; Miller; Hodge, 1996; Miller, 1996; Izotov et al., 2018). Gas-phase metallicity determinations of SFDs show they are metal-poor, with a mean distribution of $12 + \log(\mathrm{O/H}) \approx 8.1$ (Kunth; Östlin, 2000; Papaderos et al., 2008), which includes extremely metal-deficient galaxies (XMD[5]). A galaxy is classified as XMD if it presents a gas-phase abundance of $12 + \log(\mathrm{O/H}) \leqslant 7.65$ ($\lesssim 0.1\,Z_\odot$[6]) (Kniazev et al., 2003; Pustilnik; Martin, 2007; Izotov; Thuan; Guseva, 2012; Filho et al., 2015). This class of dwarfs includes the most metal-poor galaxies known, with measured nebular O abundances below 3% that of the Sun (Searle; Sargent, 1972; Izotov; Thuan; Guseva, 2012; Guseva et al., 2015; Hirschauer et al., 2016; Izotov et al., 2018).

[5] The term extremely metal-poor (XMP) is also frequently found in the literature.
[6] Throughout this work we adopt $12 + \log(\mathrm{O/H})_\odot = 8.69$ (Asplund et al., 2009).

1.4 The mass-metallicity relation

Gas-phase metallicity traces the secular and dynamic processes leading to galaxy chemical enrichment, as it is influenced by gas inflowing and outflowing into the galaxy ISM and metallic material released into the surroundings by stars. During a galaxy lifetime, metals can be ejected through several mechanisms (e.g., stellar/galactic winds, supernovae explosions, ram-pressure stripping) and (re)accreted later, in a manner that these processes also affect stellar mass (Finlator; Davé, 2008). For example, several spatially resolved studies of gas-phase metallicity in dwarfs using Integral Field Spectroscopy (IFS) have found metallicity drops associated with locations of increased Star Formation Rate (SFR), possibly tracing starbursts triggered by the infall of pristine gas from the Intergalactic Medium (IGM) (Sánchez Almeida et al., 2014; Sánchez Almeida et al., 2015; Ceverino et al., 2016; del Valle-Espinosa et al., 2023). Furthermore, metallicity inhomogeneities can be caused by the outflow of metals in stellar or galactic-scale winds and supernovae explosions (Mashchenko; Wadsley; Couchman, 2008; Chisholm et al., 2015; Silich; Tenorio-Tagle, 2017; Silich; Tenorio-Tagle, 2018), and mixing of metals within the ISM (Werk et al., 2011; Marasco; Fraternali; Binney, 2012). The environment also plays a fundamental role: Although ram-pressure stripping (Gunn; Gott J. R., 1972) compresses the gas along the leading edge of the disk (Rasmussen; Ponman; Mulchaey, 2006; Poggianti et al., 2019), causing an SFR enhancement during the peak of the stripping phase (Vulcani et al., 2018; Roman-Oliveira et al., 2019), the removal of the gas supply turns ram-pressuring stripping into an important quenching mechanism for satellite galaxies (Vollmer et al., 2001; Vulcani et al., 2020; Cortese; Catinella; Smith, 2021).

From this complex interplay between secular and dynamical processes that galaxies undergo, the Mass-Metallicity Relation (MZR) emerges as an empirical relation showing that low-mass galaxies typically exhibit a less chemically enriched ISM (Lequeux et al., 1979; Matteucci, 1994; Tissera; De Rossi; Scannapieco, 2005; Brooks et al., 2007; Revaz; Jablonka, 2018). The MZR holds for wide ranges of gas-phase metallicities and stellar masses and is used as an observational constraint for galaxy evolution models (Tremonti et al., 2004; Andrews; Martini, 2013). In Fig. 3, we present the MZR from Andrews and Martini (2013), obtained from the spectra of $\approx$ 200.000 galaxies from the Sloan Digital Sky Survey (SDSS) that were stacked in bins of mass within the range $7.4 \leqslant \log(M/M_{\odot}) \leqslant 10.5$. The solid gray line represents the trend found by Tremonti et al. (2004) using individual measurements of Oxygen abundance and stellar mass for a compilation of more than 50.000 SDSS spectra. The dashed and dotted gray lines correspond to the lines enclosing 67% and 95% of the data, respectively, where the mean trend was obtained by fitting the galaxies in stellar mass bins of 0.1 dex.

An explanation for the trend observed in the MZR, which reveals that low-mass galaxies tend to exhibit more metal-poor ISM in comparison to their massive counterparts,

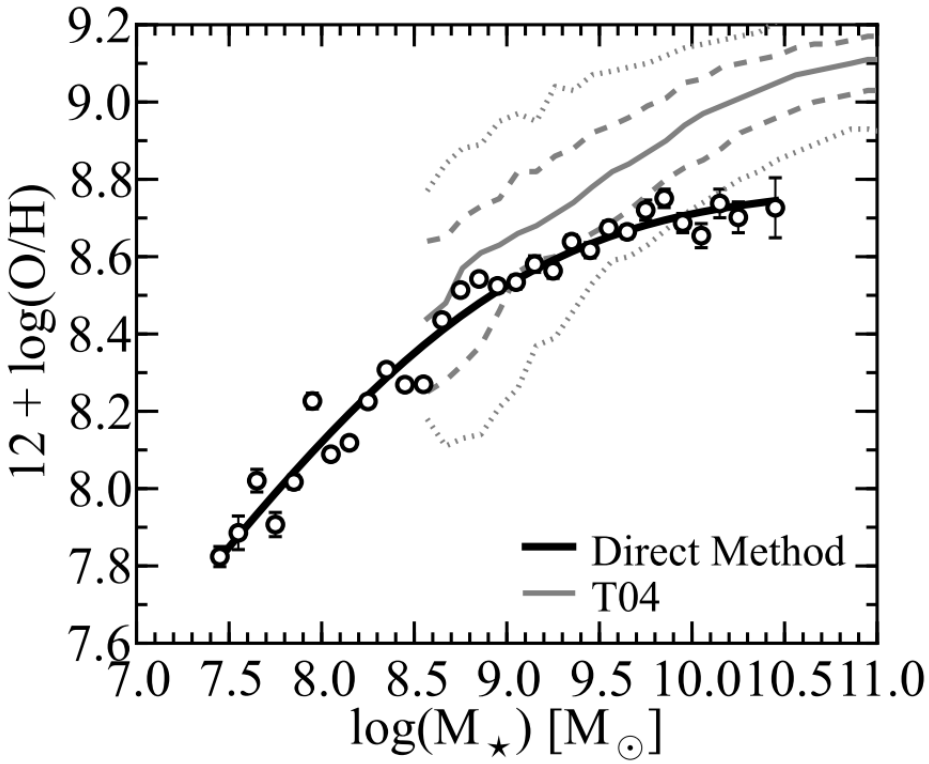

Figure 3 – Mass-Metallicity Relation (MZR), created from spectra of ≈ 200.000 SDSS galaxies, stacked in bins of mass within the range $7.4 \leqslant \log(M/M_{\odot}) \leqslant 10.5$ (white circles). Oxygen abundances were obtained from auroral emission lines in the stacked spectra using the T_e–based method (see §3.4). In gray, the MZR found by Tremonti et al. (2004) (T04) using individual measurements of more than 50.000 SDSS galaxy spectra. The solid gray line represents the T04 trend for mass bins spaced by 0.1 dex, while the dashed and dotted gray lines correspond to the lines containing 67% and 95% of the sample, respectively. Credit: Andrews and Martini (2013).

is that the shallower gravitational potentials of dwarf galaxies make them more sensitive to perturbations like those mentioned above, and less efficient in retaining the enriched material when compared to higher-mass galaxies (Finlator; Davé, 2008; Hayward; Hopkins, 2017; Christensen et al., 2018). The correlation observed in the MZR can also be explained by the relationship between star formation efficiency and stellar mass: Several chemical evolution models (Lequeux et al., 1979; Matteucci, 1994) and N-body/hydrodynamical simulations (Tissera; De Rossi; Scannapieco, 2005; Brooks et al., 2007; de Rossi; Tissera; Scannapieco, 2007; Mouhcine et al., 2008) support the scenario where more massive galaxies evolve faster, quickly forming the bulk of their stellar content and raising the metallicity of the ISM in violent bursts occuring at high redshifts (Calura et al., 2009; Magrini et al., 2012; Pipino; Calura; Matteucci, 2013).

However, at a fixed stellar mass, galaxies with higher SFRs have been found to be systematically offset towards lower metallicities (Ellison et al., 2008; Andrews; Martini, 2013; Maiolino; Mannucci, 2019). Moreover, at $\log(M/M_{\odot}) \lesssim 10.5$ a substantial scatter in the MZR is found, with a strong anti-correlation between SFR and gas-phase metallicity and systematic segregation in the MZR when galaxies are binned according to their SFR

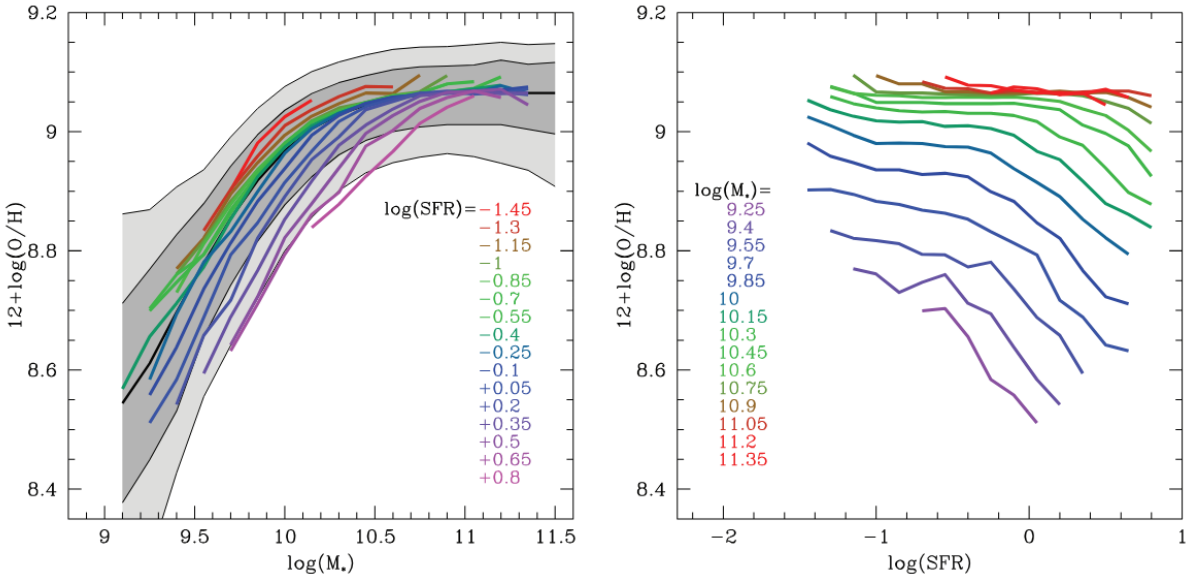

Figure 4 – *Left panel*: The dependence of SFR in the MZR. The gray shadowed regions correspond to the MZR regions containing 64% and 90% of the large SDSS galaxy sample used by Tremonti et al. (2004), with the thick black line indicating the median trend. Different lines represent the MZR now considering SFR bins over the galaxy sample (The SFR level of each bin is indicated on the label). *Right panel*: The relation between gas-phase metallicity and SFR, with the SDSS galaxy sample binned according to stellar mass (see label). Both trends show a clear segregation in the relations for galaxies with stellar masses $\log(M/M_{\odot}) \lesssim 10.5$. Credit: Mannucci et al. (2010).

(see Fig. 4) (Mannucci et al., 2010; Lara-López et al., 2010). This suggests an underlying dependence of SFR on the MZR, which led to the proposal of a 3D relation between $M_{\star}$, Z, and SFR, named the Fundamental Mass-Metallicity Relation (FMR), aiming to account for this dependency and alleviate the scatter in the MZR scatter at the lower-mass end (Maiolino; Mannucci, 2019). One possible explanation for the emergence of this secondary effect is the complex combination of outflows of enriched material due to supernovae explosions and inflows of pristine gas triggering starbursts (Davé; Finlator; Oppenheimer, 2011; Ceverino et al., 2016; Torrey et al., 2018). This is supported by N-body simulations indicating the role of rapid metal-poor gas accretion in feeding ongoing star formation in isolated BCDs (Verbeke et al., 2014).

While the FMR reveals that the ISM chemical evolution, probed by galaxy gas-phase metallicity, is tightly correlated with galaxy stellar mass, a recent study used a sample of $\gtrsim 7.000$ galaxies from the Mapping Nearby Galaxies at Apache Point Observatory (MaNGA) survey (Bundy et al., 2015) to show that this chemical evolution is imprinted in the stellar metallicity, originating a stellar Fundamental Mass-Metallicity Relation (Looser et al., 2024). In Fig. 5 we show the derived stellar FMR, where $\langle$[M/H]$\rangle$ corresponds to the luminosity-weighted mean stellar metallicity obtained through a stellar population fitting with the Penalized PiXel Fitting code (Cappellari; Emsellem, 2004; Cappellari, 2017, pPXF). The original sample was separated and color-coded into six bins according

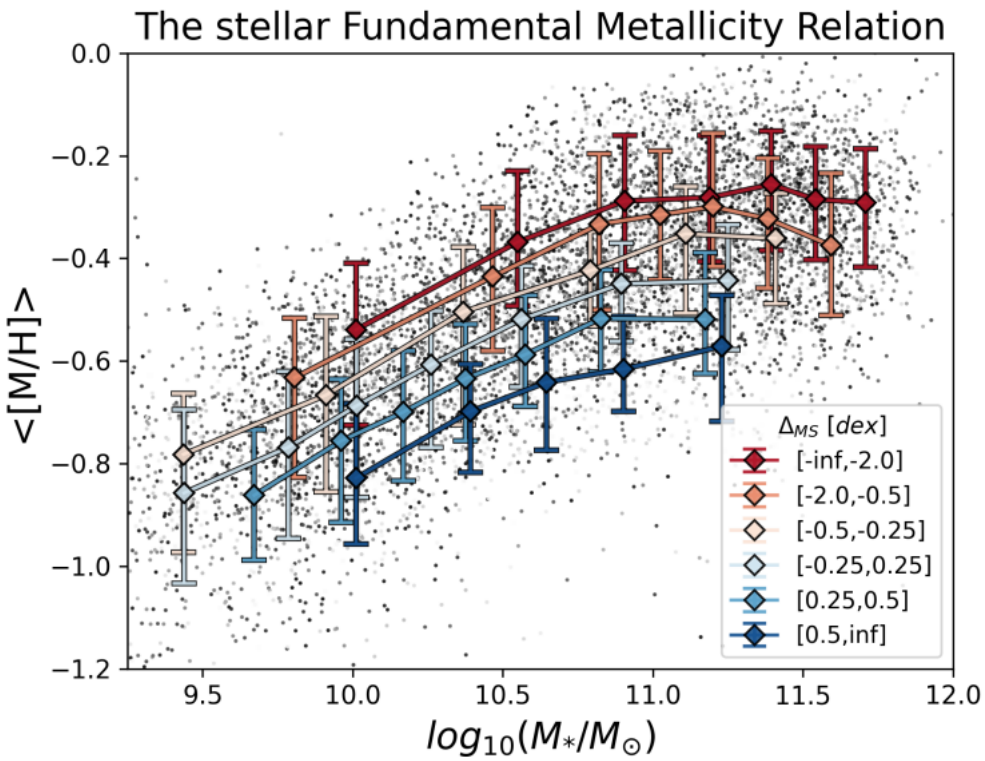

Figure 5 – Stellar fundamental mass metallicity relation. Gray dots represent individual galaxies from a sample of more than 7000 galaxies from MaNGA. Luminosity-weighted mean stellar metallicities ($\langle$[M/H]$\rangle$) are obtained through stellar population fitting with pPXF. The original sample is divided and color-coded into six bins according to the distance of each galaxy with respect to the star-forming main sequence ($\Delta_{\rm MS}$), where the bin definition is shown in the label. The six curves are fit considering adaptive bins on stellar mass (colored diamonds), where each bin is required to contain at least 80 galaxies. Credit: Looser et al. (2024).

to the distance of each galaxy with respect to the star-forming main sequence ($\Delta_{\rm MS}$), with bin definitions expressed in the label. An adaptive binning scheme with respect to stellar mass intervals is applied to all six curves (colored diamonds in Fig. 5), where each bin is required to contain at least 80 galaxies. The emerging trend is that, similar to the FMR, more massive galaxies have more metal-rich stars and a clear separation between starburst and passive galaxies is evident in Fig. 5, as observed in Fig. 4. Starvation[7] and the continuous accretion of metal-poor gas are attributed by the authors as the main processes responsible for shaping galaxy mass and chemical evolution, either via quenching or fueling new episodes of star formation (Looser et al., 2024).

1.5 Star clusters

Giant Molecular Clouds (GMC) are the birthplaces of stars and star clusters (Gieles et al., 2006; Kennicutt; Evans, 2012; Elmegreen, 2018; Rigby et al., 2019). The challenge of linking the stages between the molecular cloud physics and the formation of stars has

[7] When star formation is suppressed by the halting of gas accretion (Trussler et al., 2020).

motivated large-scale and Galactic-plane surveys over the past few decades (Rigby et al., 2019). Both simulations (Klessen et al., 2005; Padoan et al., 2016) and observations from surveys based on molecular line transitions (Elmegreen, 2000; Rathborne et al., 2009) indicate high velocity dispersion in the interior of GMCs, with turbulence levels higher than those produced solely by thermal turbulence (Larson, 1981; Rigby et al., 2019), suggesting a supersonic turbulent medium that accelerates the formation and dissipation of the clouds. Stars are formed within the densest regions of these clouds, where the gas is formed predominantly by molecular Hydrogen (H_2) with typical temperatures of $10 - 20\,\mathrm{K}$ (Roman-Duval et al., 2010). Observations in the Milky Way have shown that $\gtrsim 70\%$ of stars formed in GMCs are embedded star clusters, i.e., clusters fully or partially surrounded by interstellar gas and dust (Lada; Lada, 2003). These findings led to the generalization of star formation processes as clustered processes, with bound star clusters representing the inner group of stars in the fractal pattern produced by this hierarchical star formation model, which extends from a few pc to much larger kpc-sized stellar complexes (Gouliermis, 2018; Chevance et al., 2023).

During the collapse and fragmentation of a GMC, approximately 30% – 60% of the available molecular gas is effectively turned into stars (Lada; Lada, 2003). Soon after stars are formed, stellar winds and the first supernova explosions remove the gas from the embedded star-forming clusters on timescales shorter than a crossing time[8] (Goodwin, 1997; Bastian; Goodwin, 2006). Once the gas is removed, most of the observed young stars become unbound as they have the time to dynamically drift apart. Surveys of external galaxies support this conclusion, where the counts of star clusters as a function of age imply that about 10% of formed stars remain in bound structures after several tens of Myr after their formation (Adamo et al., 2015; Messa et al., 2018; Krumholz; McKee, 2020). The properties of GMCs and the star cluster formation process are intrinsically related to the galaxy environment and its global SFH (Schruba; Bialy; Sternberg, 2018; Schruba; Kruijssen; Leroy, 2019).

Young Star Clusters (YSCs) are luminous and compact objects embedded in dust, and the formation of massive ($> 10^5\,M_\odot$) star clusters is favored by the ISM conditions found in merging/interacting and starburst galaxies (Larsen; Richtler, 1999; Bastian; Goodwin, 2006; Whitmore et al., 2010; Whitmore et al., 2014; Adamo et al., 2020). BCDs, for instance, have been observed to host significant amounts of massive YSCs (Östlin et al., 2003; Adamo et al., 2010; Adamo; Östlin; Zackrisson, 2011; Bik et al., 2018). Analysis of the Initial Cluster Mass Function (ICMF) in present-day spiral disks provides further evidence that star cluster formation is favored by high-pressure environments such as wet mergers and galaxies with complex gas kinematics (Larsen, 2009). In the last few decades, high-resolution imaging has revealed the presence of star clusters inside star-forming

[8] The crossing time is defined as $t_{\mathrm{cross}} \equiv R/V$, where R is the radius of the cluster and V the velocity of stars in the cluster.

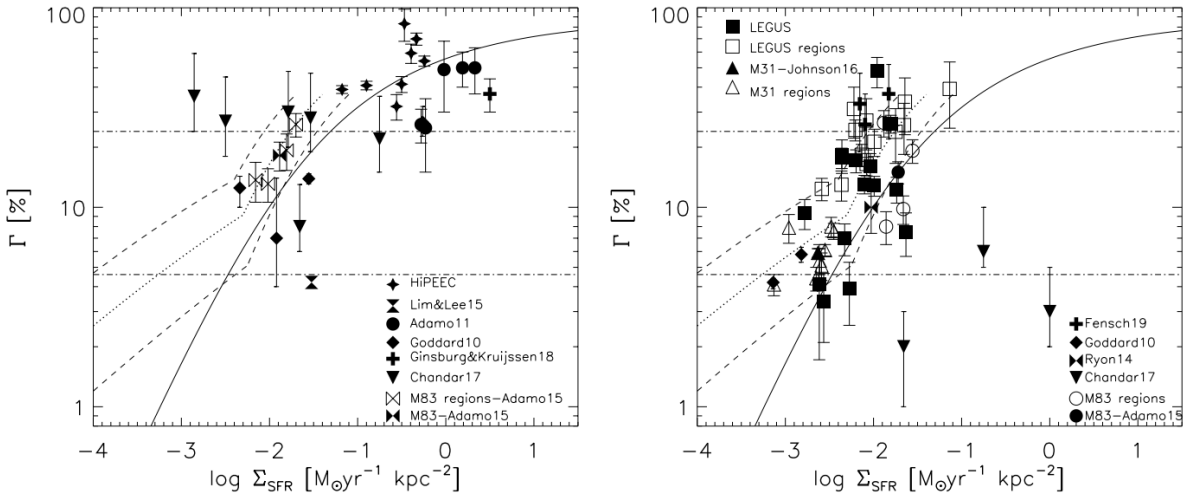

Figure 6 – Compilation of the Cluster Formation Efficiency (Γ) for star clusters in different galaxies. In the left panel, only YSCs ($1 < t\,(\mathrm{Myr}) < 10$) are included. The solid black line corresponds to the model from Kruijssen (2012), obtained using the Kennicutt-Schmidt law (Kennicutt, 1998b), while the dotted and dashed lines consider the conversion between Σ_{gas} and Σ_{SFR} proposed by Bigiel et al. (2008). Horizontal dot-dashed lines correspond to the constant Γ values proposed by Chandar et al. (2017) considering star clusters between 1 and 10 Myr (24%) and 10 Myr and 100 Myr (4.6%). In the right panel, star clusters with $t > 10\,\mathrm{Myr}$ are shown. Credit: Adamo et al. (2020).

regions within spiral galaxies (Bresolin; Kennicutt; Stetson, 1996; Christian; Schommer, 1988; Cantiello; Brocato; Blakeslee, 2009), merging systems (Whitmore; Schweizer, 1995; Ashman; Zepf, 1998; Larsen; Richtler, 1999; Wilson et al., 2006; Väisänen et al., 2008) and also in dwarf galaxies, including dwarf post-starburst galaxies (Anders et al., 2004; Annibali et al., 2009; Annibali et al., 2011) and starburst regions in BCDs (Östlin; Bergvall; Roennback, 1998; Östlin et al., 2003; Adamo et al., 2010; Zhang et al., 2020, §5.1). More recently, JWST observations have found a Globular Cluster (GC) population in the lensed $z = 1.38$ Sparkler galaxy (Mowla et al., 2022; Adamo et al., 2023), stellar clump populations in 18 high-z ($1 \lesssim z \lesssim 8.5$) galaxies within the lensing cluster field SMACS0723 (Claeyssens et al., 2023) and bound star clusters in the Cosmic Gems arc, a highly magnified lensed $z \sim 10.2$ galaxy (Adamo et al., 2024b).

Due to the aforementioned hierarchical nature of star formation, star clusters are closely related to the triggers of starburst activity and to past and ongoing star formation processes. The initial environmental conditions in which the star clusters formed and the mechanisms driving their evolution leave imprints that are incorporated into the Cluster Luminosity Function (CLF). The CLF synthesizes several star cluster populations assembled at different ages, making it intrinsically related to star formation processes (Adamo et al., 2020). Additionally, the mass and luminosity of the clusters are constrained by physical conditions such as the mass of the progenitor GMC, pressure, and ISM density (Lada; Lada, 2003). The intrinsic connection between the clusters and the star formation processes in the host galaxy are probed by the cluster-host relations (See Fig. 6). For

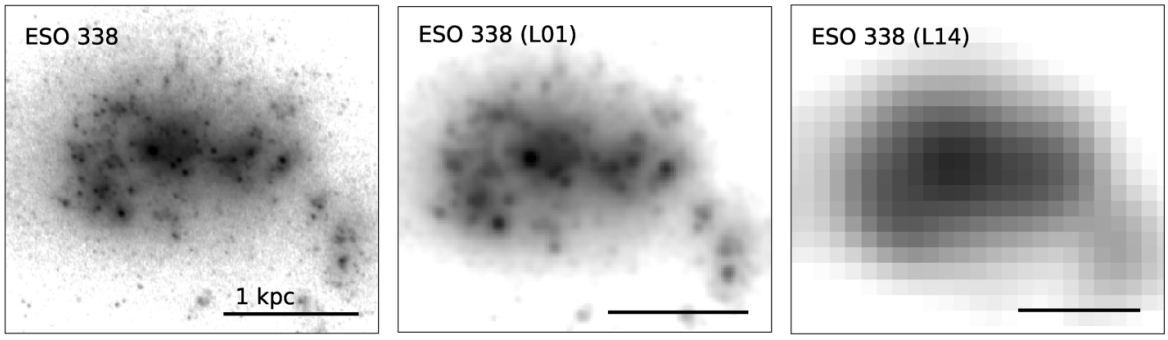

Figure 7 – Effect of decreasing spatial resolution in the detection of star clusters. In the left panel, the original HST image of ESO 338-IG04 in F140LP filter, corresponding to a rest-frame wavelength of ∼1500Å. The galaxy distance is approximately 38 Mpc, and the star clusters can be clearly observed. In the middle and right panels, simulated images of ESO 338-IG04 at the distances of 120 Mpc and 646 Mpc, respectively. Credit: Messa et al. (2019).

instance, higher Cluster Formation Efficiency[9] (CFE or Γ) has been found to correlate with the Star Formation Rate surface density ($\Sigma_{\rm SFR}$), and a correlation between the visual luminosity of the brightest star cluster ($M_V^{\rm brightest}$) and the SFR of the host galaxy has also been observed (Larsen, 2002; Bastian, 2008; Adamo; Östlin; Zackrisson, 2011).

1.6 Stellar clumps and UV clumpy galaxies

With increasing distances, star clusters become unresolved even for instruments with high spatial resolution like the Hubble Space Telescope (HST). For instance, at $d \gtrsim 20$ Mpc, star clusters appear as point-like sources at HST resolution (Chies-Santos et al., 2011; Adamo et al., 2020). At $d \gtrsim 80$ Mpc, the entire 30 Doradus[10] region would fit within a single HST pixel. Therefore, at higher distances, the observed bright compact structures are actually blends of smaller unresolved star-forming entities such as star clusters and H II regions, referred to as stellar clumps (Messa et al., 2019; Adamo et al., 2020). In Fig. 7, we illustrate the effect of spatial resolution loss due to increasing distances for ESO 338-IG04, observed with HST (left panel), from which it is possible to see several star clusters at the distance of $d \approx 38$ Mpc. However, as the distance increases, some star clusters blend together and, at even higher distances, only a few blurred clumps can be observed (right panel).

The morphologies of $z \gtrsim 1$ star-forming galaxies are usually more asymmetric than their local-Universe counterparts. Recent JWST observations focusing on the analysis of galaxy triaxial morphologies indicated that the fraction of prolate galaxies among low-mass ($9.0 < \log(M_\star/M_\odot) < 9.5$) galaxies increases with redshift, whereas the fraction of disks

[9] Defined as the fraction of total stellar mass that was formed in clusters, per unit time over a given age interval.

[10] 30 Doradus (30 Dor) is a giant H II region located in the LMC, hosting few massive stars ($\sim 300\,M_\odot$) and star clusters with stellar masses exceeding $10^5\,M_\odot$ (Chu; Kennicutt, 1994; Adamo et al., 2020).

in dwarfs increases in the local Universe (Pandya et al., 2024). High-z galaxies are also more irregular than nearby galaxies (Conselice; Bershady; Jangren, 2000; Elmegreen et al., 2005a; Fisher et al., 2017b; Huertas-Company et al., 2024), with morphologies typically dominated by kpc-sized stellar clumps (Cowie; Hu; Songaila, 1995; van den Bergh et al., 1996; Elmegreen et al., 2005b; Dekel; Sari; Ceverino, 2009; Messa et al., 2019), when very high gas fractions are usually observed (Daddi et al., 2010; Tacconi et al., 2013). In clumpy high-z galaxies, the clumps can account for ∼50% of the galaxy UV rest-frame emission (Elmegreen et al., 2005b; Messa et al., 2019), which is particularly interesting since the UV flux is an excellent tracer of young stellar populations, as it covers the wavelength range of the ionizing photons (Kennicutt, 1998a, see §3.1 and §3.6).

Using a sample of ∼17.000 galaxies observed with HST in the redshift range $0 < z < 8$, Shibuya et al. (2016) investigated the cosmic evolution of the fraction of rest-frame UV clumpy galaxies ($f^{UV}_{\rm clumpy}$). We present the obtained relation in Fig. 8, where the curve of cosmic Star Formation Rate Density (SFRD, see Fig. 9)(Madau et al., 1996; Lilly et al., 1996; Madau; Dickinson, 2014) is also included (solid black line), in arbitrary units for the y-axis. The cyan and blue circles correspond to the fraction of UV clumps among star-forming galaxies and Lyman Break Galaxies (LBGs), respectively, while the cyan solid line corresponds to the best-fit redshift-dependent $f^{UV}_{\rm clumpy}$ curve obtained by Shibuya et al. (2016). The red and green shaded regions correspond to the fractional galaxy merger rate from Lotz et al. (2011) for major (between mass ratios 1:1 and 1:4) and minor (between mass ratios 1:4 and 1:10) mergers, respectively. Interestingly, these do not correlate with the best-fit $f^{UV}_{\rm clumpy}(z)$ across a wide range of redshifts, indicating that mergers cannot solely account for clumpy star formation. Interestingly, the cosmic evolution of UV clumpy galaxies roughly follows the evolution of the SFRD, as shown in Fig. 9.

In addition to redshift, the fraction of clumpy star-forming galaxies also depends on stellar mass. In the redshift range $0.5 < z < 3$, up to 60% of galaxies with masses $\lesssim 10^{9.8}\,M_\odot$ exhibit clumpy morphologies in the UV, while this fraction drops to 15% – 55% for higher-mass star-forming galaxies in the same redshift range (Guo et al., 2018; Förster Schreiber; Wuyts, 2020). As mentioned earlier, clumps host young stellar populations and are sites of active star formation, with SFR values reaching up to $10\,M_\odot\,{\rm yr}^{-1}$ per clump in higher-z galaxies (Elmegreen et al., 2005b; Genzel et al., 2011; Soto et al., 2017; Fisher et al., 2017b; Förster Schreiber; Wuyts, 2020), with typical individual stellar masses lying in the range $10^8 \lesssim (M/M_\odot) \lesssim 10^9$ (Wisnioski et al., 2012; Tacconi et al., 2013; Messa et al., 2019). However, high-resolution data supported by gravitational lensing found lower values for clumps in the Cosmic Snake, suggesting that the reported clump sizes and masses might be systematically overestimated due to the spatial resolution limitations of current instruments (Cava et al., 2018). If the physical size of the clumps is smaller than the image resolution, several clumps could be blended together into a combined clump artificially

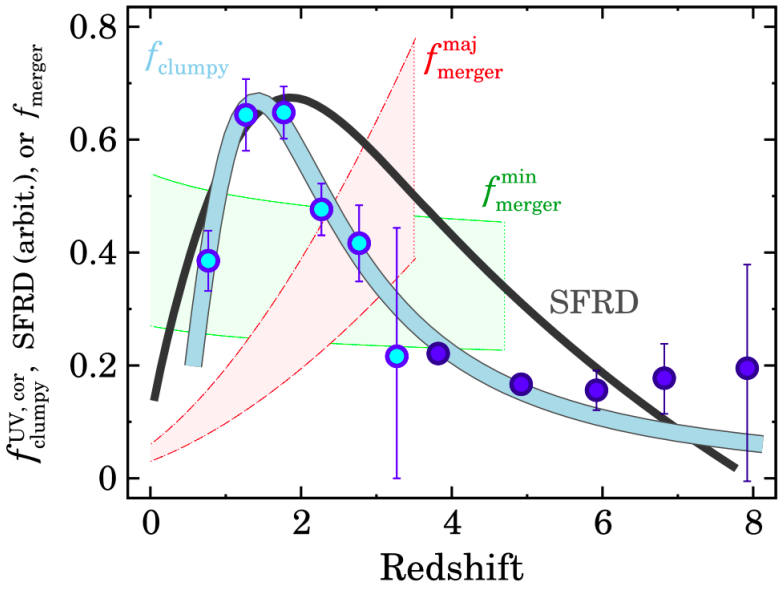

Figure 8 – Cosmic evolution of the the fraction of rest-frame UV clumpy galaxies ($f^{UV}_{\rm clumpy}$), represented by the solid cyan line. Cyan and blue circles correspond to estimated fractions of UV clumpy galaxies among star-forming and Lyman Break galaxies, respectively, from a sample of ∼17.000 galaxies observed with HST in the redshift range $0 < z < 8$. The black solid line corresponds to the SFRD (Madau et al., 1996; Lilly et al., 1996; Madau; Dickinson, 2014), and the red and green shaded regions correspond to the fractional galaxy merger rate from Lotz et al. (2011) for major and minor mergers, respectively. Credit: Shibuya et al. (2016).

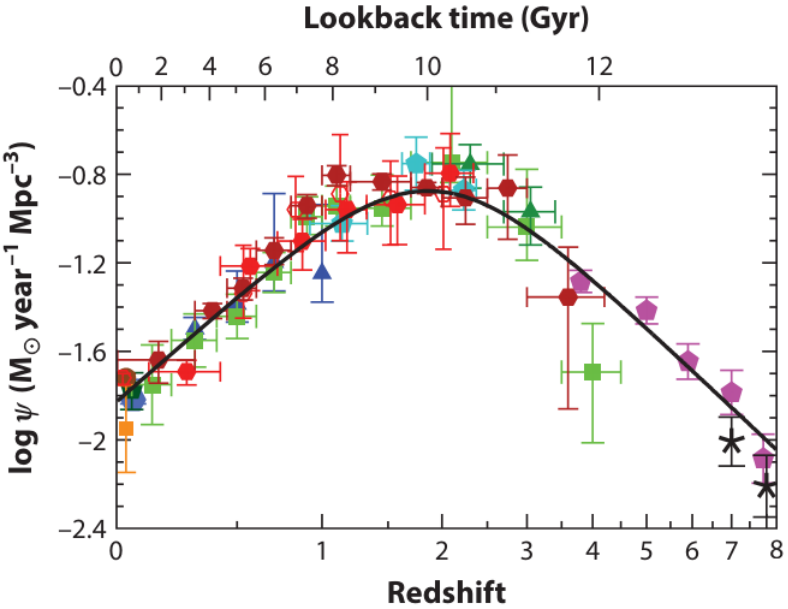

Figure 9 – Star Formation Rate Density (SFRD, ψ) across the redshift range $0 < z < 8$, obtained using compiled FUV and IR rest-frame measurements from: (Wyder et al., 2005, Blue-gray hexagon), (Schiminovich et al., 2005, Blue triangles), (Robotham; Driver, 2011, Dark green pentagon), (Cucciati et al., 2012, Green squares), (Dahlen et al., 2007, Turquoise pentagons), (Reddy; Steidel, 2009, Dark green triangles), (Bouwens et al., 2012a; Bouwens et al., 2012b, Magenta pentagons), (Schenker et al., 2013, Black crosses), (Sanders et al., 2003, Brown circle), (Takeuchi; Yoshikawa; Ishii, 2003, Dark orange square), (Magnelli et al., 2011, Red open hexagons), (Magnelli et al., 2013, Red filled hexagons), (Gruppioni et al., 2013, Dark red filled hexagons). The best-fit model indicated by the solid black line shows the Universe reached the peak of its star formation history around $z \approx 2$ (Cosmic Noon), and has been decreasing since then. Credit: Madau and Dickinson (2014).

boosted towards high stellar mass values (Elmegreen et al., 2013; Dessauges-Zavadsky et al., 2017; Tamburello et al., 2017; Cava et al., 2018). On the other hand, there is also evidence supporting the evolution of clump properties with redshift (Livermore et al., 2015). Summarizing all these considerations, clumps around the Cosmic Noon[11] tend to be larger, brighter, and more massive than their nearby analogues, also presenting much higher SFRs and specific Star Formation Rates (sSFR) (Guo et al., 2012; Fisher et al., 2017a).

In the last few decades, there have been substantial efforts to explain how these clumps formed and why they became more uncommon in the Local Universe, with two main scenarios proposed. In the first scenario, clumps are formed mainly from major and minor mergers during the early stages of host galaxy mass assembly, when satellites are stripped and the remaining accreted nucleus turns into the observed massive *ex-situ* clumps, or serves as the trigger mechanism to produce local gravitational instabilities within the host galaxy that drive further gas collapse (Somerville; Primack; Faber, 2001; Hopkins; Kereš; Murray, 2013; Ribeiro et al., 2017). Observations and simulations suggest that only a minority of the high-z clumps are formed this way, so that the *ex-situ* mechanism is more common for host galaxies with masses of $\log(M/M_{\odot}) \lesssim 10$ (Mandelker et al., 2014; Guo et al., 2015; Zanella et al., 2019; Adams et al., 2022).

NIR high-resolution IFS observations of Hα emission lines have shown not only the nearly ubiquitous presence of clumps in high-z star-forming galaxies (Elmegreen et al., 2007; Dekel; Sari; Ceverino, 2009; Cava et al., 2018), but also large velocity dispersion in the ionized gas, ranging from $30\,\mathrm{km\,s^{-1}}$ to $120\,\mathrm{km\,s^{-1}}$ (Förster Schreiber et al., 2009; Bassett et al., 2014; Wisnioski et al., 2015). The high turbulence in the disks and the large gas reservoir allow the gas to fragment at much higher scales compared to $z \sim 0$ galaxies (Burkert et al., 2010; Tamburello et al., 2015). Such high turbulence generates large Jeans lenghts, leading to the second and most supported scenario for clump formation, the *in-situ* scenario, where clumps are generated from the collapse of gas-rich disk fragments caused by the Violent Disk Instability (VDI) (Noguchi, 1999; Dekel; Sari; Ceverino, 2009; Agertz et al., 2009; Bournaud et al., 2014).

The stability of a symmetric thin gas disk in rotation can be assessed with the Toomre parameter Q, named after the seminal paper of Toomre (1964). Assuming a gas-dominated disk, Q_{gas} can be expressed as follows (Binney; Tremaine, 2008; Escala; Larson, 2008; Dekel et al., 2009):

$$Q_{\mathrm{gas}} = \frac{\sigma_0\,\kappa}{\pi G \Sigma_{\mathrm{gas}}} \tag{1.1}$$

where σ_0 is the local gas velocity dispersion, G is the Newtonian constant of gravitation,

[11] The peak of SFRD, occurring around $z \sim 2$ (See Fig. 9).

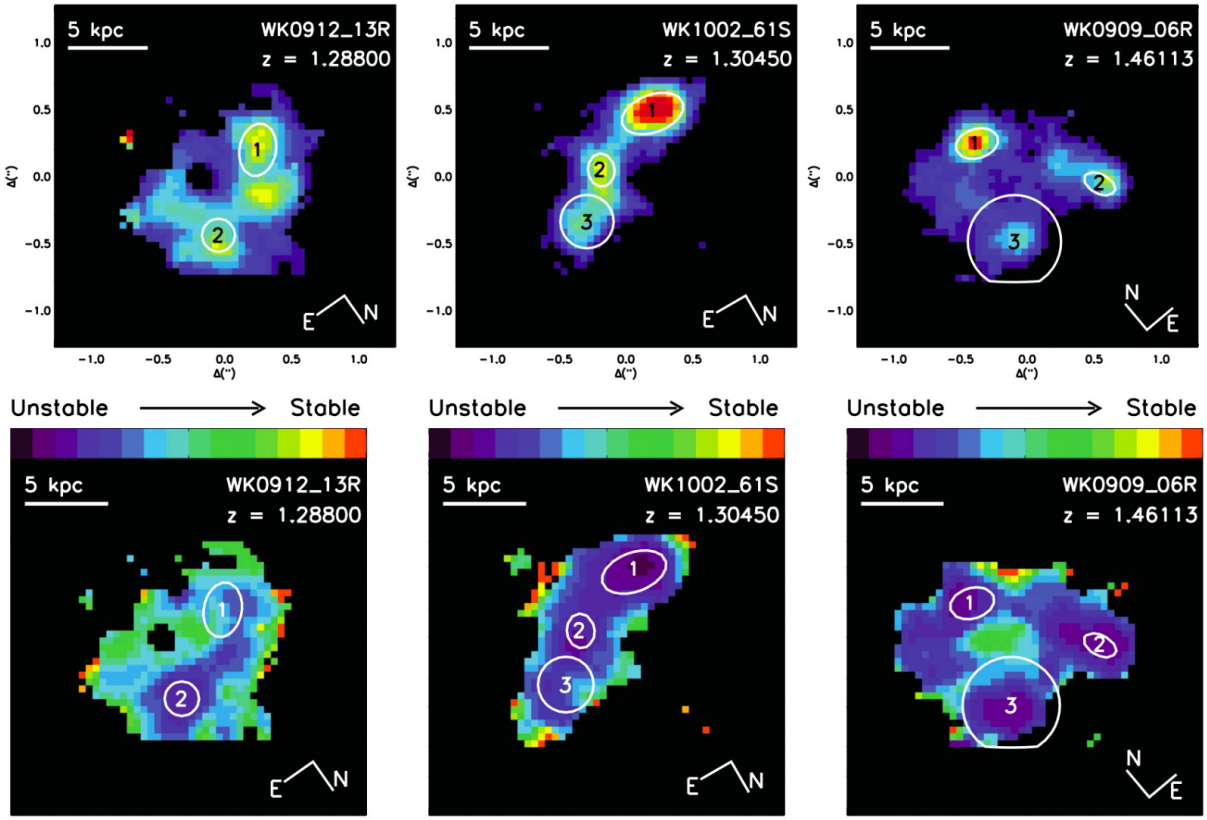

Figure 10 – *Top panel*: Smoothed Hα maps of three $z \gtrsim 1$ disk galaxies from the WiggleZ Dark Energy Survey (Drinkwater et al., 2010). The clumps are highlighted by the white circles. *Left panel*: Map of the Toomre parameter Q, where darker regions correspond to unstable regions (with lower values of Q). Noticeably, the clumps in these galaxies are located in regions of the disk with higher instability. Adapted from Wisnioski et al. (2012).

$\Sigma_{\rm gas}$ is the gas surface density and κ is the epicyclic frequency, which can be expressed in terms of the circular velocity v_c and the radius of the disk R as follow (Binney; Tremaine, 2008; Genzel et al., 2011):

$$\kappa^2 = \left(\frac{2\,v_c}{R}\right)^2 + R\,\frac{\mathrm{d}}{\mathrm{d}R}\left[\left(\frac{v_c}{R}\right)^2\right] \tag{1.2}$$

Combining Equations 1.1 and 1.2 yields (Genzel et al., 2011):

$$\begin{aligned} Q_{\rm gas} &= \frac{\sigma_0}{v_c} \times \frac{a}{\pi R^2 \Sigma_{\rm gas}} \times \frac{v_c^2 R}{G} \\ &= \frac{\sigma_0}{v_c} \times \frac{a}{f_{\rm gas}} \end{aligned} \tag{1.3}$$

where a is a constant equal to 1, $\sqrt{2}$, $\sqrt{3}$ and 2 for the Keplerian, constant velocity rotation, uniform density and solid body disk cases, respectively (Genzel et al., 2011). $Q_{\rm gas}$ represents the Toomre parameter for the gas, considering the molecular and atomic gas phases, with $Q^{-1} = Q_{\rm gas}^{-1} + Q_{\star}^{-1}$. The Toomre parameter serves as a criterion to establish

whether a given region within a disk is prone to gain density as a result of collapse driven by gravitational instability. Unstable regions are those presenting $Q \leq 1$ (Polyachenko; Polyachenko; Strel'Nikov, 1997).

One mechanism that can drive disks to become marginally stable and consequently cause the gravitational instabilities that originate the massive clumps in the *in-situ* scenario is cold accretion of intergalactic gas (Genzel et al., 2008; Bouché et al., 2013; Adams et al., 2022). The *in-situ* interpretation is supported by observations in $z \sim 1$ galaxies (Zanella et al., 2015; Dessauges-Zavadsky et al., 2019), rare analogues in the local Universe (Fisher et al., 2017a; Messa et al., 2019), simulations of turbulent high-z galaxies (van Donkelaar; Agertz; Renaud, 2022), and simulations predicting that galaxies with $f_{\rm gas} \geqslant 0.3$ have turbulent ISM and clumpy morphologies (Hayward; Hopkins, 2017). In the local Universe, highly turbulent ISM are found almost exclusively in low-mass galaxies (Bradford; Geha; Blanton, 2015). In Fig. 10, we show clumps located in regions of gravitational instability in the disks of $z \approx 1$ galaxies from the WiggleZ Dark Energy Survey (Wisnioski et al., 2012).

One of the major uncertainties in this scenario is the survival of the kpc-sized clumps in their host galaxies against the disruptive effects of tidal torques, mechanical forces and stellar feedback (Förster Schreiber et al., 2011). Low-resolution simulations of isolated gas-rich disk galaxies with gravitationally unstable disks were able to reproduce the kpc-sized clumps (Bournaud; Elmegreen; Elmegreen, 2007; Agertz et al., 2009). These clumps survived long enough to slowly migrate towards the center of the galaxy, contributing to the formation of the galactic bulge and thick disk (Ceverino; Dekel; Bournaud, 2010; Cava et al., 2018). However, this scenario is still a matter of debate, as the clump survival timescales are sensitive to the feedback prescriptions and implementations, and short-lived clumps were observed in cosmological simulations, in contrast to the long-lived clumps produced in isolated systems (Oklopčić et al., 2017; Fensch; Bournaud, 2021; Dekel et al., 2022; Claeyssens et al., 2023). Recent works suggest that the numerous massive stars within the star clusters and YSCs that make up the giant stellar clumps are responsible for extreme feedback within their host galaxies, suppressing the global star formation and, in some cases, facilitating the escape of UV radiation into the IGM (Goldbaum; Krumholz; Forbes, 2016; Bik et al., 2018).

In summary, stellar clumps are common structures at redshifts $z \approx 1-3$. These clumps are linked to the early stages of star formation and are poorly represented by the star formation processes typically occurring in nearby galaxies. However, there are rare $z \sim 0$ galaxies that share similar properties with these high-z turbulent disk galaxies, such as the DYNAMO sample (Green et al., 2014). Studying and characterizing these analogues at spatial scales unfeasible for their unlensed high-z counterparts can constrain the regulation of star formation processes and fill the gap between star clusters ($\sim$10 pc) and the massive clumps in distant galaxies ($\gtrsim$100 pc) (Fisher et al., 2017b; Fisher et al.,

2017a; Messa et al., 2019).

1.7 Extragalactic archeology

The hierarchical framework of galaxy formation originates from the ΛCDM model predictions highlighted in §1.1, setting dwarf galaxies as the "building blocks" of present-day more massive galaxies (Tosi, 2003; Revaz; Jablonka, 2018; Annibali; Tosi, 2022). As discussed in §1.2 – §1.4, SFDGs have plenty of gas to fuel future starburst events and, in terms of chemical content, they present metal-poor ($Z_{\rm gas} \lesssim 0.5\,Z_{\odot}$) ISM (Kunth; Östlin, 2000; Bergvall, 2012). Additionally, we have discussed in §1.6 that kpc-sized stellar clumps are common complexes of star formation around the Cosmic Noon (see Fig. 9), whereas the fraction of clumpy galaxies has been decreasing since then in a trend that roughly follows the SFRD evolution (Shibuya et al., 2016). Therefore, the conditions typically met around the peak of star formation in our Universe favor the formation of giant clumpy structures, suggesting that the star formation processes during the main epoch of massive galaxy build-up must have been different compared to what is observed in present-day galaxies.

The combination of low stellar masses, high gas fractions, elevated SFRs and chemically unevolved ISM make SFDGs the class of observable galaxies in the Local Universe that most closely resemble high-z star-forming galaxies (Shen et al., 2014; Izotov et al., 2021; Annibali; Tosi, 2022). In the context of galaxy formation and evolution, these galaxies represent key laboratories for studying star-formation processes and feedback under ISM physical conditions that might be representative of early Universe environments at small spatial scales unfeasible for unlensed high-z star-forming galaxies. For instance, with the small spatial scales provided by current instruments, we can study the star cluster populations in nearby dwarfs and their feedback into the host galaxy ISM, set constraints on the early stages of galaxy chemical evolution, deepen our understanding of the conditions that trigger clumpy star formation and explore the fate of the kpc-sized stellar clumps, among many other phenomena.

From a cosmological perspective, dwarf galaxies have served as important observational benchmarks for stress-testing the ΛCDM cosmological model at low scales over the last few decades, leading to several tensions between models and observations (Klypin et al., 1999; Moore et al., 1999; Boylan-Kolchin; Bullock; Kaplinghat, 2011; Boylan-Kolchin; Bullock; Kaplinghat, 2012, among others). For a complete and updated review on the challenges imposed by dwarf galaxies on the standard cosmological model, we refer to Sales, Wetzel and Fattahi (2022). Important to mention, recent JWST observations are challenging the ΛCDM cosmological model. While HST wavelength coverage primarily probed the young stellar populations of more distant galaxies, JWST covers the rest-frame

optical emission in distant galaxies, allowing us to trace the bulk of their stellar emission (Adamo et al., 2024a). This offers the exciting possibility of detailing the galaxy mass assembly processes in the first 500 Myr of our Universe (Harvey et al., 2024; Weibel et al., 2024). Unexpectedly massive galaxies were observed in the first JWST results (Labbé et al., 2023; Xiao et al., 2023), and massive quiescent galaxies have been spectroscopically reported for redshifts up to $z \sim 10$ (Carnall et al., 2023; Glazebrook et al., 2024; Setton et al., 2024). To explain the high values of stellar masses formed in such a short period, implausible star formation efficiencies have to be invoked (Boylan-Kolchin, 2023). However, spectroscopic follow-ups are necessary to learn more about the overly massive systems. Some authors have claimed, for instance, that the high stellar masses obtained via Spectral Energy Distribution (SED) fitting could be due to very high equivalent widths from strong emission lines in star-forming galaxies, dusty continuum or AGN contributions (Lovell et al., 2023; Barro et al., 2024; Desprez et al., 2024).

Although JWST is challenging the foundations of the hierarchical galaxy formation hypothesis, the study of local SFDGs remains very useful for constraining star-formation processes on small spatial scales across large galaxy samples and a wide variety of environmental conditions. To fully understand galaxy formation and evolution at high redshifts, we must continue learning from these fascinating tiny neighbors.

1.8 Goals

In this work, we present a spatially resolved detailed analysis of the ongoing star formation processes in two relatively nearby low-mass galaxies. Although two galaxies do not constitute a sample from which we can draw statistically significant conclusions about general star formation in dwarf galaxies, both galaxies exhibit unique characteristics that justify their individual detailed examination. These galaxies serve as interesting analogues of star formation processes and ISM conditions typically observed in $z \gtrsim 2$ star-forming dwarf galaxies and can help us providing insights into the processes driving galaxy formation and evolution.

The first galaxy is SDSS J020536-081424 , a $z \approx 0.04$ dwarf ($M_\star \approx 3 \times 10^9\, M_\odot$) irregular galaxy in interaction with the nearby massive ($\log(M_\star/M_\odot) \approx 11$) ETG Mrk 1172. The dwarf has sub-solar gas-phase metallicity ($8.0 \lesssim 12 + \log(\mathrm{O/H}) \lesssim 8.6$) and exhibits kpc-sized clumps when observed in the Hα wavelength range, with signs of rotation resembling a disk component. Throughout sections §4.1 and §4.2, we will focus on the characterization of the ionized gas physical conditions in the dwarf and on the investigation of the scenarios of clump formation discussed in §1.6. The second galaxy analyzed in this work (see §5.1) is ESO 400-43 , a $M_\star \approx 10^9\, M_\odot$ metal-poor (mean $12 + \log(\mathrm{O/H}) \approx 8.2$) $z \approx 0.02$ Blue Compact Galaxy (BCG) with high star formation activity and a

numerous star cluster population. We aim to combine IFS data aided by an Adaptive Optics (AO) system and high-resolution imaging from HST to constrain the properties of the star cluster population and investigate their feedback into the ionized galaxy ISM.

In §2 we present the data used in this work, including the data reduction steps. This chapter also provides further details on both galaxies, including previous related studies found in the literature. In §3, we describe the techniques employed in our analysis, including a brief discussion about the background physical motivations of each method. The analysis is divided into two chapters: One for SDSS J020536-081424 (§4), and one for ESO 400-43 (§5). We conclude this work by summarizing our findings and briefly discussing the next planned steps in §6.

2 Data and Observations

In this chapter we present the data analyzed in this work, describing the spectroscopic and imaging observations used. In §2.1 we briefly introduce the two galaxies and previous studies about them in the literature. In the data description, which includes data reduction, we separate this chapter in spectroscopic (§2.2) and imaging (§2.3) observations.

2.1 Description of the targets

2.1.1 SDSS J020536-081424

The sky region containing SDSS J020536-081424 was mapped by SDSS, providing optical photometry for the dwarf galaxy and the ETG Mrk 1172. For Mrk 1172, spectroscopic data was obtained from an integration over the typical 3″ aperture size of SDSS fibers (York et al., 2000), with a redshift of $z = 0.04115 \pm 0.00001$ determined in the SDSS Data Release 9 (Ahn et al., 2012). To the best of our knowledge, the first analysis of the dwarf irregular galaxy SDSS J020536-081424 was performed by Lassen et al. (2021, see §4.1), where strong emission lines in the integrated spectrum of SDSS J020536-081424 were used to determine a redshift of $z = 0.04025 \pm 0.00003$ (see Chapter §4). Assuming a WMAP9 cosmology (Planck Collaboration et al., 2014), this corresponds to a luminosity distance of $d_L \approx 180$ Mpc. SDSS J020536-081424 was also observed in the Near Ultra-Violet (NUV) and Ultra-Violet (UV) by the Galaxy Evolution Explorer (GALEX) space telescope (Martin et al., 2005) and on the optical and part of the Near Infrared (NIR) with the g', r', i', z', Y filters (Respective central wavelengths [Å]: 4770.8, 6371.3, 7774.2, 9157.9, 9886.3[1]) of the Dark Energy Camera (DECam) Legacy Survey (Dey et al., 2019, DECaLS) with an angular sampling of ∼0.262″ per pixel (Dey et al., 2019). In Fig. 11 we present a color-composite image of the entire tile containing SDSS J020536-081424 and Mrk 1172, using the filters g', r', and z' as RGB channels, respectively. The transmission curves of each filter are shown in the inset plot. The zoom-in region corresponds to the 1 arcmin^2 Field of View (FoV) covered by the MUSE observations analyzed in this work. In the center of the image it is possible to see Mrk 1172, and on the top of the zoom-in panel the bright object is a cataloged star (Gaia EDR3 2463146603042188160). The source with irregular morphology located between the ETG and the star on the top is SDSS J020536-081424 .

[1] https://noirlab.edu/science/programs/ctio/filters/Dark-Energy-Camera

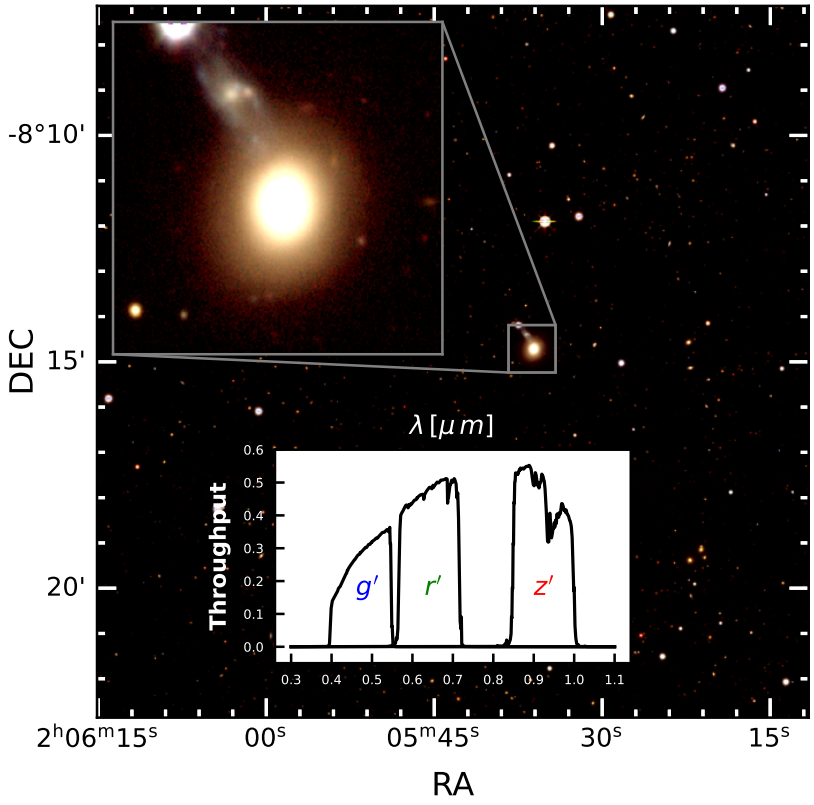

Figure 11 – Color-composite image of DECaLS on the sky region where the dwarf-ETG system is located. The RGB channels were built using the g', r' and z' filters, respectively, whose transmission curves are presented in the inset plot. Transmissions consider a median airmass of 1.4 (Dey et al., 2019). The zoom-in plot shows the MUSE FoV of our observations. SDSS J020536-081424 is the irregular source located between Mrk 1172 (bright source in the center) and the star Gaia EDR3 2463146603042188160 on top.

2.1.2 ESO 400-43

As far as we know, the first observations of ESO 400-43 were conducted between 1980 and 1982 using Charged-Coupled Device (CCD) images from the ESO 2.2 m telescope in U,B,V and i bands (Wade et al., 1979), and spectroscopy from the ESO 3.6 m (Bergvall; Jorsater, 1988). Different estimates for the stellar mass of ESO 400-43 suggest values on the order of $10^9\,M_\odot$ (Bergvall; Jorsater, 1988; Östlin et al., 2001), typical for dwarf galaxies. The fiducial redshift estimate of ESO 400-43 was obtained spectroscopically from observations with the United Kingdom Schmidt Telescope in the final redshift release (DR3) of the 6dF Galaxy Survey (Jones et al., 2009), where a value of $z = 0.019680 \pm 0.00003$ was reported. Assuming a WMAP9 cosmology (Planck Collaboration et al., 2014), this correspond to a luminosity distance of $d_L \approx 85$ Mpc. Using a large aperture covering the entire galaxy in the MUSE FoV, we extract an integrated spectrum for ESO 400-43 (see Fig. 15), from which strong emission lines are used to estimate a redshift of $z = 0.01965 \pm 0.00001$. Early studies already pointed to an irregular morphology with

blue colors, and spectroscopic analysis determined moderate extinctions ($A_V \approx 0.6$ mag), electron temperatures of $T_e \approx 1.2 \times 10^4$ and a very metal-deficient ISM with gas-phase metallicities of $Z_{\rm gas} \approx 1/8\, Z_\odot$ (Bergvall; Jorsater, 1988). Observations of ESO 400-43 in the 21 cm line from the Very Large Array of the National Radio Astronomy Observatory revealed the presence of a $\approx 5 \times 10^9\, M_\odot$ halo of atomic gas (H I) in slow rotation (Bergvall; Jorsater, 1988). This study also revealed the presence of a smaller companion located 2″ East of ESO 400-43 , typically referred as ESO 400-43 *b* (see Figures 12 and 13).

Using optical/NIR deep surface photometry, Bergvall and Östlin (2002) determined the presence of an old stellar population underlying the strong bursts of star formation in ESO 400-43 . By means of Fabry-Perot interferometry data, Östlin et al. (1999) employed a narrow-band interference filter around Hα emission line to study the kinematics of the ionized gas in ESO 400-43 , revealing a highly asymmetric behavior likely tracing past dwarf-dwarf merger events. The rotation curve was observed to reach a peak of $\pm 60\,{\rm km\,s^{-1}}$ close to the kinematic center of the galaxy, decaying even faster than expected for a Keplerian rotation curve (Östlin et al., 2001). The gas dynamics was reported to increase in complexity and irregularity towards the North-East region of the galaxy, with a possible presence of warps. Using the radial profiles of Hα and adopting a constant low-density value of electron density of $N_e = 10\,{\rm cm^{-3}}$ across the galaxy, Östlin et al. (1999) estimated an upper limit of $5.5 \times 10^8\, M_\odot$ for the mass of ionized gas in ESO 400-43 . Using long-slit spectroscopy from the FOcal Reducer/low dispersion Spectrograph 2 (FORS2) at the Very Large Telescope (VLT), Östlin et al. (2004) used the Ca triplet ([Ca II]$_{\lambda\lambda 8498,8542,8662}$) to describe the stellar kinematics in ESO 400-43 and compared it to the aforementioned Hα velocity field data to show the decoupling between stellar and gas kinematics in the ISM of ESO 400-43 , i.e. in contrast to the ionized gas, the stellar rotation curve follows the expected pattern of a solid body. Interestingly, radio observations of ESO 400-43 with the Very Large Array (VLA) in the wavelength windows 1415 MHz, 4885 MHz and 8414 MHz revealed a steeper ($S_\nu \propto \nu^{-1.2}$) slope in the emission at the galaxy center compared to the Bremsstrahlung radiation expected from typical star-forming regions. The authors speculated that sources like radiosupernovae, supernova remnants, or even a low-mass AGN could be responsible for this steepening (Bergvall; Östlin, 2002).

Using observations from the ESO Multi-Mode Instrument (EMMI) in the optical and NIR UBVRIHK$_s$ bands, Micheva et al. (2013) conducted a deep surface photometric analysis for a sample of 24 Blue Compact Galaxies (BCG), including ESO 400-43 and ESO 400-43 *b*. They reported the presence of a low surface brightness optical bridge at the isophotal level of $\mu_V \simeq 28\,{\rm mag\,arcsec^{-2}}$ (see Fig. 12) connecting the dwarf companions, separated by a projected distance of 2″ ($\sim$70 kpc).

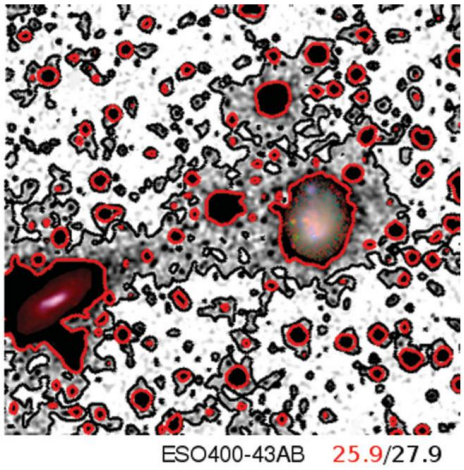

Figure 12 – Deep surface photometry for the FoV covering ESO 400-43 (center) and its dwarf companion ESO 400-43 *b* (lower left corner). They are separated by a projected distance of 2″ (corresponding roughly to a projected distance of ∼70 kpc). The red and black contours correspond to the isophotal levels of 25.9 and 27.9 mag arcsec^{-2} in the V band, respectively. A low surface brightness optical bridge connecting the dwarf pair can be observed. Credit: Micheva et al. (2013).

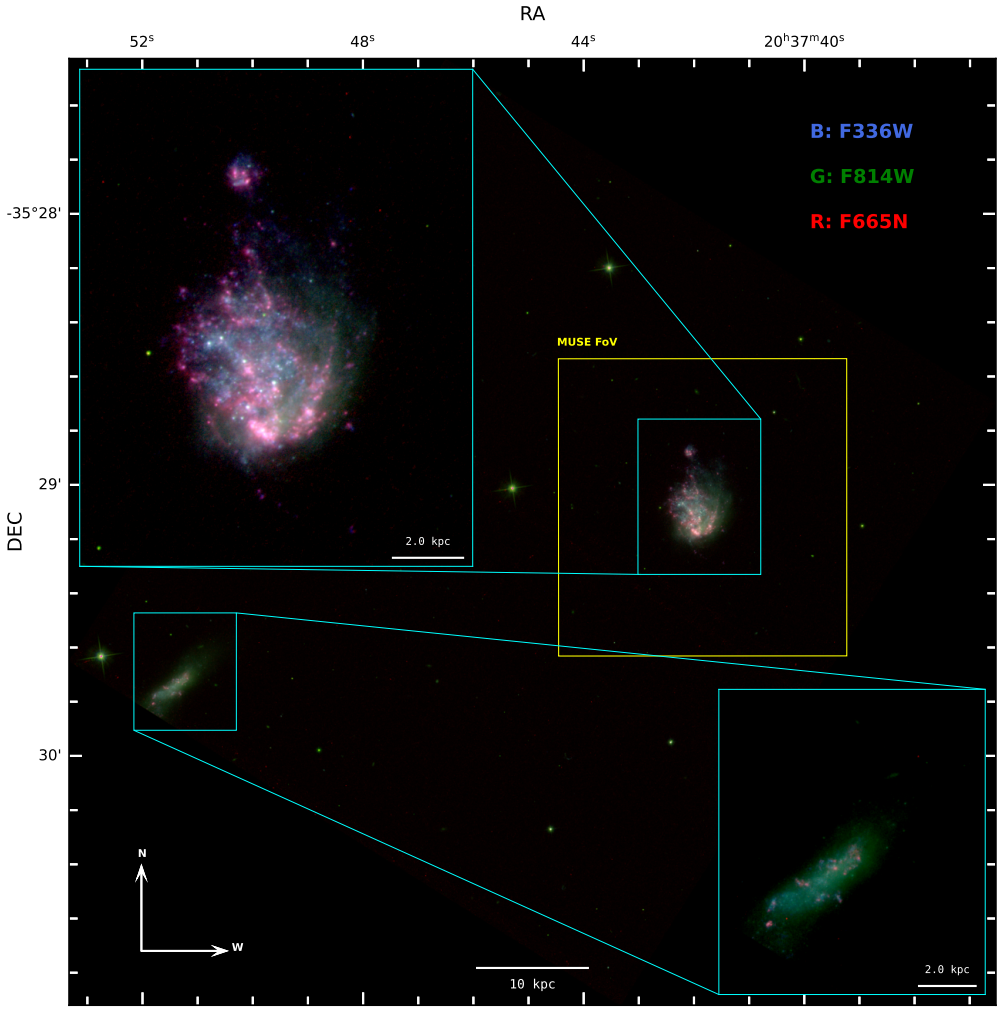

Figure 13 – Color-composite image of the HST FoV analyzed in §5, with the filters used for the RGB channels indicated on top. The MUSE 1 arcmin^2 footprint is represented by the yellow rectangle. The cyan lines indicate zoom-in insets for ESO 400-43 (top left) and its companion ESO 400-43 *b* (bottom right).

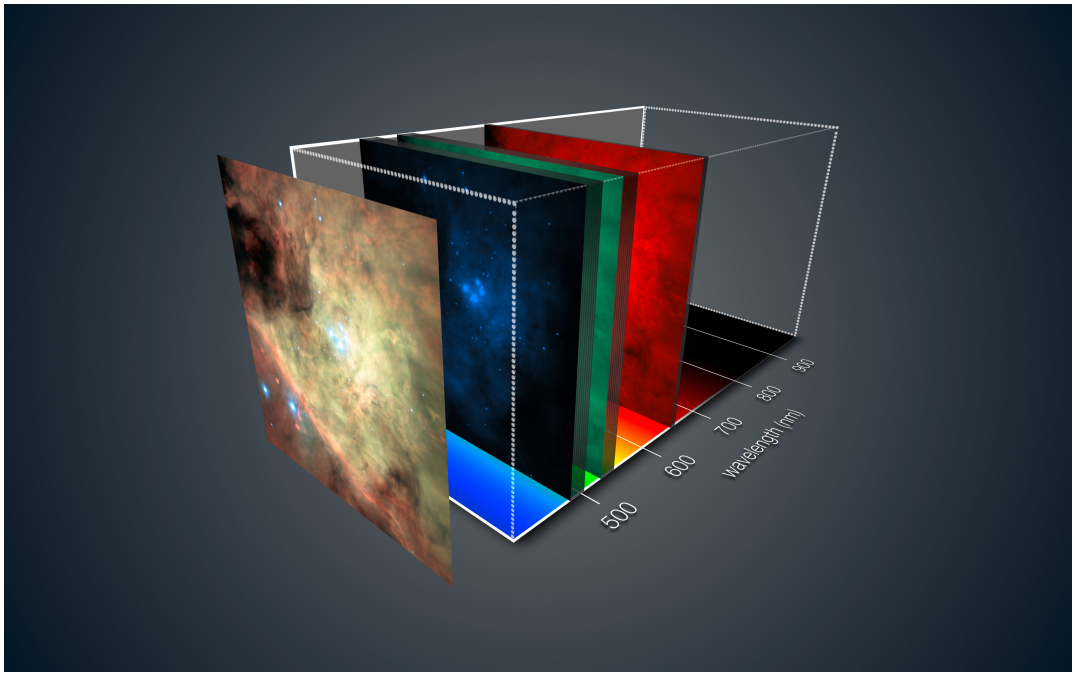

Figure 14 – Scheme representing the datacube format of the data structure. It has two spatial dimensions and one spectral dimension. The spatial dimensions contain consecutive monochromatic exposures of the target, separated by the spectrograph $\Delta\lambda$ spectral sampling. This means that each pixel has an associated spectrum across the wavelength range covered by the spectrograph. Credit: ESO/MUSE consortium/R. Bacon/L. Calçada

2.2 Observations: Integral Field Spectroscopy

2.2.1 Observations and instrument description

Integral Field Spectroscopy (IFS) observations of both galaxies were obtained with MUSE. The MUSE instrument is mounted at the 8.2 m ESO VLT on Paranal, Chile. The observations with MUSE in this work were carried on the Wide Field Mode (WFM), which covers a FoV of $1' \times 1'$ with an angular sampling of $0.2''$ per pixel. The spectrograph covers a wavelength range of 4650 –9300 Å with constant linear spectral sampling of 1.25 Å. The resolving power R[2] of the spectrograph varies from $R \sim$1750 at 4650 Å to $R \sim$3750 at 9300 Å. The data from MUSE is structured in the datacube format, as schematized in Fig. 14. In this form of data organization, we have N monochromatic exposures of the target separated by the $\Delta\lambda$ corresponding to the spectral sampling of the spectrograph. Simultaneously, each detector element (pixel) have its own spectrum, covering the wavelength range of the spectrograph.

In the case of SDSS J020536-081424 , observations were conducted over two nights in 2018 (August 10th and October 1st) under Program-ID 099.B-0411(A) (PI: Evelyn J. Johnston), with a total exposure time of 1.6 hours split into six exposures. For each night of observation a standard star was observed for flux and telluric calibrations, sky flats were taken within a week of the observations and an internal lamp flat was taken

[2] $R \equiv \Delta\lambda/\lambda$

immediately before or after each set of observations. This lamp flat image was used to correct for the time and temperature dependent variations in the background flux level of each CCD. Additional bias, flat field and arc images were observed the morning after each set of observations. In the case of ESO 400-43 the WFM was also used, and the galaxy was observed with the aid of an AO system during the night of September 17, 2017, under the Program-ID 60.A-9191(A) (PI: Arjan Bik). The total integration time was approximately 0.6 hours that were split into four exposures of 550 s each. Given that the ionized gas in ESO 400-43 extends over almost the entire $1' \times 1'$ FoV, two additional separate sky exposures with exposure time of 150 s each were requested, and the exposures were taken in the O - S - O - O - S - O order (O = Object, S = Sky exposure). In the AO mode the wavelength region 5755 –6010 Å is blocked in order to avoid contamination from the laser guide system.

2.2.2 Data reduction

The data were reduced using the MUSE pipeline v2.8.7 (Weilbacher et al., 2020) within the ESO Recipe Execution Tool (EsoRex) environment (ESO CPL Development Team, 2015). The reduction process is sequential, and the steps are presented respecting the order in which they were performed. The MUSE data reduction was carried out entirely by the author, under the supervision of Dr. Evelyn Johnston in the case of SDSS J020536-081424 and Dr. Arjan Bik in the case of ESO 400-43 . Most of the steps in the data reduction workflow described in this sub-section are either similar or identical to those in the standard ESO data reduction pipeline. The main difference between both methodologies lies in the decontamination of the residual sky lines, where we used third-party Python packages to supplement the standard procedure. However, sky lines are numerous, especially at $\lambda \gtrsim 7000$ Å, and can hardly be fully eliminated by any software or combination of methods.

In practice, it is impossible to build a CCD composed of identical pixels, and at the individual level they will exhibit slight variations in response and saturation. Additionally, pixels are subject to different physical conditions. For instance, pixels at the edge of the CCD experience higher distortion compared to the central ones. The differential response of each pixel due to these effects is relatively stable over time. A table called `BADPIX_TABLE` is available at ESO Science Archive[3], with the responses last measured in 2014. Additionally, a series of seven or more expositions must be taken in each night of observation to determine the gain (BIAS files). We used both files to build the `MASTER_BIAS` file, which accounts for the overall deviations in the photovoltaic conversion of each pixel.

The FLAT files consist of a series of exposures taken during the night of observation to identify poorly illuminated positions on the CCD, such as the inevitable gaps between

[3] https://archive.eso.org/cms.html

adjacent pixels. These exposures are taken daily, because even small temperature variations can cause pixel dilation, resulting in changes in their positions within the CCD. Using the previously created `MASTER_BIAS`, the `BADPIX_TABLE` and a file called `TRACE_TABLE`, which contains the trace solution for each slice in the form of a polynomial, we create the `MASTER_FLAT`.

On their path to the CCD, photons are collimated by a set of lenses, causing slight distortions in the observed original wavelengths. To correct this distortion, the CCD is exposed five times to the spectroscopic lamps HgCd, Xe and Ne, which have well-defined emission lines with good relative fluxes covering the spectral range of the spectrograph, allowing the quantification of this distortion effect. The relative fluxes of these emission lines are available as standard calibration files named `LINE_CATALOG` in the ESO Science Archive. The lamp exposures are taken on the night of the observation and are called ARC files. By combining the aforementioned files with `LINE_CATALOG` and the ARC files, we produce the `WAVECAL_TABLE` file. As mentioned, the pixels do not have the exact same saturation point and sensitivity. The CCD is exposed to a dark region of the sky for a long period to determine the behavior of each pixel in the interaction with light, producing the `SKY_FLAT` files. Using the file `GEOMETRY_TABLE`, which provides the relative location of each slice in the MUSE FoV, in addition to the `SKY_FLAT` files, we produce the `TWILIGHT_CUBE` file. The use of a vignetting mask is recommended.

Standard stars (STD files) are observed together with the target (OBJECT files) to calibrate the flux. This calibration is necessary because part of the light received by the telescope is reflected back into the atmosphere. Although technological advances provide increasingly efficient telescopes, the small amount of light lost due reflection is enough to decrease the spectral curve of observed sources. Since the spectral curve of standard stars is known a priori (and is available in the standard calibrations files at the ESO Science Archive under the name of `STD_FLUX_TABLE`), it is possible to compare the theoretical spectral curve to the observed one and determine the difference in monochromatic flux, extrapolating the correction to other sources. We apply the previously created `MASTER_BIAS`, `MASTER_FLAT`, `WAVECAL_TABLE`, `TWILIGHT_CUBE`, and other static calibrations to each STD and OBJECT file, producing the `PIXTABLE_OBJECT` and `PIXTABLE_STD` files. These files are tables containing information for each pixel, such as right ascension, declination, flux, flux error, wavelength, etc. These tables are transformed into data cubes by the `MUSE_SCIPOST` recipe, and flux calibration is applied considering possible effects of atmospheric extinction. Furthermore, a common problem in spectrographs is the deformation of absorption lines. The `LSF_PROFILE` file quantifies the effect of instrumental broadening in shaping absorption lines within the observed wavelength range, allowing for correction in the resulting spectrum. Finally, this step subtracts sky lines, although usually an additional subtraction is required afterwards. The main outputs of this stage are the `DATACUBE_FINAL`, `IMAGE_FOV`, and `PIXTABLE_REDUCED` files, the latter being similar to `PIXTABLE_OBJECT` but with properties

already corrected by the reduction procedure.

The produced white-light images of the FoV in the `IMAGE_FOV` files may be slightly misaligned relative to each other. To align the exposures, we employ the `MUSE_EXP_ALIGN` recipe, which uses common bright sources as references to align the individual frames to a common World Coordinate System (WCS). To avoid including cosmic rays as reference sources, an upper flux threshold for the source classification is defined by the user, and the recipe algorithm also takes into account the light distribution of sources in each frame. This recipe returns an `OFFSET_LIST` containing the offset in right ascension and declination for each source that is used in the following recipe `MUSE_EXP_COMBINE`. After the combination, besides the final image, a file named `DATACUBE_FINAL` is produced with the data fully reduced and with initial astrometric calibration provided by internal catalogs distributed within the pipeline. However, as mentioned earlier, the automatic sky subtraction alone is usually not sufficient to completely remove sky residuals in the final spectra, especially in the redder part of the spectrum. Alternatively, we use the Zurich Atmosphere Purge (ZAP)(Soto et al., 2016) to mitigate sky residuals in the final data cube. In the case of AO-assisted observations, it is also important to account for contamination from the scattered light originating from the laser guide system. A list of Raman line transitions (Raman; Krishnan, 1928) is distributed within the pipeline to subtract the residual lines caused by this contamination.

2.3 Imaging observations

2.3.1 SDSS J020536-081424 GSAOI Imaging: Observations and instrument description

High-resolution AO-assisted NIR observations of SDSS J020536-081424 were conducted via Director's Discretionary Time (DDT) under the Program ID GS-2021B-DD-103 (PI: Augusto E. Lassen) using the Gemini South Adaptive Optics Imager (GSAOI) (McGregor et al., 2004; Carrasco et al., 2012), aided by the Gemini Multi-Conjugate Adaptive Optics System (GeMS), a sodium-based multi-Laser Guide adaptive optics system mounted at the Gemini-South telescope in Cerro Pachón (Rigaut et al., 2014; Neichel et al., 2014). The FoV covered by GSAOI is approximately $85'' \times 85''$ with a spatial scale of $0.02''$ per pixel. The GSAOI camera is located at the $f/32$ output focus of Canopus and delivers images near the diffraction limit in the wavelength range from 0.95—2.5 μm. The detectors of GSAOI are four Rockwell HAWAII-2RG arrays mounted in a 2×2 mosaic that creates a focal plane of 4080×4080. The gap between the arrays is ∼2.4 mm, corresponding to $2.5''$ on the sky[4].

[4] https://www.gemini.edu/instrumentation/gsaoi/capability

Table 1 – Summary of GSAOI observations in the NIR filters J and K_s, with central wavelengths 1.250 μm and 2.150 μm, respectively. SDSS J020536-081424 was observed with an integration time of ∼40 minutes in both bands with seeing below 0.2″ (estimated from an unsaturated star within the FoV). The listed zero-point magnitudes are in Vega photometric system, and were obtained from observations of photometric standard stars in the same night of our observations. Official zero-point determinations are reported periodically in Gemini website[5].

Filter	**J**	**K_s**
Number of exposures	20	21
Integration time [s]	2400	2520
Mean airmass	1.079	1.158
Seeing [″]	0.18	0.15
Magnitude Zeropoint	25.83 ± 0.01	25.43 ± 0.02

The images of SDSS J020536-081424 were obtained using the GSAOI filters J (1.250μm) and K short (2.150μm) in 20 and 21 exposures of 120 s each, resulting in integration times of 40 and 42 minutes, respectively. Unfortunately, bright stars and galaxies are scarce in the vicinity of the sky region where SDSS J020536-081424 is located, imposing difficulties on the astrometric calibration. On the other hand, the relatively empty FoV of SDSS J020536-081424 makes it unnecessary to take separate sky exposures, which would only increase the overhead time for the observation. Instead, one of the remaining arrays can be used as a sky exposure since they also lack bright sources. The target was centered at array #3, which has the best cosmetics among the four Rockwell HAWAII-2RG arrays (McGregor et al., 2004; Carrasco et al., 2012). In Table 1 we summarize the GSAOI observations, where the seeing estimates are obtained by fitting a 2D Gaussian to an unsaturated star within the GSAOI FoV (see §2.4), and the listed zero-point magnitudes correspond to officially reported values[5] from observations of photometric standard stars in the same night of our observation. In the next section, we provide a full description of the data reduction steps.

2.3.2 SDSS J020536-081424 GSAOI Imaging: Data reduction

The data reduction of GSAOI data presented in this section was fully performed by the author under the supervision of Dr. Eleazar R. Carrasco. The data reduction was done using the THELI software (Erben et al., 2005; Schirmer, 2013). In the initialization stage we provide global information such as the number of CPUs to use and the Gemini instrument the input data was observed with, given that THELI is designed to operate with data from different Gemini instruments. In the next step we change the Header Data Unit (HDU) of the 41 raw images to a common format, splitting each exposure into four separated files, one for each array, to allow effective parallel processing. Furthermore, the modification of the headers aims to correct invalid and/or incomplete WCS keywords, retaining and

[5] https://www.gemini.edu/instrumentation/gsaoi/calibrations

translating only keywords essential for data reduction. During the same step of HDU reformatting, some detector features such as cross-talk and non-linearity effects can be corrected. The latter effect must be taken into consideration, since GSAOI detectors are intrinsically non-linear (Carrasco et al., 2012). If x_0 is the pixel value in the raw exposure (counts, in ADU units), the Linearity Correction Factor (LCF) is implemented by THELI via the following polynomial fit (Carrasco et al., 2012):

$$\mathrm{LCF} = a + bx_0 + c\,(x_0)^2 \tag{2.1}$$

where the coefficients a, b and c were obtained fitting a second-order polynomial with uniform weighting to data points corresponding to the average count values on each detector (Carrasco et al., 2012).

A set of 15 flat exposures was observed for each passband filter with the dome lamps on. For the J passband, the flats have exposure time of 7.0 s, while for the K short (K_s hereafter) filter the exposure time was 15.0 s. Additionally, a set of 15 flat exposures was observed with the dome lamps off for the K_s filter, with an exposure time of 15.0 s. These enable the estimate of the thermal emission contribution in the K_s individual exposures. Thereby we build a master flat-field file for each array and apply it to the frames while adjusting the gain. The amplitude of the dark current for GSAOI is low, of the order of 2−6 ADU, and its variations on the time scale of minutes to hours are on the order of the noise level, making it unnecessary to subtract dark frames from the images (Carrasco et al., 2012), and it is not even officially recommended, since it can induce the increase of noise[5].

GSAOI detectors present several "dead" pixels and a significant number of hot pixels with stable locations across different passbands, indicating that these are instrumental artifacts rather than observational features like cosmic rays. The hot pixels exhibit counts several thousand times the local average and affect their neighboring pixels, forming a cross-shaped feature. Although these "satellite" pixels, known as warm pixels, do not have counts as high as the hot pixels, they are considerably above the local count average. Conversely, cold pixels exhibit a very low response. While THELI routinely removes the majority of cosmetic flaws and artifacts during the flat-field correction, a few remaining features may still be present in the science exposures and can spoil the background subtraction and subsequent reduction processes if not properly treated. Indeed, a careful inspection of flat-field corrected science frames of SDSS J020536-081424 in both J and K_s passbands revealed the presence of hot, warm and cold pixels, so that a bad pixel mask (BPM) is required to mask out such artifacts before proceeding the reduction, otherwise the mean background will be overestimated.

The procedure we adopted to identify the bad pixels in the science exposures can

be summarized in two steps. First, we use the flat exposures to identify the cold pixels, as these are well exposed and it becomes easier to identify low-response elements at a given threshold. The adopted threshold is that all pixels with values below 50% of the detector median are considered cold pixels[5]. In the second step we use dark frames to identify the hot pixels. Any pixels with abnormally high signals compared to the dark current are flagged as hot pixels. Once the hot pixels are identified, the warm pixels are automatically detected due to the aforementioned cross-shape pattern. Again, the definition of a threshold is necessary: Pixels with values above 75% of the detector median $+ 3\,\sigma$ are classified as hot pixels[5]. To build the BPM, we download dark frames from the Gemini Observatory Archive[6]. The dark frames adopted have the same exposure time than the science frames (i.e. 120 s) and can be found under the data label GS-2016A-C-2-1. The 10 dark exposures were combined using the IRAF task GEMCOMBINE.

The background model, a median combination of several successive and dithered exposures, aims to correct residual variations after flat-field corrections and is subtracted from the science exposures to remove most of the sky signal. The background model in THELI can be computed in either static or dynamic mode. The static background model is a single image that is the median of a series of exposures. We apply it to all these exposures and is re-scaled to correct global variations in the background. This mode is adequate for short sequences (10–30 minutes). At this time scale, the temporal variation of the background due to several additive and multiplicative effects (e.g. fringing, moonlight and, especially in the case of NIR images, atmospheric airglow) changes little (Carrasco et al., 2012), and a static model is sufficient to subtract the sky. For longer NIR sequences, however, the sky variations become non-negligible, and it is necessary to use the dynamic mode to model the background properly (Schirmer, 2013). In this mode, THELI creates the background models by grouping a number m of exposures into k different groups, so that each group consists of images observed within a short temporal window. Given that array #4 is almost empty, we use them as separate sky observations to build the background models. Sources are masked prior to the creation of the model. After a standard collapse correction to remove typical effects such as reset anomalies in NIR cameras, we create a global weight map based on the normalized flat, forming the basis for the individual weight maps used in the subsequent co-addition step.

The astrometric calibrations rely on the choice of the reference catalog. Sufficient mutual overlap is required for the matching of source and reference catalogs to succeed. The catalog adopted in the reduction of SDSS J020536-081424 was the SDSS-DR12 catalog (Alam et al., 2015) within 6′ and a magnitude limit of 23.0. For the astrometric calibration and distortion corrections, THELI uses SCAMP (Bertin, 2006), a tool designed to operate in multi-chip cameras with internal accuracy of the resulting astrometric solution

[6] https://archive.gemini.edu/searchform

Table 2 – HST log of observations for ESO 400-43 . First columns presents the WFC3 filters used, while the second column shows the number of exposures followed by the total integration time. Zero-point magnitudes (4th column) and aperture corrections (5th column) are presented in AB magnitudes and were calculated using SYNPHOT Python package.

Filter	**Nº exposures**	**Integration time** [s]	**Zero-point** [AB mag]	a_c [AB mag]
F336W	4	3620	24.72	-0.24
F438W	2	1736	24.83	-0.27
F606W	2	1117	26.07	-0.25
F665N	2	1440	22.72	-0.27
F814W	3	1800	25.10	-0.36

on the order of ∼0.2 pixels in the regime of low source density fields observed in the NIR (Schirmer, 2013). The astrometric solution is used to register the WCS on the header of the exposures and will be necessary for the subsequent co-addition step. There are several alternative methods if the standard procedure fails at delivering an astrometric solution, but in the worst scenario where no satisfactory astrometric calibration could be performed, a possibility is to use the 0th order solution, i.e., to adopt the WCS solution already present in the raw FITS headers. Finally, the co-addition of the resulting individual frames was performed using SWARP (Bertin, 2010), adopting the median of each frame with `COMBINE_TYPE` = `MEDIAN`. The individual weight maps previously created are used as relative weights by setting `WEIGHT_TYPE` = `MAP_WEIGHT`.

2.3.3 ESO 400-43 HST Imaging: Observations and Instrument description

To spatially resolve the pc-scale star clusters in the ISM of ESO 400-43 , high-resolution imaging with HST were conducted in 2016 using the UV/Visible channel (UVIS) of the Wide Field Camera 3 (WFC3). The WFC3/UVIS detector covers a FoV of 162″ ×162″ with an angular sampling of approximately 0.04″ per pixel[7]. ESO 400-43 was observed in four broad-band filters (F336W, F438W, F606W and F814W) and one narrow-band filter covering the observed-frame Hα emission (F665N, see Fig. 15) under Program-ID GO 14066 (PI: Angela Adamo) as part of the Hubble imaging Probe of Extreme Environments and Clusters (Hi-PEEC) sample (Adamo et al., 2020). In table 2 we present a log of the observations for ESO 400-43 used in this work. The zero-point AB magnitudes and aperture corrections up to 0.8″ included in the Table 2 were calculated using the SYNPHOT Python package (STScI CPL Development Team, 2018), utilizes the most up-to-date WFC3 encircled energy tables available on the official Space Telescope Science Institute (STScI) website[8].

[7] https://hst-docs.stsci.edu/wfc3ihb
[8] https://www.stsci.edu/hst/instrumentation/wfc3

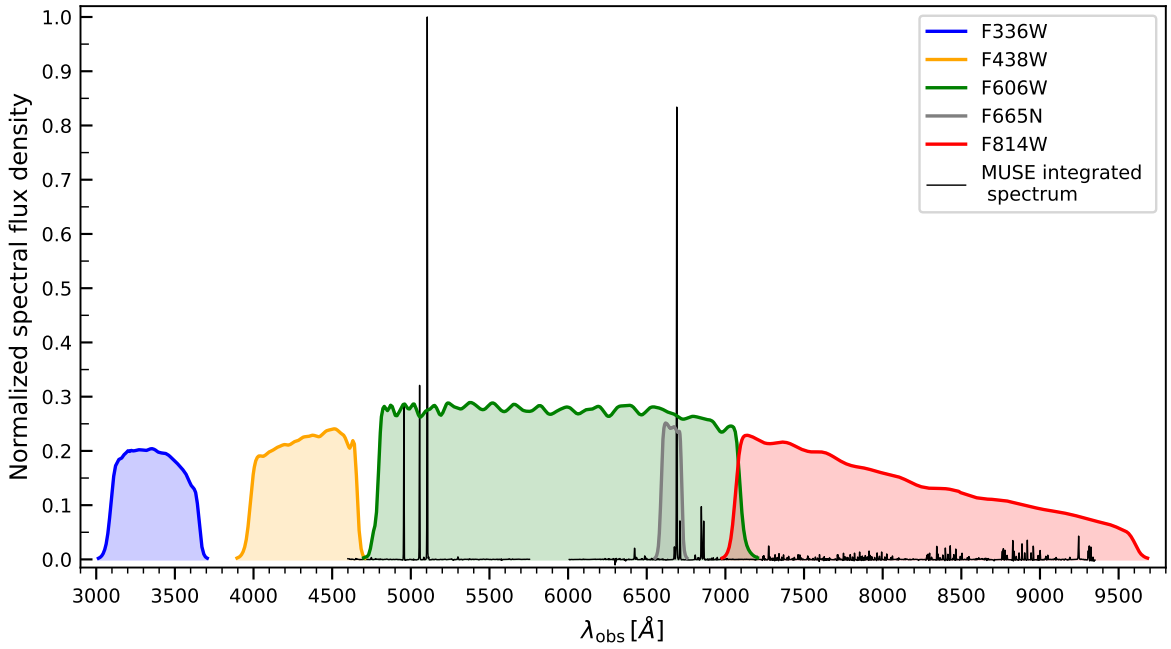

Figure 15 – Integrated spectrum of ESO 400-43 extracted from the AO-assisted MUSE observations analyzed in this work (black thin line). The spectrum was normalized to its peak, corresponding to the flux of [O III] λ5007. The transmission curves of the HST filters used in the observations analyzed in this work are also presented, indicated by the labels on the top right.

2.3.4 ESO 400-43 HST Imaging: Data reduction

The data reduction presented in this section was fully performed by the author under the supervision of Dr. Angela Adamo with assistance of Dr. Jens Mellinder in the step of cosmic ray treatment. We start the data reduction by downloading the `FLC`-calibrated files for each frame from the Mikulski Archive for Space Telescopes (MAST). These files are the output from the standard pipeline calibration that corrects for UVIS Charge Transfer Efficiency (CTE) effects. We used the LaCosmic algorithm (van Dokkum, 2001) for cosmic-ray rejection, which applies the Laplacian edge detection method (Gonzalez; Woods, 1992) to highlight count peaks with shapes that strongly deviate from the expected shape of a Point Spread Function (PSF). To align the individual exposures to a common reference frame, we used the TweakReg routine from the drizzlepac Python package (Hoffmann et al., 2021). TweakReg implements the daofind algorithm (Stetson, 1987) to search for bright sources in the FoV within user-defined flux thresholds common to all input frames, supplemented by an external GAIA DR3 (Gaia Collaboration et al., 2023) source catalog. This provides an absolute astrometric solution used to align the exposures and register them to a common WCS solution. In the final step, the frames were drizzled into the final science image using the WFC3/UVIS native spatial scale of 0.04″ per pixel with a North-up orientation. Assuming a WMAP9 cosmology, this corresponds to a spatial scale of approximately 16 pc/pixel at the distance of ESO 400-43 .

2.4 Considerations on the spatial resolutions

Point sources are bright sources with angular diameters far smaller than the maximum resolution of a given detector (a pixel). However, these sources appear spread out over an area when imaged due to several effects. In ground-based telescopes, the atmosphere is primarily responsible for this spreading, although even in space-based observations some spread occurs due to the diffraction limit of the telescope and optical aberrations (Trujillo et al., 2001). The Point Spread Function (PSF) is a useful mathematical tool to quantify the amount of spread in an image. Since it is related to observing conditions, it provides a way to assess the quality of the images obtained.

In the case of GSAOI and MUSE observations for SDSS J020536-081424 , the seeing (related to the Full Width at Half Maximum (FWHM) of the modeled PSF) was estimated by fitting a 2D Gaussian function to available unsaturated stars in the respective FoV:

$$G(x, y) = A \exp\left[-\frac{(x - x_0)^2 + (y - y_0)^2}{2\sigma^2}\right] \tag{2.2}$$

where A is a normalization constant, and x_0, y_0 are the coordinates of the center of the Gaussian (i.e., the point corresponding to the center of the luminosity-weighted light distribution), and σ is the Gaussian standard deviation[9], which relates to the seeing via the expression FWHM $= 2\sqrt{2\ln 2} \times \sigma \approx 2.355\,\sigma$. Using a Gaussian PSF for one unsaturated star in the white-light image of MUSE observations for SDSS J020536-081424 , we estimated a seeing of 1.4″ with the QFitsView tool[10]. For GSAOI observations of SDSS J020536-081424 , we used IRAF tasks to estimate the seeing on unsaturated stars for each band, obtaining 0.18″ and 0.15″ for the J and K_s bands, respectively.

Although a 2D Gaussian is a good first-order approximation to describe an observational PSF, Moffat (1969) showed that a single Gaussian profile is usually too sharp compared to the observed PSF, failing to describe the "tails" of the profile. Therefore, Moffat (1969) proposed the use of the following expression to describe how the flux f of a point source behaves as a function of the radius r, centered at its luminosity peak:

$$f(r) = A \times \left[1 + \left(\frac{r}{\alpha}\right)^2\right]^{-\beta} \tag{2.3}$$

where A is a normalization constant and α and β are radial parameters that need to be fitted and are related to the FWHM via the expression FWHM $= 2\alpha\sqrt{2^{1/\beta} - 1}$ (Akhlaghi; Ichikawa, 2015). For HST observations, we start modeling the PSF by selecting at least twelve unsaturated stars in each band that are stacked together to created the input

[9] Assuming symmetry, i.e., $\sigma_x^2 = \sigma_y^2 = \sigma^2$

[10] https://www.mpe.mpg.de/ ott/dpuser/qfitsview.html

PSF. We fit this stacked PSF using the sum of a 2D Gaussian profile and a Moffat profile (Equations 2.2 and 2.3, respectively), allowing a 5th-order polynomial to account for the residuals in the wings.

The model is fitted to the data using the SCIPY LMFIT implementation of the non-linear Levenberg-Marquardt least squares minimization for curve fitting (Levenberg, 1944; Marquardt, 1963; Newville et al., 2024). In Fig. 16, we show the stacked PSF (left panel) normalized so that the sum of the PSF is equal to 1 and the fitted PSF model for the F814W HST/WFC3 filter. In Fig. 17, we show the radial profiles for both logarithmic (left panel) and linear (right panel) flux scales, where the label indicates the stacked and model radial profiles. The dashed line corresponds to the absolute difference between input PSF model and best-fit output. The fluxes at a given radius are obtained using concentric annuli in radial steps of 0.5 pixels. The central coordinates are indicated by the cyan dashed lines in both panels of Fig. 16. The PSF results for the remaining filters are shown in Appendix C.

For the AO-assisted MUSE observations of ESO 400-43 , we use the MUSE Python Data Analysis Framework (Bacon et al., 2016, MPDAF) to fit a wavelength-dependent PSF. For that we divide the datacube into 20 collapsed exposures within the wavelength range of 4700 Å—9200 Å , adopting the circular Moffat function with wavelength-dependent β parameter:

$$\mathrm{FWHM} = p_0 \times l^n + p_1 \times l^{n-1} + p_n \tag{2.4}$$

$$\beta = k_0 \times l^m + k_1 \times l^{m-1} + k_m \tag{2.5}$$

$$l \equiv \left(\frac{\lambda - \lambda_1}{\lambda_2 - \lambda_1} \right) - 0.5 \tag{2.6}$$

where p_i and k_i are the coefficients used for FWHM and β polynomial approximation, respectively. The integers correspond to the order of the polynomial used in each fitting procedure, meanwhile λ_1 and λ_2 define the wavelength range used for normalization. We used an unsaturated star in the FoV for the fit, adopting $n = 3$ and $m = 2$. In Fig. 18, we show the normalized PSF model, and in Fig. 19 we present the values of FWHM and β as functions of wavelength, with uncertainties on the fit indicated by the error bars. The polynomial best-fit to each parameter is shown by the red dashed line. It can be seen that the FWHM varies from $\sim$1.0″ at the bluer wavelengths to $\sim$0.7″ at the red end of the spectrograph wavelength range. Throughout the work related to ESO 400-43 , we primarily consider the value estimated from the white-light image, FWHM = 0.85″. Although β shows larger error bars, the overall variation in the values is not significant, with most values lying in the range between 2.2 and 2.4.

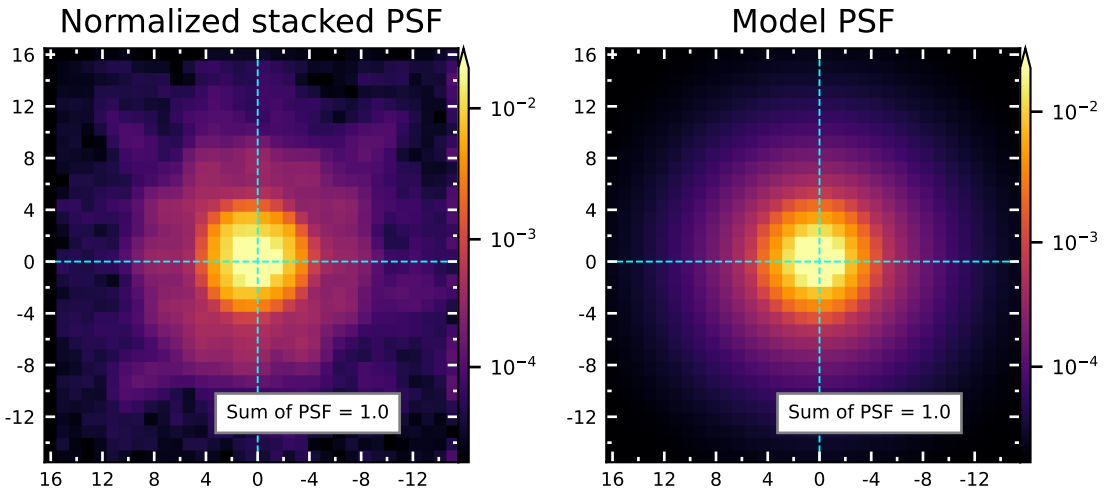

Figure 16 – *Left panel*: PSF built from the stacking of sixteen unsaturated stars in the FoV for WFC3/UVIS F814W band. The PSF was normalized so that the sum of its flux is 1. *Right panel*: Model PSF obtained using LmFit to fit the sum of a 2D Gaussian and a Moffat profiles to the stack PSF on the left panel. The fit was supplemented by a 5th-order polynomial to account for the residuals on the wings of the profile. Cyan dashed lines indicate the center of the PSF.

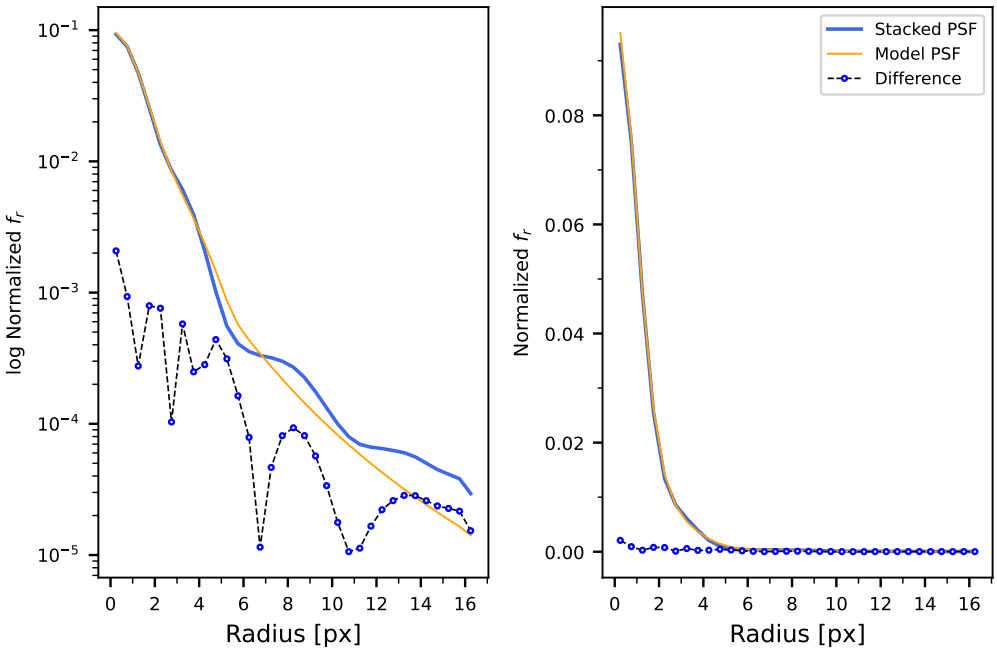

Figure 17 – PSF radial profiles for WFC3/UVIS F814W band. The flux at a given radius $f(r)$ was obtained using concentric annuli in steps of 0.5 pixels, where the lines corresponding to the model and to the stacked PSF are indicated by the label. The black dashed line corresponds to the difference between both curves. The plots are presented considering logarithmic (left panel) and linear (right panel) flux scales.

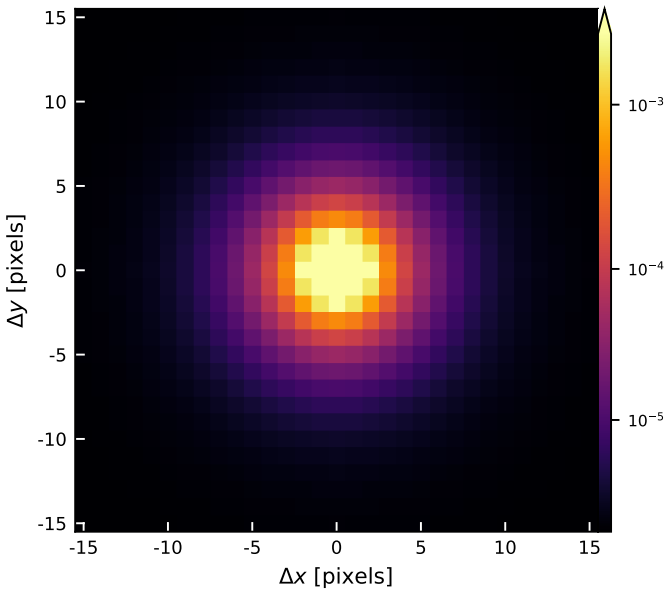

Figure 18 – Normalized PSF model for the MUSE AO-assisted observations of ESO 400-43 , built from the fit of Equation 2.4 on an observed star. The PSF model is displayed at $\lambda = 6000$ Å. The colorbar represents the counts on the image.

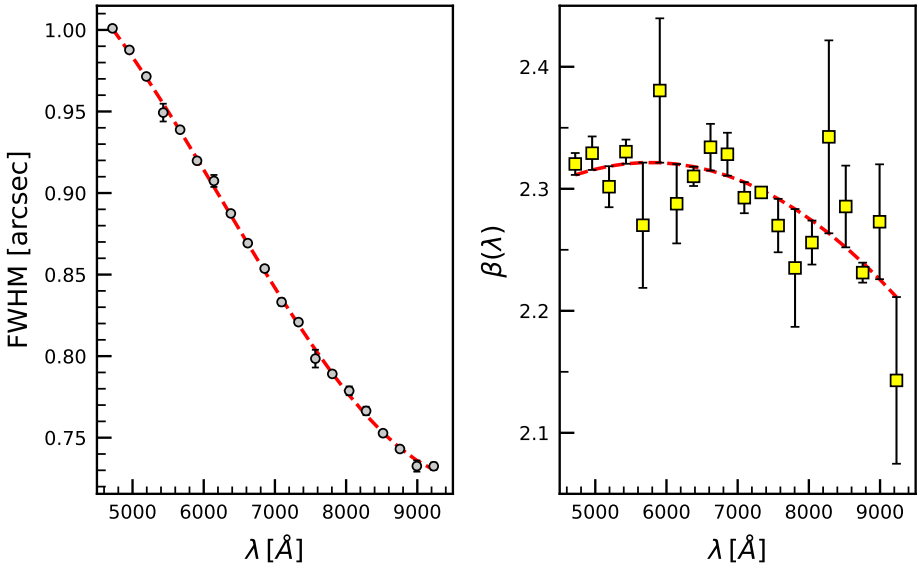

Figure 19 – *Left panel*: FWHM of the fitted PSF as a function of wavelength. The gray points represent the values of FWHM for each of the 20 exposures reconstructed from collapsed slices of the datacube. The error bars are also included, although they are mostly small. The red dashed line shows the best fit polynomial. *Right panel*: Each point corresponds to the β parameter from Equation 2.5. Unlike FWHM, the uncertainties on β are larger and the fit less accurate, but the overall values do not vary significantly, lying mostly between 2.2 and 2.4.

3 Methodology

In this chapter we will briefly describe the techniques and methodologies employed in the analysis presented in chapters §4 and §5.

3.1 Stellar Population Synthesis

Roughly speaking, the baryonic content of a galaxy consists of dust, gas and stars. The stellar content of galaxies plays a crucial role in their evolution (e.g., stellar feedback) and in describing the conditions of their ISM. Since it is intrinsically related to past episodes of star formation, the integrated light emitted by the stars within a galaxy contains imprinted information on its formation and evolution (Eldridge; Stanway, 2022). Ideally, each star within a galaxy would be studied individually, allowing the conditions of the gas cloud from which it was formed to be well constrained. However, practical challenges impose significant obstacles: Even a low-mass galaxy contains a countless number of stars, and the stars are too small and too far to be resolved individually in the overwhelming majority of galaxies. Even in the Milky Way, a complete stellar census is hindered by the 30 magnitude obscuration from the Galactic disk in the optical range (Strigari, 2013). Therefore, the alternative solution to uncover the properties of the stellar content within galaxies relies on disentangling the imprinted information from their integrated light.

Stars are formed from the gravitational collapse of GMCs (see §1.5), where the number of formed stars with different masses is described by the stellar Initial Mass Function (IMF), typically well represented by a power-law distribution, and determines, for instance, the contributions of luminosity and nucleosynthetic outputs in the ISM of the host galaxy (Serenelli et al., 2021). The stars formed in the same collapse event share the same initial chemical composition and, since the timescale between the birth of each star is negligible compared to their lifetimes, it is assumed that they have the same age. This coeval population of stars is known as a Simple Stellar Population (SSP). The spectrum of a SSP with metallicity Z for a time t after birth can be modeled using the expression (Tinsley, 1980; Conroy; Gunn; White, 2009; Conroy, 2013):

$$f_{\mathrm{SSP}}(t, Z) = \int_{M_i^{\mathrm{low}}}^{M_i^{\mathrm{upp}}(t)} \Phi(M_i) \times f_{\bigstar}\Big[L(M_i, Z, t),\, T_{\mathrm{eff}}(M_i, Z, t),\, Z\Big]\, \mathrm{dM_i} \tag{3.1}$$

where M_i is the initial mass, with lower and upper mass cutoffs M_i^{low} and M_i^{upp}, respectively. The lower mass cutoff is usually considered as the Hydrogen-burning limit, the minimum mass required for a star to sustain H fusion in its nucleus. The upper mass cutoff depends on

the stellar evolution, with time dependence arising because stellar lifetimes vary according to their initial masses (the fuel consumption is higher for more massive stars, that die earlier than their low-mass counterparts). Additionally, mass loss occurs due to strong stellar winds expelling the outer layers or other imbalances between gravity and radiation pressure at the surface of the star (Chiosi; Maeder, 1986; Eldridge; Stanway, 2022). To determine the parameter $f_\star$, isochrones, the fuel consumption theorem (Renzini; Fusi Pecci, 1988), or a combination of both, can be used to map the evolutionary tracks of stars with same age but different masses in the Hertzsprung-Russell diagram. This provides, for a given age and metallicity, the relations between mass, bolometric luminosity ($L_{\rm bol}$), effective temperature[1] ($T_{\rm eff}$) and surface gravity (g). However, to convert the stellar evolution predictions encoded by this set of parameters into stellar SEDs, stellar libraries are required (Maraston, 2005; Vazdekis et al., 2010; Vazdekis et al., 2015; Conroy, 2013; Villaume et al., 2017). Stellar libraries consist in a collection of individual stellar spectra, which can be obtained either theoretically or empirically.

The steadily improving telescope instrumentation for spectroscopic surveys offers increasingly better empirical stellar libraries based on high-quality observations of a large number of nearby resolved stars covering significant wavelength ranges and locations of the HR diagram. Increasing the coverage of both factors is of utmost importance for empirical libraries aiming to achieve the flexibility necessary to accurately model the integrated stellar emission in galaxies with very different evolutionary paths and ISM conditions. However, a shortcoming of empirical stellar libraries is that their ability to describe different stellar populations is severely limited because only stars in the Solar neighborhood can be resolved and observed individually. These stars have heavy element compositions similar to that of the Sun and reflect very specific galactic evolutionary histories (Martins et al., 2005; Sánchez-Blázquez et al., 2006; Knowles et al., 2023). Theoretical stellar libraries do not suffer from this disadvantage, as stellar SEDs can be calculated for a variety of stellar spectral types, luminosity classes, and chemical abundance patterns with high spectral resolution (Coelho et al., 2005). Given an initial chemical composition, $T_{\rm eff}$ and g, and using radiative transfer codes to model the stellar layers, star properties such as density, temperature and ionization structure can be determined (Kurucz, 1979; Kurucz, 1992; Coelho, 2014). The limitation of the theoretical libraries reside in the current limitations of atomic and molecular line lists (Kurucz, 2011; Allard; Homeier; Freytag, 2011) and on the assumptions upon which radiative transfer models are typically based, such as local thermodynamic equilibrium (LTE) and one-dimensional plane-parallel atmospheres (Villaume et al., 2017; Coelho; Bruzual; Charlot, 2020; Bertoldo-Coêlho et al., 2024). The former assumption is particularly unsuitable for hot and/or metal-poor stars and for very

[1] Considering $P_\star$ the power radiated by a star with radius R, the effective temperature is given by the Stefan–Boltzmann law: $P_\star = 4\pi R^2 \sigma T_{\rm eff}^4$, where σ is the Stefan–Boltzmann constant ($\sigma = 5.670 \times 10^{-8} \mathrm{W\,m^{-2}\,K^{-4}}$).

cool stars (Martins; Coelho, 2007). Although techniques to implement non-LTE conditions or to extend the plane-parallel atmosphere models to three dimensions already exist, they are still computationally expensive (Lanz; Hubeny, 2003; Lind; Bergemann; Asplund, 2012; Magic et al., 2013; Pacheco et al., 2021). In summary, the construction of a SSP requires three major ingredients: An IMF, isochrones that provide stellar evolutionary tracks and a stellar library.

3.1.1 Stellar Population Fitting: Starlight

The Stellar Population Synthesis (SPS) technique uses a grid of SSPs spanning different ages and metallicities to fit the observed SED from the contribution of each element in the base. This full spectral fitting technique provides a physically meaningful solution, as the best-fit contributions of each SSP represent a non-parametric Star Formation History (SFH), i.e. *a priori* there is no need to assume a functional form for the SFH, as the SSPs mass fractions provide the relative stellar mass formed in age bins. This describes fairly well what is done by the SPS code STARLIGHT[2] (Cid Fernandes et al., 2005), employed in the analysis presented in §4.1. For the input base of SSPs, STARLIGHT performs a linear combination of the elements in the base and adopts the combination with the minimum χ^2 as the best-fit synthetic spectrum. Considering O_λ as the observed flux and M_λ as the model flux vector given by the linear combination of the elements in the base, χ^2 is given by the expression:

$$\chi^2 = \sum_\lambda \Big[(O_\lambda - M_\lambda)\, w_\lambda \Big]^2 \tag{3.2}$$

where w_λ is a wavelength-dependent weighting factor that can be set by the user. Usually, there are spectral regions that are masked during the fit, including emission lines and spurious data, for instance. In this case, one can set $w_\lambda = 0$ for these regions in the spectrum. To determine M_λ, STARLIGHT uses the equation:

$$M_\lambda = M_{\lambda_0} \left[\sum_{j=1}^{N_\star} x_j\, b_{j,\lambda}\, r_\lambda \right] \otimes G(v_\star, \sigma_\star) \tag{3.3}$$

where the index j covers all the $N_\star$ elements in the base, x_j is the j-th element of the population vector, $b_{j,\lambda}$ is the j-th base element, and $r_\lambda \equiv 10^{-0.4(A_\lambda - A_{\lambda_0})}$ is the term for reddening correction (discussed in §3.2). The term inside the brackets is convolved with a Gaussian whose center is determined by the stellar velocity ($v_\star$) and the velocity dispersion ($\sigma_\star$), and then multiplied by the model flux vector evaluated at $\lambda = \lambda_0$, ideally a featureless region in the original spectrum set by the user before the fit.

[2] http://www.starlight.ufsc.br/

3.1.2 Stellar Population Fitting: pPXF

In the case of the Penalized PiXel Fitting code[3] (Cappellari; Emsellem, 2004; Cappellari, 2017; Cappellari, 2023, pPXF) adopted in the analysis presented in §5.1, the observed galaxy spectrum is modeled from the convolution between stellar templates T and the Line-Of-Sight Velocity Distribution (LOSVD). If we assume that the differences between the input stellar templates and observed galaxy spectrum are originated purely from the broadening caused by LOSVD of the galaxy, the G model describing the observed spectrum can be expressed as follows:

$$G(x) = T(x) \ * \text{LOSVD}\,(cx) \tag{3.4}$$

where $x \equiv \ln \lambda$ and c is the speed of light. Although the shifting of absorption lines due to the LOSVD could be evaluated on a spectrum with linear spectral sampling (i.e., with constant spectral steps $\Delta\lambda$), the logarithmic axis provides constant velocity steps[4], making the use of Fast Fourier Transform (FFT) methods for the convolution in Equation 3.4 more straightforward (Cappellari, 2017).

However, the assumption used in Equation 3.4 is only occasionally met, especially because the adopted stellar templates either have different spectral resolutions compared to the observed spectrum, or because many stellar templates mix empirical and theoretical libraries with wavelength-dependent spectral resolutions. To match the spectral resolution of observed and stellar template spectra, a convolution with a wavelength-dependent one-dimensional Gaussian kernel $K(x, \lambda)$ is performed:

$$\text{LSF}_{\text{inst}}\,(x, \lambda) = \text{LSF}_{T}\,(x, \lambda) * K(x, \lambda) \tag{3.5}$$

where the Line Spread Function (LSF) parameterizes the wavelength-dependent broadening of a infinitesimally narrow line profile (a δ function) caused by the spectrographs used to observe the input spectrum[5] (LSF_{inst}) and the stellar spectra that make up the template (LSF_{T}). Thus, the templates $T(x)$ in Equation 3.4 are modified to match the input spectral resolution using the convolution $T(x) \ * \ K(x, \lambda)$. Despite the criteria based on χ^2 minimization, pPXF penalizes solutions for which the LOSVD strongly deviates from a Gaussian shape to determine the best-fit synthetic model (Cappellari; Emsellem, 2004).

[3] https://pypi.org/project/ppxf/

[4] From $\Delta \ln \lambda = \ln(\lambda_{\text{obs}}/\lambda_{\text{emit}}) = \ln(1 + z)$ and considering that for small velocity values $V \approx \Delta V$, $V \approx c(\Delta\lambda/\lambda_{\text{emit}}) \approx c\Delta \ln \lambda$.

[5] Throughout this work, we adopt the LSF polynomial parametrization of MUSE spectrograph from Guérou et al. (2017): $\text{FWHM}_{\text{inst}}\,[\text{Å}] = 5.866 \times 10^{-8}\lambda^2 - 9.187 \times 10^{-4}\lambda + 6.04$.

3.1.3 Stellar Population Fitting: FADO

Besides providing information about the stellar populations in a galaxy, the SPS technique is also often employed to model the continuum in order to separate stellar emission from the strong emission lines originated in electronic transitions within the ionized gas. Although there are several effective methods to model the featureless continuum, the SPS technique offers a significant advantage when the entire continuum is being modeled, as it provides physically motivated estimates of the absorption features underlying Hα and Hβ emission lines. This correction becomes non-negligible as the contributions from young and intermediate-age stellar populations increase (González Delgado; Leitherer, 1999; González Delgado; Leitherer; Heckman, 1999; Gomes; Papaderos, 2017).

In regions with high star-formation activity, nebular emission can contribute up to 70% of the total optical/IR continuum emission (Krueger; Fritze-v. Alvensleben; Loose, 1995; Gomes; Papaderos, 2017; Cardoso; Gomes; Papaderos, 2019). Nebular emission can be divided in two components: The first comes from the radiation field originating in the short-lived massive stars that ionize the gas, producing electronic transitions that result in emission lines in the spectrum. The second component is the nebular continuum, which arises from free-free[6], free-bound[7] and two-photon emission[8] (Mollá; García-Vargas; Bressan, 2009; Reines et al., 2010; Byler et al., 2017). When nebular emission is significant, neglecting it can cause stellar population fitting codes to overestimate both the fraction of older stellar populations and the stellar mass (Izotov; Guseva; Thuan, 2011).

In the analysis presented in §4.2, we used the FADO code[9] (Gomes; Papaderos, 2017, **F**itting **A**nalysis using **D**ifferential evolution **O**ptimization) to include nebular emission treatment during the SPS fitting. FADO also performs a self-consistent SPS fitting, i.e., while using stellar signatures (e.g., the wings from the absorption feature underlying Hβ emission) to model the stellar emission, it simultaneously takes into account the amount of ionizing photons necessary to reproduce the flux estimates of the Hydrogen recombination lines. This can be calculated from the expression below (Byler et al., 2017):

$$Q_{\mathrm{H}} \equiv \int_{\nu_0}^{\infty} \frac{f_\nu}{h\nu}\, \mathrm{d}\nu = \frac{1}{hc} \int_{0}^{\lambda_0} \lambda f_\lambda \, \mathrm{d}\lambda \tag{3.6}$$

[6] Also known as *Bremsstrahlung* radiation, it is called free-free because the scattered electron remains unbounded before and after the emission. This emission occurs when charged particles are (de)-accelerated (Rybicki; Lightman, 1986).

[7] The radiation originated when a free electron is captured by an ion (radiative recombination continuum), with the excess excitation energy radiated as photons (Osterbrock; Ferland, 2006).

[8] Instead of the well-known production of single photon, these transitions produce two photons with variable individual energies, although the total energy for both photons must always equal the energy difference between the initial and final quantum levels. This gives rise to a continuum emission from $\lambda = 1216\,\text{Å}$ to $\lambda \to \infty$, peaking around $\lambda \approx 1400\,\text{Å}$ (Gurzadyan, 1997).

[9] https://www.spectralsynthesis.org/fado

where h is the Planck constant, c the speed of light and f_λ the spectral flux density. Since we are interested in the number of photons capable of ionizing Hydrogen ($Q_{\rm H}$), the integration is performed bluewards of $\lambda_0 = 912\,\text{Å}$, the threshold energy required for a photon to ionize H (13.6 eV). For this, the SPS fitting must be done with SSP models that include the UV part of the spectrum, such as the Bruzual and Charlot (2003) models with STELIB stellar libraries (Le Borgne et al., 2003).

Throughout this work, all three SPS techniques described in §3.1.1 through §3.1.3 were employed. Despite their different approaches, previous studies comparing STARLIGHT and pPXF, along with other SPS techniques, have shown that both methods recover consistent stellar population properties and gas kinematics (after subtraction of stellar emission continuum) when the same initial assumptions and input spectra are used, given sufficient S/N levels (Dias et al., 2010; Cid Fernandes, 2018; Bellocchi et al., 2019; Woo et al., 2024). As mentioned earlier, if the nebular-to-stellar continuum emission is significant, neglecting it can lead to overestimated fractions of old stellar populations and stellar masses (Izotov; Guseva; Thuan, 2011). To prevent misinterpretations of the stellar populations properties of the clumps in SDSS J020536-081424, we adopted FADO in §5.1. In contrast, in §5.2 we did not analyze the stellar population properties in ESO 400-43, using SPS strictly for subtracting the stellar continuum emission. Given the strong Balmer emission lines exhibited by the ionized gas surrounding the star clusters, the underlying absorption features account for only a small fraction of the total emission line fluxes, alleviating potential biases originated from the choice of the SPS method. The use of pPXF in §5.2 was therefore motivated mostly by learning purposes.

3.2 Extinction

The light from extragalactic sources reaching an observer on Earth is partially scattered and/or absorbed due to dust in Milky Way, causing an attenuation on the intensity that depends on the location of the source in the sky (Schlegel; Finkbeiner; Davis, 1998; Schlafly; Finkbeiner, 2011, see Fig. 20). Besides the foreground Galactic extinction, attenuation might also occur due to the dust within the ISM, for instance. The effect of dust on the apparent magnitude for a given passband centered at λ can be expressed by an additive term A_λ:

$$m_\lambda = M_\lambda + 5\log_{10} d - 5 + A_\lambda \tag{3.7}$$

where d is the distance of the source, whereas M_λ and m_λ are the absolute and apparent magnitudes, respectively. The term A_λ refers to the attenuation along the observer line of sight, in magnitude units. The intensity of this attenuation depends on the number density of dust grains, the thickness of the dust cloud and especially on the wavelength of the light.

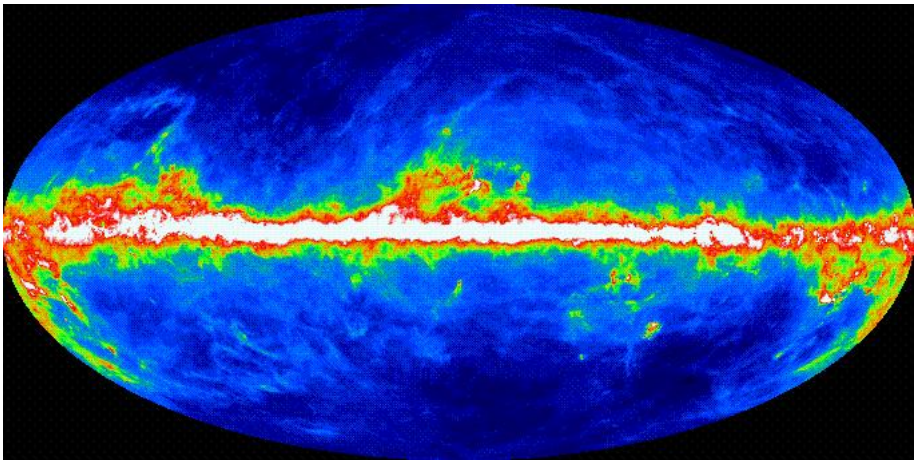

Figure 20 – Aitoff projection of the sky at 100μm observed by the Infrared Astronomy Satellite (IRAS) using its redder broadband channel. The map shows the degree of foreground extinction caused by Milky Way dust. The red and white regions correspond to the Galactic plane, where the extinction is higher, while the bluer regions correspond to lower extinction levels. This map was constructed by combining the individual images presented in Schlegel, Finkbeiner and Davis (1998). Credit: NASA/IPAC Infrared Science Archive (IRSA).

Due to the composition of the dust grains, shorter wavelengths are more affected than the longer ones, resulting in the reddening of the emitted light (see Fig. 21). Considering I_λ as the observed intensity and $I_{\lambda,0}$ the intensity that would be observed in the absence of any extinction, the change in the intensity is related to the optical depth τ_λ via the expression:

$$\frac{I_\lambda}{I_{\lambda,0}} = \mathrm{e}^{-\tau_\lambda} \tag{3.8}$$

The optical depth is related to the transparency of the dust column density along the line of sight and to the mean free path of a photon. The mean free path depends on the wavelength, as photons with different energies will interact differently with the matter. The optical depth is related to A_λ via (Carroll; Ostlie, 2017):

$$A_\lambda = m_\lambda - m_{\lambda,0} = -2.5\log_{10}(\mathrm{e}^{-\tau_\lambda}) = 1.086\tau_\lambda \tag{3.9}$$

Measuring A_λ directly is difficult, but the extinction difference between two wavelengths can be determined by comparing the observed and expected colors of a given source. Considering the B and V bands, the color excess is defined as:

$$E(B-V) \equiv (B-V)_{\text{intrinsic}} - (B-V)_{\text{observed}} \tag{3.10}$$

From 3.9 it is possible to determine how the extinction affects the flux:

$$A_\lambda = m_\lambda - m_{\lambda,0} = 2.5\log_{10}\left[\frac{F(\lambda)_{\text{int}}}{F(\lambda)_{\text{obs}}}\right] \tag{3.11}$$

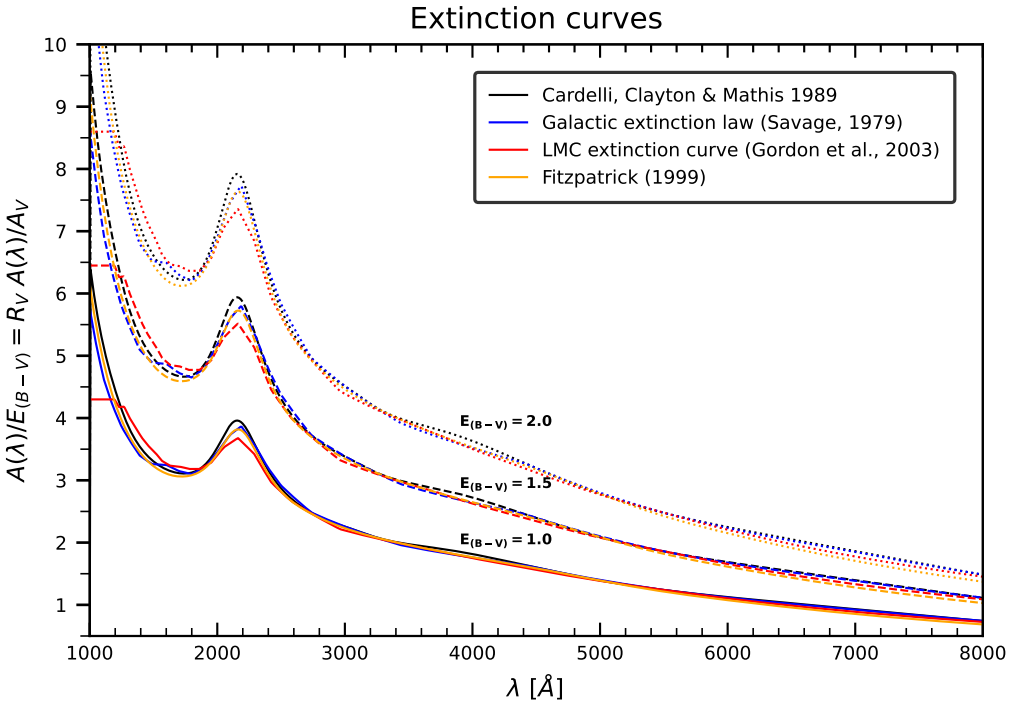

Figure 21 – Attenuation as a function of wavelength $A(\lambda)$. Four different attenuation curves from the literature are shown (indicated by the color of the curves): Cardelli, Clayton and Mathis (1989), Savage and Mathis (1979), Gordon et al. (2003), Fitzpatrick (1999). The attenuation curves are plotted considering three different color excess values between bands B and V: $E_{(B-V)} = 1.0$ (solid lines), $E_{(B-V)} = 1.5$ (dashed lines) and $E_{(B-V)} = 2.0$ (dotted lines). The broad bump centered at ≈2175 Å occurs due to graphite and other carbon-rich hydrogenated particles (Osterbrock; Ferland, 2006).

where $F(\lambda)_{\rm int}$ and $F(\lambda)_{\rm obs}$ correspond to the intrinsic and the observed flux, respectively. Rewriting the expression, we have:

$$F_{\rm int}(\lambda) = F_{\rm obs}(\lambda) \times 10^{0.4\,A_\lambda} \tag{3.12}$$

At the same time, the color excess is related to the extinction via the value of the attenuation curve at a given wavelength $k(\lambda)$, i.e. $A_\lambda = k(\lambda)\,E(B-V)$. The reddening laws are normalized to have $k(B) - k(V) = 1$, which yields the identity $A_\lambda = k(\lambda)\,A_V/R_V$. The emission line ratios of the Balmer emission lines are sensitive to the effects of dust, causing the attenuated observed values to be smaller than the intrinsic ones. Using the emission lines Hα and Hβ, the difference in extinction on both fluxes can be expressed using both the relation above and equation 3.11:

$$\begin{aligned} A(\mathrm{H}\beta) - A(\mathrm{H}\alpha) &= 2.5 \log_{10}\left[\frac{(\mathrm{H}\alpha/\mathrm{H}\beta)_{\rm obs}}{(\mathrm{H}\alpha/\mathrm{H}\beta)_{\rm int}}\right] \\ &= \frac{A_V}{R_V}\Big[k(\lambda_{\mathrm{H}\beta}) - k(\lambda_{\mathrm{H}\alpha})\Big] \end{aligned}$$

Combining both sides of the equality to isolate A_V, and using the identity $E_{(B-V)} = A_V/R_V$, we have the expression (Momcheva et al., 2013):

$$E_{(B-V)} = \frac{2.5}{k(\lambda_{\mathrm{H}\beta}) - k(\lambda_{\mathrm{H}\alpha})} \log_{10}\left[\frac{(\mathrm{H}\alpha/\mathrm{H}\beta)_{\mathrm{obs}}}{(\mathrm{H}\alpha/\mathrm{H}\beta)_{\mathrm{int}}}\right] \tag{3.13}$$

The uncertainty on the estimated values of color excess can be obtained with error propagation of the analytical expression in 3.13 (see Appendix D for details in the mathematical derivation):

$$\delta E(B-V) = \frac{1.086}{k(\lambda_{\mathrm{H}\beta}) - k(\lambda_{\mathrm{H}\alpha})} \sqrt{\left(\frac{\delta\mathrm{H}\alpha}{\mathrm{H}\alpha}\right)^2 + \left(\frac{\delta\mathrm{H}\beta}{\mathrm{H}\beta}\right)^2} \tag{3.14}$$

where Hα, Hβ are the observed fluxes and δHα, δHβ the associated flux uncertainties. In the so-called case B of recombination, it is considered that the photons in a nebula are absorbed as soon as they are emitted (Osterbrock; Ferland, 2006; Pérez-Montero, 2017). For a fixed electron density of $N_e = 100\,\mathrm{cm}^{-3}$ and with the case B of recombination, López-Sánchez et al. (2015) provide a polynomial fit to parameterize the intrinsic Balmer ratios as a function of the electronic temperature T_e:

$$\left[\frac{I(\mathrm{H}\alpha)}{I(\mathrm{H}\beta)}\right]_{\mathrm{int}} = 10.35 - 3.254 \times \log T_e + 0.3457 \times (\log T_e)^2 \tag{3.15}$$

3.3 Electron temperature and density

To determine the electron temperature (T_e) in an ionized gas nebula, a common approach is to use the intensity ratio between transitions from two different levels of the same ion species (Osterbrock; Ferland, 2006). When choosing the set of emission lines to estimate T_e, the main requirements are (*i*) that they are produced (and observed above the detection limit) in different energy levels, as the relative electron population of each quantum level in an ion depends on T_e (Nicholls; Kewley; Sutherland, 2020), and (*ii*) that the adopted transitions occur within the the observed wavelength range. While the latter condition depends on the instrumental configuration, the most widely used lines meeting the first condition are the collisionally excited transitions from the ^{1}S $\rightarrow^1$ D levels in the [O III] and [N II] ions (Keenan et al., 1997; Nicholls; Kewley; Sutherland, 2020, see Fig. 22). The sensitivity of these emission line intensities with respect to T_e variations arises from the fact that the relative rates of excitation to the ^{1}S and ^{1}D levels are strongly dependent on the gas temperature (Osterbrock; Ferland, 2006; Nicholls; Kewley; Sutherland, 2020). Considering typical values of collision strengths, approximate analytical expressions for the dependence of some ions on T_e are presented in Osterbrock and Ferland (2006):

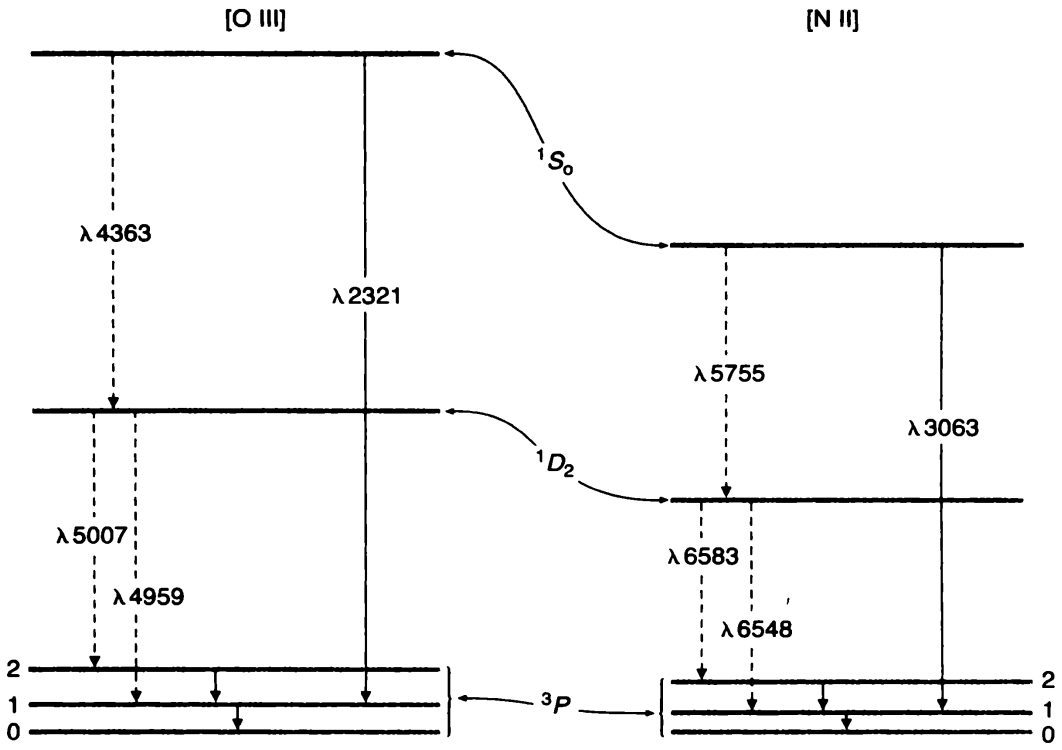

Figure 22 – Energy-level diagrams of [O III] and [N II] ions, from the excited levels ^{1}S and ^{1}D to the ground state. Transitions in the NIR and UV are shown as solid lines, whereas transitions in the optical are depicted as dashed lines. The difference between energy levels in the ground state have been exaggerated for clarity. Credit: Osterbrock and Ferland (2006).

$$[\mathrm{O\,III}]\ \frac{j_{\lambda4959}+j_{\lambda5007}}{j_{\lambda4363}} = \frac{7.9\,\exp\left(3.29\times10^4\,T_e^{-1}\right)}{1+4.5\times10^{-4}\times N_e T_e^{-1/2}} \tag{3.16}$$

$$[\mathrm{N\,II}]\ \frac{j_{\lambda6548}+j_{\lambda6583}}{j_{\lambda5755}} = \frac{8.23\,\exp\left(2.50\times10^4\,T_e^{-1}\right)}{1+4.4\times10^{-3}\times N_e T_e^{-1/2}} \tag{3.17}$$

$$[\mathrm{S\,III}]\ \frac{j_{\lambda9532}+j_{\lambda9069}}{j_{\lambda6312}} = \frac{5.44\,\exp\left(2.28\times10^4\,T_e^{-1}\right)}{1+3.5\times10^{-4}\times N_e T_e^{-1/2}} \tag{3.18}$$

where j represents the emission coefficients of each line. In Fig. 23 we present the curves for the temperature dependency of the line ratios in equations 3.16, 3.17 and 3.18, as well as for other ions. Notoriously, these emission line ratios also depend on the nebular electron density. In Fig. 23 they are presented considering the low-density regime of $N_e = 1\,\mathrm{cm}^{-3}$. However, these emission line ratios are nearly invariant to density changes within the typical regime observed in nebulae ($N_e \ll 10^3\,\mathrm{cm}^{-3}$).

Similarly, density-sensitive collisionaly excited emission lines can be used to determine N_e. The most commonly used transitions are [S II] $\lambda\lambda$6716,6731 and [O II] $\lambda\lambda$3726,3729 ions. These strong emission lines are accessible over a wide range of redshifts, being close in the spectral direction, having nearly the same excitation energy and showing low sensitivity to temperature variations (Osterbrock; Ferland, 2006; Kakkad et al., 2018). The

emission lines that compose the doublet [O II] $\lambda\lambda$3726,3729 are separated by only 3 Å, and eventually some spectrographs may have the necessary spectral resolution to resolve the doublet. [S II] $\lambda\lambda$6716,6731 is more used than the [O II] doublet, being sensitive to electron densities in the approximate range of $50 - 2000\,\mathrm{cm}^{-3}$, while the latter is more sensitive for lower-density systems (Kakkad et al., 2018). The electron density dependency for both doublets can be visualized in Fig. 24, where the asymptotic behavior of the functions corresponds to the density limits for which the emission line ratios become insensitive to density variations. The curve of density-dependent [S II] $\lambda\lambda$6717,31 emission line ratios presented in Fig. 24 can be parameterized with the following polynomial, with coefficients fitted by PYNEB (Luridiana; Morisset; Shaw, 2015) considering the collision strengths from Tayal and Zatsarinny (2010):

$$N_e\left([\mathrm{S\ II}]\right) = 10^3 \times \frac{R_{\mathrm{S2}}\left(16.05 - 7.79t^{-1} - 11.32t\right) - 22.66 + 11.08t^{-1} + 16.02t}{R_{\mathrm{S2}}\left(-21.61 + 11.89t^{-1} + 14.59t\right) + 9.17 - 5.09t^{-1} - 6.18t} \tag{3.19}$$

where $R_{\mathrm{S2}} \equiv [\mathrm{S\ II}]\ (j_{\lambda6717}/j_{\lambda6731})$ and t is the electron temperature calculated with expression 3.16 in units of 10^4 K. This expression is valid for the ranges of $10 < N_e\,[\mathrm{cm}^{-3}] < 1000$ and $0.6 < t < 2.2$ (Pérez-Montero, 2017).

By being related to nebular conditions through the relative electronic populations in the ions, the emission line ratios probe the flux-weighted inner thermal and density structures of H II regions. However, ions have different ionization potentials and are produced in different regions of the nebula. A simple and widely used sketch to study the thermal inner structure of nebulae is the one proposed by Garnett (1992), which defines three zones: The high-excitation zone, corresponding to the innermost nebular regions and traced by ions such as [O III], He II, [Ne III]; the intermediate-excitation zone, traced by ions such as [S III] and [Ar III]; and the low-excitation zone, the outermost nebular region traced by ions with lower ionization potentials such as [S II], [N II] and [O II] (Pérez-Montero, 2017).

3.4 Gas-phase chemical abundances

To determine the ISM chemical enrichment due to past stellar generations and to address the chemical evolution in a galaxy, it is essential to estimate the abundances of a given ion in the galaxy gas-phase from the corresponding Collisionally Excited Emission Lines (CEELs) commonly observed in the spectra of star-forming regions. The abundance of a given ion X with respect to Hydrogen can be expressed by:

$$\frac{N(X)}{N(H)} = \sum_i \frac{N(X^i)}{N(H^+)} \tag{3.20}$$

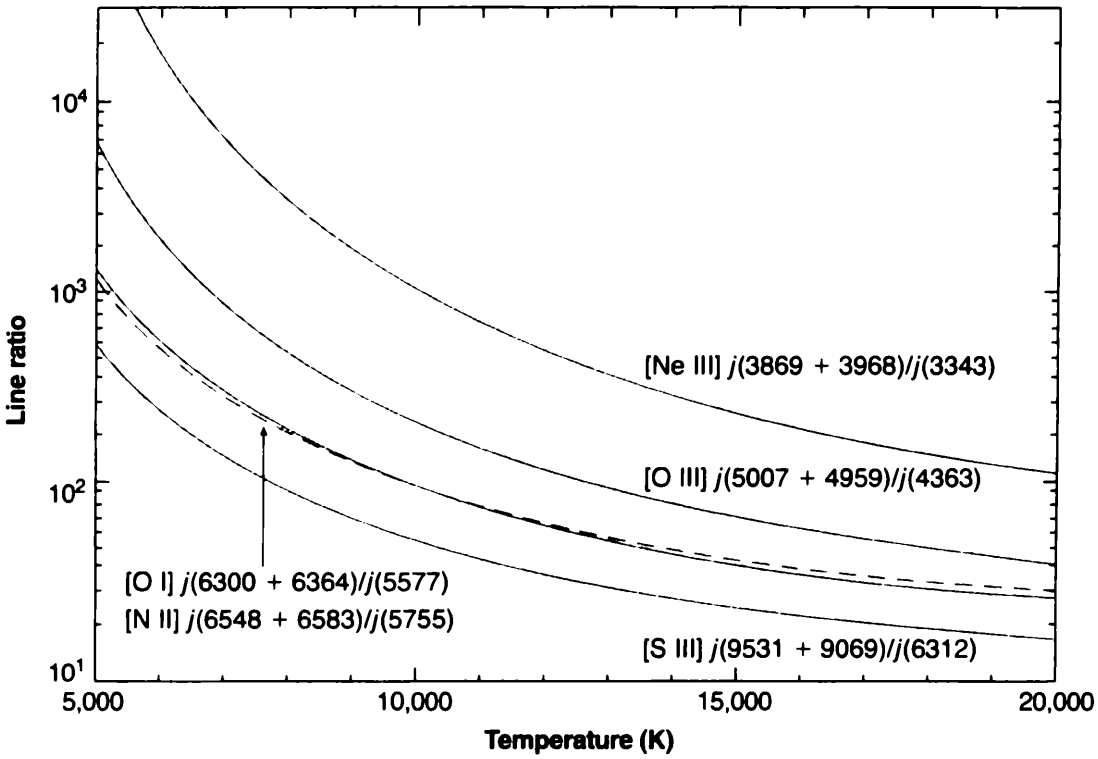

Figure 23 – Relation between emission line ratios with electron temperature T_e for a set of temperature-sensitive emission lines. The presented ratios were calculating considering the low-density regime of $N_e = 1\,\mathrm{cm}^{-3}$. Credit: Osterbrock and Ferland (2006).

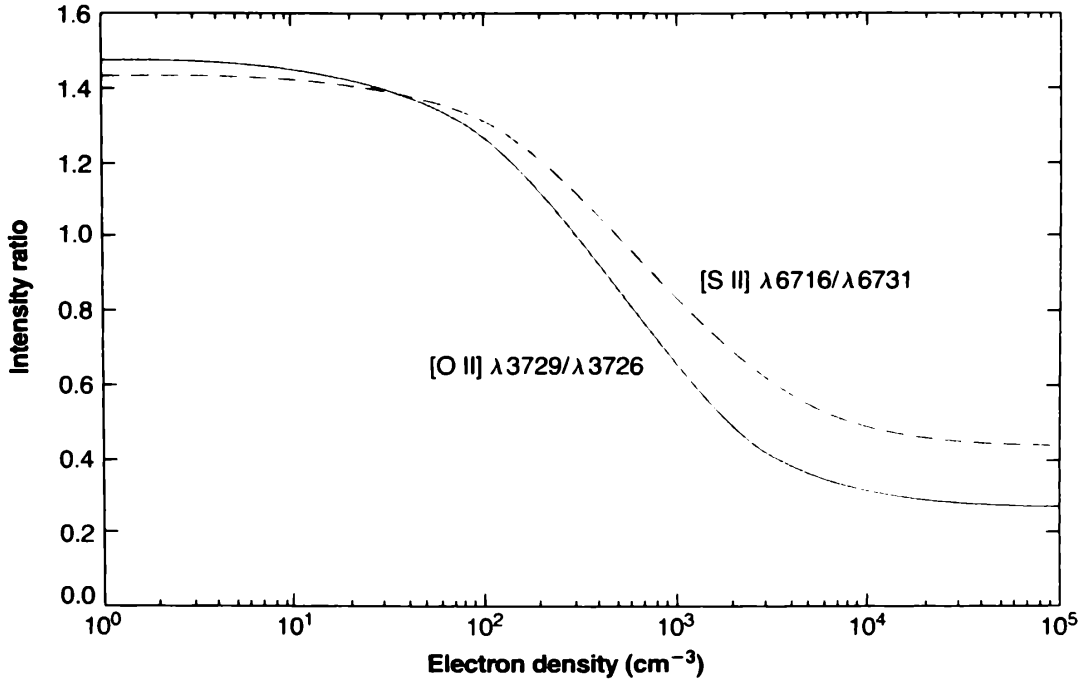

Figure 24 – Relation between emission line ratios and electron density for a set of the most density-sensitive emission lines in the optical, where the presented values of emission line ratios were calculated assuming $T_e = 10^4\,\mathrm{K}$. The asymptotic behavior of the curves indicates the values of density for which these lines saturate. Credit: Osterbrock and Ferland (2006).

where i is the degree of ionization of the ion X responsible for the observed CEELs. However, it is highly challenging to determine spectroscopically the abundances of any ion by direct application of equation 3.20, as it requires the observation of emission lines produced in transitions from all excited levels. Many transitions are often too faint to be detected, and the set of all transitions covers a very wide wavelength range that is usually unavailable. To circumvent this obstacle, Peimbert (1967), Peimbert and Costero (1969) proposed the use of an Ionization Correction Factor (ICF) to determine the total relative abundances of a given ion from the subset of its emission lines observed in the optical range (Luridiana; Morisset; Shaw, 2015; Pérez-Montero, 2017):

$$\frac{N(X)}{N(H)} = \mathrm{ICF}(X_{\mathrm{obs}}) \times \frac{N(X_{\mathrm{obs}})}{N(H^+)} \tag{3.21}$$

where $N(X_{\mathrm{obs}})$ corresponds to the ionic abundance obtained from the observed emission lines. In the case of Oxygen, its most abundant ions, O^+ and O^{2+}, are easily detected in the optical range (Izotov et al., 2006). From Equation 3.21 we have:

$$\frac{O}{H} = \mathrm{ICF}(O^+ + O^{2+}) \times \frac{O^+ + O^{2+}}{H^+} \tag{3.22}$$

The ionization potentials of O and H are very similar[10], making the charge-exchange reaction[11] highly efficient (Kreckel et al., 2022). If we consider an H II region without a radiation field hard enough to produce significant amounts of O^{3+}, whose ionization potential is 54.9 eV (Biémont; Frémat; Quinet, 1999; Pottasch; Bernard-Salas; Roellig, 2008), the approximation $O^0/(O^0+O^+) \approx H^0/(H^0+H^+)$ is valid and often adopted (Izotov et al., 2006; Pérez-Montero, 2017). This is equivalent to the approximation $\mathrm{ICF}(O^+ + O^{2+}) \approx 1$ in Equation 3.22. In the presence of hard ionization fields, the production of small fractions of O^{3+} is expected and, despite contributing only to a few percent of the total O/H, it can be accounted for by $\mathrm{ICF}(O^+ + O^{2+})$. A good tracer for hard ionization fields in the optical range is the He II λ4686 emission line, from the He^{2+} ion, which has a similar ionization potential[12] compared to O^{3+} and thus can be used to fine-tune the expression for $\mathrm{ICF}(O^+ + O^{2+})$ (Torres-Peimbert; Peimbert, 1977; Armah et al., 2021):

$$\mathrm{ICF}(O^+ + O^{2+}) = \frac{\mathrm{He}^+ + \mathrm{He}^{2+}}{\mathrm{He}^+} \tag{3.23}$$

Another ion of particular interest is N^+, which has a similar ionization potential compared to O^+[13], often leading to the simplification $N^+/(N^0+N^+) \approx O^+/(O^0+O^+)$ and

[10] 13.618 eV and 13.598 eV, respectively (Moore, 1976; Mohr; Taylor, 2005)

[11] In this context, the reaction that ionizes a neutral O atom by electron capture from H^+, which is attracted towards neutral O by polarization forces (Osterbrock; Ferland, 2006): $O^0 + H^+ \rightarrow O^+ + H^0$

[12] The ionization potential of the He^{2+} ion is 54.42 (Yerokhin; Shabaev, 2015).

[13] The ionization potentials of N^+ and O^+ are 14.5 eV and 13.6 eV, respectively (Eriksson; Pettersson, 1971; Moore, 1976; Pottasch; Bernard-Salas; Roellig, 2008).

thus (Pérez-Montero, 2017):

$$\mathrm{ICF}(\mathrm{N}^+) \approx \frac{\mathrm{O}}{\mathrm{O}^+} \tag{3.24}$$

Using a merged sample consisting of ∼310 SDSS DR3 galaxies with high-excitation H II regions and 109 BCDs, including several very metal-poor ($\log(\mathrm{O/H}) < 7.6$) galaxies (Izotov et al., 2004), Izotov et al. (2006) determined the ICF of several ions, including N, where a very good agreement with earlier predictions from Stasińska (1990) was obtained:

$$\begin{aligned}
\mathrm{ICF}(\mathrm{N}^+) &= 0.718 - 0.825v + 0.853v^{-1}, \quad \log(\mathrm{O/H}) \leqslant 7.2 \\
&= 0.712 - 0.809v + 0.852v^{-1}, \quad 7.2 < \log(\mathrm{O/H}) < 8.2 \\
&= 1.752 - 1.476v + 0.688v^{-1}, \quad \log(\mathrm{O/H}) \geqslant 8.2
\end{aligned}$$

where $v \equiv \mathrm{O}^+/(\mathrm{O}^+ + \mathrm{O}^{2+})$, with validity of the expressions above in the range $0 \leqslant v \leqslant 1$. In Fig. 25, we present the ICFs for several ions typically observed in star-forming spectra as a function of O^+ and O^{2+}.

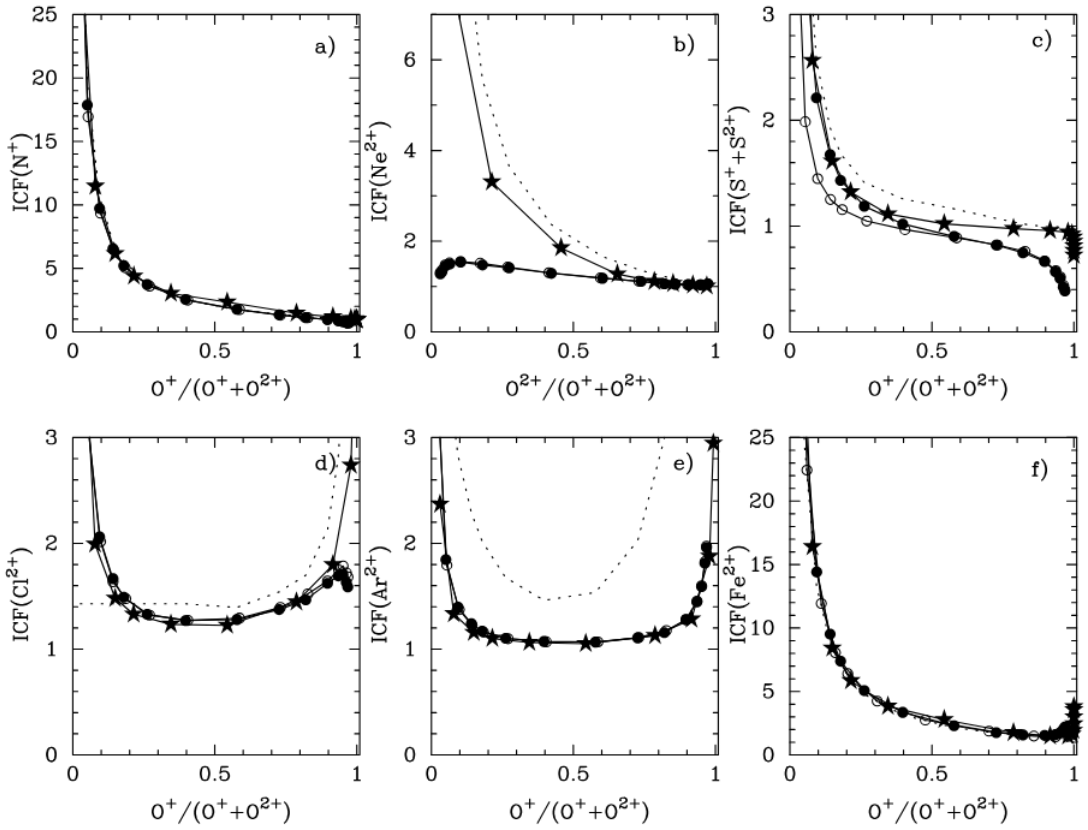

Figure 25 – Ionization Correction Factor of several ions typically observed in star-forming spectra as a function of O^+ and O^{2+}, obtained using photoionization models. Filled circles, open circles and stars correspond to photoionization models with $Z = 0.02\,Z_\odot$, $Z = 0.05\,Z_\odot$ and $Z = 0.2\,Z_\odot$, respectively. The dashed lines correspond to the ICF predictions from the models of Stasińska (1990). Credit: Izotov et al. (2006).

3.4.1 T_e–method for abundance determination

The most reliable estimates of ionic abundances from CEELs are obtained using derived values of T_e, through the so-called T_e–method (also known as the "direct method"). As highlighted in §3.3, T_e can be estimated using transitions from high quantum levels (the "auroral" lines). Examples of auroral emission lines in the optical are [O III] λ4363, [S II] λ4069, [N II] λ5755, [S III] λ6312, and [O II] $\lambda\lambda$7320,30 (Castellanos; Díaz; Terlevich, 2002). Below, we provide a few relations between ionic abundances and their corresponding emission line fluxes (Izotov et al., 2006; Pérez-Montero, 2017; Kumari et al., 2018):

$$12 + \log\left(\frac{O^{2+}}{H^+}\right) = \log\left[\frac{[\text{O III}](I_{\lambda4959} + I_{\lambda5007})}{H\beta}\right] + 6.1868 + \frac{1.2491}{T_{e,h}} - 0.5816\,\log(T_{e,h}) \tag{3.25}$$

$$12 + \log\left(\frac{O^{+}}{H^+}\right) = \log\left[\frac{[\text{O II}](I_{\lambda3726} + I_{\lambda3729})}{H\beta}\right] + 5.887 + \frac{1.641}{T_{e,l}} - 0.543\,\log(T_{e,l}) + 1.14 \times 10^{-4} \times N_e \tag{3.26}$$

$$12 + \log\left(\frac{N^{+}}{H^+}\right) = \log\left[\frac{[\text{N II}](I_{\lambda6548} + I_{\lambda6583})}{H\beta}\right] + 6.234 + \frac{0.95}{T_{e,l}} - 0.42\,\log(T_{e,l}) - 0.027\,T_{e,l} + \log(1 + 0.116 \times 10^{-4} \times N_e T_{e,l}^{-1/2}) \tag{3.27}$$

$$12 + \log\left(\frac{N^{+}}{O^+}\right) = \log\left[\frac{[\text{N II}]\,\lambda6583}{[\text{O II}](I_{\lambda3726} + I_{\lambda3729})}\right] + 0.493 - 0.025\,T_{e,l} - \frac{0.687}{T_{e,l}} + 0.162\,\log(T_{e,l}) \tag{3.28}$$

where the relations with temperature consider the three-zone sketch from Garnett (1992) to describe the nebular ionization structure. For instance, $T_{e,h}$ corresponds to the electron temperature in the high-ionization zone, i.e., $T_{e,h} \approx T_e([\text{Fe III}]) \approx T_e([\text{Ar IV}]) \approx T_e([\text{O III}]) \approx T_e(\text{He II})$. On the other hand, $T_{e,l}$ corresponds to the low-excitation zone, i.e., $T_{e,l} \approx T_e([\text{O II}]) \approx T_e([\text{N II}])$. Although not listed in the equations above, there is also the intermediate excitation zone traced by ions whose ionization potentials lie between the ones aforementioned, e.g., $T_{e,m} \approx T_e([\text{S III}]) \approx T_e([\text{Ar III}])$. All the temperatures in equations 3.25 — 3.28 are in units of 10^4 K. Ideally, an emission line spectrum contains all the transitions necessary to determine T_e for each zone. However, in practice, the observed wavelength range may not cover all the lines or, as often happens, the required auroral lines are too weak to be detected. As an alternative, relations between temperatures in different zones (T_e—T_e relations) were built either using photoionization models (Campbell; Terlevich; Melnick, 1986; Pagel et al., 1992; Garnett, 1992; López-Sánchez et al., 2012) or by empirical observations of objects with T_e estimates available for multiple zones (Pilyugin et al., 2009; Croxall et al., 2016; Berg et al., 2020; Rogers et al., 2021).

In the specific case of MUSE observations, as highlighted in §2.2.1, the spectrograph

does not cover the necessary wavelength range to detect the [O II] $\lambda\lambda$3726,29, preventing the application of Equation 3.26 to determine the abundance of O^+. This limitation is common in many observations, but fortunately Kniazev et al. (2003) provides an alternative expression relying on the [O II] $\lambda\lambda$7319,30 doublet that does not introduce biases in the O^+ abundance determination:

$$12 + \log\left(\frac{O^+}{H^+}\right) = \log\left[\frac{[O\ II](I_{\lambda7320} + I_{\lambda7330})}{H\beta}\right] + 6.901 + \frac{2.487}{T_{e,l}} - 0.483\ \log(T_{e,l}) - 0.013\,T_{e,l} + \log(1 - 3.48 \times 10^{-4} \times N_e T_{e,l}^{-1/2}) \quad (3.29)$$

For the same reason highlighted above, Equation 3.28 cannot be applied directly to estimate the Nitrogen abundance with respect to Oxygen in the case of MUSE observations. This limitation can be circumvented by using Equations 3.29 and 3.27 to calculate N/O via the expression $N^+/O^+ = (N^+/H^+)/(O^+/H^+)$.

3.4.2 Strong-line calibrations for abundance determination

The auroral emission lines are considerably weaker than the nebular lines and and are therefore harder to detect. As a result, the application of the T_e–based method described in §3.4.1 often becomes restricted to galactic regions with enhanced signal or is not feasible at all. This challenge led to the development of empirical calibrations between T_e and strong nebular emission lines (Pettini; Pagel, 2004; Marino et al., 2013; Dopita et al., 2016; Curti et al., 2017; Curti et al., 2020b; Sanders et al., 2021, among many others), which can be observed more easily even in spectra with low SNR or at higher redshifts, albeit at the cost of less accurate and more biased abundance determinations. These biases primarily arise from the fact that metallicity diagnostics are degenerated with other physical parameters such as, for instance, the ionization parameter and density (Pérez-Montero; Contini, 2009; Maiolino; Mannucci, 2019). Moreover, metallicity variations are not the only mechanism capable of changing emission line ratios. Although empirical calibrations are usually based on observations of emission lines from H II regions and star-forming galaxies carefully selected based on their location in diagnostic diagrams (see §3.5), it is difficult to fully eliminate contamination from Diffuse Ionized Gas (DIG), fast radiative shocks and Active Galactic Nuclei (Maiolino; Mannucci, 2019; Kumari et al., 2019).

Among the many indices (combinations of different emission line fluxes used to calibrate the gas-phase metallicity) in the optical range used in the literature, we will list those used throughout this work, starting with the definitions of O_3N_2 (Alloin et al., 1979), N_2 (Storchi-Bergmann; Calzetti; Kinney, 1994) and N_2S_2 (Sabbadin; Minello; Bianchini, 1977; Viironen et al., 2007):

$$N_2 \equiv \log\left(\frac{[\mathrm{N\,II}]\,\lambda6583}{\mathrm{H}\alpha}\right) \tag{3.30}$$

$$N_2S_2 \equiv \log\left(\frac{[\mathrm{N\,II}]\,\lambda6583}{[\mathrm{S\,II}]\,\lambda\lambda6717,31}\right) \tag{3.31}$$

$$O_3N_2 \equiv \log\left(\frac{[\mathrm{O\,III}]\,\lambda5007}{\mathrm{H}\beta} \times \frac{\mathrm{H}\alpha}{[\mathrm{N\,II}]\,\lambda6583}\right) \tag{3.32}$$

In §4.1 we used the empirical calibrations from Marino et al. (2013), which were built using a sample of H II regions from the Calar Alto Legacy Integral Field Area (CALIFA) survey (Sánchez et al., 2012):

$$12 + \log(\mathrm{O/H}) = 8.533(\pm0.012) - 0.214(\pm0.012) \times O_3N_2 \tag{3.33}$$

$$12 + \log(\mathrm{O/H}) = 8.743(\pm0.027) + 0.462(\pm0.024) \times N_2 \tag{3.34}$$

Both indices, O_3N_2 and N_2, are widely used, although the latter does not account for the ionization parameter of the gas (Kehrig et al., 2013). For this reason, we also used the calibration from Dopita et al. (2016) in §4.1 and §4.2. This calibration was developed using a grid of photoionization models for H II regions, resulting in a metallicity diagnostic that is nearly insensitive to changes in gas pressure and ionization parameter (Dopita et al., 2016, see their Fig. 3):

$$12 + \log(\mathrm{O/H}) = 8.77 + N_2S_2 + 0.264 \times N_2 \tag{3.35}$$

Although the indices used in the presented calibrations involve line ratios that are sufficiently close in the spectral domain to mitigate reddening effects, caveats arise from the fact that all of them are based on the use of [N II] λ6583. For instance, the metallicity diagnostic from Equation 3.35 depends on an intrinsic calibration of N production as a function of metallicity, based on observational data for stellar and nebular sources (see Figures 26 and 27). This intrinsic calibration is particularly important for the photoionization models, as N acts as an important nebular coolant (Dopita et al., 2016).

The dashed lines indicate the curves for primary and secondary N production. In the low metallicity regime ($12 + \log(\mathrm{O/H}) < 7.6$), N production is mainly primary, i.e., it is produced only by massive stars without influence of the gas-phase metallicity (Izotov; Thuan, 1999; Pérez-Montero et al., 2013), although see Meynet and Maeder (2005). In the metallicity range of $7.6 < 12 + \log(\mathrm{O/H}) < 8.3$, the N production is still predominantly primary, but the N abundance starts to increase due to ISM enrichment from low and intermediate-mass stars (Berg et al., 2012). At higher metallicities ($12 + \log(\mathrm{O/H}) > 8.3$), the contribution from secondary N production increases, as it depends on the existing

amounts of N via the CNO cycle (Pérez-Montero; Contini, 2009), giving rise to the positive slope observed in the N/O – O/H relation shown in Fig. 26 (Dopita et al., 2016; Kumari et al., 2018). This behavior on the N/O – O/H relation is also supported by closed-box chemical evolution models (Henry; Edmunds; Köppen, 2000; Mollá et al., 2006; Vincenzo et al., 2016), as depicted in Fig. 27, where the blue lines correspond to two models from Henry, Edmunds and Köppen (2000) with and without secondary N production (Pérez-Montero; Contini, 2009). In this figure, observational data for 271 H II galaxies (black squares), 161 Giant Extragalactic H II Regions (GEHRs, white squares) and 43 H II regions in the Milky Way and Magellanic Clouds (white triangles) is presented, where the metallicities in both axes were determined using the T_e–based method. On average, observations tend to follow the predictions from chemical evolution models in both Figures 26 and 27, despite the significant scatter in the latter. Therefore, even though empirical calibrations like those from Equations 3.34 and 3.33 do not require any prior calibration on the N/O – O/H relation, they reflect the average N enrichment processes of the sample they are based on (Maiolino; Mannucci, 2019).

The N/O – O/H relation is sensitive to evolutionary processes such as the time delay between O and secondary N production (Garnett, 1990; Pettini et al., 2008). It can deviate from the expected curves shown in Figures 26 and 27, exhibiting flat metallicity distributions caused by the efficient mixing of metals in the ISM (Marasco; Fraternali; Binney, 2012; Petit et al., 2015; del Valle-Espinosa et al., 2023), mergers and pair collisions (Kewley et al., 2010), or even presenting negative slopes when there is an inflow of pristine gas fueling new episodes of star formation and localized nitrogen enrichment due to nucleosynthetic ejecta from Wolf-Rayet (WR) stars (Kobulnicky; Skillman, 1997; López-Sánchez; Esteban, 2010; Amorín et al., 2012; Kumari et al., 2018). In these cases, the use of strong-line calibrations based on nitrogen emission lines can lead to deceiving abundance determinations (Maiolino; Mannucci, 2019). Alternatively, the following calibrations, based on S indices, can be used to determine O/H (Curti et al., 2020b) and N/O (Pérez-Montero et al., 2021):

$$\log(O_3S_2) = 0.191 - 4.292\,x - 2.538\,x^2 + 0.053\,x^3 + 0.332\,x^4 \tag{3.36}$$

$$\log(N/O) = (-1.005 \pm 0.005) + (0.857 \pm 0.013) \times N_2S_2 \tag{3.37}$$

where $x \equiv Z_{\rm gas} - Z_\odot$, with $12 + \log(O/H)_\odot = 8.69$ (Asplund et al., 2009; Asplund; Amarsi; Grevesse, 2021) and the index O_3S_2 is defined as follows (Curti et al., 2017):

$$O_3S_2 \equiv \log\left(\frac{[\text{O III}]\,\lambda5007}{\text{H}\beta} \times \frac{\text{H}\alpha}{[\text{S II}]\,\lambda\lambda6717,31}\right) \tag{3.38}$$

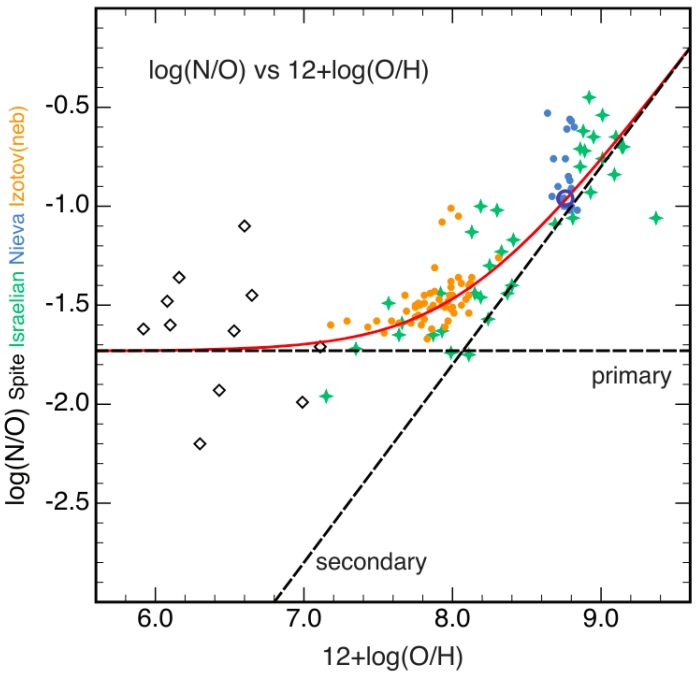

Figure 26 – N/O *vs.* O/H relation used to calibrate metallicity diagnostics from Dopita et al. (2016), based on observational data. Dashed lines indicate abundance patterns driven by primary and secondary N production. Stellar sources: Black circles represent extremely metal-poor stars observed with ESO VLT/UVES by Spite et al. (2005), and pink stars represent stars observed by Israelian et al. (2004). Blue dots are from a compilation of stellar spectroscopic data by Nieva and Przybilla (2012). Nebular sources: Orange dots represent a sample of 54 giant H II regions in low-metallicity blue compact galaxies with gas-phase metallicity in the range $7.1 < 12 + \log(\mathrm{O/H}) < 8.3$. Credit: Dopita et al. (2016), Nicholls et al. (2017).

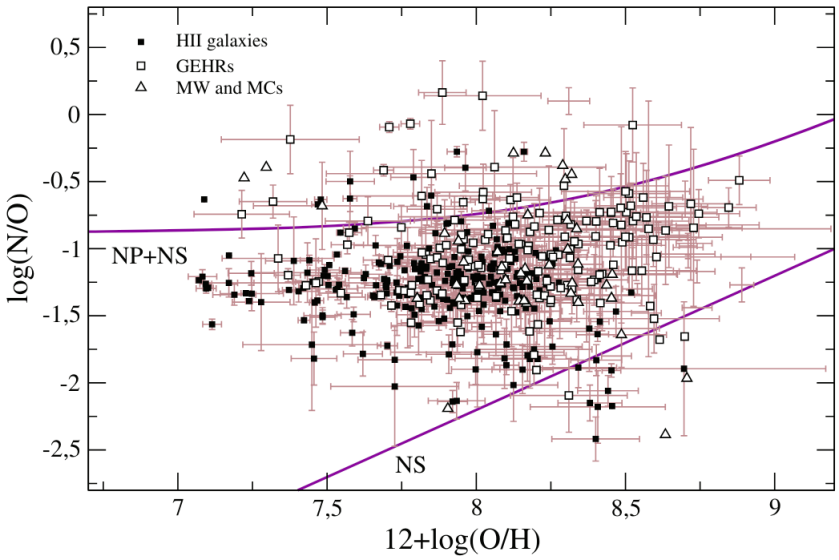

Figure 27 – N/O *vs.* O/H relation for 271 H II galaxies (black squares), 161 Giant Extragalactic H II Regions (GEHRs, white squares), and 43 H II regions in the Milky Way and Magellanic Clouds (white triangles). Both metallicity measurements were estimated using the T_e-based method. Blue solid lines correspond to Henry, Edmunds and Köppen (2000) closed-box chemical evolutionary models, with and without secondary N production. Credit: Pérez-Montero and Contini (2009).

3.4.3 Photoionization-based method for abundance determination

As an alternative to the strong-line calibrations presented in §3.4.2, abundance determinations can be made by comparing the observed emission lines with those predicted by emission line grids from photoionization models. Throughout this work, we use the H II - χ - MISTRY code[14] (Pérez-Montero, 2014) to infer nebular metallicities and compare the results with those obtained through the application of strong-line calibrations.

H II - χ - MISTRY was initially developed using the large sample of emission line fluxes from Marino et al. (2013), with known nebular conditions (e.g., the ionization parameter U, T_e, and N_e) that enable the application of the T_e-based method. Photoionization models were used to produce a grid of emission line fluxes spanning different abundances and excitation conditions using CLOUDY (Ferland et al., 2013). Starting from an input SED of an ionizing source and plane-parallel geometrical configuration, CLOUDY computes the spectrum originated from an 1D gas distribution. In the original work of H II - χ - MISTRY (Pérez-Montero, 2014), POPSTAR (Mollá; García-Vargas; Bressan, 2009) synthesis evolutionary models were used to produce the input ionizing SED, assuming a 1 Myr instantaneous burst with Chabrier (2003) IMF, although nowadays BPASS (Eldridge et al., 2017; Stanway; Eldridge, 2018) has also been implemented in the code to account for stellar binary evolution. The photoionization grid spans the range of $-4.0 < \log U < -1.5$ in steps of 0.125 dex, $7.1 < 12 + \log(O/H) < 9.1$ in steps of 0.1 dex and $-2.0 < \log(N/O) < 0.0$ in steps of 0.125 dex. Comparing the T_e-based abundance determinations with the χ^2-weighted mean abundances, the latter are found to agree with the direct method within 0.1 dex for $12 + \log(\mathrm{O/H}) > 8$ (Pérez-Montero, 2014). The output value of log(N/O), for instance, is calculated as the weighted sum of the log(N/O) values in the photoionization grid:

$$\log(\mathrm{N/O})_{\mathrm{out}} = \frac{\sum_i \log(\mathrm{N/O})_i/\chi_i}{\sum_i 1/\chi_i} \tag{3.39}$$

where i represents individual elements in the full photoionization grid, with χ_i calculated as the sum over the normalized differences between the de-reddened observed emission line ratios O_j and model predictions M_j (Pérez-Montero et al., 2016):

$$\chi_i = \sqrt{\sum_j \frac{(O_j - M_{ji})^2}{O_j}} \tag{3.40}$$

Similar approaches are also used to calculate both O abundance and the ionization parameter U. In the absence of input auroral emission lines, H II - χ - MISTRY restricts the space of metallicity and excitation conditions using empirical relations between N/O, O/H and log U, as shown in Fig. 28. The blue points represent the sample of Extreme

[14] https://home.iaa.csic.es/ epm/HII-CHI-mistry-opt.html

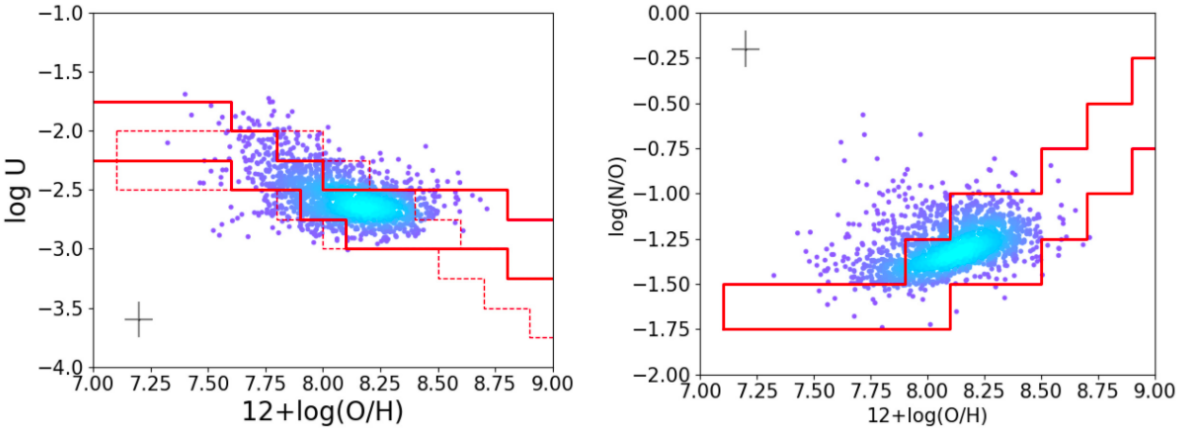

Figure 28 – Restrictions imposed by H II - χ - MISTRY code on the parameter space for nebular metallicity and excitation conditions in the absence of any auroral emission lines required to apply the T_e-based method among the input de-reddened emission line fluxes. The cloud of blue points correspond to the conditions of the EELGs sample analyzed in Pérez-Montero et al. (2021). The solid red lines highlight the grid restrictions for the EELG sample, while the dashed red lines correspond to the grid restriction on the "regular" sample of star-forming galaxies from Marino et al. (2013), Pérez-Montero (2014). Credit: Pérez-Montero et al. (2021).

Emission Line Galaxies (EELGs) analyzed in Pérez-Montero et al. (2021), obtained using an automated spectroscopic classification of SDSS-DR7 galaxies through k-means clustering algorithm (Sánchez Almeida et al., 2010). The solid red lines represent the allowed locus for the models in the $\log U - \log(\mathrm{O/H})$ and $\log(\mathrm{N/O}) - \log(\mathrm{O/H})$ planes, while the red dashed lines correspond to the grid restrictions considering the star-forming sample analyzed in Marino et al. (2013), Pérez-Montero (2014).

The photoionization-based methods for abundance determination have the advantage of not having to assume any intrinsic behavior on the N/O – O/H relation (Kumari et al., 2018), and their flexibility regarding the properties of the ionizing spectrum, combined with the wide metallicity range covered, makes this technique particularly useful for high-z galaxies with extremely metal-poor ISM environments without proper analogs in the local Universe (Kewley et al., 2013; Jaskot; Ravindranath, 2016). However, this method also has its limitations. For instance, the assumed nebular ionization structure in the photoionization models might be too simplistic to describe the complexity of real H II regions (Maiolino; Mannucci, 2019). Furthermore, an ionization-bounded structure is assumed for the ionized gas cloud, which might be problematic in young star-forming regions with escaping ionizing radiation (Nakajima; Ouchi, 2014; Maiolino; Mannucci, 2019).

3.5 Emission line diagnostic diagrams

The observation of emission lines in a spectrum indicates the presence of ionized gas. However, determining the mechanism responsible for producing this radiation field

is not always straightforward, as there are several candidate astrophysical mechanisms, and different mechanisms might operate simultaneously in nearby regions within a galaxy. Given that different ions in the gas have different ionization potentials, emission line ratios originating from electronic transitions in different ionic species hold the key to disentangle the dominant ionization mechanism, as they are sensitive to the shape of the ionizing source SED.

The two main photoionization sources are the short-lived, hot, and massive OB stars and AGNs. The continuum emission of a star in thermodynamic equilibrium is nearly that of a black body with the same temperature as $T_{\rm eff}$ (Anders; Fritze-v. Alvensleben, 2003; Mo; van den Bosch; White, 2010). Therefore, although stars emit light across the entire electromagnetic spectrum, OB stars produce higher amounts of UV photons than stars of other spectral types (see §3.1), making them the primary ionizing mechanism in star-forming regions, despite being less numerous than their less massive counterparts. On the other hand, the continuous emission of an AGN can be roughly approximated by a power law of the type $F_\nu \propto \nu^{-1.5}$ (Koski, 1978; Cid Fernandes et al., 2004; Riffel et al., 2009; Riffel et al., 2024).

Other mechanisms might also contribute to the ionization of the gas. For instance, shock waves are frequent in regions close to jets and high-velocity outflows originating from radio-loud AGNs, where part of their kinetic energy can be converted into thermal energy, which might then be converted into ionizing radiation (Laor, 1998; Keel et al., 2019). Likewise, supersonic shocks are common in outflows from young stellar sources and starburst galaxies, collisions between galaxies, supernova explosions, and other astrophysical phenomena, when the fast radiative shock waves contribute significantly to the total energy budget within the ISM, affecting directly the emission line ratios (Allen et al., 2008). Observed emission lines might also originate in Low-Ionization Nuclear Emission Line Regions (LINERs), with ionizing radiation resembling that typically seen in Seyfert galaxies, but with much lower L([OIII]) (Heckman, 1980; Kewley et al., 2006). In the last decade, this type of emission has been also found in regions extending much farther (on the order of kpc) than the nuclear galactic regions, when it was proposed to drop the "N" letter from the acronym, i.e. LIER (Stasińska et al., 2008; Sarzi et al., 2010; Cid Fernandes et al., 2011; Singh et al., 2013; Belfiore et al., 2016). It has been suggested that the ionizing radiation field from LINERs/LIER could be produced by low-luminosity AGNs (Halpern; Steiner, 1983; Ho, 1999), but especially by hot low-mass evolved stars (Binette et al., 1994; Stasińska et al., 2008; Cid Fernandes et al., 2011; Yan; Blanton, 2012). Moreover, the presence of DIG can also bias metallicity measurements and result in changes on emission line ratios, especially in low sSFR galaxies and/or regions with low $\Sigma_{\rm H\alpha}$ (Lacerda et al., 2018; Vale Asari et al., 2019). Finally, the delimiting lines used in the diagnostics are based on SDSS spectra, obtained with fixed fiber apertures of 3″ diameter (York et al., 2000), and recent studies have reported that ignoring aperture effects can lead to

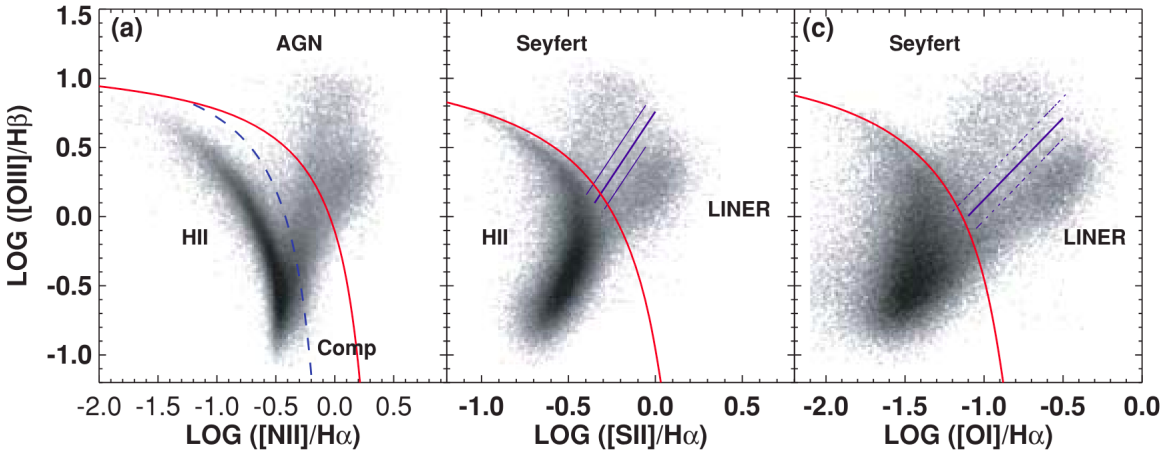

Figure 29 – Emission-line diagnostic diagrams used to distinguish the dominant ionization source. *Left*: The [N II] diagram proposed by Baldwin, Phillips and Terlevich (1981), with delimiting lines from Kewley et al. (2001) (solid red line) and Kauffmann et al. (2003) (dashed blue line) separating galaxies ionized by OB stars and AGNs. *Center*: The [S II] diagram, with the Kewley et al. (2006) line separating regions excited by AGNs from LINER-like regions. *Right*: The [O I] diagram, with solid blue and red lines from Kewley et al. (2006) and Kewley et al. (2001), respectively. Credit: Kewley et al. (2006).

misclassifications (Sánchez, 2020; Albán; Wylezalek, 2023; Riffel et al., 2023).

In summary, emission line ratios probe the shape of the ionizing radiation field and can be used as diagnostics to investigate the dominant ionizing source. This is the principle behind the BPT diagrams, an emission line-based diagnostic diagram first proposed by Baldwin, Phillips & Terlevich (Baldwin; Phillips; Terlevich, 1981, BPT). Although other diagnostic diagrams have been proposed in the literature (Cid Fernandes et al., 2011; Shirazi; Brinchmann, 2012; Pérez-Montero et al., 2023), in this work we focus on the three most commonly used diagrams: The [N II], [S II] and [O I] diagrams. These diagrams are presented in Fig. 29, where the gray-scale clouds represent the emission line ratios for a sample of over 85.000 nearby galaxies ($0.04 < z < 0.1$) from the SDSS – DR4 (Kewley et al., 2006). The emission line ratios in the diagrams involve lines that are close in the spectral direction, making reddening effects negligible.

Using a grid of photoionization models for H II regions powered by star clusters, Kewley et al. (2001) proposed a theoretical upper boundary on the [N II], [S II] and [O I] diagnostic diagrams. This boundary (the red solid line in all three diagrams in Fig. 29) delimits the most extreme starburst scenarios under varying nebular conditions. Emission line ratios exceeding this boundary require harder predominant ionizing sources than OB stars. The lines are described as follows:

$$\log\left(\frac{[\mathrm{O\,III}]\,\lambda5007}{\mathrm{H}\beta}\right) = 1.19 + \frac{0.61}{\log\left([\mathrm{N\,II}]\,\lambda6583/\mathrm{H}\alpha\right) - 0.47} \tag{3.41}$$

$$\log\left(\frac{[\mathrm{O\,III}]\,\lambda5007}{\mathrm{H}\beta}\right) = 1.30 + \frac{0.72}{\log\left([\mathrm{S\,II}]\,\lambda\lambda6717,31/\mathrm{H}\alpha\right) - 0.32} \tag{3.42}$$

$$\log\left(\frac{[\mathrm{O\,III}]\,\lambda5007}{\mathrm{H}\beta}\right) = 1.33 + \frac{0.73}{\log\left([\mathrm{O\,I}]\,\lambda6300/\mathrm{H}\alpha\right) + 0.59} \tag{3.43}$$

The star-forming envelope occupies well-defined regions in all the BPT diagrams, where the shape of the clouds in Fig. 29 suggests that L([O III]) acts as a discriminator for ionizing sources harder than OB stars. With this in mind, Kauffmann et al. (2003) used SDSS spectra of nearby galaxies ($0.02 < z < 0.3$) to develop an empirical-based line that separates the star-forming envelope from galaxies hosting narrow-line AGNs in the [N II] diagram. This delimiting line is shown in the [N II] diagram in Fig. 29 as a blue dashed line and can be described by the expression:

$$\log\left(\frac{[\mathrm{O\,III}]\,\lambda5007}{\mathrm{H}\beta}\right) = 1.3 + \frac{0.61}{\log\left([\mathrm{N\,II}]\,\lambda6583/\mathrm{H}\alpha\right) - 0.05} \tag{3.44}$$

From an analysis of the properties of galaxies hosting AGNs or LINERs/LIERs, Kewley et al. (2006) proposed an empirical relation to separate both categories in the [S II] and [O I] diagrams. These delimiting lines are shown as solid blue lines in the central and right panels of Fig. 29) and can be described by the following expressions:

$$\log\left(\frac{[\mathrm{O\,III}]\,\lambda5007}{\mathrm{H}\beta}\right) = 0.76 + 1.89 \times \log\left(\frac{[\mathrm{S\,II}]\,\lambda\lambda6717,31}{\mathrm{H}\alpha}\right) \tag{3.45}$$

$$\log\left(\frac{[\mathrm{O\,III}]\,\lambda5007}{\mathrm{H}\beta}\right) = 1.30 + 1.18 \times \log\left(\frac{[\mathrm{O\,I}]\,\lambda6300}{\mathrm{H}\alpha}\right) \tag{3.46}$$

Interestingly, it is possible to observe in Fig. 29) that the delimiting lines proposed by Kewley et al. (2001) and Kauffmann et al. (2003) are offset compared to the star-forming envelope, especially in the [N II] diagram. According to Stasińska et al. (2006), the galaxy samples used to define both delimiting lines present AGN contamination, leading to less restrictive upper boundaries. Using SDSS spectra with close inspection of nuclear activity, Stasińska et al. (2006) proposed a more restrictive boundary for the star-forming envelope in the [N II] diagram:

$$\log\left(\frac{[\mathrm{O\,III}]\,\lambda5007}{\mathrm{H}\beta}\right) = (-30.787 + 1.1358x + 0.27297x^2)\,\tanh(5.7409x) - 31.093 \tag{3.47}$$

with $x \equiv [\mathrm{N\,II}]\ \lambda6583/\mathrm{H}\alpha$.

3.6 Star Formation Rate

The SFR is one of the most important parameters for investigating galaxy evolution, as it traces how gas has been converted into stars. Different stellar populations dominate the continuous emission across the spectral range, making the SFR estimate sensitive to different timescales depending on the wavelength range considered.

For instance, in the rest-frame UV ($< 0.3\,\mu$m) the integrated spectrum of star-forming galaxies is dominated by massive ($M_\star \gtrsim 5\,M_\odot$) young stars that emit the bulk of their energy in this wavelength range (Kennicutt, 1998a). These young stars have typical lifetimes ranging from ∼6 Myr for an O6 stellar spectral type to ∼350 Myr for a B8 star (Calzetti, 2013). Using synthesis models to convert continuum UV flux into SFR and adopting constant SFR over timescales longer than the typical $< 10^8$ yr lifetimes of the dominant UV emitting population, the following relation between UV luminosity and SFR was obtained, assuming a Salpeter (Salpeter, 1955) stellar IMF (Kennicutt, 1998a; Madau; Pozzetti; Dickinson, 1998):

$$\mathrm{SFR}(M_\odot\,\mathrm{yr}^{-1}) = 1.4 \times 10^{-28} L_\nu\ [\mathrm{erg\,s^{-1}\,Hz^{-1}}] \tag{3.48}$$

where L_ν is the luminosity at a given frequency ν, nearly flat over the range 1500 – 2800 Å. As mentioned in §3.1, the detection of Balmer recombination lines in the optical indicates the presence of significant amounts of $\lambda < 912$ Å which, considering only stellar sources, corresponds to OB stars with lifetimes $\lesssim 20$ Myr (Kennicutt, 1998a). Thus, a relation of proportionality SFR $\propto Q_H$ is expected, and several calibrations between these quantities have been explored in the literature (Kennicutt R. C.; Kent, 1983; Kennicutt R. C.; Tamblyn; Congdon, 1994; Leitherer; Robert; Heckman, 1995; Madau; Pozzetti; Dickinson, 1998; Ly et al., 2016). Using a Salpeter stellar IMF with mass cutoffs of $0.1\,M_\odot$ and $100\,M_\odot$, Kennicutt (1998a) finds the following calibration at Solar abundances:

$$\mathrm{SFR}\,[M_\odot\,\mathrm{yr}^{-1}] = 7.9 \times 10^{-42}\,L(\mathrm{H}\alpha)\,[\mathrm{erg\,s^{-1}}] \tag{3.49}$$

where the conversion between Q_H and the de-reddened $L(\mathrm{H}\alpha)$ is computed assuming the case B of recombination at $T_e = 10^4$ K (Kennicutt, 1998a). Under the same assumptions but with a Chabrier (2003) stellar IMF, the calibration between SFR and Q_H from Equation 3.49 becomes:

$$\mathrm{SFR}\,[M_\odot\,\mathrm{yr}^{-1}] = 4.4 \times 10^{-42}\,L(\mathrm{H}\alpha)\,[\mathrm{erg\,s^{-1}}] \tag{3.50}$$

However, as mentioned, those calibrations are performed assuming Solar abundances. This assumption might result in overestimated SFRs at lower metallicities, given that the escape of ionizing photons in metal-poor O star atmospheres is greater (Ly et al., 2016).

With this in mind, Ly et al. (2016) uses $L(\mathrm{H}\alpha)$ predictions from STARBURST99 evolutionary models with PADOVA stellar evolutionary tracks (Alongi et al., 1993; Bressan et al., 1993; Fagotto et al., 1994a; Fagotto et al., 1994b; Girardi et al., 1996) and metallicities of $0.02\,Z_{\odot}$, $0.2\,Z_{\odot}$, $0.4\,Z_{\odot}$, $1.0\,Z_{\odot}$ and $2.5\,Z_{\odot}$ to derive a metallicity-dependent version of Equation 3.50:

$$\log\left[\frac{\mathrm{SFR}}{L(\mathrm{H}\alpha)}\right] = -41.34 + 0.39y + 0.127y^2 \tag{3.51}$$

where $y \equiv \log(\mathrm{O/H}) + 3.31$, so that $y = 0$ corresponds to the Solar metallicity, and with SFR and $L(\mathrm{H}\alpha)$ in units of $M_{\odot}\mathrm{yr}^{-1}$ and $\mathrm{erg\,s}^{-1}$, respectively. Since these calibrations probe the short-lived stellar populations, the SFR measured from optical recombination lines is often referred to as "instantaneous" SFR.

4 Analysis: SDSS J020536-081424

In this chapter, we present the analysis regarding SDSS J020536-081424 . This work began as a collaboration with my advisors Dr. Rogério Riffel, Dra. Ana Chies Santos, Dr. Evelyn Johnston and Dr. Boris Häußler during my Master's research. Initially, our aim was to study a sample of 10 ETGs with bulges and pseudo-bulges, including Mrk 1172. We serendipitously found SDSS J020536-081424 in the Fov of Mrk 1172, with no previous analysis of its properties reported in the literature, to the best of our knowledge. Part of the work presented in §4.1 was developed during the Master's period[1], and was completed during the first year of my PhD. We present this work in the form of a paper accepted for publication in the Monthly Notices of the Royal Astronomical Society journal. We also include a subsequently published correction on the original reported value for the systemic velocity of SDSS J020536-081424 . This work focuses on the spatially resolved description of the physical conditions of the ionized gas in the star-forming system, and on using the velocity fields of the emitting gas in SDSS J020536-081424 and of the stellar component in Mrk 1172 to confirm their interaction.

In §4.2 we present the second work related to ESO 400-43 , dedicated to investigate possible scenarios of clumpy star formation. submitted to Monthly Notices of the Royal Astronomical Society journal and is currently under review.

We separate the clump components from the underlying ionized gas and analyze their properties individually. We compare their gas-phase metallicities with those found in the ionized gas component to determine whether clump formation could have been caused by the infall of metal-poor gas from the IGM due to tidal torques caused by the interaction with Mrk 1172. Using velocity-sliced Hα maps we have shown that these clumps reside in a rotating component, providing further evidence for the presence of a disk in SDSS J020536-081424 , which reinforces the scenario of *in-situ* clump formation from violent gravitational instabilities in the disk.

4.1 The metal-poor dwarf irregular galaxy candidate next to Mrk 1172

[1] https://lume.ufrgs.br/handle/10183/217484

Monthly Notices of the ROYAL ASTRONOMICAL SOCIETY

MNRAS **506,** 3527–3539 (2021) https://doi.org/10.1093/mnras/stab1838
Advance Access publication 2021 July 1

The metal-poor dwarf irregular galaxy candidate next to Mrk 1172

Augusto E. Lassen [1]★ Rogerio Riffel [1] Ana L. Chies-Santos [1] Evelyn Johnston,[2,3] Boris Häußler,[4] Gabriel M. Azevedo,[1] Daniel Ruschel-Dutra [5] and Rogemar A. Riffel [6]

[1] *Universidade Federal do Rio Grande do Sul, Departamento de Astronomia, Av. Bento Gonçalves 9500, Porto Alegre, RS, Brazil*
[2] *Universidad Diego Portales, Núcleo de Astronomía de la Facultad de Ingeniería y Ciencias, Av. Ejército Libertador 441, Santiago, Chile*
[3] *Pontificia Universidad Católica de Chile, Institute of Astrophysics, Av. Vicuña Mackenna 4860, 7820436 Macul, Santiago, Chile*
[4] *European Southern Observatory, Alonso de Córdova 3107, Vitacura, Santiago, Chile*
[5] *Universidade Federal de Santa Catarina, Departamento de Física, P.O. Box 476, 88040-900, Florianópolis, SC, Brazil*
[6] *Universidade Federal de Santa Maria, Departamento de Física, Centro de Ciências Naturais e Exatas, 97106-900 Santa Maria, RS, Brazil*

Accepted 2021 June 25. Received 2021 June 25; in original form 2021 February 12

ABSTRACT

In this work, we characterize the properties of the object SDSS J020536.84−081424.7, an extended nebular region with projected extension of 14 × 14 kpc^2 in the line of sight of the ETG Mrk 1172, using unprecedented spectroscopic data from MUSE. We perform a spatially resolved stellar population synthesis and estimate the stellar mass for both Mrk 1172 (1×10^{11} M$_\odot$) and our object of study (3×10^9 M$_\odot$). While the stellar content of Mrk 1172 is dominated by an old (∼10 Gyr) stellar population, the extended nebular emission has its light dominated by young to intermediate age populations (from ∼100 Myr to ∼1 Gyr) and presents strong emission lines such as H β; [O III] λλ4959, 5007 Å; H α; [N II] λλ6549, 6585 Å; and [S II] λλ6717, 6732 Å. Using these emission lines, we find that it is metal poor (with $Z \sim 1/3\,Z_\odot$, comparable to the LMC) and is actively forming stars (0.70 M$_\odot$ yr^{-1}), especially in a few bright clumpy knots that are readily visible in H α. The object has an ionized gas mass $\geq 3.8 \times 10^5$ M$_\odot$. Moreover, the motion of the gas is well described by a gas in circular orbit in the plane of a disc and is being affected by interaction wtih Mrk 1172. We conclude that SDSS J020536.84−081424.7 is most likely a dwarf irregular galaxy (the dIGal).

Key words: ISM: abundances – H II regions – galaxies: dwarf.

1 INTRODUCTION

Dwarf galaxies are the most abundant class of galaxies in the Universe, and play a fundamental role in models of galaxy formation and evolution. In the hierarchical framework of galaxy formation, they are the building blocks of larger objects, contributing to the assembly of larger galaxies via successive mergers (e.g. Mateo 1998; Revaz & Jablonka 2018; Digby et al. 2019; and references therein). Since these galaxies are numerous, they probe many different environmental conditions and are sensitive to perturbations such as stellar feedback, for example, because their shallower gravitational potential wells make the pressure of the gas within these galaxies lower when compared to more massive galaxies (Navarro, Eke & Frenk 1996; Mashchenko, Wadsley & Couchman 2008). While some dwarf galaxies may evolve in isolation, many of them are found within systems where the effects of tidal and ram-pressure forces, for example, leave imprints in their star formation histories (SFHs). In the former case, these objects represent ideal laboratories to study internal drivers of galaxy evolution, like gas accretion (van Zee 2001; van Zee & Haynes 2006; Bernard et al. 2010; González-Samaniego et al. 2014). In the latter case, these compose an important set of galaxies to study the effects of environment in the determination of the mass and the structure of satellites (Mayer et al. 2001; Kazantzidis et al. 2011; Fattahi et al. 2018; Steyrleithner, Hensler & Boselli 2020).

Traditionally, dwarf galaxies are classified in two main categories, the dwarf Irregular (dI) and the dwarf Spheroidal (dSph). The dI galaxies are rich in gas and actively forming stars, usually located in the field, while dSph galaxies do not present significant star formation activity (Mayer et al. 2001; Gallart et al. 2015). The differences between both categories of dwarfs are usually based on current properties, and probably do not reflect their evolutionary histories. Since dIs and dSphs share many structural and evolutionary properties, the categorization is most likely to be related to the fact that in dSphs the star formation (SF) has ceased recently, while in dIs this SF persists until the present day (Skillman & Bender 1995; Kormendy & Bender 2012; Kirby et al. 2013).

In general, dIs are metal-poor, and the abundance of heavy elements in these galaxies, measured from their H II regions, lies in the range of 1/3–1/40 Z$_\odot$ (Kunth & Östlin 2000). As examples of metal-poor dIs we have the SMC and the LMC, with a metallicity of roughly 1/8 Z$_\odot$ and 1/3 Z$_\odot$, respectively (Kunth & Östlin 2000). There are also the blue compact dwarf galaxies (BCGDs), which can reach lower metallicities in their interstellar mediums (ISMs), as it is the case of I Zw 18. This BCDG has the lowest nebular Oxygen abundance among star-forming galaxies in the nearby Universe, with $Z \sim 1/50\,Z_\odot$ (Aloisi et al. 2007).

Understanding the chemical evolution of dwarf galaxies is essential to constrain models of galaxy formation and evolution, since the fraction of heavy elements within a galaxy is not only related to secular processes but can also carry imprints of past merging episodes (Lequeux et al. 1979; Skillman, Kennicutt & Hodge 1989;

★ E-mail: augusto.lassen@gmail.com

Croxall et al. 2009). The mass–metallicity relation is a widely studied empirical trend that holds from dwarfs to very massive galaxies, where the most massive galaxies are also more metal rich (Rubin, Ford & Whitmore 1984; Pilyugin & Ferrini 2000; Tremonti et al. 2004; Andrews & Martini 2013). An explanation for this relation is the easier retention of the metallic content by galaxies with deeper gravitational potential wells, since the mechanisms of gas transport such as gas accretion (infall) and winds (outflows), which are able to affect the metallicity of a galaxy, depend on the mass of the system (Gibson & Matteucci 1997; Dalcanton 2007). Thus, dwarf galaxies are excellent laboratories to study the chemical evolution of metal-deficient galaxies and offer unique conditions to improve our understanding of galaxy formation and evolution.

In this paper, we analyse an intriguing object in the vicinity of the massive early-type galaxy (ETG) Mrk 1172. This object has available photometric data in the optical (Sloan Digital Sky Survey, SDSS) and in the NUV and FUV (Galaxy Evolution Explorer, *GALEX*), but, to the best of our knowledge, has no previous detailed analysis on the literature (see Section 2.2). In Section 2, we introduce the data and the adopted analysis methodologies. In Section 3, we briefly describe the techniques and present the results obtained. In Section 4, we discuss our results and the conclusions are presented in Section 5. Throughout this work, we adopt $H_0 = 69.32\,\mathrm{km\,s^{-1}\,Mpc^{-1}}$, $\Omega_\mathrm{m} = 0.2865$, $\Omega_\Lambda = 0.7135$ (Hinshaw et al. 2013), and oxygen abundance as a tracer of the overall gas phase metallicity, using the two terms interchangeably, and a solar oxygen abundance of $\log(\mathrm{O/H}) + 12 = 8.76$ (Steffen et al. 2015).

2 OBSERVATIONS AND DATA REDUCTION

In this work, we present integral field spectroscopy (IFS) of the Mrk 1172 region (J020536.18-081443.23) from Program-ID 099.B-0411(A) (PI: Johnston). The data were obtained using the Multi-Unit Spectroscopic Explorer (MUSE; Bacon et al. 2010) on the Very Large Telescope (VLT) in the wide-field mode (WFM), covering the nominal wavelength range of 4650–9300 Å with mean spectral sampling of 1.25 Å, a field of view (FoV) of 1x1 arcmin^2, angular sampling of 0.2 arcsec and seeing of ∼1.4 arcsec. Mrk 1172 was observed on the nights of 2018 August 10 and 2018 October 1, with a total exposure time of 1.6 h split over six exposures. The images were rotated and offset to remove the effect of slicers and channels.

2.1 Data reduction

For each night of observations a standard star was observed for flux and telluric calibrations, sky flats were taken within a week of the observations and an internal lamp flat was taken immediately before or after each set of observations. This lamp flat image was used to correct for the time- and temperature-dependent variations in the background flux level of each CCD. Additional bias, flat-field, and arc images were observed the morning after each set of observations.

The data were reduced using the ESO MUSE pipeline (Weilbacher et al. 2020) within the ESO Recipe Execution Tool (EsoRex) environment (ESO CPL Development Team 2015). First, we created master bias and flat-field images and a wavelength solution for each detector and for each night of observations. The flux calibration solution obtained from the standard star observations and the sky flats were then applied to the science frames as part of the post-processing steps. The reduced pixel tables created for each exposure by the post-processing steps were combined to produce final data cube. Since the sky-subtraction applied as part of the EsoRex pipeline leaves behind significant residuals that may contaminate the spectra of faint sources, particularly at the NIR wavelengths, we applied the Zurich Atmosphere Purge (ZAP; Soto et al. 2016) to the final data cube in order to improve sky subtraction and minimize these artefacts.

2.2 Data specifications

During the inspection the data cubes from the MUSE Program-ID 099.B-0411(A), we identified an extended nebular region in the FoV of the ETG Mrk 1172 ($\alpha = 02^\mathrm{h}05^\mathrm{m}36\overset{\mathrm{s}}{.}19$, $\delta = -08^\mathrm{h}14^\mathrm{m}43\overset{\mathrm{s}}{.}25$). This region occupies a projected area of approximately 92 arcsec^2 in the observed FoV, calculated by defining a rectangle containing the correspondent object. The FoV is shown in the top left-hand panel of Fig. 1. We inspected this FoV in SDSS, and found that the bright source to the north-east of MRK 1172 (SDSS J020537.54−081411.5) and the two sources to the south (SDSS J020538.07−081501.2 and SDSS J020537.43−081502.2) are stars. The SDSS data also showed many small galaxies around Mrk 1172, most of them not visible in our data, indicating that this system could perhaps be a fossil group. Our object of interest is listed as SDSS J020536.84−081424.7, and has photometric information, though no spectra is available. This object also appears in the GALEX catalogue as GALEX J020536.7−081424, where photometric information on the NUV and FUV is available. For simplification, throughout this paper we will refer to it as the dwarf irregular galaxy (dIGal).

To illustrate the spectra of the dIGal and Mrk 1172, we selected the spaxels with highest SNR in each galaxy, the locations of which are represented by blue crosses in the top left-hand panel of Fig. 1. Both spectra are shown in the right-hand panel of Fig. 1, with main emission and absorption lines labelled. There are two prominent lines in Mrk 1172 spectrum red-wards of the H α absorption line that resemble emission lines. Comparing our spectrum with the one available in SDSS, we notice that these features are absent in the SDSS spectrum. These features are not normal sky lines, since they are broad and do not appear in the spaxels corresponding to sky background. There are other lines that appear in the red part of the spectrum, but curiously they are present only on the data corresponding to the second night of observation. We believe that these features are actually artefacts from the telluric correction. Usually telluric lines appear as broad absorption lines. However, in the case observations from the second night, the telluric lines are stronger in the standard star datacube than in the science datacube, causing an overcorrection of these features, and thus appearing as emission lines in the final datacube.

In the left-hand of panel of Fig. 1, we present the FoV now centred on the wavelength range corresponding to the main emission lines seen in the dIGal spectrum, subtracting the adjacent continuum. The emission lines and the continuum regions used in Fig. 1 are listed below:

(i) H α + [N II]: 6525–6535 Å, 6590–6600 Å
(ii) [O III] λ5007: 4990–5000 Å, 5015–5044 Å
(iii) [S II] : 6650–6700 Å, 6800–6900 Å

Using the strong emission lines in the spectra of the dIGal, we were able to measure its redshift as $z = 0.04025 \pm 0.00003$. In SDSS, Mrk 1172 has a reported redshift of $z = 0.04115$ (Ahn et al. 2012). The redshift measured for Mrk 1172 with MUSE observations is consistent with this previous measurement, and this is the value used throughout the paper.

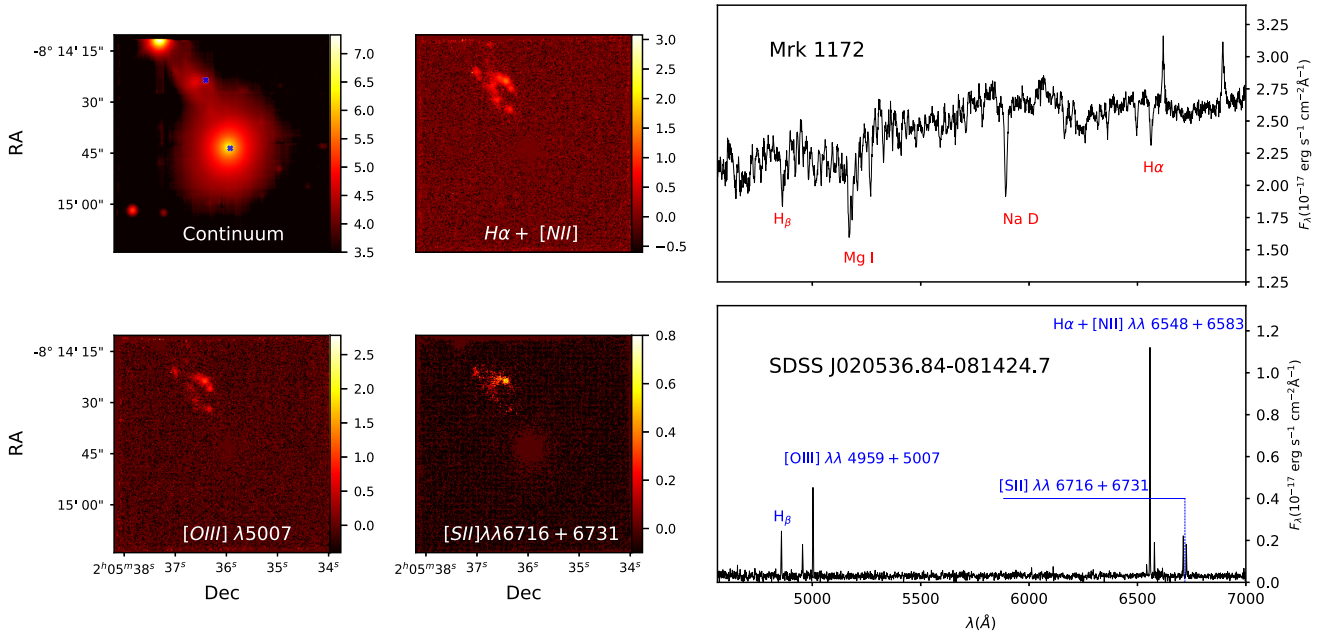

Figure 1. The MUSE FoV continuum centred in Mrk 1172 (top left), H α + [N II]$\lambda\lambda$6550 + 6585 (top central), [O III]λ5007 (bottom left), and [S II]$\lambda\lambda$6716 + 6731 (bottom central) wavelength ranges. The wavelength windows used to subtract the continuum from the flux of each emission lines are presented in Section 2. The spectrum of Mrk 1172 highest SNR spaxel is presented in top right-hand panel, while in bottom right-hand panel we present the spectrum for the highest SNR spaxel for the dIGal. The location of these spaxels within the FoV is indicated in blue in the top left-hand panel. The colourbars represent in logarithmic scale the flux in each image, in units of 10^{-20} erg s^{-1} cm^{-2}.

3 ANALYSIS

3.1 Stellar population fitting

A spatially resolved stellar population synthesis analysis is essential to reveal information regarding the formation, evolution and current state of the observed systems. With such techniques we can obtain the star-formation history (SFH) of both Mrk 1172 and the dIGal, as well as separating the stellar continuum/absorption features and the emission lines from the gas. This analysis will allow us to estimate several properties of the galaxies, such as extinction, SFR and other properties that shall be discussed further, and which can be illustrated via 2D maps (Cid Fernandes et al. 2013; Mallmann et al. 2018; do Nascimento et al. 2019).

To perform the stellar population synthesis we use the MEGACUBE module, which was developed to work as a front-end for the STARLIGHT code, operating in three main modules (Cid Fernandes et al. 2005; Mallmann et al. 2018; Riffel et al. 2021). Since STARLIGHT is designed to operate with ASCII-format files, the spectrum of each spaxel needs to be extracted from the original *fits* files, applying several pre-processing corrections, i.e. rest-frame spectrum shifting and galactic extinction correction. We used the dust maps from Schlegel, Finkbeiner & Davis (1998) and the CCM reddening extinction law (using $R_V = 3.1$, Cardelli, Clayton & Mathis 1989; O'Donnell 1994).

In order to increase the SNR of the individual spaxels, we have binned the original data cube 2x2 along the spatial direction. In order to increase the SNR of the individual spaxels, we have binned the original data cube 2x2 along the spatial direction. Since the spatial coverage of MUSE is large, many spaxels within the FoV cover empty regions in the sky or correspond to objects in the FoV that we would like to mask out from the analysis, such as stars. Therefore, it is useful to create a 2D boolean mask to flag valid and invalid spaxels. However, to create the mask we must adopt a reliable criteria to separate valid spaxels from the invalid ones. In this work, we adopt the following criteria:

(i) The flux vector of the individual spaxel must present 5 per cent or lower of negative and infinite numbers within the array in order to avoid the noisy spaxels, especially from the edges. In the case of spaxels considered to be valid by the above criterion but that still have few invalid numbers, we replace this numbers by applying an interpolation with neighbouring valid values.

(ii) The maximum of the flux (emission or absorption lines) must be at least 1.5 times greater than the standard deviation for that flux vector. In this way only spaxels with high SNR and/or strong emission and absorption lines are set as valid.

The values used to create the criteria were obtained after several tests, for example by comparing the final 2D mask with the continuum image added with H α emission, as shown in Fig. 2. Finally, each spaxel was convoluted with a Gaussian function[1] in order to match the spectral resolution of the target spectra ($R \sim 2850$ at 7000Å) with that of the simple stellar population (SSP) models [which have a full width at half-maximum (FWHM) = 2.51 Å resolution (Vazdekis et al. 2010, 2016)] and rebinned them to $\delta\lambda = 1$ Å. For the spaxel meeting, the above criteria and with the corrections applied we performed the stellar population synthesis. We used the Granada-Miles SSP models computed with the PADOVA200 isochrones and Salpeter IMF (Vazdekis et al. 2010; Cid Fernandes et al. 2014). We adopted 21 ages (0.001, 0.0056, 0.01, 0.014, 0.020, 0.031, 0.056,

[1]The new Gaussian kernel was obtained by subtracting the data and model σ values in quadrature and taking its root square mean value.

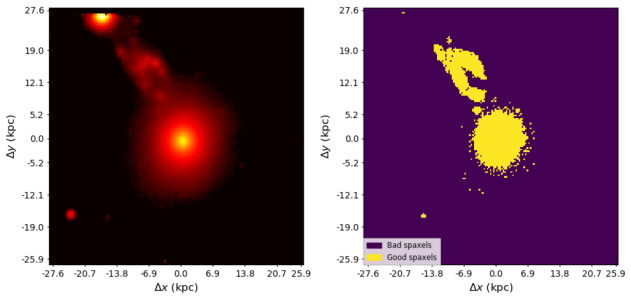

Figure 2. Comparison between Mrk 1172 FoV in continuum plus H α emission (left-hand panel) with a binary map (left-hand panel), where the yellow regions represent the spaxels used in the synthesis, while the purple spaxels are discarded. Undesired high SNR spaxels, such as those corresponding to the stars in the FoV were masked manually. The coordinates presented represent the offset in kpc from the reference spaxel of the FoV, centred in Mrk 1172.

0.1, 0.2, 0.316, 0.398, 0.501, 0.638, 0.708, 0.794, 0.891, 1, 2, 5, 8.9, and 12.6 Gyr) and four metallicities (0.19, 0.39, 1.0 and 1.7 $Z_{\odot}$). The fit was performed in the 4800–6900 Å spectral range with the normalization point at $\lambda_0 = 5600$ Å, a spectral region free of absorption/emission lines. The prominent lines present in Mrk 1172 spectra do not interfere in the stellar population synthesis, since they were masked out. For safety, we also used the sigma clipping algorithm of STARLIGHT in order to remove any additional spurious features (see Fig. 3).

With the stellar population synthesis done, we inspect the result for individual spaxels in Mrk 1172 and the dIGal. The locations of the spaxels with the highest SNR (approximately 90 and 7, respectively) spaxels in each target are marked in blue in Fig. 1. In Fig. 3, we show examples fits to these spectra, with Mrk 1172 in the top panels and for the dIGal in the bottom panels. We present the observed spectrum in black with the best-fitting synthetic spectrum in red, and below we show the residual spectrum and the regions masked by the sigma clipping method from STARLIGHT for both cases. In the right-hand panels, we show the histograms of the contribution weighted by luminosity of each stellar population with its respective ages. Mrk 1172 has dominant old stellar populations ($\sim 10^{10}$ yr), with the contribution of an artificial young stellar population ($\sim 10^{7}$ yr) that appears due to the AGN in this galaxy (Cid Fernandes et al. 2005; Riffel et al. 2009). Meanwhile, the dIGal is predominantly young, presenting two dominant stellar populations with ages between $\sim$100 Myr and $\sim$1 Gyr.

The luminosity-weighted mean age ($<t_L>$) for each spaxel can be obtained using (Cid Fernandes et al. 2005):

$$< t_L >= \sum_j a_j \log t_j, \quad (1)$$

where t_j is the age of the jth SSP model spectrum, and a_j is a normalization factor that takes into account the fact that the sum of the SSPs used to reproduce the input spectrum is not necessarily 100 per cent (Cid Fernandes et al. 2005). The resulting map is presented in Fig. 4, showing that the dIGal is dominated by young and intermediate stellar populations, while Mrk 1172 is dominated by old stellar populations. This figure shows the spatial distribution of the information, given by the histogram in Fig. 3. It can be seen in Fig. 4 that the stellar populations dominating the light emitted from the dIGal are considerably younger than those in Mrk 1172.

3.2 Fitting of the emission-line profiles

Having fitted the underlying spectrum of each spaxel, we subtract it from our observed data, resulting in pure emission line spectra. No

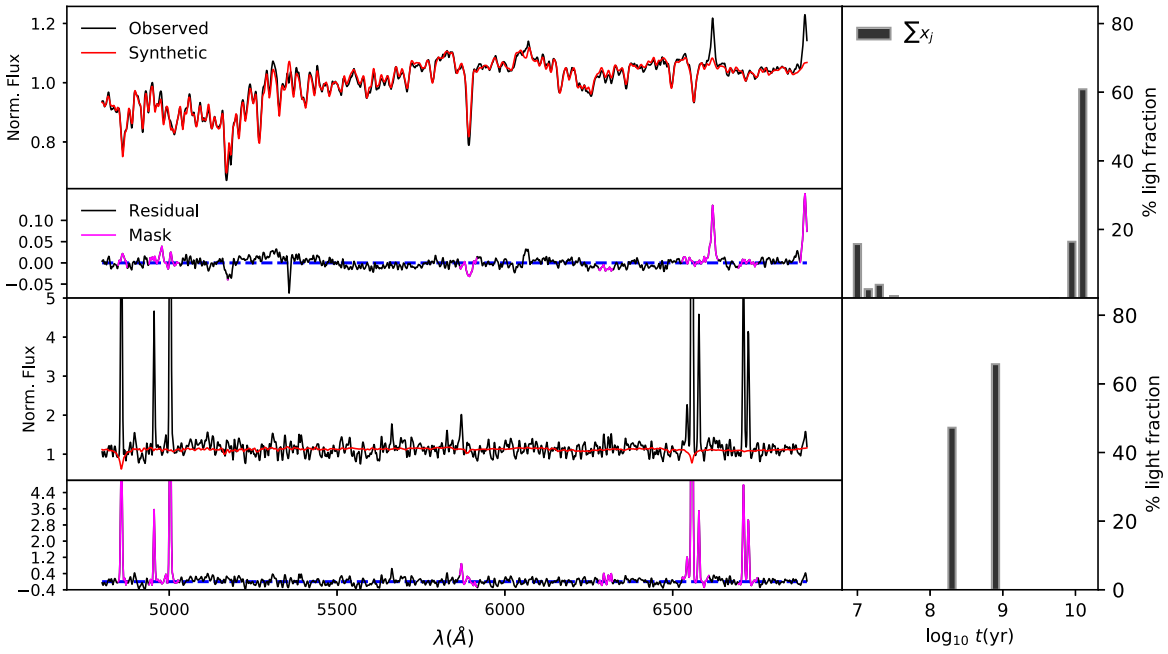

Figure 3. Synthesis results for the highest SNR spaxel for Mrk 1172 and the dIGal. *Top left-hand panel*: In black, the observed spectrum of Mrk 1172, where the flux is normalized using $F(\lambda_0)$. In red, the synthetic spectrum (the best fit from the stellar population synthesis). *Second top left-hand panel:* Residual spectrum for Mrk 1172 in black, with the regions masked by sigma clipping method in magenta. At the bottom left-hand panels, the same for the dIGal. *Top right-hand panel*: Histogram presenting the luminosity-weighted contribution of each stellar population for Mrk 1172 best fit and their ages. At the bottom right-hand panels, the same for the dIGal.

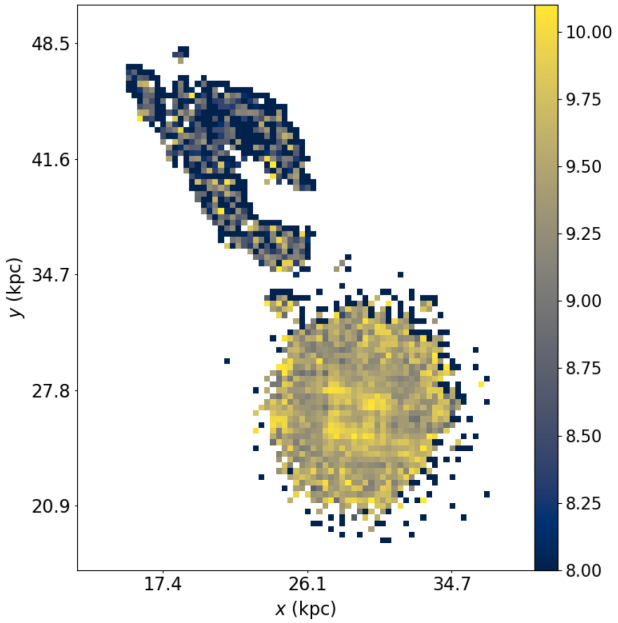

Figure 4. Mean luminosity-weighted age map for Mrk 1172 and the dIGal in Gyr, obtained via spatially resolved stellar population synthesis.

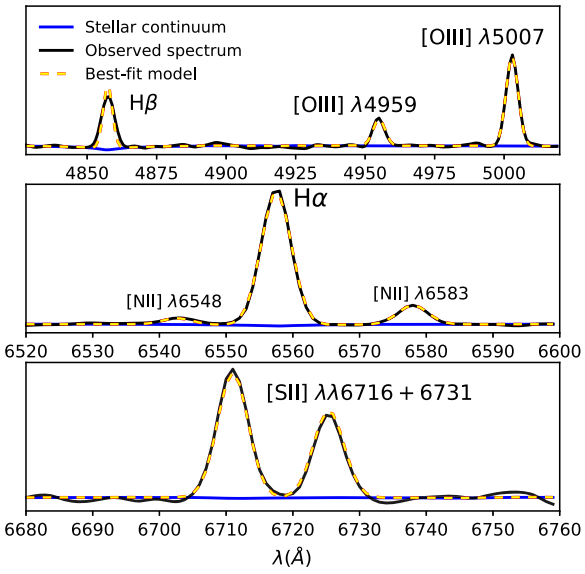

Figure 5. Emission lines in the dIGal spectrum fitted using Gaussian profiles with IFSCUBE. In black, the observed spectrum, in blue the continuum, and the dashed yellow line represents the model fit.

emission lines were detected in locations corresponding to Mrk 1172, while strong emission features were found in the spectra of the dIGal, as seen in Fig. 1. We measured the fluxes using the IFSCUBE (Ruschel-Dutra & de Oliveira 2020) tool, which fits the emission-line profiles at each position by single Gaussian curves.

3.2.1 *Single Gaussian fitting*

Fig. 3 shows that the synthetic spectrum produced through the stellar population synthesis models the continuum very well, thus we have not added a polynomial function to fit the continuum. The fitting of the emission lines was performed on the residual cube, obtained by the subtraction of the modelled continuum/absorption spectra from the cube used in the stellar population synthesis (i.e. a rest-frame spectrum, resampled in $\Delta\lambda = 1$ Å and corrected for Galactic reddening). As a first approach, we assume that emission lines corresponding to transitions on the same atom (i.e. [O III] λ4959 and [O III] λ5007) belong to the same kinematic group.[2] Since the strongest emission lines in the spectrum of the dIGal are from transitions of H, O, N and S, we use four different kinematic groups, one for each element. We also used specific constraints for the line ratios, e.g. [N II] λ6583 $= 3.06 \times$ [N II] λ6548 and $0.4 <$ [S II]λ 6717/[S II]λ 6731 < 1.4 (Osterbrock & Ferland 2006). The ratio of [O III] emission lines was kept free of constraints during the fitting process.

Fig. 5 shows an example of the outcomes of this fitting procedure, where we present the spectral regions containing the fitted emission lines. The observed spectrum is shown as a solid black line, the stellar continuum is shown in the solid blue lines and the best-fitting model is represented by a dashed yellow line. Besides fluxes, IFSCUBE also provides the gas kinematic parameters (gas velocity and velocity dispersion). In the next sections, we analyse these quantities.

An important side note is that the S doublet, which can be used to estimate the electron gas density (n_e, Osterbrock & Ferland 2006; Ryden & Pogge 2021), presents an emission line ratio that falls in the limit of sensibility of the density relation for the dIGal, making it impossible to determine n_e with accuracy. Therefore, we have assumed the lower limit of $n_e \sim 100$ cm^{-3} for the galaxy in the following analysis.

3.2.2 *Gas excitation*

The emission-line ratios allow us to determine the nature of the ionization source of the gas in the dIGal. For this analysis, we used the traditional BPT diagnostic diagram (Baldwin, Phillips & Terlevich 1981) to create spatially resolved maps of the likely ionization sources (for a similar analysis see Wylezalek et al. 2017; do Nascimento et al. 2019). In Fig. 6, we show these maps for the dIGal. In the diagram involving the lines ratios [N II]/H α *versus* [O III]/H β (top left-hand panel) the solid blue line separating H II from the transition region, as well as the solid red line separating Seyfert and LINER regions were taken from Kauffmann et al. (2003). The solid green line separating transition region from the AGN region was obtained from Kewley et al. (2001). The symbols are the positions of individual spaxels in the diagnostic diagram and the spatial distribution within the galaxy is shown on the right-hand panel. For the diagram involving [S II]/H α *versus* [O III]/H β line ratios (left bottom) the solid magenta line is from Kewley et al. (2001), while the solid red line is from Kewley et al. (2006).

Both diagrams show that the gas is ionized by young massive stars rather than by an AGN. Ionization by shocks are investigated using the fast radiative shock models from Allen et al. (2008), adopting solar metallicity, $n_e = 100\,\mathrm{cm}^{-3}$, and varying the values of magnetic field. With an inspection of the curves of emission line ratio versus shock velocity, we observe that the values for the gas in the dIGal are coherent to shock velocities $<100\,\mathrm{km\,s}^{-1}$. In the regime of such

[2]Many spectral features are physically linked, being produced in the same region of the target of study. Therefore, it is reasonable to assume that different transitions of the same atom were produced in the same region, and their emission lines share properties like velocity and velocity dispersion. When both lines share these properties, we say that they belong to the same kinematic group.

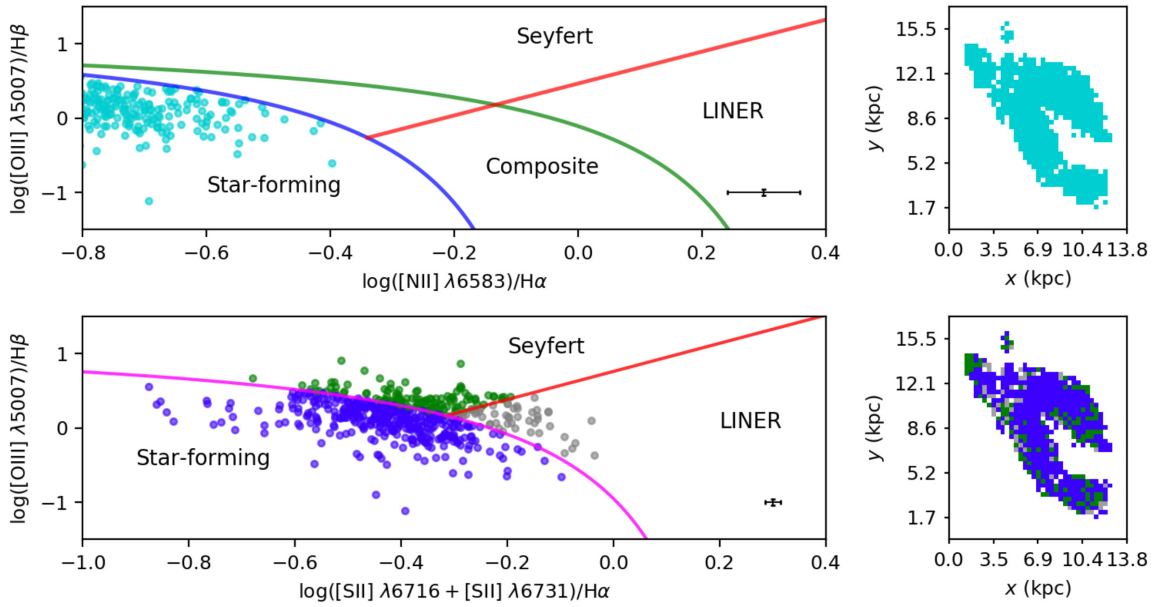

Figure 6. Spatially resolved diagnostic diagram for the dIGal. *Top left-hand panel:* The circles represent the position of individual spaxels in the diagnostic diagram. The relations for the solid blue and red lines were taken from Kauffmann et al. (2003). The relation for the solid green line was obtained from Kewley et al. (2001). *Bottom left-hand panel*: Same as top left-hand panel, now using different emission line ratio for the diagram. The red and magenta solid lines are given by Kewley et al. (2006) and Kewley et al. (2001), respectively. *Top/bottom right-hand panel*: The dIGal with each spaxel coloured corresponding to its position in the diagnostic diagram. The bars in the bottom right-hand corner of the right-hand panels indicate the mean error associated with the position of each point in the diagram.

low velocities, it is unlikely for shock ionization to be the dominant mechanism of photoionization in the dIGal.

3.3 Extinction

We have already corrected the observed spectra for the Galactic dust extinction using the Schlegel et al. (1998) dust maps, but the intrinsic attenuation of the dIGal still remains, and correcting for this effect is essential for obtaining many of the important properties concerning the gas components.

To perform this correction, we have followed Osterbrock & Ferland (2006). By considering I_λ as the observed intensity for a given wavelength and I_{λ_0} as the intrinsic intensity, we have

$$I_\lambda = I_{\lambda_0} \times 10^{-cf(\lambda)}, \tag{2}$$

where c is an undetermined constant and $f(\lambda)$ is the extinction curve. The number of magnitudes of extinction, A_λ, is related to the lines intensity ratio by

$$A_\lambda = -2.5 \log\left(\frac{I_\lambda}{I_{\lambda_0}}\right). \tag{3}$$

A_λ is related to A_V via the reddening law. By assuming the case B of recombination, with an intrinsic intensity ratio of H α/H β $= 2.87$, electron temperature of 10^4 K and $R_V = 3.1$, A_V can be derived using

$$A_V = 7.23 \times \log\left[\frac{F(\mathrm{H}\,\alpha)}{F(\mathrm{H}\,\beta)}\right] - 3.31,$$

where $F(\mathrm{H}\,\alpha)$ and $F(\mathrm{H}\,\beta)$ are the observed fluxes. This equation represents the attenuation caused by dust and molecular gas surrounding the H II regions. The extinction map produced with this equation for the dIGal is shown in Fig. 7.

3.4 Star formation rate

From the diagnostic diagram one can see that all spaxels of the dIGal are in the star-forming region, so it is interesting to estimate its SFR. We can calculate it using the Balmer recombination lines. Assuming case B of recombination and a Salpeter initial mass function (IMF), we can use the expression below to estimate the instantaneous SFR of the dIGal (Kennicutt 1998):

$$\mathrm{SFR}(\mathrm{M}_\odot\ \mathrm{yr}^{-1}) = 7.9 \times 10^{-42} L(\mathrm{H}\,\alpha)\ (\mathrm{erg\ s}^{-1}). \tag{4}$$

The luminosity $L(\mathrm{H}\,\alpha)$ was obtained from the flux of H α emission line using the distance of the dIGal, which was derived from its redshift of $z = 0.04025 \pm 0.00003$. Fig. 8 shows the resulting SFR map. The colourbar shows the SFR in units of 10^{-3} $\mathrm{M}_\odot\ \mathrm{yr}^{-1}$. Integrating the SFR over all spaxels results in a total SFR of 0.70 $\mathrm{M}_\odot$ yr^{-1} and a ΣSFR of 1.4×10^{-2} $M_\odot\ \mathrm{yr}^{-1}\ \mathrm{kpc}^{-2}$, which was obtained by dividing the SFR by the area of each spaxel. The peak value for an individual spaxel reaches 6.75×10^{-3} $\mathrm{M}_\odot\ \mathrm{yr}^{-1}$.

3.5 Stellar mass

We can use the information acquired with the stellar population synthesis to estimate the current stellar mass $M_\star$[3]:

$$M_\star(\mathrm{M}_\odot) = 4\pi d^2 \times M_{\mathrm{tot}}^{\mathrm{cor}} \times (3.826 \times 10^{33})^{-1}, \tag{5}$$

where d is the distance to the galaxy in units of cm and the base spectra used is in a proper unit of $\mathrm{L}_\odot\ \text{Å}^{-1}\mathrm{M}_\odot^{-1}$ and the observed spectra in units of $\mathrm{erg\ s}^{-1}\ \mathrm{cm}^{-2}\ \text{Å}^{-1}$. $M_{\mathrm{tot}}^{\mathrm{cor}}$ is a STARLIGHT output parameter in units of $\mathrm{M}_\odot\ \mathrm{erg}^{-1}\ \mathrm{cm}^{-2}$, which gives the current mass of stars in the galaxy based on the contribution of each SSP to the best-fitting synthetic spectrum. We can apply equation (5) to each spaxel of our

[3]https://minerva.ufsc.br/starlight/files/papers/Manual_StCv04.pdf

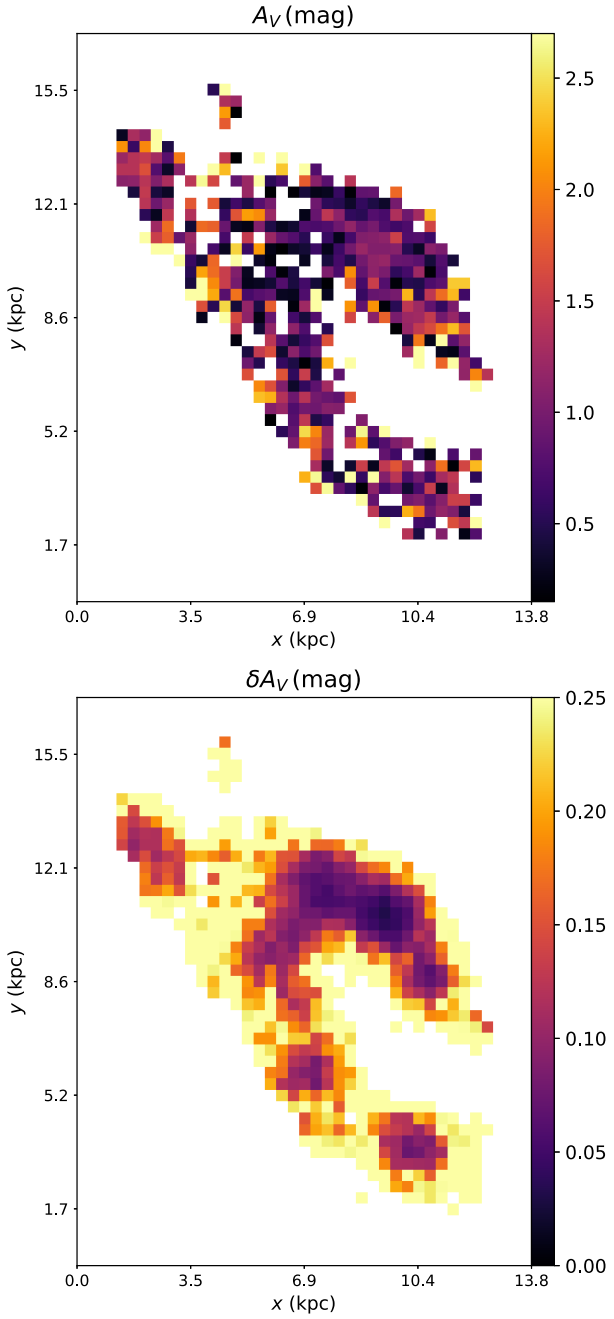

Figure 7. *Top panel*: The extinction map for the dIGal. The lighter regions of the map represent higher light extinction, while the darker regions represent lower extinction. In white, the masked points, excluded from the plot. The colourbar shows the range of extinction values measured in the region in magnitude units. *Bottom panel*: Map with the uncertainties of the A_v measurement, represented by δA_v, where we observe that the uncertainties drop as the spaxel is closer to the edge of the dIGal.

datacube to obtain the total stellar mass for both Mrk 1172 and the dIGal. We obtain $M_\star \sim 1.2 \times 10^{11}\mathrm{M}_\odot$ for Mrk 1172 and $M_\star \sim 3.0 \times 10^{9}\mathrm{M}_\odot$ for the dIGal. Similarly, we can estimate how many solar masses have been processed into stars through the lifetime of the system $(M_\star^{\mathrm{ini}})^3$ by using

$$M_\star^{\mathrm{ini}}\,(\mathrm{M}_\odot) = 4\pi d^2 \times M_{\mathrm{tot}}^{\mathrm{ini}} \times (3.826 \times 10^{33})^{-1}, \quad (6)$$

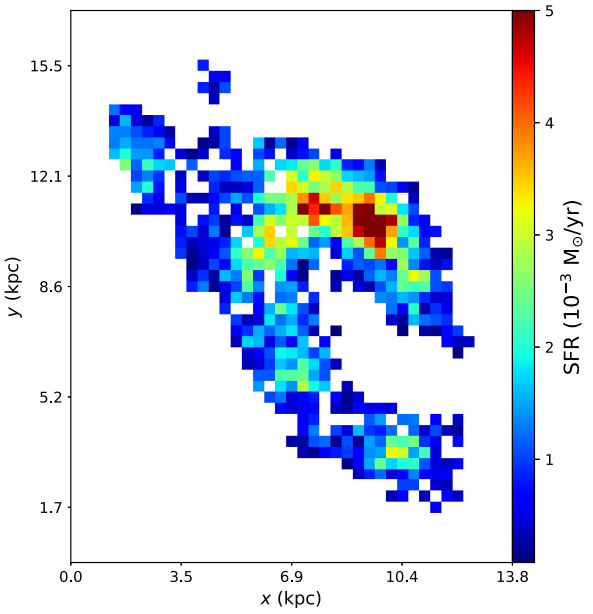

Figure 8. The dIGal SFR distribution map. Regions with high SFR appear in red, while regions without significant star formation appear in blue. The colourbar indicates the values of SFR associated with each colour in units of $\mathrm{M}_\odot\ \mathrm{yr}^{-1}$.

where M_{tot}^{ini} represents the mass that has been converted into stars and is given in units of $\mathrm{M}_\odot\ \mathrm{erg}^{-1}\ \mathrm{cm}^{-2}$(Riffel et al. 2021)[3]. Applying equation (6) to all valid spaxels, we obtain $M_\star^{\mathrm{ini}} \sim 1.7 \times 10^{11}\mathrm{M}_\odot$ for Mrk 1172 and $M_\star^{\mathrm{ini}} \sim 3.9 \times 10^{9}\mathrm{M}_\odot$ for the dIGal. $M_\star^{\mathrm{ini}}$ is expected to be higher than the current stellar mass of the system due to the mass returned to the ISM by SNe and winds.

3.6 Ionized gas mass

Following, for example, do Nascimento et al. (2019), we can calculate the mass of the ionized gas by using the expression:

$$M = n_{\mathrm{e}} m_{\mathrm{p}} V f, \quad (7)$$

where n_{e} is the electron density of the gas, m_{p} is the proton mass, V is the volume of the ionized region, and f is the filling factor. Using the emissivity of H β ($j_{\mathrm{H}\,\beta}$), we can calculate the total luminosity of this line:

$$L(\mathrm{H}\,\beta) = \int\int j_{\mathrm{H}\,\beta}\ \mathrm{d}\Omega\mathrm{d}V. \quad (8)$$

We know from Osterbrock & Ferland (2006) that for recombination case B (in the low-density limit), assuming $T = 10^4$ K we have

$$\frac{4\pi j_{\mathrm{H}\,\beta}}{n_{\mathrm{e}} n_{\mathrm{p}}} = 1.24 \times 10^{-25}\ \frac{\mathrm{erg\ cm^3}}{\mathrm{s}},$$

where n_{e} and n_{p} are the electric and proton densities, respectively. Using this result into the integral in equation (8), we obtain $L(\mathrm{H}\,\beta)$ in units of erg s^{-1}:

$$L(\mathrm{H}\,\beta) = 1.23 \times 10^{-25}\ n_{\mathrm{e}} n_{\mathrm{p}} V f.$$

Assuming the gas is completely ionized ($n_{\mathrm{e}} = n_{\mathrm{p}} = n$), we can isolate Vf from the expression above and use it in equation (7). Considering the lower limit of $n_{\mathrm{e}} = 100\,\mathrm{cm}^{-3}$, we obtained the mass of the ionized gas:

$$M(\mathrm{M}_\odot) = 6.782 \times 10^{-35} L(\mathrm{H}\,\beta), \quad (9)$$

where $L(\mathrm{H}\ \beta)$ is the luminosity of H β emission line, in units of erg s^{-1}. Since we used $n_e = 100\,\mathrm{cm}^{-3}$, the mass resulting from equation (9) should be interpreted as a lower limit mass. We applied equation (9) to the dIGal, where H β is strong for the majority of the spaxels in the region, by using the reddening corrected $F(\mathrm{H}\ \beta)$ to calculate $L(\mathrm{H}\ \beta)$ for each spaxel in the dIGal. Integrating over the whole region corresponding to the dIGal, we have obtained $M = 3.8 \times 10^5 M_\odot$ for the ionised gas mass.

3.7 Oxygen abundances

We aim to characterize the dIGal with respect to metallicity, using as proxy the oxygen abundance in its ISM. Since we are not able to directly measure the electron temperature (T_e) because the [O III] λ4363 Å emission line is out of our observed region we cannot use the direct method (e.g. Osterbrock & Ferland 2006). However, many calibrations were made in the past decades without the need of T_e determination (e.g. Pettini & Pagel 2004; Nagao, Maiolino & Marconi 2006; Pérez-Montero & Contini 2009; Marino et al. 2013; known as indirect methods). Useful calibrations are given in Marino et al. (2013):

$$\log(\mathrm{O/H}) + 12 = 8.533(\pm0.012) - 0.214(\pm0.012) \times \mathrm{O3N2}, \quad (10)$$

$$\log(\mathrm{O/H}) + 12 = 8.743(\pm0.027) + 0.462(\pm0.024) \times \mathrm{N2}, \quad (11)$$

where O3N2 and N2 indices are defined as follows (Alloin et al. 1979; Storchi-Bergmann, Calzetti & Kinney 1994):

$$\mathrm{O3N2} = \log\left(\frac{[\mathrm{O\,III}]\lambda5007}{\mathrm{H}\,\beta} \times \frac{\mathrm{H}\,\alpha}{[\mathrm{N\,II}]\lambda6583}\right), \quad (12)$$

$$\mathrm{N2} = \log\left(\frac{[\mathrm{N\,II}]\lambda6583}{\mathrm{H}\,\alpha}\right). \quad (13)$$

The ionization parameter in galaxies between $0 < z < 0.6$ changes such that the line ratios [O III]/H β and [N II]/H α from giant low-surface brightness H II regions begin to rise and lower, respectively. When using a metallicity tracer for galaxies in that redshift range is crucial either to take into consideration the behaviour of the ionization parameter and the change in the emission-line ratios or to use a tracer that is independent of the conditions of ionization of the ISM (Monreal-Ibero et al. 2011; Kewley et al. 2015). With this in mind, we used a calibration based on [N II] and [S II] in addition to the previous calibrations, given by Dopita et al. (2016):

$$\log(\mathrm{O/H}) + 12 = 8.77 + \log([\mathrm{N\,II}]/[\mathrm{S\,II}]) + 0.264 \times \log([\mathrm{N\,II}]/\mathrm{H}\,\alpha). \quad (14)$$

These calibrations were applied to each spaxel of the dIGal, producing three Oxygen abundance maps, two for each tracer of Marino et al. (2013) and the third for the calibration from Dopita et al. (2016). These are shown in Fig. 9. In the first two cases, we obtain values in the range of $8.0 < \log(\mathrm{O/H}) + 12 < 8.6$, which represents a range of approximately $0.2\,Z_\odot < Z < 0.7\,Z_\odot$. In the third case, the metallicity spans a wider range of $7.5 < \log(O/H) + 12 < 8.5$ (i.e. $0.05\,Z_\odot < Z < 0.5\,Z_\odot$). To have a representative value, we calculated the average metallicity for each map. We have obtained $\log(\mathrm{O/H}) + 12 = 8.28 \pm 0.03$ for the O3N2 index and $\log(\mathrm{O/H}) + 12 = 8.296 \pm 0.004$ for the N2 index. For the calibration given in Dopita et al. (2016), we obtained $\log(\mathrm{O/H}) + 12 = 8.2 \pm 0.2$. As a sanity check, we have calculated the abundance derived from the emission lines measured in an integrated spectrum of the dIGal, and the values are consistent.

3.8 Kinematics

There are many intriguing aspects of the dIGal: its irregular morphology, its proximity to Mrk 1172 and its physical properties that indicate it may be interacting with Mrk 1172. Thus it is important to explore the kinematics of the dIGal. We can obtain the radial velocity, v, of the gas for the identified emission lines in the dIGal spectra directly from IFSCUBE single Gaussian fit, as well as the velocity dispersion, σ. In the fit process, we fixed the doublets as being in the same kinematic group, meaning that the resulting velocity values will be the same for the same ion. In Fig. 10, we show both velocity, corrected by subtracting off the mean velocity of the system, and velocity dispersion (σ) maps for H α, [O III]λ5007, [N II]λ6548, and [S II]λ6731 emission lines.

First we observe, especially in the maps of centroid velocity, that the gradient seen is more smooth in the case of H α emission-line maps. This is due to the fact that in spaxels near the edge of the dIGal (which was defined using the strongest emission line in its spectra, i.e. H α) the SNR is low and the measurement of emission lines other than H α have higher uncertainties. Even so, all velocity maps exhibit the same trend for the motion of the gas, where the upper part of the galaxy is moving away from us while the bottom is approaching. Since we do not know the distances with precision, we cannot determine the orientation of the motion of the dwarf galaxy around the ETG.

The maps of velocity dispersion of the gas seem to replicate the trend seen in the maps of radial velocity. In the case of the kinematical group corresponding to the emission lines of [O III], we observe that more spaxels reach values of $\sigma < 90\,\mathrm{km\,s^{-1}}$ in comparison to the other maps. Such a difference could be caused, for instance, if this zone of ionization is closer to the region with higher flux of ionizing photons in comparison to the other zones of ionization and being strongly affected by the winds of massive stars. However this difference rarely becomes larger than $20\,\mathrm{km\,s^{-1}}$, as can be observed in Fig. 10, and the most likely is that it is not significant. To determine the zero-point in the velocity scale of Fig. 10, we used the rest-frame velocity, calculated using the integrated spectrum of the dIGal. The values of velocity dispersion were corrected by instrumental width, assuming a resolving power R of 1750 at $\lambda \sim 5000$ Å and $R \approx 2500$ at $\lambda \sim 6500$ Å.

Although we do not have information about the gas of Mrk 1172, we can explore its stellar kinematics using the results obtained in the stellar population synthesis. In Fig. 11 we present, in the top left-hand panel, the stellar velocity field for the ETG. To better understand the interaction between both galaxies, we used an analytical model that assumes that the gas has circular orbits around the plane of a disc (van der Kruit & Allen 1978; Bertola et al. 1991). For this model, we used the stellar velocity field of Mrk 1172 and the gas velocity field measured from H α shown in Fig. 10 and shown in bottom left-hand panel of Fig. 11. The equation that gives the model velocity field is given by

$$V(R,\Psi) = v_s + \frac{A\,R\cos(\Psi-\Psi_0)\sin(i)\cos^p(i)}{\{R^2[\sin^2(\Psi-\Psi_0)+\cos^2(i)\cos^2(\Psi-\Psi_0)]+C_0^2\cos^2(i)\}^{p/2}},$$

where R is the radial distance to the nucleus projected in the plane of the sky with a corresponding position angle Ψ, v_s is the systemic velocity of the analysed galaxy, A is the velocity amplitude, Ψ_0 is the position angle of the line of nodes, C_0 is a concentration parameter defined as the radius where the rotation curve reaches 70 per cent of

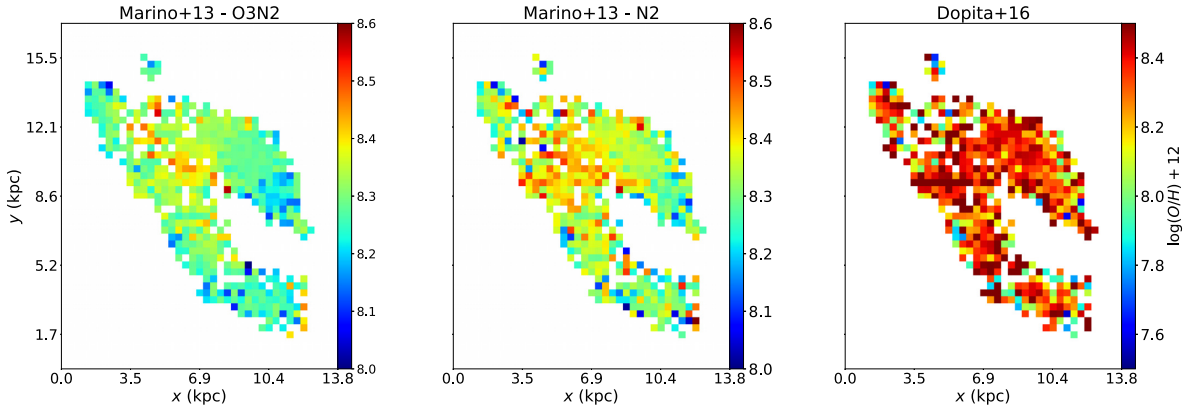

Figure 9. Maps for oxygen abundance obtained using the indirect method, in units of $\log(O/H) + 12$. In left and central panels, the results using O3N2 and M2 indexes from Marino et al. (2013). In right-hand panel, the result using the calibration from Dopita et al. (2016).

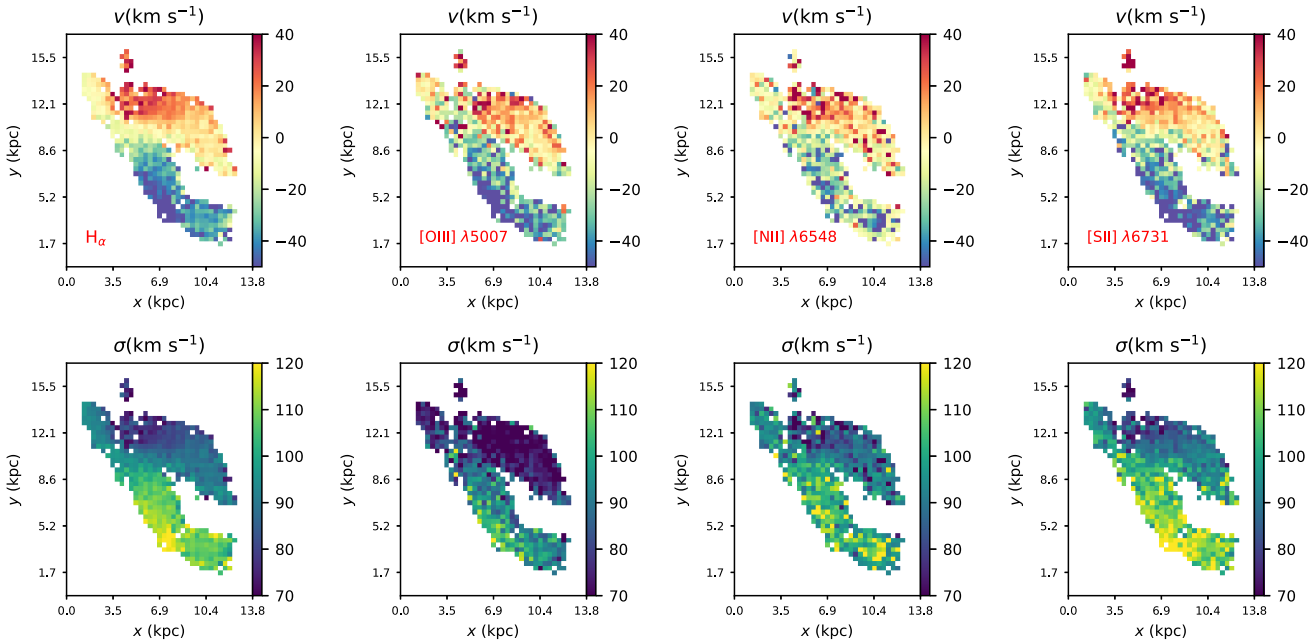

Figure 10. Kinematic maps for H α, [O III]λ 5007, [N II]λ 6548, and [S II]λ 6731 emission lines. In the upper panel, radial velocity maps, and in the lower panel, the turbulence of the gas. Both parameters are obtained from a single Gaussian used to fit the observed emission lines using IFSCUBE.

the velocity amplitude and i is the disc inclination in relation to the plane of the sky. The parameter p varies from 1.0 to 1.5. In Table 1, we summarize the results obtained for the fit. The values of v_s presented were obtained by adding the heliocentric velocity of each galaxy. The residual maps of the fit are presented in the right-hand panel of Fig. 11.

4 DISCUSSION

One important question that arises at this point is: *what is the origin and nature of the nebular emission region identified throughout this paper as the dIGaland how is it connected to ETG Mrk 1172?* In this section, we will use the results presented previously to build possible scenarios for the observed system.

From the stellar population analysis, it is clear that Mrk 1172 and the dIGal do not share similar SFHs. While the ETG is dominated by an old stellar population with no signs of ionised gas, the dIGal presents a rich emission-line spectra with its stellar emission dominated by very young stellar populations ($t < 10^9$, see Figs 3 and 4). It is worthwhile mentioning that although Fig. 3 displays information for individual spaxels, the results are representative of all the spaxels in each system, and arguments based on this figure can be extended to the entirety of both systems. In Fig. 3, we also observe a significant contribution of very young stellar populations ($t < 10^8$ yr) in the spectra of Mrk 1172. These are probably artificial stellar populations caused by (i) the presence of an AGN in Mrk 1172 or (ii) the absence of blue horizontal branch stars in the models, forcing a young population to take into account the blue light of these stars in the ETG (Cid Fernandes & González Delgado 2010; González Delgado & Cid Fernandes 2010).

An interesting parameter to explore is the magnitude in the B band, since it probes the young stellar populations in the galaxy. Although we lack the spectral range to measure the B-band magnitude by integrating the spectra, we can use the photometric values of SDSS

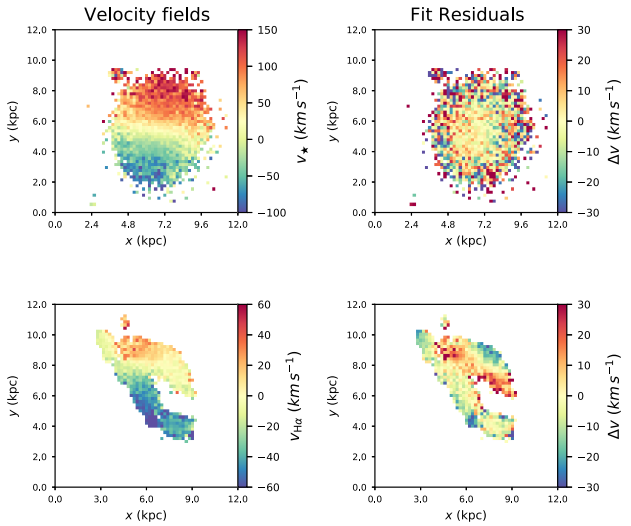

Figure 11. Top left-hand panel: Stellar velocity field of Mrk 1172. Bottom left-hand panel: Velocity field for the gas in the dIGal measured using H α emission line. The values of velocity were obtained by subtracting the systemic velocity of the galaxy ($v_s = -240$ km s^{-1}) from the centroid velocity obtained previously. Right-hand panels: Residual maps for the model fitted.

Table 1. Final result of the fitting process for both galaxies.

	Mrk 1172	the dIGal
v_s (km s^{-1})	12373 ± 5	11835 ± 3
A (km s^{-1})	720 ± 180	310 ± 97
i (°)	30 ± 9	28 ± 10
C_0 (arcsec)	4.8 ± 0.5	4.0 ± 0.9
Ψ_0 (°)	167 ± 4	165 ± 4
p	1.5	1.5

to convert to B band using (Jordi, Grebel & Ammon 2006)

$$B - g = (0.349 \pm 0.009)\,(g - r) + (0.245 \pm 0.006). \quad (15)$$

From SDSS, we have the magnitudes of dIGal: $u = 22.81 \pm 0.52$, $g = 20.65 \pm 0.04$, $r = 20.19 \pm 0.04$, $i = 19.70 \pm 0.04$, and $z = 19.69 \pm 0.11$. By applying equation (15), we obtain $B = 21.00 \pm 0.37$, which corresponds to an absolute magnitude of $M_B \sim -15$ mag, which means the observed dwarf galaxy is faint in the blue band.

We also wish to understand the mechanism responsible for the gas excitation, evidenced by the strong emission lines observed in the dIGal spectra. From the BPT diagnostic diagrams shown in Fig. 6, it is clear that the gas within the dIGal is excited by young hot stars rather than by a hard radiation field. The few spaxels falling in the Seyfert region of the diagnostic diagram are located at the edges of the galaxy and have low SNR, as indicated by the transparency of the circles. We compared our line ratios with predictions of shock models from Allen et al. (2008) and concluded that fast radiative shocks are unlikely to be a significant mechanism of ionization of the gas in the dIGal.

Due to the presence of young stellar populations and the excitation mechanism of the gas, we can say that the dIGal is forming stars, although the efficiency of the process is unknown. The young stars that are ionizing the gas seem to be located in a few clumpy knots along the structure of the dIGal, better traced by the SFR map in Fig. 8. This structure also becomes visible when looking at the H α collapsed image in Fig. 1 and in the continuum H α emission in Fig. 2, and are typical structures formed in regions with active star formation. Using the Balmer decrement, we produced a reddening map for the dIGal, shown in Fig. 7. The mean A_V is 0.9 mag, but in few spaxels this value is up to ∼2.0 mag, reinforcing the inhomogeneity of the medium, or also the uncertainty in the emission-line ratio for these spaxels. The intensities of the emission lines, used through this paper, have been corrected for dust attenuation.

Using the emission-line fluxes, we calculated the instantaneous SFR using equation (4), obtaining an SFR of 0.70 $M_\odot$ yr^{-1}. We also derived the spatial distribution of SFR for the dIGal ($\sum_{SFR}$), resulting in 1.4×10^{-2} $M_\odot$ yr^{-1} kpc^{-2}. Finally, we calculated a lower limit for the mass of ionized gas in the dIGal using the H β emission-line strength, resulting in a mass of 3.8×10^5 $M_\odot$.

From the stellar population synthesis, we obtained an estimate for the stellar mass of both galaxies. We estimate the values of 3.0×10^9 $M_\odot$ for the dIGal and 1.2×10^{11} $M_\odot$ for Mrk 1172. In the case of the latter, the order of magnitude of this value is coherent to what is expected for massive ETG like Mrk 1172, and is in agreement with a previous estimates for the stellar mass for this galaxy (8.91×10^{10} $M_\odot$; Omand, Balogh & Poggianti 2014). On the other hand, the dIGal has an estimated value of stellar mass comparable to dwarf galaxies, like the SMC, for example (6.5×10^9 $M_\odot$; Bekki & Stanimirović 2009).

With the values of stellar mass and SFR, we can estimate the specific star formation rate (sSFR) for the dIGal, which can be compared with a previous value found in the catalogue of Delli Veneri et al. (2019; DV19 throughout this paper), where the sSFR is measured using photometric information for a large sample of galaxies from SDSS DR7. We have obtained a value of log(sSFR) $= -9.63$, which is considerably different than the log(sSFR) $= -10.85$ found in DV19. However, these two values were derived using different techniques, and the photometry of the dIGal is flagged as medium quality in DV19, meaning the direct comparison between both values is hard to perform.

As observed before in this work, the dIGal has an irregular shape and lies next in projection to Mrk 1172. Thus, a natural first assumption is that both galaxies are interacting, and the irregular shape of the dIGal could be partially explained by tidal forces. Analysing the available redshift for Mrk 1172 (which is consistent with our determination) and our measurement for the dIGal, one can calculate a distance of approximately 4 Mpc between both galaxies, for which gravitational interactions could be neglected. However, this calculation does not take into account that the shift in the emission lines of the dIGal could be also caused by its motion in relation to Mrk 1172. Considering that Mrk 1172 has a massive halo, it is possible that this halo is populated by faint dwarf galaxies. In this case, the participation of the dIGal in this group of galaxies should not be discarded, and the estimate of 4 Mpc of distance between both galaxies could be incorrect. As an exercise, if we assume 300 km s^{-1} for the group velocity, for example, it would affect the above-mentioned distance estimate by approximately 3 Mpc, i.e. the uncertainty in the distance estimate due to the relative motion of the dwarf galaxy is large.

To investigate deeper the interaction between both galaxies, we fit a model to the stellar velocity field of Mrk 1172 and to the H α velocity field of the dIGal (see Fig. 11). The final results of the fit are listed in Table 1. It can be seen that both galaxies present similar results for the disc inclination and the position angle of the line of the nodes (i and Ψ_0, respectively). Although the presence of a disc in the dIGal is uncertain, the model fit is satisfactory, and this result

indicates that the motion of the gas in the dwarf galaxy is affected by the ETG. These considerations, combined to the irregular shape of the dwarf galaxy, lead us to the conclusion that Mrk 1172 and the dIGal are currently interacting.

Finding a low-metallicity system next to an ETG, as seems to be the case for Mrk 1172 and the dIGal, deserves further investigation. Here, we use oxygen abundance as a tracer for the metallicity of the ISM of the dIGal and we employ the calibrations from Marino et al. (2013) for each spaxel of the dIGal. The average metallicity obtained is $\log(O/H) + 12 = 8.28 \pm 0.03$ for the O3N2 index and $\log(O/H) + 12 = 8.296 \pm 0.004$ for the N2 index. Since O3N2 is based in emission lines both in the blue and red parts of the spectrum and suffers a strong dependence on the ionization parameters for the ISM ionization conditions of the dIGal. Thus, we used the calibration from Dopita et al. (2016), which has no dependence on the ionization parameters of the galaxy, to compare with the previous results. Using this calibration, we obtained an average value of $\log(O/H) + 12 = 8.2 \pm 0.2$. In general, this third calibration gives slightly lower values of metallicity in comparison to the other maps. Combining the values obtained it is possible to estimate that the metallicity of the dIGalis approximately $1/3\,Z_{\odot}$. The range of metallicities observed in the dIGalis also observed in metal-poor systems such as dwarf irregulars and some BCDGs (Kunth & Östlin 2000; Gil de Paz, Madore & Pevunova 2003). This feature raises another question: *what is the origin of this metal-deficient content?*

Models of galaxy formation in the Lambda cold dark matter (Λ-CDM) context predict the inflow of metal-deficient gas from the cosmic web. Numerical simulations indicate that this gas can trigger star formation in disc galaxies and dwarf galaxies of the Local Universe (Sánchez Almeida et al. 2015). The triggering of a starburst may happen, as the infalling gas gets compressed when it approaches the disc or also it may be accreted and build up the gas mass of the galaxy to eventually give rise to the starburst due to internal instabilities (Dekel, Sari & Ceverino 2009; Ceverino et al. 2016). In many cases, chemical inhomogeneities can be observed in galaxies in the Local Universe, where localized kpc-size starbursts present considerably lower abundances in comparison to the surrounding ISM. The scenario described above is a plausible interpretation for the metallicity drop in these starburst regions. We believe that the origin of the metal deficient gas in the dIGal could be caused by infalling gas from the cosmic web, but if this is true, should we not observe a gradient in metallicity in Fig. 9 instead of the homogeneous distribution that is actually observed? As we have seen, the gas in the dIGal is subject to the interaction with Mrk 1172 and to the inner kinematics of the galaxy. In a scenario of accretion is possible that this metal deficient content has mixed with the ISM.

Therefore our *conclusions about the nature of this object is that it is a dwarf irregular galaxy interacting with the massive ETG Mrk 1172*. It contains young stellar populations that have formed recently, and shows evidence of ongoing star formation. The star formation seems to be taking place mainly in clumpy knots along the structure of the galaxy. The gas phase of the galaxy is metal-poor, which could be related to infalling gas from the cosmic web, although we lack the information to support this hypothesis. To further investigate this hypothesis, observations of cold molecular gas would be needed, and, to the best of our knowledge, so far these observations are not available.

5 SUMMARY AND CONCLUSIONS

In this work we present a characterisation of chemical and physical properties of a dwarf galaxy (SDSS J020536.84–081424.7; dIGal) located approximately 2.5 arcsec from the ETG Mrk 1172. To the best of our knowledge, the spectrum of this galaxy was not presented in the literature before, thus the analysis of this work is unprecedented. Below, we summarize the main conclusions of this work:

(i) Despite its low SNR in the continuum, the spectra of the dIGal presents strong emission lines, namely: H α, H β, [O III] $\lambda\lambda 4959 + 5007$, [N II] $\lambda\lambda 6548 + 6583$, and [S II] $\lambda\lambda 6716 + 6731$. The stellar population synthesis reveals that Mrk 1172 is predominantly dominated by old stellar populations with $t \geq 10^{10}$ yr, while the dIGal contains young to intermediate-age stellar populations, with ages of $10^7 \sim 10^8$ yr and 10^9 yr. From analysis of the light-weighed stellar populations, we conclude that both galaxies have very different SFHs.

(ii) From the stellar content of the dIGal and Mrk 1172, we are able to estimate the stellar mass of both galaxies. We obtain $M_{\star} \sim 1.2 \times 10^{11} M_{\odot}$ for Mrk 1172, a value that lies close to a previous measurement found in the literature (Omand et al. 2014). The dIGal presents a stellar mass of $M_{\star} \sim 3 \times 10^9 M_{\odot}$, which is comparable to the mass of dwarf galaxies like the SMC ($M_{\star} = 6.5 \times 10^9\,M_{\odot}$; Bekki & Stanimirović 2009) and to the BCDG Henize 2–10 ($M_{\star} = 3.7 \times 10^9 M_{\odot}$; Reines et al. 2011), for example. We have also estimated the lower limit of $3.8 \times 10^5 M_{\odot}$ for the ionized gas mass.

(iii) In order to investigate the gas excitation mechanism, we perform a spatially resolved study making use of emission-line diagnostic diagrams such as the BPT. Both diagrams indicate that the gas within the dIGal is being photoionized by young massive hot stars rather than by an AGN. Shock models are also investigated, but they are negligible.

(iv) The metallicity of the ionized gas phase of the dIGal is $\log(O/H) + 12 = 8.28 \pm 0.03$ for the O3N2 index, $\log(O/H) + 12 = 8.296 \pm 0.004$ for the N2 index and $\log(O/H) + 12 = 8.2 \pm 0.2$ when considering the calibration independent of ionization parameters from Dopita et al. (2016). These values represent an overall metallicity of approximately $1/3\,Z_{\odot}$ for the dIGal. This galaxy can be considered metal deficient, presenting typical values for dIs.

(v) Our measurements and observations strongly suggest that the dIGal is actively forming stars. We observe clumpy knots in H α emission along the structure of the dIGal, which we interpret as being sites of active star formation. We obtain an integrated value of SFR $= 0.70\ M_{\odot}\,yr^{-1}$; $\sum_{SFR} = 1.4 \times 10^{-2}\,M_{\odot}\,yr^{-1}\,kpc^{-2}$, and a $\log(sSFR) = -9.63$. The latter differs significantly from a previous measurement of $\log(sSFR) = -10.85$ found in the literature (DV19). We attribute this difference to the quality of photometric data for the dIGal(flagged as medium in DV19) and the distinct procedures adopted in both works.

(vi) Radial velocity maps indicate a trend in the motion of the gas, which seems to be in rotation. Using the velocity field considering H α and the stellar velocity field of Mrk 1172 we fit a kinematic model that considers a gas orbiting in a plane of a disc. From this fit, we observe that the position angle of the line of the nodes and the disc inclination are similar for both galaxies, thus indicating that the motion of the gas is being affected by the ETG. We thus conclude that both galaxies are interacting.

From the results summarized above, we conclude that the faint nebular emission-line region close in projection to Mrk 1172 is actually a gas-rich low-metallicity dwarf galaxy, most likely a dwarf irregular. The origin of this galaxy is still uncertain, and we are still unsure as to which specific processes triggered the recent star formation episodes in the dIGal. Bright knots are readily visible in the H α images of the dIGal, where the highest fraction of its stellar

content seems to be located. Detailed analysis of these knots and how they are ionizing the surrounding gas may shed more light on the nature and origins of the dIGal. With access to images with lower seeing, velocity sliced Hα maps of the dIGal (i.e. the analysis of Haro 11 in Menacho et al. 2019) may help to probe the internal structure of the galaxy. We are interested in the sizes of these knots, since they are seeing limited in MUSE data. With good spatial resolution in the NIR, for example, we can search for sub-structures in these knots and model surface brightness profiles for them. Modelling the light profile of both galaxies is essential to improve our understanding on their detailed structure, which can trace mergers in the past history of both systems. It also allows us to measure the Cluster Formation Efficiency, defined as the fraction of total stellar mass formed in clusters per unit time in a given age interval divided by the SFR of the region where the clusters are detected. This quantity relates to the SFR surface density to quantify the intrinsic connection between massive star cluster formation processes and the mean properties of the host galaxies and compare to other galaxies, including dwarf irregulars and BCDGs (Adamo, Östlin & Zackrisson 2011; Adamo et al. 2020). This posterior analysis may help us to understand better how this metal-deficient galaxy is interacting with Mrk 1172 by improving the accuracy in its distance estimate, and thus shed some light about the formation and evolution of such systems. All these efforts are, however, beyond the scope of this paper, and are left for a future publication.

ACKNOWLEDGEMENTS

We thank the referee for constructive comments and suggestions that have helped to improve the paper. This work was supported by Brazilian funding agencies CNPq and CAPES and by the *Programa de Pós Graduaçóo em Física* (PPGFis) at UFRGS. AL acknowledges the hospitality in the visit to PUC Chile and ESO during 2018 Jan/Feb. The authors also acknowledge the suggestions from Angela Adamo, Angela Krabbe, Laerte Sodré, Marina Trevisan, and Cristina Furlanetto. ACS acknowledges funding from CNPq and the Rio Grande do Sul Research Foundation (FAPERGS) through grants CNPq-403580/2016-1, CNPq-11153/2018-6, PqG/FAPERGS-17/2551-0001, FAPERGS/CAPES 19/2551-0000696-9, and L'Oréal UNESCO ABC *Para Mulheres na Ciência*. EJ acknowledges support from FONDECYT Postdoctoral Fellowship Project No. 3180557 and FONDECYT Iniciación 2020 Project No. 11200263. RR thanks CNPq, CAPES, and FAPERGS for partial financial support to this project. RAR acknowledges financial support from CNPq (302280/2019-7) and FAPERGS (17/2551-0001144-9). This study was based on observations collected at the European Organisation for Astronomical Research in the Southern Hemisphere under ESO programme 099.B-0411(A), PI: Johnston. This research has made use of the NASA/IPAC Extragalactic Database (NED), which is operated by the Jet Propulsion Laboratory, California Institute of Technology, under contract with NASA.

DATA AVAILABILITY

The data used in this paper is available at ESO Science Archive Facility under the program-ID of 099.B-0411(A).

REFERENCES

Adamo A. et al., 2020, Space Sci. Rev., 216, 69
Adamo A., Östlin G., Zackrisson E., 2011, MNRAS, 417, 1904
Ahn C. P. et al., 2012, ApJS, 203, 21
Allen M. G., Groves B. A., Dopita M. A., Sutherland R. S., Kewley L. J., 2008, ApJS, 178, 20
Alloin D., Collin-Souffrin S., Joly M., Vigroux L., 1979, A&A, 78, 200
Aloisi A. et al., 2007, ApJ, 667, L151
Andrews B. H., Martini P., 2013, ApJ, 765, 140
Bacon R. et al., 2010, in McLean I. S., Ramsay S. K., Takami H., eds, SPIE Conf. Ser. Vol. 7735, Ground-based and Airborne Instrumentation for Astronomy III. SPIE, Bellingham, p. 773508
Baldwin J. A., Phillips M. M., Terlevich R., 1981, PASP, 93, 5
Bekki K., Stanimirović S., 2009, MNRAS, 395, 342
Bernard E. J. et al., 2010, ApJ, 712, 1259
Bertola F., Bettoni D., Danziger J., Sadler E., Sparke L., de Zeeuw T., 1991, ApJ, 373, 369
Cardelli J. A., Clayton G. C., Mathis J. S., 1989, ApJ, 345, 245
Ceverino D., Sánchez Almeida J., Muñoz Tuñón C., Dekel A., Elmegreen B. G., Elmegreen D. M., Primack J., 2016, MNRAS, 457, 2605
Cid Fernandes R. et al., 2013, A&A, 557, A86
Cid Fernandes R. et al., 2014, A&A, 561, A130
Cid Fernandes R., González Delgado R. M., 2010, MNRAS, 403, 780
Cid Fernandes R., Mateus A., Sodré L., Stasińska G., Gomes J. M., 2005, MNRAS, 358, 363
Croxall K. V., van Zee L., Lee H., Skillman E. D., Lee J. C., Côté S., Kennicutt Robert C. J., Miller B. W., 2009, ApJ, 705, 723
Dalcanton J. J., 2007, ApJ, 658, 941
Dekel A., Sari R., Ceverino D., 2009, ApJ, 703, 785
Delli Veneri M., Cavuoti S., Brescia M., Longo G., Riccio G., 2019, MNRAS, 486, 1377
Digby R. et al., 2019, MNRAS, 485, 5423
do Nascimento J. C. et al., 2019, MNRAS, 486, 5075
Dopita M. A., Kewley L. J., Sutherland R. S., Nicholls D. C., 2016, Ap&SS, 361, 61
ESO CPL Development Team, 2015, Astrophysics Source Code Library, record ascl:1504.003
Fattahi A., Navarro J. F., Frenk C. S., Oman K. A., Sawala T., Schaller M., 2018, MNRAS, 476, 3816
Gallart C. et al., 2015, ApJ, 811, L18
Gibson B. K., Matteucci F., 1997, ApJ, 475, 47
Gil de Paz A., Madore B. F., Pevunova O., 2003, ApJS, 147, 29
González Delgado R. M., Cid Fernandes R., 2010, MNRAS, 403, 797
González-Samaniego A., Colín P., Avila-Reese V., Rodríguez-Puebla A., Valenzuela O., 2014, ApJ, 785, 58
Hinshaw G. et al., 2013, ApJS, 208, 19
Jordi K., Grebel E. K., Ammon K., 2006, A&A, 460, 339
Kauffmann G. et al., 2003, MNRAS, 346, 1055
Kazantzidis S., Łokas E. L., Callegari S., Mayer L., Moustakas L. A., 2011, ApJ, 726, 98
Kennicutt Robert C. J., 1998, ARA&A, 36, 189
Kewley L. J., Dopita M. A., Sutherland R. S., Heisler C. A., Trevena J., 2001, ApJ, 556, 121
Kewley L. J., Groves B., Kauffmann G., Heckman T., 2006, MNRAS, 372, 961
Kewley L. J., Zahid H. J., Geller M. J., Dopita M. A., Hwang H. S., Fabricant D., 2015, ApJ, 812, L20
Kirby E. N., Cohen J. G., Guhathakurta P., Cheng L., Bullock J. S., Gallazzi A., 2013, ApJ, 779, 102
Kormendy J., Bender R., 2012, ApJS, 198, 2
Kunth D., Östlin G., 2000, A&AR, 10, 1
Lequeux J., Peimbert M., Rayo J. F., Serrano A., Torres-Peimbert S., 1979, A&A, 500, 145
Mallmann N. D. et al., 2018, MNRAS, 478, 5491
Marino R. A. et al., 2013, A&A, 559, A114
Mashchenko S., Wadsley J., Couchman H. M. P., 2008, Science, 319, 174
Mateo M. L., 1998, ARA&A, 36, 435
Mayer L., Governato F., Colpi M., Moore B., Quinn T., Wadsley J., Stadel J., Lake G., 2001, ApJ, 547, L123
Menacho V. et al., 2019, MNRAS, 487, 3183

Monreal-Ibero A., Relaño M., Kehrig C., Pérez-Montero E., Vílchez J. M., Kelz A., Roth M. M., Streicher O., 2011, MNRAS, 413, 2242
Nagao T., Maiolino R., Marconi A., 2006, A&A, 459, 85
Navarro J. F., Eke V. R., Frenk C. S., 1996, MNRAS, 283, L72
O'Donnell J. E., 1994, ApJ, 422, 158
Omand C. M. B., Balogh M. L., Poggianti B. M., 2014, MNRAS, 440, 843
Osterbrock D. E., Ferland G. J., 2006, Astrophysics of Gas Nebulae and Active Galactic Nuclei. University Science Books. California, USA
Pérez-Montero E., Contini T., 2009, MNRAS, 398, 949
Pettini M., Pagel B. E. J., 2004, MNRAS, 348, L59
Pilyugin L. S., Ferrini F., 2000, New Astron. Rev., 44, 335
Reines A. E., Sivakoff G. R., Johnson K. E., Brogan C. L., 2011, Nature, 470, 66
Revaz Y., Jablonka P., 2018, A&A, 616, A96
Riffel R. et al., 2021, MNRAS, 501, 4064
Riffel R., Pastoriza M. G., Rodríguez-Ardila A., Bonatto C., 2009, MNRAS, 400, 273
Rubin V. C., Ford W. K. J., Whitmore B. C., 1984, ApJ, 281, L21
Ruschel-Dutra D., de Oliveira B. D., 2020, danielrd6/ifscube: Modeling (Version v1.1). Available at: http://doi.org/10.5281/zenodo.4065550
Ryden B., Pogge R., 2021, Interstellar and Intergalactic Medium. Cambridge University Press, Cambridge
Sánchez Almeida J. et al., 2015, ApJ, 810, L15
Schlegel D. J., Finkbeiner D. P., Davis M., 1998, ApJ, 500, 525
Skillman E. D., Bender R., 1995, Rev. Mex. Astron. Astrofis. Ser. Conf., 3, 25
Skillman E. D., Kennicutt R. C., Hodge P. W., 1989, ApJ, 347, 875
Soto K. T., Lilly S. J., Bacon R., Richard J., Conseil S., 2016, MNRAS, 458, 3210
Steffen M., Prakapavičius D., Caffau E., Ludwig H. G., Bonifacio P., Cayrel R., Kučinskas A., Livingston W. C., 2015, A&A, 583, A57
Steyrleithner P., Hensler G., Boselli A., 2020, MNRAS, 494, 1114
Storchi-Bergmann T., Calzetti D., Kinney A. L., 1994, ApJ, 429, 572
Tremonti C. A. et al., 2004, ApJ, 613, 898
van der Kruit P. C., Allen R. J., 1978, ARA&A, 16, 103
van Zee L., 2001, AJ, 121, 2003
van Zee L., Haynes M. P., 2006, ApJ, 636, 214
Vazdekis A., Sánchez-Blázquez P., Falcón-Barroso J., Cenarro A. J., Beasley M. A., Cardiel N., Gorgas J., Peletier R. F., 2010, MNRAS, 404, 1639
Vazdekis A., Koleva M., Ricciardelli E., Röck B., Falcón-Barroso J., 2016, MNRAS, 463, 3409
Weilbacher P. M. et al., 2020, A&A, 641, A28
Wylezalek D. et al., 2017, MNRAS, 467, 2612

This paper has been typeset from a TEX/LATEX file prepared by the author.

Monthly Notices of the ROYAL ASTRONOMICAL SOCIETY

MNRAS **524,** 3912 (2023) https://doi.org/10.1093/mnras/stad1815

Correction to: The metal-poor dwarf irregular galaxy candidate next to Mrk 1172

by Augusto E. Lassen [1]★ Rogerio Riffel [1]★ Ana L. Chies-Santos [1] Evelyn Johnston [2,3] Boris Häußler [4] Gabriel M. Azevedo,[1] Daniel Ruschel-Dutra [5] and Rogemar A. Riffel [6]

[1]*Universidade Federal do Rio Grande do Sul, Departamento de Astronomia, Av. Bento Gonçalves 9500, Porto Alegre, RS, Brazil*
[2]*Instituto de Estudios Astrofísicos, Facultad de Ingeniería y Ciencias, Universidad Diego Portales, Av. Ejército Libertador 441, Santiago, Chile*
[3]*Pontificia Universidad Católica de Chile, Institute of Astrophysics, Av. Vicuña Mackenna 4860, 7820436 Macul, Santiago, Chile*
[4]*European Southern Observatory, Alonso de Córdova 3107, Vitacura, Santiago, Chile*
[5]*Universidade Federal de Santa Catarina, Departamento de Física, P.O. Box 476, 88040-900, Florianópolis, SC, Brazil*
[6]*Universidade Federal de Santa Maria, Departamento de Física, Centro de Ciências Naturais e Exatas, 97106–900, Santa Maria, RS, Brazil*

Key words: errata, addenda – ISM: abundances – H II regions – galaxies: dwarf.

This is a correction to the paper entitled 'The metal-poor dwarf irregular galaxy candidate next to Mrk 1172' that was published in Monthly Notices of the Royal Astronomical Society Volume 506, September 2021, pages 3527–3539, 10.1093/mnras/stab1838.

Some of the values reported for the dwarf galaxy in Table 1 are incorrect, in special the systemic velocity v_s. We have noticed that we fitted the analytical model to the dwarf velocity field adopting the rest-frame of the Early-type galaxy instead, causing an underestimation of v_s. The velocity fields used in the fit in fig. 11 are correct though. We performed the fit again and the correct values are listed in Table 1. In this sense, the paragraph in page 3536 about the possible separation of the targets:

'Analysing the available redshift for Mrk 1172 (which is consistent with our determination) and our measurement for the dIGal, one can calculate a distance of approximately 4 Mpc between both galaxies, for which gravitational interactions could be neglected. However, this calculation does not take into account that the shift in the emission lines of the dIGal could be also caused by its motion in relation to Mrk 1172. Considering that Mrk 1172 has a massive halo, it is possible that this halo is populated by faint dwarf galaxies. In this case, the participation of the dIGal in this group of galaxies should not be discarded, and the estimate of 4 Mpc of distance between both galaxies could be incorrect. As an exercise, if we assume 300 km s^{-1} for the group velocity, for example, it would affect the above mentioned distance estimate by approximately 3 Mpc, i.e. the uncertainty in the distance estimate due to the relative motion of the dwarf galaxy is large.'

Table 1. Corrected values for the fitting of the rotation model for both galaxies.

	Mrk 1172	the dIGal
v_s (km s^{-1})	12373 ± 5	12071 ± 3
A (km s^{-1})	720 ± 180	220 ± 97
i (°)	30 ± 9	27 ± 10
C_0 (arcsec)	4.8 ± 0.5	7.0 ± 1.1
Ψ_0 (°)	167 ± 4	165 ± 4
p	1.5	1.5

Should be read as follows:

Analysing the available redshift for Mrk 1172 (which is consistent with our determination) and our measurement for the dIGal, one can calculate a line-of-sight separation velocity of 270 km s^{-1}. This value is in agreement with values expected for interacting systems with the masses of our galaxies (Stierwalt et al. 2015).

This does not affect our conclusions, but actually reinforce the scenario of interaction between both galaxies.

REFERENCE

Stierwalt S., Besla G., Patton D., Johnson K., Kallivayalil N., Putman M., Privon G., Ross G., 2015, ApJ, 805, 2

★ E-mail: augusto.lassen@gmail.com (AEL); riffel@ufrgs.br (RR)

This paper has been typeset from a TEX/LATEX file prepared by the author.

4.2 Investigating the clumpy star formation in an interacting dwarf irregular galaxy

Monthly Notices
of the Royal Astronomical Society

Investigating the clumpy star formation in an interacting dwarf irregular galaxy

Journal:	*Monthly Notices of the Royal Astronomical Society*
Manuscript ID	MN-24-1302-MJ
Manuscript type:	Main Journal
Date Submitted by the Author:	14-Jun-2024
Complete List of Authors:	Lassen, Augusto; Universidade Federal do Rio Grande do Sul, Departamento de Astronomia, Instituto de Física Chies-Santos, Ana; Universidade Federal do Rio Grande do Sul, Departamento de Astronomia, Instituto de Física Riffel, Rogério; Universidade Federal do Rio Grande do Sul, Departamento de Astronomia, Instituto de Física Johnston, Evelyn; Universidad Diego Portales, Núcleo de Astronomía Carrasco, Eleazar; Gemini Observatory Southern Operations Center, Haeussler, Boris; European Southern Observatory, ESO; Azevedo, Gabriel; Universidade Federal do Rio Grande do Sul, Departamento de Astronomia Gomes, Jean Michel; Instituto de Astrofisica e Ciencias do Espaco, Galaxies TL Riffel, Rogemar A.; Universidade Federal de Santa Maria, Departamento de Física Werle, Ariel; Osservatorio Astronomico di Padova, Departamento de Física Machado, Rubens; Universidade Tecnologica Federal do Parana, Departamento Academico de Fisica Ruschel-Dutra, Daniel; Universidade Federal de Santa Catarina Centro de Ciencias Fisicas e Matematicas, Departamento de Física
Keywords:	galaxies: dwarf < Galaxies, galaxies: interactions < Galaxies, galaxies: irregular < Galaxies, galaxies: ISM < Galaxies, galaxies: abundances < Galaxies

MNRAS **000**, 1–19 (2024) Preprint 14 June 2024 Compiled using MNRAS LATEX style file v3.0

Investigating the clumpy star formation in an interacting dwarf irregular galaxy

Augusto E. Lassen[1]★, Ana L. Chies-Santos[1], Rogerio Riffel[1], Evelyn J. Johnston[2], Eleazar R. Carrasco[3], Boris Häußler[4], Gabriel M. Azevedo[1,5], Jean M. Gomes[6], Rogemar A. Riffel[7], Ariel Werle[8], Rubens E. G. Machado[9], Daniel Ruschel-Dutra[10]

[1] *Instituto de Física, Departamento de Astronomia, Universidade Federal do Rio Grande do Sul, Av. Bento Gonçalves 9500, Porto Alegre, RS, Brazil*
[2] *Instituto de Estudios Astrofísicos, Facultad de Ingeniería y Ciencias, Universidad Diego Portales, Av. Ejército Libertador 441, Santiago, Chile*
[3] *International Gemini Observatory/NSF NOIRLab, Casilla 603, La Serena, Chile*
[4] *European Southern Observatory, Alonso de Cordova 3107, Casilla 19001, Santiago, Chile*
[5] *Departamento de Física Teórica y del Cosmos, Facultad de Ciencias, Universidad de Granada, Av. de Fuente Nueva, Granada, Spain*
[6] *DTx–Digital Transformation CoLab, Building 1, Azurém Campus, University of Minho, PT4800-058 Guimarães, Portugal*
[7] *Departamento de Física, Centro de Ciências Naturais e Exatas, Universidade Federal de Santa Maria, 97105-900, Santa Maria, RS, Brazil*
[8] *INAF – Osservatorio Astronomico di Padova, Vicolo dell'Osservatorio 5, 35122 Padova, Italy*
[9] *Departamento Acadêmico de Física, Universidade Tecnológica Federal do Paraná, Av. Sete de Setembro 3165, Curitiba, PR, Brazil*
[10] *Departamento de Física, Universidade Federal de Santa Catarina, P.O. Box 476, 88040-900 Florianópolis, SC, Brazil*

Accepted XXX. Received YYY; in original form ZZZ

ABSTRACT

Clumpy morphologies are more frequent in distant and low-mass star-forming galaxies. The less numerous nearby galaxies presenting kpc-sized clumps thus represent a unique laboratory to address the mechanisms driving the formation of these features, why they become less common in the local Universe and why they tend to exhibit smaller sizes and lower star formation rate in nearby dwarfs than in their high-z counterparts. We use high spatial resolution Integral Field Unit observations from VLT/MUSE to investigate the properties of several kpc-sized clumps seen in SDSS J0205-0814, a $z \approx 0.04$ dwarf irregular galaxy interacting with its more massive companion Mrk 1172 ($\log(M/M_\odot) \sim 11$). Using Hα channel maps we show that the clumps lie in a rotating gas component, with the kinematical centre consistent with the location of the peak of stellar continuum emission. By combining STARBURST99 evolutionary models with self-consistent stellar population synthesis with FADO we show that the most recent star formation episodes in clumps happened between 6 Myr and 7.5 Myr ago, and that clumps on the receding part host slightly older stellar populations. An underlying $t \geq 2$ Gyr stellar population is also found. We find no evidence of accretion of metal-poor gas, favouring the scenario of gravitational instabilities in the rotating component as the trigger of clumpy star formation. Flat gas-phase metallicity distributions are observed, indicating that the dwarf next to Mrk 1172 might result from a low-mass pair collision.

Key words: galaxies: dwarf – galaxies: interactions – galaxies: irregular – galaxies: ISM – galaxies: abundances

1 INTRODUCTION

The morphologies of distant ($z \gtrsim 1$) galaxies are statistically more asymmetric than that of nearby galaxies: Recent observations with the James Webb Space Telescope (JWST) indicate that the fraction of prolate galaxies among low-mass ($9.0 < \log(M_\star/M_\odot) < 9.5$) galaxies increases with redshift, meanwhile the fraction of disks in dwarfs increases towards the local Universe (Pandya et al. 2024). The morphology of high-redshift ($z \gtrsim 1$) star-forming galaxies is also more irregular in comparison to local galaxies (Conselice et al. 2000; Elmegreen et al. 2005a; Fisher et al. 2017a; Huertas-Company et al. 2023), being dominated by massive kpc-sized "clumps" (Cowie et al. 1995; van den Bergh et al. 1996; Elmegreen et al. 2005b; Dekel et al. 2009b). The fraction of galaxies with Ultra-Violet (UV) clumps was observed to increase with redshift in a trend that roughly follows the evolution of the Star Formation Rate Density (SFRD, Madau & Dickinson 2014; Shibuya et al. 2016).

In addition to the redshift, the fraction of clumpy Star-Forming

★ augusto.lassen@ufrgs.br

Galaxies (SFGs) also depends on the stellar mass: Considering the range $0.5 < z < 3$, up to 60 per cent of low-mass galaxies ($M_\star \lesssim 10^{9.8}\,M_\odot$) present clumpy UV morphologies, while this fraction drops to 15–55 per cent in the case of high-mass SFGs in the same redshift range (Guo et al. 2018; Förster Schreiber & Wuyts 2020). With overall contributions to the galactic rest-frame UV emission in the range of 20–40 per cent, the clumps correspond to sites of elevated Star Formation Rate (SFR), reaching up to $10\,M_\odot\,\mathrm{yr}^{-1}$ per clump (Elmegreen et al. 2005b; Genzel et al. 2011; Soto et al. 2017; Fisher et al. 2017a; Förster Schreiber & Wuyts 2020). The stellar mass of typical individual clumps lie in the range of $10^8 - 10^9\,M_\odot$ (Wisnioski et al. 2012; Tacconi et al. 2013; Messa et al. 2019), thereby the clumps are not only larger, brighter and more massive than local star-forming regions, but also presents much higher SFRs and specific SFRs (sSFR) (Guo et al. 2012; Fisher et al. 2017b). Observations of clumps in lensed galaxies and high-resolution simulations suggest, however, that clump properties such as sizes and stellar masses are systematically overestimated due to resolution limitations, e.g., if the physical size of the clumps is smaller than the imaging resolution, several clumps will be blended as a source artificially boosted towards high stellar masses (Elmegreen et al. 2013; Dessauges-Zavadsky et al. 2017; Tamburello et al. 2017; Cava et al. 2018).

In the last decades there have been substantial efforts to explain how these clumps formed and why they are so much rarer in Local Universe galaxies, giving rise to two major scenarios. The first scenario asserts that clumps are formed from major or minor mergers during the early build-up of the host galaxy, when the satellite is stripped and its nucleus becomes the massive *ex-situ* clump or generates local instabilities within the host galaxy that drive further collapse of the gas (Somerville et al. 2001; Hopkins et al. 2013; Ribeiro et al. 2017). Observations and simulations suggest that only a minority of the high-z clumps are formed this way and that clump formation depends on the galaxy mass, so that the *ex-situ* mechanism is more common for $M \lesssim 10^{10}\,M_\odot$ galaxies (Mandelker et al. 2014; Guo et al. 2015; Zanella et al. 2019; Adams et al. 2022). The second and most supported scenario is the *in-situ* formation of the clumps, generated from the collapse of gas-rich disc fragments due to Violent Disk Instability (VDI, Noguchi 1999; Dekel et al. 2009b; Agertz et al. 2009; Bournaud et al. 2014). Smooth cold accretion of intergalactic gas, for instance, can drive disks to be marginally stable (i.e., the Toomre parameter is $Q \sim 1$; Toomre 1964), causing the gravitational instabilities that give rise to the massive clumps (Genzel et al. 2008; Bouché et al. 2013; Adams et al. 2022). At high-z, disks can fragment at much larger scales than their local-Universe counterparts, given that they are highly turbulent ($\sigma_{\mathrm{H}\alpha} \sim 30 - 80\,\mathrm{km\,s}^{-1}$, Green et al. 2010; Bassett et al. 2014) and present gas-to-stellar mass ratios two times larger than local disks (Tacconi et al. 2008, 2013; Saintonge et al. 2013), a combination of ingredients that increase the Jeans lengths at the same time that large gas reservoirs fuel the star formation. The *in-situ* interpretation is supported by observations in $z \sim 1$ galaxies (Zanella et al. 2015; Dessauges-Zavadsky et al. 2019) and local analogues (Fisher et al. 2017a,b; Messa et al. 2019) and by simulations of turbulent high-z galaxies (van Donkelaar et al. 2022). In accordance with that, simulations predict that galaxies with baryonic mass fractions $\gtrsim 0.3$ have turbulent Interstellar Medium (ISM) and clumpy morphology (Hayward & Hopkins 2017). In the Local Universe such turbulent ISM is found almost exclusively in low-mass systems (Bradford et al. 2015).

In the the hierarchical framework of galaxy formation, metal-poor dwarf galaxies are considered the building blocks of the present-day larger galaxies (White & Frenk 1991; De Lucia & Blaizot 2007; Annibali & Tosi 2022). Furthermore, star formation follows a hierarchical behaviour (Lada & Lada 2003), so that the clumpy morphologies frequently observed in high-z galaxies are associated with early stages of star formation. Notwithstanding, the fraction of clumpy galaxies is uncommon among local galaxies ($z \sim 0$; e.g., Shibuya et al. 2016; Fisher et al. 2017a), there are few local metal-poor starburst dwarf galaxies that represent the most promising analogues for typical high-z clumpy galaxies. Besides the metal-poor content, they usually present strong stellar feedback and high H I mass fractions (Muratov et al. 2015; Trebitsch et al. 2017). The large distances to high-z galaxies do not allow us to spatially resolve the sub-structures that make up the clumps, so these local analogues enable us to explore the physics underlying star formation processes at intermediate scales (i.e., at higher scales than the typical ~10 pc of Young Star Clusters and smaller than the kpc-sized giant stellar clumps; Adamo et al. 2020) and to constrain stellar processes in metal-deficient environments.

In Lassen et al. (2021) (L21 hereafter) we studied the local ($z = 0.04025$) dwarf irregular companion of the Early-Type Galaxy (ETG) Mrk 1172, SDSS J020536-081424 . The dwarf galaxy occupies a projected region of $14\times\,14\,\mathrm{kpc}^2$ ($\sim 10''$) and, although faint in the stellar continuum, is bright in Hα and presents a clumpy morphology (see Fig. 1). The typical radii of the clumps are of the order of the observational seeing ($\sim 1.4''$), which corresponds to a Point Spread Function (PSF) radius of ~1 kpc. At this spatial scale, PSF-convolved star-forming complexes likely represent a blend of smaller star-forming regions with surrounding ionised gas. SDSS J020536-081424 represents an interesting system to study: It lies at a considerably large distance ($d_L \sim 185\,\mathrm{Mpc}$) compared to typical Integral Field Unit (IFU) studies of low-mass galaxies (e.g. Bik et al. 2018; James et al. 2020; del Valle-Espinosa et al. 2023; Heesters et al. 2023, among many others) but at the same time it is close enough to identify and analyse the clumps separately, correlating with properties from the host low-mass galaxy. Furthermore in L21 it was shown that SDSS J020536-081424 is in interaction with the Early-Type Galaxy (ETG) Mrk 1172, turning this system into a unique opportunity to use the powerful spatially resolved analysis from IFU spectroscopy to explore the role played by gravitational interaction in the formation of clumps. By comparing the metallicities of clumps and underlying ionised gas component we also aim to investigate the scenario of infall of metal-poor gas as the trigger of clumpy star formation.

Throughout this work we adopt the ΛCDM cosmological parameters with a Hubble constant of $H_0 = 67.4\,\mathrm{km\,s}^{-1}\,\mathrm{Mpc}^{-1}$ and density parameters $(\Omega_\mathrm{m}, \Omega_\Lambda) = 0.315, 0.685$, as reported by Planck Collaboration et al. (2020) results, and Oxygen abundance as a tracer of the overall gas phase metallicity, using the two terms interchangeably, adopting $\log(\mathrm{O/H}) + 12 = 8.69$ as the solar Oxygen abundance (Asplund et al. 2009, 2021). In §2 we outline the data and summarise key findings previously determined in L21. For details on the data reduction, we refer to L21. In §3 we present the spectroscopic analysis performed on the clumps, including methods for extracting the clump spectra. In §4 we discuss the clump properties obtained via the spectroscopic analysis and explore the scenarios of clump formation via Violent Disk Instability and infall of metal-poor gas. We also inspect the results from the Stellar Population Synthesis of the clumps. We summarise our results and findings in §5.

2 OBSERVATIONS WITH MUSE INTEGRAL FIELD SPECTROSCOPY

The dwarf-ETG system was observed with the integral field spectroscopy Multi-Unit Spectroscopic Explorer (MUSE, Bacon et al. 2010) mounted at the 8.2 m ESO Very Large Telescope (VLT) on Paranal (Chile), using the Wide-Field Mode (WFM). The WFM covers a nominal wavelength covers the spectral range of 4600 – 9350 Å with mean spectral sampling of 1.25 Å over a 1 arcmin^2 field-of-view with angular sampling of 0.2″. The resolving power ($R \equiv \Delta\lambda/\lambda$) of MUSE spectrograph varies from $R \sim$1750 at 465 nm to $R \sim$3750 at 930 nm. In L21 a spatially resolved characterisation of several physical and chemical properties of the dwarf galaxy was presented, which we briefly summarise here.

The integrated instantaneous SFR (i.e., the Star Formation Rate in timescales of ∼10 Myr) estimated using the Kennicutt (1998) calibration with L(Hα) resulted in 0.7 $M_\odot$ yr^{-1}, assuming a Salpeter stellar Initial Mass Function (IMF). Using stellar population synthesis we estimated a total stellar mass of 3×10^9 $M_\odot$, hence leading to log(sSFR) = −9.63. The mean gas-phase metallicity, estimated from the indirect method, was log(O/H) + 12 = 8.2 ± 0.2 (∼1/3 $Z_\odot$), indicating a metal-deficient ISM. A kinematic model assuming gas in circular orbits was fitted to the system using the stellar and gas velocity field of the ETG and the dwarf, respectively. The alignment of both line of the nodes and disc inclination indicates that the gas in the dwarf is under the gravitational influence of Mrk 1172.

In the left panel of Fig. 1 we show the 1 arcmin^2 Field of View of the dwarf-ETG system in the rest-frame continuum window from 4570 Å to 7000 Å, considering the dwarf reference frame. The ETG is located at the centre of the image, while the dashed red rectangle encompasses the dwarf galaxy. The bright source at the top of the image is the star Gaia EDR3 2463146603042188160. In the upper and lower right panels, we display zoom-in images of the dwarf in the continuum and the Hα emission after subtracting the continuum, respectively. The continuum modelling was achieved by applying a median filter with a window size of 150 Å, as detailed in (Herenz & Wisotzki 2017). In the latter panel, it is possible to observe that in Hα the morphology of SDSS J020536-081424 is dominated by off-centre star-forming clumps. The red marks represent the spaxel with highest flux in the continuum (circle) and in Hα (cross).

In Appendix A we also present observations of SDSS J020536-081424 in the Near-Infrared (NIR) using the the Gemini South Adaptive Optics Imager (GSAOI, McGregor et al. 2004; Carrasco et al. 2012). The high spatial resolution of GSAOI provides images with enhanced seeing ($\gtrsim$ 7 times lower than MUSE) that indicate the sizes of the clumps could be smaller than the ones estimated from the spectroscopy. Unfortunately only the brightest clump could be detected in the NIR due the faint continuum emission from SDSS J020536-081424 , so it is not possible to dig deeper on the internal structure to quantify by how much the sizes of the clumps are overestimated from the seeing-limited optical spectroscopy.

3 SPECTROSCOPIC ANALYSIS

3.1 Extracting individual clump spectra

As observed in Fig. 1, the 2D Hα morphological map of SDSS J020536-081424 is dominated by several star-forming clumps superimposed on an extended component of ionised gas. To conduct a spectroscopic analysis of the clumps, it is essential to establish clear criteria that will allow for the distinction and separation of these compact structures from the adjacent extended gas component.

The identification of the clumps was performed using astrodendro[1] on the continuum-subtracted Hα image to build a hierarchical tree-diagram of structures, which are categorised in branches, i.e. structures that split into multiple sub-structures including other branches, and leaves, that do not contain sub-structures. The construction of a dendrogram is based on an isophotal-like analysis, since the code starts from the highest-flux pixel of the image and assigns subsequent pixels to branches and leaves based on the flux intensity level (Goodman et al. 2009). We allow detection from a minimum flux threshold of F(Hα) = 1.6×10^{-20} erg s^{-1} cm^{-2}, roughly corresponding to the background level estimated from an empty region on the Hα image (see, for instance, bottom right panel in Fig. 1), and for a minimum size of 10 pixels per source (≈ 0.3 kpc^2). For the `min_delta` parameter that controls the minimum flux difference that a peak must exhibit to be considered as a new structure, we adopted the value of 6.0×10^{-19} erg s^{-1} cm^{-2}. A few isolated pixels exhibit anomalously high fluxes, thus prior to detection a sigma-clipping was applied to the image with cut of 3σ.

The hierarchical flux levels are presented in the top panel of Fig. 2. The black contours represent the flux level of the branches, highlighting the ionised gas component from the background level. The red contours represent the leaves, which include clumps separated from the extended component and islands of flux (Clumps I, J and H). In the bottom panel, we present the resulting hierarchical tree-diagram, where the logarithmic flux scale stands for the integrated F(Hα) of each structure. Since the area covered by each clump can vary significantly, we label them in alphabetic order according to their flux surface density, which is more accurate to trace compact star-forming structures than the integrated flux alone. We use the output segmentation map to create spatial masks and integrate the spectrum of each clump highlighted in Fig. 2.

3.2 Self-consistent continuum modelling

To accurately assess the intensity of nebular lines in the clump spectra, it is essential to address the continuum (stellar plus nebular) appropriately, especially in highly ionised regions. It is crucial to account for the absorption features of the underlying stellar populations, especially when measuring the profiles and intensities of emission lines like Hα and Hβ. This correction becomes significant when the contributions from young and intermediate stellar populations are non-negligible(González Delgado & Leitherer 1999; González Delgado et al. 1999). A common approach to model the stellar emission is via stellar population synthesis techniques, under the assumption that the stellar emission can be fairly described by linear combinations of Simple Stellar Populations (SSPs), e.g. pPXF (Cappellari & Emsellem 2004; Cappellari 2017), starlight (Cid Fernandes et al. 2005; Werle et al. 2019), fado (Gomes & Papaderos 2017), pipe3D (Sánchez et al. 2016; Lacerda et al. 2022), among many others.

Besides the light emitted by stars, nebular emission can be significant in regions of high star formation activity, reaching contributions to the total optical/IR continuum emission of up to 70 per cent (Krueger et al. 1995; Gomes & Papaderos 2017; Cardoso et al. 2019). The nebular emission can be divided into two components: The first component stands for the forbidden and fine structure line transitions caused by the ionising radiation field produced by the

[1] https://dendrograms.readthedocs.io/en/stable/

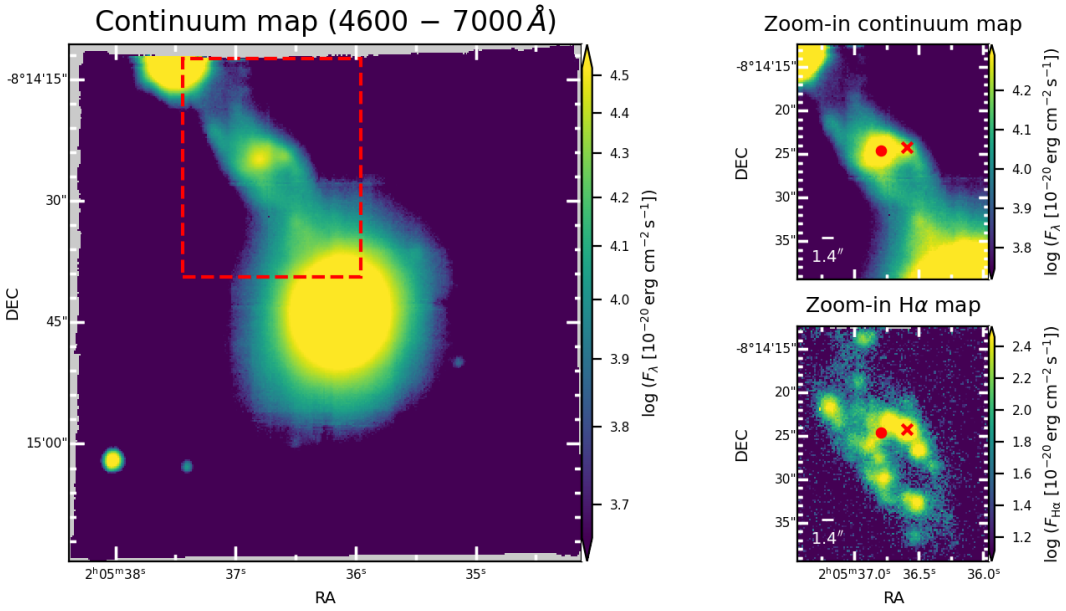

Figure 1. *Left:* MUSE FoV of the dwarf-ETG system integrated in the rest-frame wavelength window 4570 Å to 7000 Å. The ETG Mrk 1172 is located at the centre of the image, and the bright source on the top left corner is a catalogued star. The red rectangle shows the region covered by the dwarf. *Top right:* Zoom-in of the region covered by the red rectangle in the continuum. The scale bar represents the PSF size (~1.1 kpc). The red circle shows the luminosity peak of the dwarf in the continuum. *Bottom right:* Same region as top right panel but now in the continuum-subtracted Hα, where the presence of off-centre star-forming clumps become clear. The red cross represents the luminosity peak of the dwarf in Hα.

short-lived massive stars, and the second component stands for the nebular continuum originated due to free-free, free-bound and two-photon emission (Mollá et al. 2009; Reines et al. 2010; Byler et al. 2017). When the contribution from the nebular component becomes significant, stellar population fitting codes were reported to overestimate both the fraction of older stellar populations and the stellar mass (Izotov et al. 2011).

With this in mind, we perform a stellar population synthesis with FADO[2] (**F**itting **A**nalysis using **D**ifferential evolution **O**ptimisation, Gomes & Papaderos 2017) to model the continuum of the extracted clump spectra self-consistently, i.e. in addition to the stellar emission, flux estimates of the strongest nebular lines in the spectra are used to infer the nebular continuum and the number of young stars necessary to achieve the estimated ionisation parameter U. In this work we adopted the SSP models from Bruzual & Charlot (2003) [3] with the so-called 'PADOVA 1994'(Alongi et al. 1993; Bressan et al. 1993; Fagotto et al. 1994a,b; Girardi et al. 1996) evolutionary tracks, STELIB stellar library (Le Borgne et al. 2003), and assuming a Chabrier (Chabrier 2003) IMF with lower and upper mass cutoffs of 0.1 $M_\odot$ and 100 $M_\odot$, respectively.

Using the complete set of SSPs largely increases the computational time without necessarily improving the quality of the fit, thus we follow the methodology described in Dametto et al. (2014) to optimise the choice of SSP models that make up the final grid. The final grid contains 144 SSPs spanning 6 metallicities ($Z_\star$ [$Z_\odot$] = 0.005, 0.02, 0.2, 0.4, 1, 2.5) and 24 ages (t [Myr] = 1, 1.66, 2.09, 2.30, 2.40, 2.63, 3.02, 3.16, 3.31, 3.63, 3.98, 5.01, 9.55, 13.8, 20.0, 64.1, 161.0, 1.3×10^3, 2.0×10^3, 2.5×10^3, 4.5×10^3, 7.0×10^3, 1.0×10^4, 1.3×10^4). Prior to fitting each spectrum is shifted to the rest-frame using the redshift estimate from L21 and correction for extinction due to the dust of Milky Way is performed using the far-infrared emission dust maps from Schlegel et al. (1998), assuming the homogeneous dust screen model described by the CCM reddening law with R_V = 3.1 (Cardelli et al. 1989; O'Donnell 1994).

3.3 Emission-line profile fitting

To estimate various gas-phase conditions and physical properties of clumps, we fit the emission lines observed in their individual integrated spectra. For modelling the emission-line profiles, we use the IFSCUBE[4] Python package (Ruschel-Dutra et al. 2021), adopting single Gaussian components and covering the optical wavelength range from 4570 to 7000 Å. The continuum is modelled using the sum of the best-fit stellar and nebular emission obtained with FADO, supplemented by a pseudo-continuum described by a 5th-order polynomial with a 2σ rejection threshold to account for residuals from the continuum subtraction. Equivalent widths are computed within an integration radius of five times the velocity

[2] https://spectralsynthesis.org/fado

[3] The incorporation of BC03 SSP models into FADO is crucial for encompassing the UV-ionising spectral range emitted by stellar populations younger than 20 Myr. These are responsible in ionising the majority of the interstellar gas within star-forming regions.

[4] https://ifscube.readthedocs.io/en/latest/

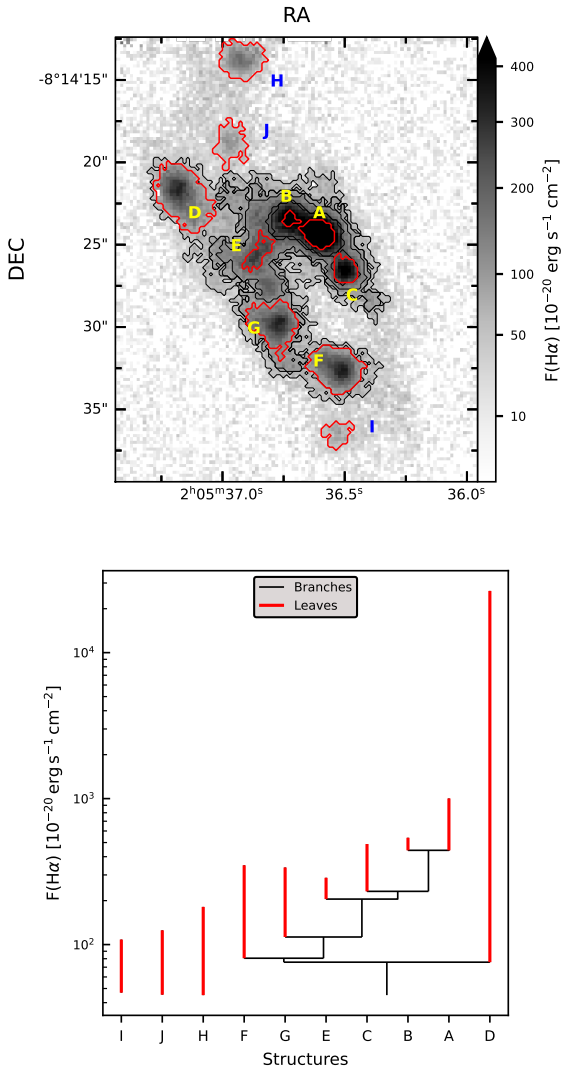

Figure 2. *Top panel*: Continuum-subtracted Hα image of SDSS J020536-081424 with overlaid hierarchical contours from ASTRODENDRO. Black and red contours stand for structural branches and leaves (i.e. structures with no sub-structures), respectively. In yellow and blue we present the labels assigned to each leaf, according to their F(Hα) surface density. *Bottom panel*: Hierarchical tree-diagram of the detected structures. The flux scale on the *y* axis shows the integrated flux of the structures, which were labelled according to their F(Hα) surface density.

dispersion of the line profiles. As constraints, we assume the theoretical line ratios [O III]λ5007 / [O III]λ4959 = 2.98 and [N II]λ6583 / [N II]λ6548 = 3.06 (Storey & Zeippen 2000; Osterbrock & Ferland 2006) and kinematic groups are considered, i.e. emission lines produced by the same ion species share identical kinematical properties. The latter assumption holds for all emission lines except for Hβ and Hα, which, due to their spectral separation, may experience different instrumental broadening (Mentz et al. 2016; Guérou et al. 2017). To estimate the uncertainties in the fitted parameters (velocity, velocity dispersion and Gaussian amplitude), we perform 500 Monte Carlo Markov Chain (MCMC) iterations for each clump.

The spectra and the best fit model are presented in Figs. 3 and 4. The spectrum is represented by the solid black line, meanwhile the solid red line shows the continuum represented by the addition of the best-fit stellar and nebular emission with the pseudo-continuum. The shadowed cyan regions correspond to the $\pm 3\sigma$ deviations from the original spectra. Given that the pseudo-continuum fits only the residuals of continuum subtraction and thus tends to average to 0 and that the nebular-to-stellar emission is less than 3% for all clumps, the continuum is approximately the best-fit stellar emission itself. The fitting residuals are shown in grey. All spectra were normalised with respect to the mean flux within the featureless continuum from 5500 to 5600 Å. The signal-to-noise ratio of the featureless continuum (SNR_{FC}) in this wavelength range is inspected for each clump following the prescription from Rosales-Ortega et al. (2012) and obtain, respectively, (SNR_{FC} = 11.4, 6.5, 8.0, 12.6, 15.3, 15.0, 11.6, 4.7, 9.9 and 7.2. To estimate the errors associated with derived emission-line fluxes IFSCUBE implements the prescriptions from Lenz & Ayres (1992); Wesson (2016).

3.4 Clump gas-phase properties

3.4.1 *Dust attenuation*

The dust attenuation of each clump can be estimated using PYNEB (Luridiana et al. 2015). Assuming the lower limit for electron density, a typical electron temperature of $T_e = 10^4$ K for H II regions and a CCM reddening law with $R_V = 3.1$, the expected intrinsic line ratio of Hα and Hβ is $(H\alpha/H\beta)_{int} = 2.863$ (Osterbrock & Ferland 2006; Pérez-Montero 2017). The uncertainty on the colour excess $E(B-V)$ is estimated by error propagation of the analytical expression (Momcheva et al. 2013):

$$\delta E(B-V) = \frac{1.086}{k(\lambda_{H\beta}) - k(\lambda_{H\alpha})} \sqrt{\left(\frac{\delta H\alpha}{H\alpha}\right)^2 + \left(\frac{\delta H\beta}{H\beta}\right)^2} \quad (1)$$

where $k(\lambda_{H\beta})$ and $k(\lambda_{H\alpha})$ are the values of the CCM reddening curve evaluated at Hβ and Hα rest-frame wavelengths, respectively. The terms δHβ and δHα are the errors associated with the flux of Hβ and Hα emission line fluxes, respectively. The values of $E(B-V)$ lie in the range of 0.06 to 0.3. They are listed together with their associated uncertainties in Table 1. The attenuation exhibits a minor elevation in clumps C, H and J. However, the enhanced attenuation in clumps H and J could be ascribed to their lower spectral SNR, clump C presents a comparable spectral SNR and proximity to clump A (where the peak of SF is observed) as clump B. Nevertheless, clump C shows an observed discrepancy in the excess colour of $E(B-V) \approx 0.1$ mag.

3.4.2 *Gas-phase metallicity*

The most reliable estimates of ionic abundances are obtained using the electron temperature T_e derived from the auroral-to-nebular emission line ratios of temperature-sensitive lines, e.g. [O III]$\lambda\lambda$4959, 5007/λ4363, [O II]$\lambda\lambda$3726, 29/λ7319, 30, [N II]$\lambda\lambda$6548, 83/λ5755 and [S III]$\lambda\lambda$9069, 9532/λ6312 (Pérez-Montero 2017). In many instances, auroral lines are too weak to be detected, so empirical calibrations based on prominent emission lines are frequently used to estimate the gas-phase metallicity. This is also the case in this work since none of the auroral lines required

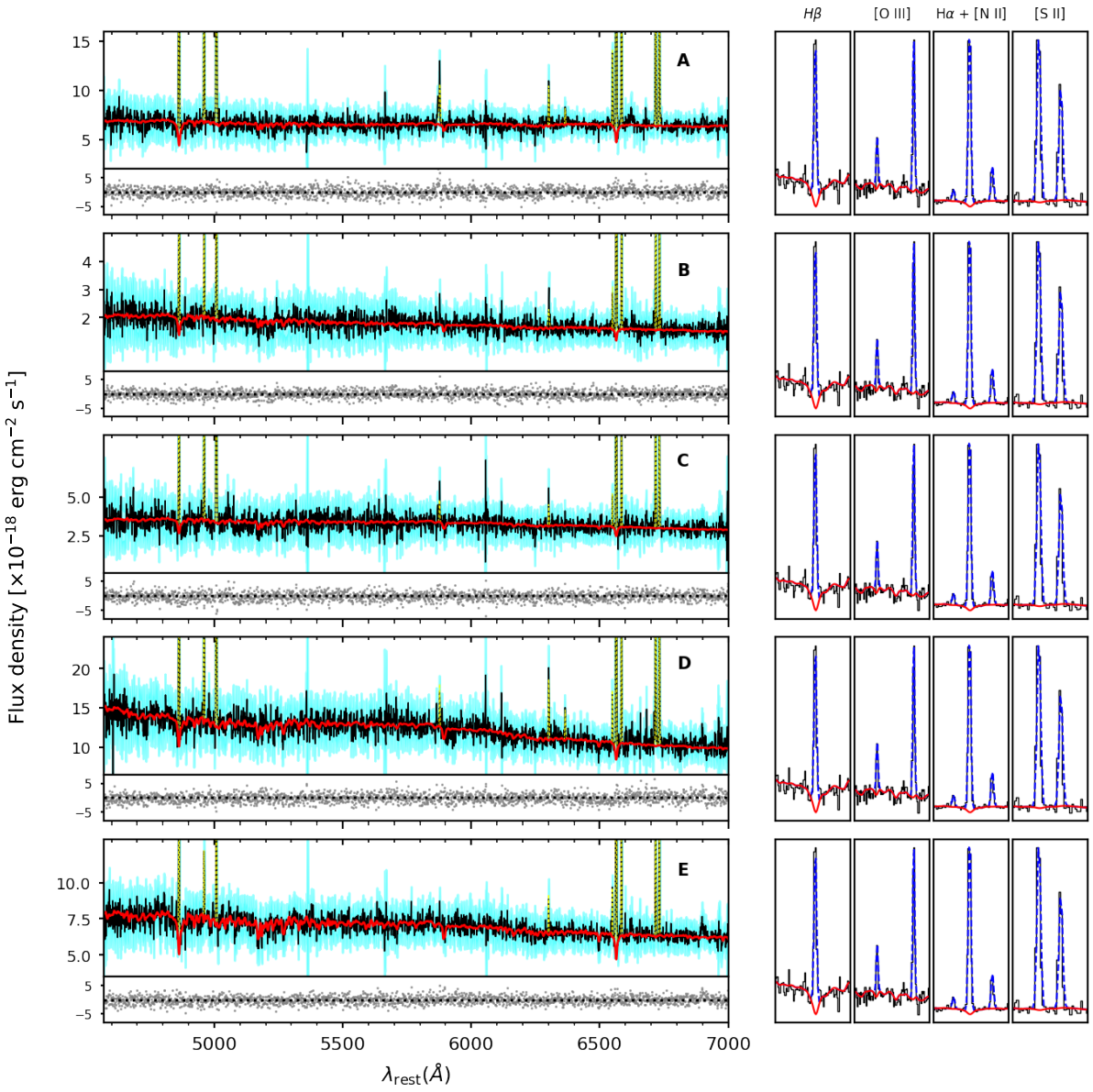

Figure 3. *Left panel*: Integrated spectrum (black solid lines) for clumps A to E. The red line represents the best fit for the continuum that includes the sum of the stellar and nebular emission from FADO and the polynomial pseudo-continuum to account for stellar subtraction residuals. The fitted emission lines are presented in yellow. The cyan shadowed region corresponds to the spectral flux density $\pm 3\sigma$. The residuals of the fit are presented below each spectrum. The SNR of the featureless continuum across the wavelength range of 5500 – 5600 Å is, respectively, 11.4, 6.5, 8.0, 12.6 and 15.3. *Right panel*: Zoom-in of the single Gaussians (blue dashed lines) fitted to the strongest emission-line profiles of each spectrum. Fluxes are normalised to the flux peak within each spectral window.

to apply the direct method can be detected, even when examining the integrated clump spectra where the SNR is improved relative to the spectra at the single spaxel resolution. For the sake of comparison with the results obtained in L21 on a spaxel-by-spaxel basis, we calculate the Oxygen abundance of the clumps using the calibration proposed by Dopita et al. (2016):

$$12 + \log_{10}(\mathrm{O/H}) = 8.77 + \mathrm{N2S2} + 0.264 \times \mathrm{N2} \quad (2)$$

where the strong-line indexes N2 (Storchi-Bergmann et al. 1994) and N2S2 (Sabbadin et al. 1977; Viironen et al. 2007) are defined as follows:

$$\mathrm{N2} = \log_{10}\left(\frac{[\mathrm{N\,II}]\lambda 6583}{\mathrm{H}\alpha}\right)$$

$$\mathrm{N2S2} = \log_{10}\left(\frac{[\mathrm{N\,II}]\lambda 6583}{[\mathrm{S\,II}]\lambda\lambda 6717,31}\right)$$

One of the advantages of this calibration is that it is nearly

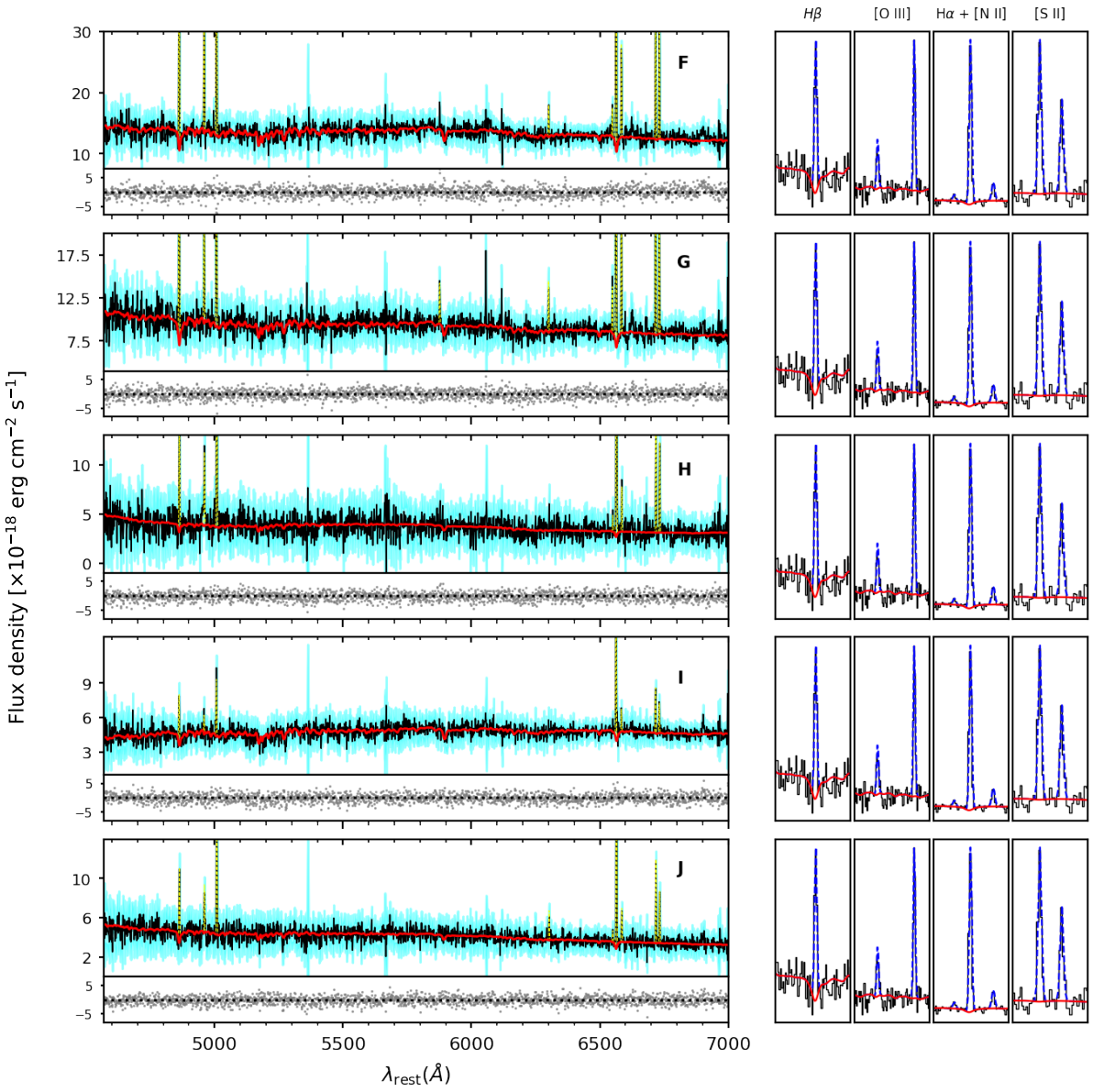

Figure 4. Same as Fig.3 but now for clumps F to J. The SNR of the featureless continuum across the wavelength range of 5500 – 5600 Å is, respectively,15.0, 11.6, 4.7, 9.9 and 7.2.

independent of variations in the ionisation parameter in the ISM. Since the emission-line ratios in equation 2 are close in the spectral domain, we can use the original fluxes in order not to propagate errors associated with the reddening correction. With that procedure, we obtain O abundances ranging from 7.9 to 8.2, as detailed in Table 1.

Additionally, in this work we make use of the H II-CHI-MISTRY[5] v5.3 (Pérez-Montero 2014) code to provide a second measurement of Oxygen abundances with additional measurements of log(N/O) and log U. H II-CHI-MISTRY compares the de-reddened emission-line fluxes with photoionisation models from CLOUDY (Ferland et al. 2013) to produce consistent results compared to those obtained via the direct method. The assumed ionising SED corresponds to a BPASS (Eldridge et al. 2017; Stanway & Eldridge 2018) instantaneous burst model with age of 1 Myr. The grid spans the range of $-4.0 < \log U < -1.5$ in steps of 0.125 dex, $7.1 < 12 + \log(\mathrm{O/H}) < 9.1$ in steps of 0.1 dex and $-2.0 < \log(\mathrm{N/O}) < 0.0$ in steps of 0.125 dex. In the absence of the necessary auroral lines to apply the direct method, H II-CHI-MISTRY relies on empirical relations between the parameters above that are calibrated on samples of local-Universe galaxies. Using this methodology for the clump spectra

[5] https://home.iaa.csic.es/~epm/HII-CHI-mistry.html

and allowing for an interpolation on the grid of log(N/O) and 2000 MCMC iterations to estimate the uncertainties, we obtain a slightly lower scatter of O abundance values in comparison to the strong-line calibration (0.16 dex and 0.37 dex, respectively) with a systematic increase of ~0.5 dex in the values of O abundance, which are also listed in Table 1. Possible reasons for such discrepancy are discussed further on.

3.4.3 *Star Formation Rates*

The SFR is proportional to the production rate of ionising photons (Kennicutt 1998). Consequently, Hydrogen recombination lines, particularly Hα, trace the SFR over timescales of $\lesssim 10$ Myr, which is the lifetime of the very massive stars responsible for the ionising flux in SF regions. It is assumed that the SFR remains constant throughout this timespan. We estimate the SFR of the clumps using the metallicity-dependent relation between SFR and the de-reddened luminosity of Hα detailed in Ly et al. (2016), assuming the calibration with STARBURST99 (Leitherer et al. 1999) considering a Padova stellar track and a Chabrier IMF:

$$\log\left[\frac{\mathrm{SFR}}{L(\mathrm{H}\alpha)}\right] = -41.34 + 0.39y + 0.127y^2 \quad (3)$$

where $y \equiv \log(\mathrm{O/H}) + 3.31$, so that $y = 0$ corresponds to the solar metallicity. For the estimation of the SFR we adopt the values obtained with H II-CHI-MISTRY. The mean difference of 0.5 dex observed for the metallicities yields a difference of ~ 0.2 dex in the SFR calculated following equation 3. Since the extension of the clumps as determined by ASTRODENDRO varies, in Table 1 we compare the the surface SFR (Σ_{SFR}), obtained by dividing the integrated SFR by the area of each region.

3.4.4 *Equivalent widths and starburst age*

Besides fluxes and kinematical parameters, we also use IFSCUBE to estimate the equivalent widths of each emission-line feature fitted. The associated uncertainties are estimated following the formalism described by Vollmann & Eversberg (2006):

$$\delta \mathrm{W}_\lambda = \frac{(\Delta\lambda - \mathrm{W}_\lambda)}{\mathrm{SNR}} \times \sqrt{1 + \frac{\overline{\mathrm{F}}_\mathrm{c}}{\overline{\mathrm{F}}}} \quad (4)$$

where the interval $\Delta\lambda \equiv \lambda_2 - \lambda_1$ corresponds to the wavelength range covered by the emission-line feature, where we have assumed $\lambda_{2,1} = \lambda_0 \pm 5\sigma_\lambda$, with λ_0 as the centre of the emission-line feature after correction for velocity shifts and σ_λ as the Gaussian dispersion of the line in units of Å. The mean fluxes of the line ($\overline{F}$) and of the continuum ($\overline{F}_c$) are calculated within this range, and SNR corresponds to the signal-to-noise ratio of the emission-line feature. The values of $W(\mathrm{H}\alpha)$ and $W(\mathrm{H}\beta)$ for each clump are listed on Table 1.

As the short-lived massive stars responsible for most of the ionising photon flux die, a steady decrease in the intensity of the emission lines from the Balmer series is expected. On the other hand, the lower-mass stars live longer and thus their contribution to the underlying absorption component of these line profiles decreases at a slower rate (e.g. stars from O6 – F2 stellar types; Dottori 1981). The combined effect of decreasing the number of ionising photons with increasing the proportion of stars contributing to the continuum luminosity is imprinted on the equivalent widths of the emission lines from the Balmer series, thus representing a direct proxy to date star formation events up to $t \sim 10$ Myr (Dottori 1981; Copetti et al. 1986; Stasińska & Leitherer 1996; Levesque & Leitherer 2013). Although this correlation is metallicity-dependent, no dependency of the adopted SFH is observed: Within the aforementioned short timescale, $W(\mathrm{H}\beta)$ serves as a good age indicator even in the case of multiple starbursts (Stasińska et al. 2001; Martín-Manjón et al. 2008; Levesque et al. 2010).

In order to infer the age of the most recent episode of star formation in the clumps we compare our estimates of W(Hα) and W(Hβ) with the predicted equivalent widths and ages of the evolutionary synthesis models generated by STARBURST99 (SB99 hereafter; Leitherer et al. 1999), assuming $Z_\star = 0.4\,Z_\odot$, which is the model with closer stellar metallicity compared to the $\overline{Z}_{\mathrm{gas}} \approx 1/3\,Z_\odot$ value estimated in L21. Since we are interested in the $\lesssim 10$ Myr stellar populations, the assumption $Z_{\mathrm{gas}} \approx Z_\star$ is fairly reasonable. The age estimates listed in Table 1 for each clump were obtained considering W(Hα), since Hα is detected in all spectra. In addition to the equivalent widths of single regions we present the spatially resolved map of W(Hα) in the upper panel of Fig. 5 with a cut of SNR(Hα) = 5. Using SB99 models we can map the age of the most recent SF episodes in the galaxy, which is shown in the lower panel of Fig. 5. In order to smooth these spatially resolved maps taking into account the existent spatial correlations between adjacent spaxels, we have applied the Integrated Nested Laplace Approximation method (INLA[6], Rue et al. 2009; González-Gaitán et al. 2019; Azevedo et al. 2023). In the case of the equivalent width map we have provided the uncertainties estimated via equation 4 to build the co-variance matrix, meanwhile for the ages we have adopted equal statistical weights for the valid spaxels.

4 DISCUSSION

4.1 Clump individual properties

The clumpy morphology of SDSS J020536-081424 indicates several sub-structures of active star formation. Using ASTRODENDRO we separated regions with higher Hα surface brightness from the remaining ionised gas. However not all the structures highlighted in Fig. 2 are compact and round-shaped, e.g. SF complex E, although it presents a higher flux in Hα compared to the surroundings. Clumps A and B, on the other hand, are round-shaped but barely separable at the 1.4″ spatial resolution of our IFU observation. Due to their proximity, it comes as no surprise that they present similar values of dust attenuation and gas-phase metallicity.

In Fig. 5 we presented the distribution of Hα equivalent widths across the galaxy and cross-correlated these values with the starburst age predicted by SB99. By taking into consideration the co-variance between pixels it becomes easier to distinguish in the upper panel of Fig. 5 that clumps A, B, C, D, G and H present more compact surface brightness than the remaining SF structures, in special structure E. This is not exactly traced by Σ_{SFR}, which points that E and G have nearly the same SFR surface density. However this direct comparison is not possible since the areas used to calculate Σ_{SFR} are different in each case and also biased by the selection criteria adopted for the structure detection in §3.1.

In order to offer a more direct manner to compare the size of each SF region we added to Table 1 the parameter r_{g}, defined as $r_{\mathrm{g}} \equiv \sqrt{A/\pi}$, i.e. the radius of a circle with same area A as the clumps. The overall sizes span the range from ~ 1 kpc to ~ 5 kpc. The smaller clumps have sizes close or even equal to the MUSE PSF

[6] https://www.r-inla.org/home

Table 1. Table summarising spectroscopic properties from the clumps observed in SDSS J020536-081424. Clumps labels were defined according to the surface F(Hα) density. The following columns are (i) Surface density SFR determined using Ly et al. (2016) calibration for Kennicutt (1998) relation to include metallicity dependence. (ii) The radius of a circular region with the same area as the clumps. (iii) Colour excess determined from the Balmer decrement. (iv) Gas-phase metallicities determined using **(a)** calibration from Dopita et al. (2016) and **(b)** H II-CHI-MISTRY (Pérez-Montero 2014). Equivalent widths for (v) Hα and (vi) Hβ. Age of the most recent starburst in each clump, determined by correlating the W(Hα) predictions from STARBURST99 models.

Clump ID	log Σ_{SFR} [$M_\odot yr^{-1} kpc^{-2}$]	r_g [kpc]	$E(B-V)$	log(O/H) + 12	W(Hα) [Å]	W(Hβ) [Å]	Starburst Age [Myr]
A	-2.09 ± 0.05	2.4	0.17 ± 0.04	[a] 8.153 ± 0.008 [b] 8.63 ± 0.05	88 ± 1	24.8 ± 0.9	5.98
B	-2.22 ± 0.05	1.1	0.16 ± 0.05	[a] 8.17 ± 0.03 [b] 8.67 ± 0.05	58 ± 1	14.2 ± 0.9	6.32
C	-2.35 ± 0.04	2.0	0.26 ± 0.03	[a] 8.05 ± 0.02 [b] 8.51 ± 0.06	67 ± 1	16.7 ± 0.7	6.22
D	-2.77 ± 0.07	4.6	0.12 ± 0.07	[a] 8.02 ± 0.08 [b] 8.64 ± 0.08	45 ± 1	10.9 ± 0.9	6.57
E	-2.61 ± 0.05	2.0	0.06 ± 0.05	[a] 8.23 ± 0.08 [b] 8.68 ± 0.06	24.4 ± 0.8	6.8 ± 0.8	7.45
F	-2.73 ± 0.02	3.9	0.11 ± 0.02	[a] 8.06 ± 0.02 [b] 8.62 ± 0.03	31.2 ± 0.7	9.4 ± 0.7	7.03
G	-2.64 ± 0.02	3.7	0.16 ± 0.02	[a] 8.11 ± 0.01 [b] 8.68 ± 0.02	45 ± 1	12 ± 1	6.57
H	-2.9 ± 0.1	3.3	0.22 ± 0.09	[a] 7.86 ± 0.04 [b] 8.6 ± 0.1	51 ± 1	12 ± 1	6.45
I	-3.10 ± 0.08	2.1	0.10 ± 0.07	[a] 7.86 ± 0.03 [b] 8.71 ± 0.07	9.8 ± 0.4	3.2 ± 0.6	10.1
J	-3.0 ± 0.2	2.8	0.3 ± 0.2	[a] 7.99 ± 0.08 [b] 8.5 ± 0.2	24.8 ± 0.7	5.2 ± 0.8	7.44

aperture size of ~ 1 kpc, indicating that the region corresponding to the ongoing starburst is likely smaller. Additionally by measuring the sizes from Hα it is hard to separate the size of the starburst region from the surrounding ionised gas component. In Appendix A) we present high-resolution imaging for SDSS J020536-081424 in the J and K_s NIR bands, obtained using GSAOI. The AO-assisted images provide a significant ($\approx 7\times$) enhancement on the seeing, allowing to quantify the sizes of the star-forming regions (although comparing sizes measured in different wavelength ranges requires caution). Unfortunately SDSS J020536-081424 is faint in the continuum and only the brightest clump (A) could be detected with counts at least $3\times$ the background level (see Fig. A1). For this clump it is possible to notice a radius of ≈ 200 pc, about $5\times$ smaller than the MUSE PSF, hence the values of log Σ_{SFR} represent lower limits.

The clumpy structure is also observed in the starburst age map (bottom panel of Fig. 5), where the clumps are tracing SF episodes in the last ~ 7 Myr. The SF structure I is a clear exception in that case, with its last SF episode around 10 Myr ago. This structure is separated from the main ionised gas component and presents faint emission-lines (see Fig. 4). Effects introduced by the low SNR in this spectrum could be invoked to explain such an age difference, but intriguingly the SNR of the featureless continuum in this spectrum is 9.9, higher than, for instance, B and C. One would not expect a raise in the continuum signal and potentially in the stellar emission in the tail of the galaxy. A careful inspection of this spectrum in the observed frame indicates the clear presence of at least two absorption lines with peak intensities of $\sim 2\times10^{-18}$erg s cm^{-2}Å^{-1} below the continuum level (see, for instance, the sudden drops on the continuum level for I clump spectrum around 5200 Å and 5900 Å in Fig 4). These two lines match the position of Mg*b* index 5177 Å and NaD 5869 Å if shifted to the ETG rest-frame. Given that the former index is one of the most intense tracers for the kinematics of old stellar populations in the optical (Bender et al. 1996; Goudfrooij & Emsellem 1996), and due to the proximity of clump I relative to Mrk 1172, these signatures most likely indicate contamination from the ETG halo in the spectrum of the SF region I. The contamination leads the stellar continuum fitting to be biased towards the old stellar population in the ETG and thus to overestimate the intensity of the absorption features underneath Hα and Hβ, producing lower equivalent widths and thus predicting older starbursts.

The inspection of starburst ages shows that the North-East SF complex composed by clumps A, B and C is slightly younger ($\gtrsim 0.3$ Myr) than the remaining clumps. The big clumps D and G have nearly the same starburst age, pointing towards a correlated triggering of recent star-formation; the clump F, on the other hand, is slightly older. This general inspection shows that SF episodes are increasingly older as we move from the North-East to West and South. At a certain extent the effect of increasingly older clumps as we approach the ETG could be caused by contamination. However, except for clump I, the ETG spectral signatures (Mg*b* 5177 Å and NaD 5869 Å) are likely much fainter than the wings around the Hβ emission-line, spectral signatures originated in the ISM of SDSS J020536-081424, that will hence determine the best SSP combination. For a quantification of the exact contribution from the luminous halo of Mrk 1172 on the derived SB99 starburst ages, a careful modelling and subtraction of the ETG brightness profile would be required, which is beyond the scope of this paper. Regarding these properties region E is an outlier even placed among

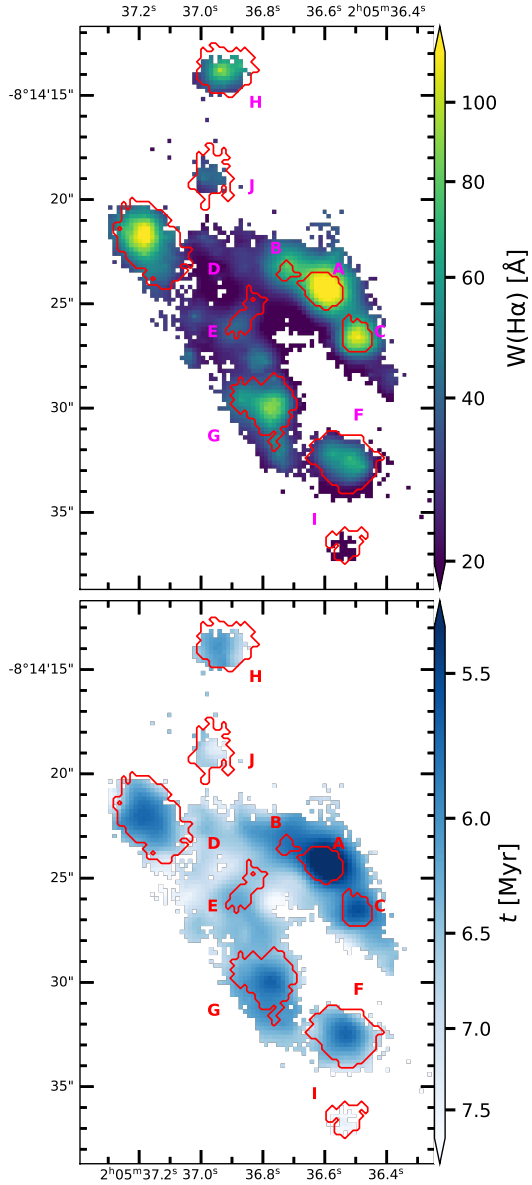

Figure 5. *Top panel*: 2D morphological map of W(Hα), which peaks at the location of the clumps. Red contours in both panels indicate the extraction regions presented in Fig. 2. Spaxels with SNR(Hα) < 5 are masked. *Bottom panel*: 2D morphological map tracing the age of the most recent bursts of star formation in the dwarf. Built using a spaxel-to-spaxel correspondence between STARBURST99 model (see text) and W(Hα). INLA was used to smooth both maps, considering the spatial correlation among individual spaxels.

the cited clumps: meanwhile it presents an extended distribution of emitting gas, it overlaps with the emission peak in the continuum (see Fig. 1). At the same time its spectrum presents the highest SNR in the featureless continuum among all spectra it has the lowest W(Hα) (if I is not considered due to the reasons discussed above). Additionally, the dust attenuation reduces almost to 0 in comparison to the other SF regions. The combination of all these factors point to region E as the centre of mass of SDSS J020536-081424 , with the presence of an older stellar population underlying the ionized gas component.

4.2 Gas rotation pattern

In L21 we presented the map of rotation velocity of the emitting gas traced by Hα, where we observed that the axis of rotation represented by the $v = 0$ line crosses the peak of the continuum emission shown in Fig. 1. However the position of the clumps in the $v_{\rm rot}$(Hα) is not clearly distinguishable when we look only at the velocity map of the emitting gas. Velocity channel maps can be used to further investigate the gas dynamics and to trace the kinematics of the clumps (e.g. see Riffel et al. 2006; Genzel et al. 2011). In Fig. 6 we present the behaviour of Hα emission-line profile in velocity slices, i.e. given λ_0 as the Hα rest-frame wavelength, each frame of Fig. 6 represents a velocity interval with respect to the emission-line centre calculated by the expression $\Delta v = c\Delta\lambda/\lambda_0$. Each channel covers a velocity range of $\sim 54\,{\rm km\,s^{-1}}$, roughly corresponding to the resolution limit of MUSE spectrograph at λ_0. The maps are built considering the continuum-subtracted cube and the colour scale represents the logarithm of the flux above the continuum level, in units of $10^{-20}{\rm erg\,s^{-1}\,cm^{-2}\,\AA^{-1}}$. A mask was applied to the spaxels with SNR(Hα) < 3.

Noticeably the flux rapidly drops to the continuum level for velocities exceeding $\sim$ 150 $\rm km\,s^{-1}$, but the rotation pattern indicated by the $v_{\rm rot}$(Hα) map is also observed: The southern part of the dwarf, which includes the clumps G and F is moving towards the observer line-of-sight, meanwhile the clumps from the upper half of SDSS J020536-081424 are moving away from the observer line-of-sight. Thus the clumps are located within the rotating component, with the most recent starburst happening preferentially in the northern part of the dwarf. On the other hand the region corresponding to the peak of the continuum emission shows little to no evidence of rotation: At $\Delta v \sim 100\,{\rm km\,s^{-1}}$ the flux corresponding to the region tracing the peak of the continuum emission already drops to the continuum-level. The observed rotating structure and the fact that the velocity field of the gas was fairly described by the kinematic model from Bertola et al. (1991) that assumes gas rotating in circular orbits reinforce the possibility of a disk component in SDSS J020536-081424 . If this disk component exists, it is expected that it is subject to the tidal forces arising from the interaction with the companion ETG.

The origin of the galactic-scale gravitational instabilities that give rise to the formation of these massive clumps is commonly attributed to gas inflows onto an existing disk (Agertz et al. 2009; Dekel et al. 2009a; Bournaud 2010). In addition, simulations indicate that the tidal torques caused by interactions are able to channel significant amounts of gas from the outskirts to the central regions of the galaxy (Muratov et al. 2015). In view of that and the fact that the ETG is forcing the gas velocity field of the dwarf to align to its stellar motion (L21), it is reasonable to argue that the sites of enhanced SFR in SDSS J020536-081424 might be correlated to perturbations induced by Mrk 1172.

4.3 Metal-poor gas accretion as the trigger of clumpy SF

Continuous accretion of metal-poor cold gas was proposed to explain the inverted metallicity gradients (i.e. metallicity decreasing towards the centre) observed in $z \sim 3$ galaxies (Cresci et al. 2010),

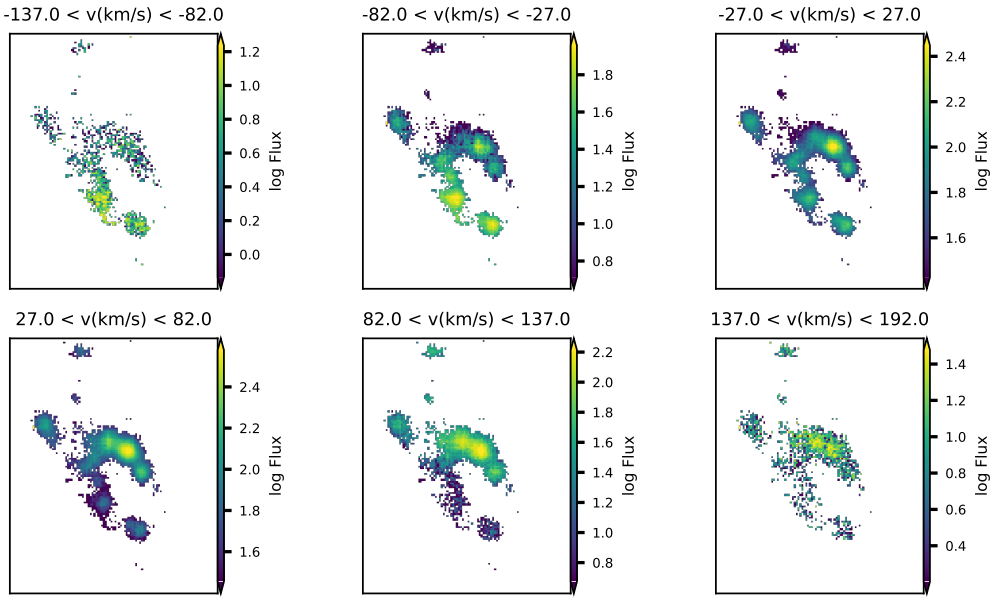

Figure 6. Velocity-sliced maps of the emitting gas in SDSS J020536-081424 . The velocity intervals covered by each channel are presented on top of each frame. The scale bar represents the logarithm of the flux above the continuum level in units of 10^{-20}erg s^{-1} cm^{-2} Å^{-1}. A SNR-cut in the spaxels with SNR(Hα) < 3 was applied.

and in low-mass nearby galaxies this mechanism typically leads to off-centre star-forming clumps, whose positions coincide with drops of the gas-phase metallicity (Ceverino et al. 2016; Sánchez Almeida et al. 2018; Kumari et al. 2018; Hwang et al. 2019; Ju et al. 2022; del Valle-Espinosa et al. 2023). In such cases an anti-correlation between the O abundance and Σ_{SFR} is expected (Sánchez Almeida et al. 2018; del Valle-Espinosa et al. 2023)

In L21 we presented maps of the O abundance in SDSS J020536-081424 using different strong-line calibrations, but the metallicity distribution on a spaxel basis was revealed to be fairly flat. For most of the regions in SDSS J020536-081424 the signal enhancement provided by larger apertures is considerable in comparison to single spaxels only, as evidenced by the detection of [O I] λ6300. Thus to inspect a possible anti-correlation between O abundance and SFR surface density in SDSS J020536-081424 we spatially bin our data using the weighted adaptation (Diehl & Statler 2006) of the Voronoi tessellation technique (Cappellari & Copin 2003) target. The bins were targeted to reach SNR~ 7 on [N II] λ6583, the weakest emission line necessary to calculate the O abundance following the prescriptions detailed in §3.4.2. We allowed a maximum cell area of 3 arcsec^2, resulting in 286 bins. The continuum of each bin was fitted with FADO and the emission lines were de-reddened following the prescriptions detailed in §3.4.1. The results are presented in Fig. 7. In the upper and middle panels, we show the behaviour of the metallicity values as a function of Σ_{SFR} obtained using H II-CHI-MISTRY and the strong-line method, respectively. In both cases, a flat ($\Delta \approx 0.3$ dex) metallicity distribution is observed, in agreement with the metallicity maps from L21. Despite in the former case a slight decrease of ~ 0.1 dex is observed for log $\Sigma_{SFR} \gtrsim -2.4$ M$_\odot$ yr^{-1} kpc^{-2}, the associated uncertainties are higher than this difference and nearly all bins lie within $\pm 2\sigma$ the median metallicity.

We stress that this does not necessarily discard the presence of accretion of pristine gas. At the distance of SDSS J020536-081424 even single spaxels cover regions of hundreds of pc, thus smaller drops of metallicity could be smeared out to the average metallicity of the ionised gas component. At the same time that spatially binning the data increases the signal, larger areas will also include more contribution from an underlying older stellar population, if it exists (Ju et al. 2022). In this case, we would not be considering the star formation induced by the newly accreted gas, and the absorption lines underneath Hα and Hβ would yield underestimations of the fluxes used to calculate either the N2 index or the dust attenuation estimates from Balmer decrement. Although the continuum of SDSS J020536-081424 is generally weak to trace with accuracy the distribution of a possible underlying host component, Stellar Population Synthesis (SPS) performed in L21 indicated the presence of two distinct stellar components with ages between 0.1 and 1 Gyr and in the next section we present and discuss the self-consistent SPS results for each clump, where this intermediate-age stellar component is also predicted.

In Table 1 we report the metallicities derived from the integrated spectra of the selected clumps, where a systematic offset between the strong-line calibration based on N2 and N2S2 indices and photoionization-based results from H II-CHI-MISTRY is observed. In the bottom panel of Fig. 7 we present the differences in O abundances using both methodologies. Although the difference decreases and becomes less scattered toward spaxels with higher $F(\mathrm{H}\alpha)$, it becomes clear that the strong-line calibration systematically underestimates the gas-phase metallicity in SDSS J020536-081424 by $\sim$ 0.4 dex. In the case where only the optical strong-lines from the ions [O III], [S II] and [N II] are provided, H II-CHI-MISTRY relies on empirical limited grids of log U-log(O/H) and log(N/O)-log(O/H) to obtain good match with the direct method within $\sim$ 0.2 dex in the metallicity range analysed in this work (Pérez-Montero 2014; Pérez-Montero et al. 2021). Although the

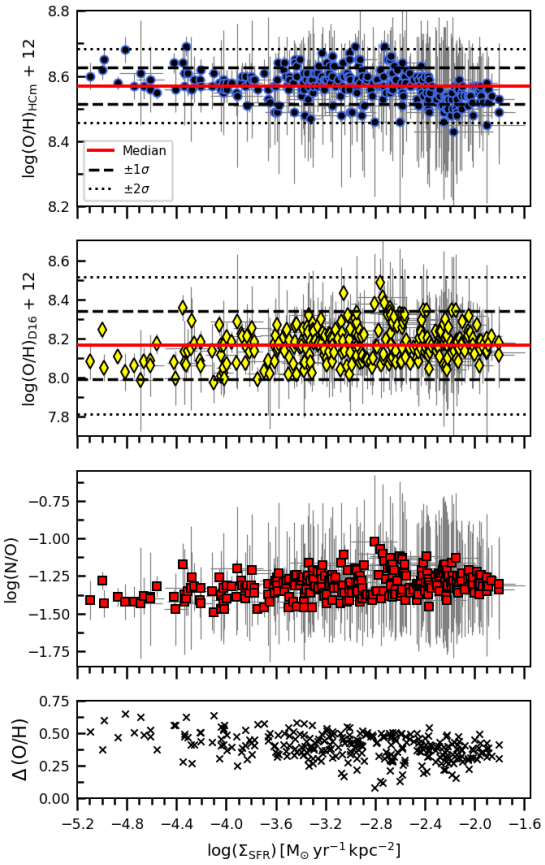

Figure 7. Metallicity values as a function of the surface density SFR for Voronoi bins in SDSS J020536-081424 targeting a SNR ~ 7 in [N II]λ6583. *Upper panel*: Values of O abundance from the H II-CHI-MISTRY run. Median of the values is indicated by the red solid lines. The black dotted lines indicate $\pm 2\sigma$ and the dashed bold black lines indicate $\pm 1\sigma$, as it is stated in the plot. Same for the second panel. *Second panel:* Values of O abundance determined from the calibration from Dopita et al. (2016). *Third panel*: Distribution of log(N/O) from the the H II-CHI-MISTRY run. *Bottom panel*: Difference between O abundance values in the upper and second panels, indicating a systematic offset.

strong-line calibration from equation 2 has the great advantage of being nearly insensitive to variations in the ionization parameter and reddening, the use of Nitrogen-based indices like N2 and N2S2 usually comes with the assumption of a secondary production of N, i.e., in addition to the production of primary N by massive stars, at higher metallicities N production by low and intermediate-mass stars is dominant (Pérez-Montero & Contini 2009). In the regime of log(O/H) + 12 > 8.3, chemical evolution models predict a positive slope in the relation N/O *vs.* O/H (Mollá et al. 2006; Vincenzo et al. 2016; Kumari et al. 2018), although this slope is is subject to variation as the relation is sensitive to several evolutionary processes

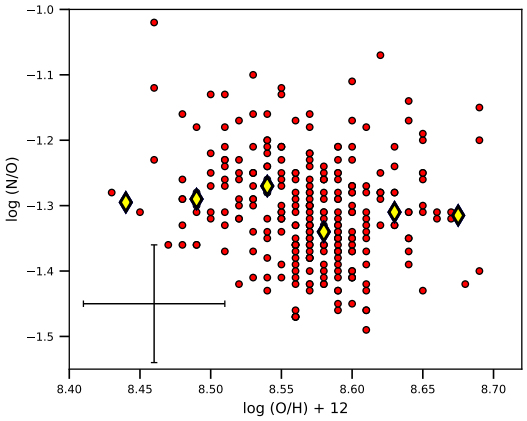

Figure 8. N/O *vs.* O/H relation for SDSS J020536-081424 , where the red points represent metallicity values for Voronoi bins targeting a SNR~ 7 in [N II] λ6583 calculated using H II-CHI-MISTRY. Yellow diamonds represent the median values of log(O/H) in bins of 0.05 dex. The mean error in each point of the diagram is represented in the lower left corner.

like the time delay between O and secondary N production (Garnett 1990; Pettini et al. 2008), gas inflow (Amorín et al. 2012), and localised N enrichment due to nucleosynthetic ejecta from Wolf-Rayet (WR) stars (Kobulnicky et al. 1997; López-Sánchez & Esteban 2010; Kumari et al. 2018).

Thus many phenomena can cause deviations in the expected log (N/O) *vs.* log (O/H) relation in SDSS J020536-081424 , and consequently produce the systematic differences in the O abundances derived from N-based calibrations. The log(N/O) shown in the third panel from Fig. 7 is also flat. The flattening of the metallicity gradients is expected in galaxy interactions and mergers as a result of gas inflow (Kewley et al. 2010; Bresolin et al. 2012; Bresolin 2019) and simulations of a disc galaxy have found that metal mixing can result from turbulence driven by gravitational instabilities (Petit et al. 2015). In Fig. 8 we inspect the N/O–O/H relation for SDSS J020536-081424 . Despite the high scatter and uncertainties in the derived values, no evidence of a positive slope can be observed. A flat metallicity distribution is observed instead, where the yellow diamonds indicate the median of the distribution in bins of 0.05 dex, which is in agreement with the first and third panels from Fig. 7. The large scatter in the N/O *vs.* O/H diagram does not allow to constrain accurately how the N production occurs in SDSS J020536-081424 , but despite the large associated errors, the slope of this relation shows no trend of increase for log(O/H) + 12 > 8.3. In Fig. 9 we present the spatially resolved maps for the H II-CHI-MISTRY with the regions corresponding to the extracted clumps are highlighted in blue. As indicated by the previous trends, the distributions are fairly homogeneous.

4.4 SFH under the scope of the results from the stellar population synthesis

In Fig. 10 we present the stellar population synthesis results for the clump spectra obtained with FADO. A good way to describe the SFH via stellar population synthesis results is by grouping the population vector (PV) in age bins (Cid Fernandes et al. 2001; Riffel

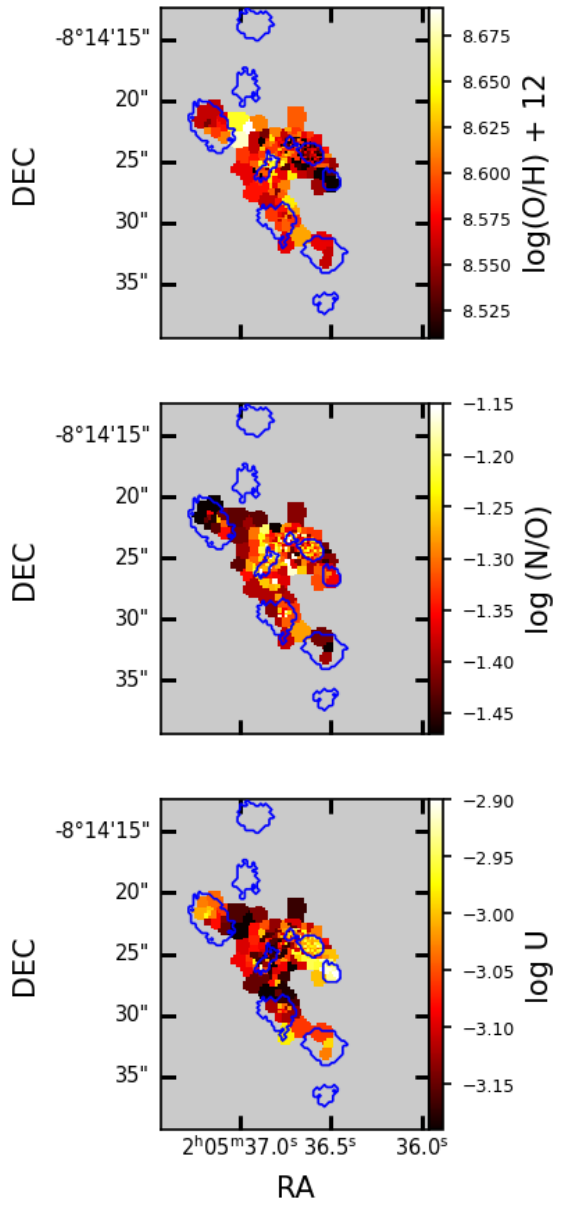

Figure 9. Spatially resolved maps for metallicity values (upper and middle panels) and for the ionization parameter $\log U$. Blue contours stand for the clump regions.

et al. 2011), thus we analyse the contribution of each PV to the best-fit stellar emission adopting the following age bins: Young (x_y; $t \leq 10$ Myr), Intermediate (x_i; 10 Myr $< t \leq 2$ Gyr), Old (x_o; 2 Gyr $< t$). The old PV spans a larger range of ages due to the known degeneracy of SSPs with $t \gtrsim 2$ Gyr, and the definition of 10 Myr for the young PV is to trace the young stellar population responsible for the ionisation in the clumps (see also SB99 starburst age predictions in §3.4.4). The luminosity (x_j) and mass (μ_j) weighted contributions for each spectrum are shown in the first and second panels of Fig. 10, respectively. The luminosity/mass-weighted stellar mean age and metallicity presented in the third and fourth panels, respectively, are defined as follows:

$$< \log t_\star >_L = \sum_j^{N_\star} x_j \log(t_j) \qquad < \log t_\star >_M = \sum_j^{N_\star} \mu_j \log(t_j)$$

$$< Z_\star >_L = \sum_j^{N_\star} x_j Z_j \qquad < Z_\star >_M = \sum_j^{N_\star} \mu_j Z_j$$

where $N_\star$ is the number of SSPs used in the SPS. t_j and Z_j are the age and metallicity of the j-th SSP in the grid, respectively. The weighted means are presented in the third and fourth panels of Fig. 10. In order to recover reliable results for the stellar population synthesis we include only the spectra with SNR$\geq$ 10 in the undisturbed featureless continuum around 4750 Å (this SNR threshold was succesfully implemented in several previous analysis with STARLIGHT, e.g. Asari et al. 2007; Cid Fernandes et al. 2007; Vale Asari et al. 2009). This excludes clumps H and J, with SNR = 7.8 and 9.6, respectively. Clump I is excluded due to the contamination from the ETG, that would produce synthesis results more more representative of the stellar population from the ETG than from the clump itself. In the presence of young stellar populations, mass and luminosity weighted stellar ages and metallicities might differ because even a few OB stars can outshine other stellar spectral types and thus tend to dominate the overall light-weighted stellar populations. On the other hand, these stars have a very short lifetime and are less numerous than low-mass stars. Therefore, the latter tend to dominate the bulk of the stellar mass (Hopkins 2018). This effect is also observed in Fig. 10, where the mean age weighted by luminosity is always lower than the mass-weighted one.

Even when we consider only the mean age weighted by luminosity that is more sensitive to the young stellar populations responsible for the ionisation in the clumps, ages of $t \gtrsim 500$ Myr are observed. Despite the expected non-negligible contribution from the young PV in the upper panel of Fig. 10, all clumps, except for F, have their higher contributions from the intermediate-age PV. In the case of SF region E which is located at the peak of the continuum emission, this contribution exceeds 90 % in both mass and luminosity cases. Clump B, located very close to region E, also does not present a contribution from the $t \geq 2$ Gyr component with dominance from the intermediate PV. Interestingly, for both regions and clump A (SF complex composed by A+B+E) the values of mean metallicity are in fair agreement and lower compared to the remaining clumps ($\overline{Z}_\star \approx 1/2\, Z_\odot$), even when compared to clumps C and D that share similar contributions from the young PV in the luminosity weighted case. Raising the contribution from the younger stellar population only slightly increases the luminosity-weighted mean metallicity of clumps B and E, indicating that the intermediate-age stellar population that dominates the central region of SDSS J020536-081424 is best described by the $Z = 0.4\, Z_\odot$ SSP models.

In clump D the contribution from the intermediate and old PV are nearly equivalent and even higher for the old stellar population in the mass-weighted case. As stated above, the old stellar population dominates clump F in both light- and mass-weighted quantities, despite the difficulty related to the determination of the relative contamination level from Mrk 1172, or even if there is contamination at all. However, if we observe Fig. 1, clumps C and D are arguably far enough from the ETG to suffer from contamination and nevertheless present a significant contribution from $t \gtrsim 2$ Gyr stellar populations. For both clumps A and B raising the contribution for the younger PV results in slightly increased stellar metallicities,

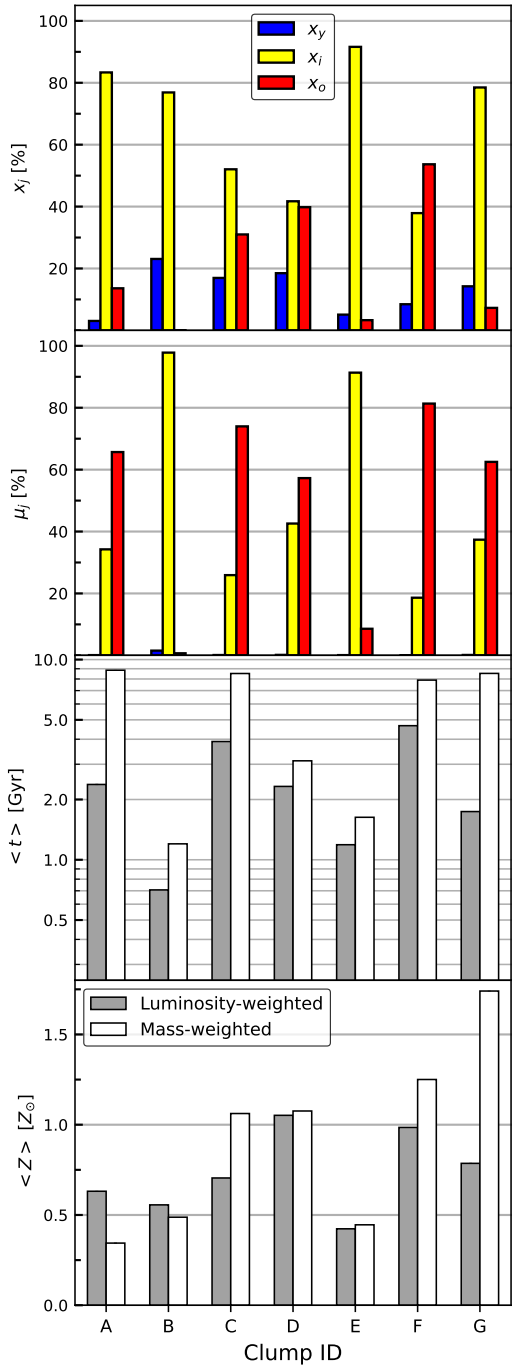

Figure 10. Stellar population synthesis results for the clumps with enough signal in the featureless continuum and without evidence of contamination from the nearby ETG. *Upper panel*: Luminosity-weighted contribution for the population vector divided in the following age bins: Young (x_y: $t \leq$ 10 Myr), Intermediate(x_i: 10 Myr $<$ t $\leq$ 2 Myr), Old ($t >$ 2 Gyr). *Second panel*: Mass-weighted contributions for stellar populations divided in three age bins. *Third panel*: Mean age weighted by luminosity (grey bars) and by mass (white bars). *Bottom panel*: Mean stellar metallicity weighted by luminosity and mass.

which imposes setbacks to the scenario of infalling metal-poor gas as the trigger of clumpy star formation in SDSS J020536-081424 , as long as new generations of stars are expected to be more metal-rich if formed from the gas enriched by past stellar generations. On the other hand clumps exhibiting higher ages due to increased contribution from the old PV (e.g. clumps C, F and G) also exhibit increased stellar metallicities. This could be due to the well-known degeneracy between age and metallicity, i.e. at a fixed mass more metal-rich SSPs look cooler/older than SSPs with lower metallicity (Worthey 1994; Dametto et al. 2014). Increasing the contribution from the older PV has the opposite effect in the mass-weighted SPS results of clump A, considerably decreasing the metallicity. It is easier to understand the presence of metal-poor old stellar populations since the long-lived stars are expected to have retained gas that was not enriched by the ISM pollution from several stellar generations, but at the same time clump A does have young stellar populations. Given that their mass-weighted contribution is negligible, the appearance of an old metal-poor stellar population could simply reflect the age-metallicity degeneracy compensating for the lack of a young PV.

Despite the intriguing star-forming clumps observed in its rotating component, SDSS J020536-081424 stellar emission seems to be originated by an intermediate-age stellar component (10 Myr $<$ t $\leq$ 2 Gyr) that traces the brightest region in the continuum emission map in Fig. 1. The fact that no stellar population older than 1 Gyr is found at the spaxel resolution possibly indicates that the older component has low-surface brightness, possibly similar to the underlying older stellar hosts observed, for instance, in many Blue Compact Dwarfs (BCDs, Loose & Thuan 1986; Amorín et al. 2007). Slightly higher stellar metallicities are found in the southern part of SDSS J020536-081424 (clumps C, D, F and G), where the starburst ages are slightly older (see Table 1). The core of SDSS J020536-081424 composed by the peak of the continuum emission (region E) and the peak of SFR (SF complex A+B) presents considerably lower metallicities, despite the flat gas-phase metallicity distribution, which could be explained by rapid enrichment from clumps formed via disk instabilities (Perez et al. 2011) or due to the violent inflows of gas caused in pair collisions and mergers (Kewley et al. 2010; Torrey et al. 2012).

5 SUMMARY AND CONCLUSIONS

This work aims to extend the analysis of the dwarf irregular galaxy SDSS J020536-081424 first presented in Lassen et al. (2021). The dwarf is in interaction with the massive ($\log(M/M_\odot) \approx 11.0$, Omand et al. 2014; Lassen et al. 2021) Early-Type Galaxy Mrk 1172. While in L21 we focused our analysis on general properties of the dwarf via spatially resolved analysis, here we constrain physical and chemical properties of a few kpc-sized star-forming clumps, investigating mechanisms that might have triggered clumpy star formation in SDSS J020536-081424 , including infall of pristine gas and clump formation on gravitationally unstable regions on the disc. Below we summarise our conclusions.

- The clumpy morphology of SDSS J020536-081424 becomes visible only when looking at Hα wavelength. Although in the continuum the dwarf still presents an irregular morphology with tidal signatures, its luminosity distribution is concentrated in a compact rounded structure that nearly disappears in Hα.
- Using the Hα channel maps (velocity-sliced maps), we have demonstrated that the clumps are not only displaced in comparison

to this central region but reside in a rotating gaseous structure resembling a disc. L21 previously proposed the existence of a disk in SDSS J020536-081424 , based on the observed rotational pattern exhibited by the $v(\mathrm{H}\alpha)$ map. The location of the clumps in a disk favours the scenario of clump formation via Violent Disk Instability (VDI). The gravitational instabilities specific regions of the disk may have arisen due to the interaction with the massive companion. Notably, the gas in the dwarf galaxy aligns with the stellar velocity field of the ETG (L21). During this alignment, certain disk regions could have experienced compression, resulting in zones of higher instability (indicated by a higher Toomre Q parameter). To gain more precise insights into the role played by Mrk 1172 in the clump formation, hydrodynamical simulations of the interacting pair would be valuable. These simulations could address whether the dwarf is being disrupted due to a fly-by or if it is on the verge of being accreted by the ETG.

- We used ASTRODENDRO in the Hα image to separate the clumps from the extended ionised gas component. With this procedure, we identified 10 clump candidates, whose spectra were extracted from the original datacube by integrating over the spatial region defined by ASTRODENDRO. The sizes of the clumps vary between 1 kpc and 4 kpc. The continuum was modelled self-consistently with FADO and spectroscopic properties such as reddening, SFR and equivalent widths of Hα and Hβ were inferred from the extracted spectra. The colour excess $E(B-V)$ ranges from ~ 0 to 0.3 mag. The position of one of the extracted star-forming regions (SF region E) coincides with the continuum peak, where $E(B-V)$ reaches its lower values.
- We used STARBURST99 models to correlate the measured equivalent widths with the age of the most recent starburst in each SF region (Dottori 1981). If we consider only regions without contamination from the ETG, the ages of the starbursts vary from 6 Myr to 7.5 Myr. The youngest SF episodes are located on clumps A (tracing peak of Hα emission) and on clump C, whereas the oldest SF episodes are located on the position of the continuum peak. This region does not belong to the rotating component (it lies on the $v(\mathrm{H}\alpha) = 0$ line) and presents the highest value of SNR (as measured from the featureless continuum) among all clump candidates.
- We measured the Oxygen abundances of the clumps using both strong-line calibrations based on the $\mathrm{N_2S_2H}\alpha$ index (Dopita et al. 2016) and from photoionization grids with H II-CHI-MISTRY (Pérez-Montero 2014). With the latter we also measured the N/O abundance. The distribution of gas-phase metallicities across the dwarf is flat in both methods, and no correlation is observed between Z_{gas} and $\Sigma_{\mathrm{H}\alpha}$. Although the lack of such (anti-)correlation argues against the scenario of the infall of metal-poor gas as the trigger of clumpy star formation, metallicity gradients might be diluted due to the relatively low spatial resolution we can reach (~ 160 pc per spaxel at $z = 0.04$).
- A difference of ~ 0.4 dex was observed between metallicities measured using both methods. An inspection of the N/O vs. O/H diagram reveals a flat relation, despite the large scatter and associated uncertainties. This is in opposition to the typical positive slope in this relation that is assumed in the calibration of the $\mathrm{N_2S_2H}\alpha$ index as a tracer of Z_{gas}. Flat metallicity gradients are usually associated with efficient mixing of metals in the disk (Petit et al. 2015) or due to late stages of major wet mergers and collisions (Kewley et al. 2010). Hydrodynamical simulations could be used to test if the orbit, morphology and SFR levels of SDSS J020536-081424 could be reproduced by a merger between two low-mass galaxies.
- Besides using Stellar Population Synthesis (SPS) from FADO to subtract the total continua (stellar plus nebular), we used it to assess the SFH of the SF regions by separating the resulting stellar populations in bins of age. SPS results point to the existence of an underlying old (≥ 2 Gyr) stellar population that appears in SDSS J020536-081424 only when spectra extracted in larger apertures (thus with increased signal) are analysed, consistent with a low surface brightness stellar population. SF region E is dominated by an intermediate-age stellar population that is likely the source of the emission that dominates the optical continuum in SDSS J020536-081424 . The combined SPS results and comparison with SB99 models indicate that the northern part of the dwarf (especially clumps A and B) are slightly younger than the rest of the galaxy and represent the sites of most recent SF episodes in the galaxy. The clumps lying below the $v(\mathrm{H}\alpha) = 0$ line (D, F, G) are generally older and present less recent SF episodes, suggesting the SF episodes in SDSS J020536-081424 are linked to its rotation.

The rotating pattern observed in SDSS J020536-081424 is likely originated either due to a disk disrupted by tidal forces caused by the interaction with Mrk 1172 or to gas that was forced to align with the stellar velocity field of the companion ETG. No evidence was found for the accretion of metal-poor gas, and the clumpy SF in SDSS J020536-081424 is more likely associated with the formation of regions of higher gravitational instability in the rotating component that favoured the collapse of cold gas. The flat gas-phase metallicity distributions give a hint that SDSS J020536-081424 could be a collision between two low-mass galaxies, but the relatively large distance of ~ 180 Mpc imposes spatial resolution limits that prevent us to constrain more precisely the size and other clump properties, as well as the inner structure and ISM properties of the dwarf. High-resolution imaging observations of SDSS J020536-081424 would help to overcome these difficulties and test the hypothesis raised in this work. Additionally, hydrodynamical simulations represent a powerful tool to constrain how the ETG affects the SFH in SDSS J020536-081424 , how it is linked to the clumpy SF and whether the dwarf properties are better reproduced by a low-mass pair collision (like in the case of the extremely metal-poor dwarf irregular galaxy DDO 68, Pascale et al. 2022) or to a dwarf with ongoing disruption due to tidal forces, but this is beyond the scope of this work and will be explored in the future.

ACKNOWLEDGEMENTS

AEL thanks Cid Fernandes and Angela Adamo for the fruitful discussions and also Natalia Vale Asari, Miriani Pastoriza and Charles Bonatto for the insightful feedback about this work during its earliest phases. AEL acknowledges the support from *Coordenação de Aperfeiçoamento de Pessoal de Nível Superior* (CAPES) in the scope of the Program CAPES-PrInt, process number 88887.837405/2023-00 and CAPES-PROEX fellowship, process number 88887.513351/2020-00. ACS acknowledges funding from the *Conselho Nacional de Desenvolvimento Científico e Tecnológico* (CNPq) and the *Fundação de amparo à pesquisa do Rio Grande do Sul* (FAPERGS) through grants CNPq-314301/2021-6, FAPERGS/CAPES 19/2551-0000696-9. RR thanks to *Conselho Nacional de Desenvolvimento Científico e Tecnológico* (CNPq, Proj. 311223/2020-6, 304927/2017-1 and 400352/2016-8), *Fundação de amparo à pesquisa do Rio Grande do Sul* (FAPERGS, Proj. 16/2551-0000251-7 and 19/1750-2), *Coordenação de Aperfeiçoamento de Pessoal de Nível Superior* (CAPES, Proj. 0001). E.J.J. acknowledges support from FONDECYT Iniciación en investigación 2020 Project 11200263 and the ANID BASAL project FB210003. REGM acknowledges support from the Brazilian agency *Conselho Nacional de Desenvolvimento Científico e Tecnológico* (CNPq)

through grants 406908/2018-4 and 307205/2021-5, and from *Fundação de Apoio à Ciência, Tecnologia e Inovação do Paraná* through grant 18.148.096-3 – NAPI *Fenômenos Extremos do Universo*. RAR acknowledges the support from *Conselho Nacional de Desenvolvimento Científico e Tecnológico* (CNPq; Proj. 303450/2022-3, 403398/2023-1, & 441722/2023-7), *Fundação de Amparo à pesquisa do Estado do Rio Grande do Sul* (FAPERGS; Proj. 21/2551-0002018-0), and CAPES (Proj. 88887.894973/2023-00). GMA thanks the *Coordenação de Aperfeiçoamento de Pessoal de Nível Superior* (CAPES) for the project 88887.629085/2021-00, for the CAPES-PrInt program 88887.936546/2024-00, and for the people of the Departamento de Física Teórica y del Cosmos for receiving him very well in the University of Granada. JMG expresses gratitude to FCT for supporting years of research in Portugal, as well as to the Fundo Europeu de Desenvolvimento Regional (FEDER) through COMPETE2020–Programa Operacional Competitividade. JMG also acknowledges the FCT-CAPES Transnational Cooperation Project. JMG had a DL 57/2016/CP1364/CT0003 contract and past fellowships (within the context of the FCT project UID/FIS/04434/2013) and POCI-01-0145-FEDER-007672. JMG was further funded by SFRH/BPD/66958/2009, supported by FCT and POPH/FSE (EC). The main FADO documentation and examples are at www.spectralsynthesis.org. This research made use of ASTRODENDRO, a Python package to compute dendrograms of Astronomical data (http://www.dendrograms.org/). This work made use of ASTROPY[7], a community-developed core Python package and an ecosystem of tools and resources for astronomy (Astropy Collaboration et al. 2022).

DATA AVAILABILITY

The data used in this paper is public and is available at ESO Science Archive Facility under the program-ID of 099.B-0411(A) and at the Gemini Observatory Archive (GOA) under the program-ID GS-2021B-DD-103.

REFERENCES

Adamo A., et al., 2020, Space Sci. Rev., 216, 69
Adams D., Mehta V., Dickinson H., Scarlata C., Fortson L., Kruk S., Simmons B., Lintott C., 2022, ApJ, 931, 16
Agertz O., Lake G., Teyssier R., Moore B., Mayer L., Romeo A. B., 2009, MNRAS, 392, 294
Alongi M., Bertelli G., Bressan A., Chiosi C., Fagotto F., Greggio L., Nasi E., 1993, A&AS, 97, 851
Amorín R. O., Muñoz-Tuñón C., Aguerri J. A. L., Cairós L. M., Caon N., 2007, A&A, 467, 541
Amorín R., Vílchez J. M., Hägele G. F., Firpo V., Pérez-Montero E., Papaderos P., 2012, ApJ, 754, L22
Annibali F., Tosi M., 2022, Nature Astronomy, 6, 48
Asari N. V., Cid Fernandes R., Stasińska G., Torres-Papaqui J. P., Mateus A., Sodré L., Schoenell W., Gomes J. M., 2007, MNRAS, 381, 263
Asplund M., Grevesse N., Sauval A. J., Scott P., 2009, ARA&A, 47, 481
Asplund M., Amarsi A. M., Grevesse N., 2021, A&A, 653, A141
Astropy Collaboration et al., 2022, ApJ, 935, 167
Azevedo G. M., Chies-Santos A. L., Riffel R., Gomes J. M., Lassen A. E., Benedetti J. P. V., de Souza R. S., Xu Q., 2023, MNRAS, 523, 4680
Bacon R., et al., 2010, in McLean I. S., Ramsay S. K., Takami H., eds, Society of Photo-Optical Instrumentation Engineers (SPIE) Conference Series Vol. 7735, Ground-based and Airborne Instrumentation for Astronomy III. p. 773508, doi:10.1117/12.856027
Bassett R., et al., 2014, MNRAS, 442, 3206
Bender R., Ziegler B., Bruzual G., 1996, ApJ, 463, L51
Bertin E., 2010, SWarp: Resampling and Co-adding FITS Images Together, Astrophysics Source Code Library, https://ascl.net/1010.068
Bertola F., Bettoni D., Danziger J., Sadler E., Sparke L., de Zeeuw T., 1991, ApJ, 373, 369
Bik A., Östlin G., Menacho V., Adamo A., Hayes M., Herenz E. C., Melinder J., 2018, A&A, 619, A131
Bouché N., Murphy M. T., Kacprzak G. G., Péroux C., Contini T., Martin C. L., Dessauges-Zavadsky M., 2013, Science, 341, 50
Bournaud F., 2010, in Smith B., Higdon J., Higdon S., Bastian N., eds, Astronomical Society of the Pacific Conference Series Vol. 423, Galaxy Wars: Stellar Populations and Star Formation in Interacting Galaxies. p. 177 (arXiv:0909.1812), doi:10.48550/arXiv.0909.1812
Bournaud F., et al., 2014, ApJ, 780, 57
Bradford J. D., Geha M. C., Blanton M. R., 2015, ApJ, 809, 146
Bresolin F., 2019, MNRAS, 488, 3826
Bresolin F., Kennicutt R. C., Ryan-Weber E., 2012, ApJ, 750, 122
Bressan A., Fagotto F., Bertelli G., Chiosi C., 1993, A&AS, 100, 647
Bruzual G., Charlot S., 2003, MNRAS, 344, 1000
Byler N., Dalcanton J. J., Conroy C., Johnson B. D., 2017, ApJ, 840, 44
Cappellari M., 2017, MNRAS, 466, 798
Cappellari M., Copin Y., 2003, MNRAS, 342, 345
Cappellari M., Emsellem E., 2004, PASP, 116, 138
Cardelli J. A., Clayton G. C., Mathis J. S., 1989, ApJ, 345, 245
Cardoso L. S. M., Gomes J. M., Papaderos P., 2019, A&A, 622, A56
Carrasco E. R., et al., 2012, in Ellerbroek B. L., Marchetti E., Véran J.-P., eds, Society of Photo-Optical Instrumentation Engineers (SPIE) Conference Series Vol. 8447, Adaptive Optics Systems III. p. 84470N, doi:10.1117/12.926240
Cava A., Schaerer D., Richard J., Pérez-González P. G., Dessauges-Zavadsky M., Mayer L., Tamburello V., 2018, Nature Astronomy, 2, 76
Ceverino D., Sánchez Almeida J., Muñoz Tuñón C., Dekel A., Elmegreen B. G., Elmegreen D. M., Primack J., 2016, MNRAS, 457, 2605
Chabrier G., 2003, PASP, 115, 763
Cid Fernandes R., Sodré L., Schmitt H. R., Leão J. R. S., 2001, MNRAS, 325, 60
Cid Fernandes R., Mateus A., Sodré L., Stasińska G., Gomes J. M., 2005, MNRAS, 358, 363
Cid Fernandes R., Asari N. V., Sodré L., Stasińska G., Mateus A., Torres-Papaqui J. P., Schoenell W., 2007, MNRAS, 375, L16
Conselice C. J., Bershady M. A., Jangren A., 2000, ApJ, 529, 886
Copetti M. V. F., Pastoriza M. G., Dottori H. A., 1986, A&A, 156, 111
Cowie L. L., Hu E. M., Songaila A., 1995, AJ, 110, 1576
Cresci G., Mannucci F., Maiolino R., Marconi A., Gnerucci A., Magrini L., 2010, Nature, 467, 811
Dametto N. Z., Riffel R., Pastoriza M. G., Rodríguez-Ardila A., Hernandez-Jimenez J. A., Carvalho E. A., 2014, MNRAS, 443, 1754
De Lucia G., Blaizot J., 2007, MNRAS, 375, 2
Dekel A., et al., 2009a, Nature, 457, 451
Dekel A., Sari R., Ceverino D., 2009b, ApJ, 703, 785
Dessauges-Zavadsky M., Schaerer D., Cava A., Mayer L., Tamburello V., 2017, ApJ, 836, L22
Dessauges-Zavadsky M., et al., 2019, Nature Astronomy, 3, 1115
Diehl S., Statler T. S., 2006, MNRAS, 368, 497
Dopita M. A., Kewley L. J., Sutherland R. S., Nicholls D. C., 2016, Ap&SS, 361, 61
Dottori H. A., 1981, Ap&SS, 80, 267
Eldridge J. J., Stanway E. R., Xiao L., McClelland L. A. S., Taylor G., Ng M., Greis S. M. L., Bray J. C., 2017, Publ. Astron. Soc. Australia, 34, e058
Elmegreen D. M., Elmegreen B. G., Rubin D. S., Schaffer M. A., 2005a, ApJ, 631, 85
Elmegreen B. G., Elmegreen D. M., Vollbach D. R., Foster E. R., Ferguson T. E., 2005b, ApJ, 634, 101

[7] http://www.astropy.org

Elmegreen B. G., Elmegreen D. M., Sánchez Almeida J., Muñoz-Tuñón C., Dewberry J., Putko J., Teich Y., Popinchalk M., 2013, ApJ, 774, 86
Erben T., et al., 2005, Astronomische Nachrichten, 326, 432
Fagotto F., Bressan A., Bertelli G., Chiosi C., 1994a, A&AS, 104, 365
Fagotto F., Bressan A., Bertelli G., Chiosi C., 1994b, A&AS, 105, 29
Ferland G. J., et al., 2013, Rev. Mex. Astron. Astrofis., 49, 137
Fisher D. B., et al., 2017a, MNRAS, 464, 491
Fisher D. B., et al., 2017b, ApJ, 839, L5
Förster Schreiber N. M., Wuyts S., 2020, ARA&A, 58, 661
Garnett D. R., 1990, ApJ, 363, 142
Genzel R., et al., 2008, ApJ, 687, 59
Genzel R., et al., 2011, ApJ, 733, 101
Girardi L., Bressan A., Chiosi C., Bertelli G., Nasi E., 1996, A&AS, 117, 113
Gomes J. M., Papaderos P., 2017, A&A, 603, A63
González Delgado R. M., Leitherer C., 1999, ApJS, 125, 479
González Delgado R. M., Leitherer C., Heckman T. M., 1999, ApJS, 125, 489
González-Gaitán S., de Souza R. S., Krone-Martins A., Cameron E., Coelho P., Galbany L., Ishida E. E. O., COIN Collaboration 2019, MNRAS, 482, 3880
Goodman A. A., Rosolowsky E. W., Borkin M. A., Foster J. B., Halle M., Kauffmann J., Pineda J. E., 2009, Nature, 457, 63
Goudfrooij P., Emsellem E., 1996, A&A, 306, L45
Green A. W., et al., 2010, Nature, 467, 684
Guérou A., et al., 2017, A&A, 608, A5
Guo Y., Giavalisco M., Ferguson H. C., Cassata P., Koekemoer A. M., 2012, ApJ, 757, 120
Guo Y., et al., 2015, ApJ, 800, 39
Guo Y., et al., 2018, ApJ, 853, 108
Hayward C. C., Hopkins P. F., 2017, MNRAS, 465, 1682
Heesters N., et al., 2023, A&A, 676, A33
Herenz E. C., Wisotzki L., 2017, A&A, 602, A111
Hopkins A. M., 2018, Publ. Astron. Soc. Australia, 35, e039
Hopkins P. F., Kereš D., Murray N., 2013, MNRAS, 432, 2639
Huertas-Company M., et al., 2023, arXiv e-prints, p. arXiv:2305.02478
Hwang H.-C., et al., 2019, ApJ, 872, 144
Izotov Y. I., Guseva N. G., Thuan T. X., 2011, ApJ, 728, 161
James B. L., Kumari N., Emerick A., Koposov S. E., McQuinn K. B. W., Stark D. P., Belokurov V., Maiolino R., 2020, MNRAS, 495, 2564
Ju M., et al., 2022, ApJ, 938, 96
Kennicutt R. C. J., 1998, ARA&A, 36, 189
Kewley L. J., Rupke D., Zahid H. J., Geller M. J., Barton E. J., 2010, ApJ, 721, L48
Kobulnicky H. A., Skillman E. D., Roy J.-R., Walsh J. R., Rosa M. R., 1997, ApJ, 477, 679
Krueger H., Fritze-v. Alvensleben U., Loose H. H., 1995, A&A, 303, 41
Kumari N., James B. L., Irwin M. J., Amorín R., Pérez-Montero E., 2018, MNRAS, 476, 3793
Lacerda E. A. D., Sánchez S. F., Mejía-Narváez A., Camps-Fariña A., Espinosa-Ponce C., Barrera-Ballesteros J. K., Ibarra-Medel H., Lugo-Aranda A. Z., 2022, New Astron., 97, 101895
Lada C. J., Lada E. A., 2003, ARA&A, 41, 57
Lassen A. E., Riffel R., Chies-Santos A. L., Johnston E., Häußler B., Azevedo G. M., Ruschel-Dutra D., Riffel R. A., 2021, MNRAS, 506, 3527
Le Borgne J. F., et al., 2003, A&A, 402, 433
Leitherer C., et al., 1999, ApJS, 123, 3
Lenz D. D., Ayres T. R., 1992, PASP, 104, 1104
Levesque E. M., Leitherer C., 2013, ApJ, 779, 170
Levesque E. M., Berger E., Kewley L. J., Bagley M. M., 2010, AJ, 139, 694
Loose H.-H., Thuan T. X., 1986, ApJ, 309, 59
López-Sánchez Á. R., Esteban C., 2010, A&A, 517, A85
Luridiana V., Morisset C., Shaw R. A., 2015, A&A, 573, A42
Ly C., Malkan M. A., Rigby J. R., Nagao T., 2016, ApJ, 828, 67
Madau P., Dickinson M., 2014, ARA&A, 52, 415
Mandelker N., Dekel A., Ceverino D., Tweed D., Moody C. E., Primack J., 2014, MNRAS, 443, 3675
Martín-Manjón M. L., Mollá M., Díaz A. I., Terlevich R., 2008, MNRAS, 385, 854
McGregor P., et al., 2004, in Ground-based Instrumentation for Astronomy. pp 1033–1044, doi:10.1117/12.550288
Mentz J. J., et al., 2016, MNRAS, 463, 2819
Messa M., Adamo A., Östlin G., Melinder J., Hayes M., Bridge J. S., Cannon J., 2019, MNRAS, 487, 4238
Mollá M., Vílchez J. M., Gavilán M., Díaz A. I., 2006, MNRAS, 372, 1069
Mollá M., García-Vargas M. L., Bressan A., 2009, MNRAS, 398, 451
Momcheva I. G., Lee J. C., Ly C., Salim S., Dale D. A., Ouchi M., Finn R., Ono Y., 2013, AJ, 145, 47
Muratov A. L., Kereš D., Faucher-Giguère C.-A., Hopkins P. F., Quataert E., Murray N., 2015, MNRAS, 454, 2691
Neichel B., et al., 2014, MNRAS, 440, 1002
Noguchi M., 1999, ApJ, 514, 77
O'Donnell J. E., 1994, ApJ, 422, 158
Omand C. M. B., Balogh M. L., Poggianti B. M., 2014, MNRAS, 440, 843
Osterbrock D. E., Ferland G. J., 2006, Astrophysics of gaseous nebulae and active galactic nuclei. University Science Books
Pandya V., et al., 2024, ApJ, 963, 54
Pascale R., et al., 2022, MNRAS, 509, 2940
Pérez-Montero E., 2014, MNRAS, 441, 2663
Pérez-Montero E., 2017, PASP, 129, 043001
Pérez-Montero E., Contini T., 2009, MNRAS, 398, 949
Pérez-Montero E., Amorín R., Sánchez Almeida J., Vílchez J. M., García-Benito R., Kehrig C., 2021, MNRAS, 504, 1237
Perez J., Michel-Dansac L., Tissera P. B., 2011, MNRAS, 417, 580
Petit A. C., Krumholz M. R., Goldbaum N. J., Forbes J. C., 2015, MNRAS, 449, 2588
Pettini M., Zych B. J., Steidel C. C., Chaffee F. H., 2008, MNRAS, 385, 2011
Planck Collaboration et al., 2020, A&A, 641, A6
Reines A. E., Nidever D. L., Whelan D. G., Johnson K. E., 2010, ApJ, 708, 26
Ribeiro B., et al., 2017, A&A, 608, A16
Riffel R. A., Storchi-Bergmann T., Winge C., Barbosa F. K. B., 2006, MNRAS, 373, 2
Riffel R., Riffel R. A., Ferrari F., Storchi-Bergmann T., 2011, MNRAS, 416, 493
Rigaut F., et al., 2014, MNRAS, 437, 2361
Rosales-Ortega F. F., Arribas S., Colina L., 2012, A&A, 539, A73
Rue H., Martino S., Chopin N., 2009, Journal of the Royal Statistical Society Series B: Statistical Methodology, 71, 319
Ruschel-Dutra D., et al., 2021, MNRAS, 507, 74
Sabbadin F., Minello S., Bianchini A., 1977, A&A, 60, 147
Saintonge A., et al., 2013, ApJ, 778, 2
Sánchez Almeida J., Caon N., Muñoz-Tuñón C., Filho M., Cerviño M., 2018, MNRAS, 476, 4765
Sánchez S. F., et al., 2016, Rev. Mex. Astron. Astrofis., 52, 21
Schirmer M., 2013, The American Astronomical Society, 209, 21
Schirmer M., Carrasco E. R., Pessev P., Garrel V., Winge C., Neichel B., Vidal F., 2015, ApJS, 217, 33
Schlegel D. J., Finkbeiner D. P., Davis M., 1998, ApJ, 500, 525
Shibuya T., Ouchi M., Kubo M., Harikane Y., 2016, ApJ, 821, 72
Somerville R. S., Primack J. R., Faber S. M., 2001, MNRAS, 320, 504
Soto E., et al., 2017, ApJ, 837, 6
Stanway E. R., Eldridge J. J., 2018, MNRAS, 479, 75
Stasińska G., Leitherer C., 1996, ApJS, 107, 661
Stasińska G., Schaerer D., Leitherer C., 2001, A&A, 370, 1
Storchi-Bergmann T., Calzetti D., Kinney A. L., 1994, ApJ, 429, 572
Storey P. J., Zeippen C. J., 2000, MNRAS, 312, 813
Tacconi L. J., et al., 2008, ApJ, 680, 246
Tacconi L. J., et al., 2013, ApJ, 768, 74
Tamburello V., Rahmati A., Mayer L., Cava A., Dessauges-Zavadsky M., Schaerer D., 2017, MNRAS, 468, 4792
Toomre A., 1964, ApJ, 139, 1217
Torrey P., Cox T. J., Kewley L., Hernquist L., 2012, ApJ, 746, 108

Trebitsch M., Blaizot J., Rosdahl J., Devriendt J., Slyz A., 2017, MNRAS, 470, 224
Vale Asari N., Stasińska G., Cid Fernandes R., Gomes J. M., Schlickmann M., Mateus A., Schoenell W., 2009, MNRAS, 396, L71
Viironen K., Delgado-Inglada G., Mampaso A., Magrini L., Corradi R. L. M., 2007, MNRAS, 381, 1719
Vincenzo F., Belfiore F., Maiolino R., Matteucci F., Ventura P., 2016, MNRAS, 458, 3466
Vollmann K., Eversberg T., 2006, Astronomische Nachrichten, 327, 862
Werle A., Cid Fernandes R., Vale Asari N., Bruzual G., Charlot S., Gonzalez Delgado R., Herpich F. R., 2019, MNRAS, 483, 2382
Wesson R., 2016, MNRAS, 456, 3774
White S. D. M., Frenk C. S., 1991, ApJ, 379, 52
Wisnioski E., Glazebrook K., Blake C., Poole G. B., Green A. W., Wyder T., Martin C., 2012, MNRAS, 422, 3339
Worthey G., 1994, ApJS, 95, 107
Zanella A., et al., 2015, Nature, 521, 54
Zanella A., et al., 2019, MNRAS, 489, 2792
del Valle-Espinosa M. G., Sánchez-Janssen R., Amorín R., Fernández V., Sánchez Almeida J., García Lorenzo B., Papaderos P., 2023, MNRAS, 522, 2089
van Donkelaar F., Agertz O., Renaud F., 2022, MNRAS, 512, 3806
van den Bergh S., Abraham R. G., Ellis R. S., Tanvir N. R., Santiago B. X., Glazebrook K. G., 1996, AJ, 112, 359

APPENDIX A: HIGH-RESOLUTION NIR IMAGING WITH GSAOI

A1 Observation and data reduction

Observations of SDSS J020536-081424 were also carried with the high-resolution AO-assisted imaging in the NIR from the Gemini South Adaptive Optics Imager (GSAOI, McGregor et al. 2004; Carrasco et al. 2012) with the Gemini Multi-Conjugate Adaptive Optics System (GeMS), a sodium-based multi-Laser Guide adaptive optics system mounted at the Gemini-South telescope in Cerro Pachón (Rigaut et al. 2014; Neichel et al. 2014). GSAOI is a NIR camera located at the $f/32$ output focus of Canopus and delivers images near diffraction limit in the wavelength range $0.95-2.5\,\mu$m. The instrument covers a FoV of $\sim 85\times85$ arcsec^2 with a spatial scale of $0.02''$per pixel. The GSAOI detector is formed by four Rockwell HAWAII-2RG arrays mounted in a 2×2 mosaic that creates a 4080×4080 pixel focal plane. The gap between the arrays is ~ 2.5 mm, which corresponds to $\sim 2.4''$on the sky. The target was observed (Program-ID: GS-2021B-DD-103) using the GSAOI filters J ($1.250\,\mu$m) and K_s ($2.150\,\mu$m) in 20 and 21 exposures, respectively, with an exposure time of 120 s each, resulting in total observing times of 40 min and 42 min. A dithering pattern was adopted around the target and separate sky exposures were not requested. The seeing delivered is $0.18''$and $0.15''$in bands J and K_s, respectively.

The data reduction was performed using THELI software package (Erben et al. 2005; Schirmer 2013). Initially, the Header Data Unit (HDU) of the 41 raw images is reformatted to split each exposure into separate files, one for each chip, to allow parallelisation. Detector-level effects such as non-linearity and cross-talk are corrected and the gain of each frame is adjusted. A set of 15 flat field observations with the dome lamps on was taken for each band. Additionally, a set of 15 flat exposures were taken with the dome lamps off for K_s band with an exposure time of 15 s. Those are used to create a master flat field which is applied to each array. To model the background we adopt the dynamic mode in THELI, given that for image sequences in the NIR exceeding 30 min temporal variations of the background due to multiplicative and additive effects (e.g. fringing, moonlight and atmospheric airglow) become non-negligible (Schirmer et al. 2015). The dynamic mode groups the exposures in 4 groups of 5 distinct exposures to mitigate background variations. After a standard collapse correction, the reduced sky-subtracted exposures of each band are resampled and co-added using SWARP (Bertin 2010).

A2 Sizes of SF regions

In Fig. A1 we present a zoom-in of GSAOI FoV on the same region presented in the right panels of Fig. 1, covering SDSS J020536-081424 . Most of the dwarf emission is below the background level, given that in the outermost regions of SDSS J020536-081424 the emission is almost entirely originated from the ionised gas. However, the region corresponding to clump A is clearly observed, and it is also possible to see a faint and more extended emission in the region corresponding to the peak of the continuum emission. In the zoom-in insets, we present contours that represent the background median + 2,3σ in the J band and the background median + 2,3,4σ in the K_s band. With the aid of the AO-assisted high-resolution image delivered by GSAOI it is possible to see that the diameter of clump A is ≈ 400 pc, smaller than the ~ 1 kpc that we derive based on MUSE observations.

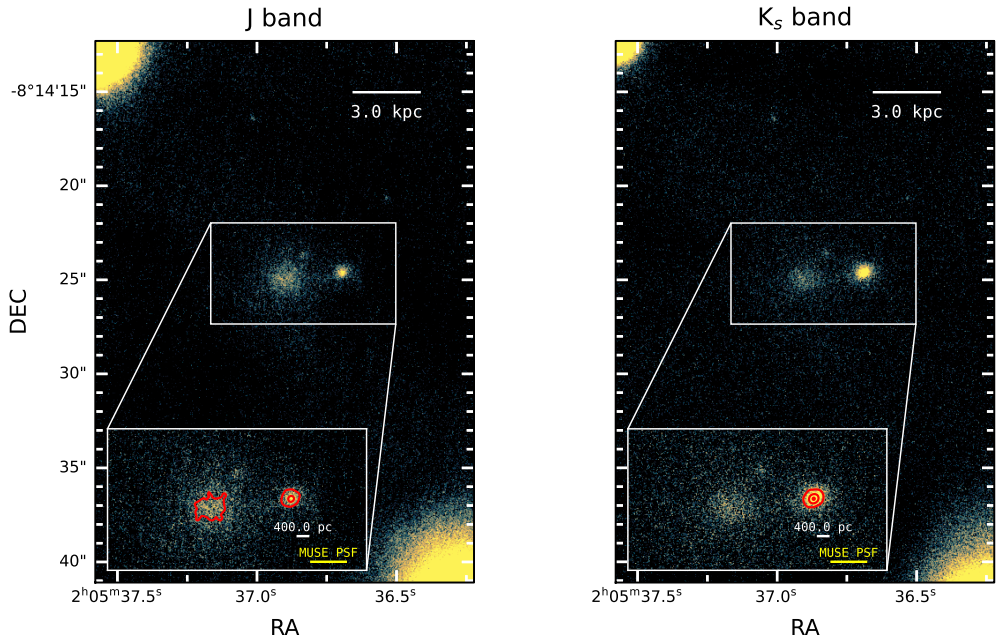

Figure A1. Zoom-in of GSAOI FoV on SDSS J020536-081424 for J and K_s bands. The inset plots on both frames present a zoom-in on the region corresponding to the emission peak in the optical continuum and the emission peak in Hα (clump A). The red contours represent the levels of the median background + (2, 3)×σ for J band and the median background + (2, 3, 4)×σ for K_s band. The white scale bar indicates the approximate diameter of 400 pc that is estimated for clump A, whereas the yellow scale bar represent the PSF size of our MUSE observations (~ 1.1 kpc).

This paper has been typeset from a TEX/LATEX file prepared by the author.

5 Analysis: ESO 400-43

In this chapter, we present the analysis regarding the BCG ESO 400-43 . This analysis was primarily developed during the sandwich PhD at Stockholm University, under the supervision of Dr. Angela Adamo e Dr. Arjan Bik. The 6-months sandwich PhD is part of the Print–CAPES[1] program, which supports the internationalization of Brazilian PhD students.

We have divided the analysis into two sub-sections. In §5.1, we present the analysis in the format of a paper, which is currently circulating among the co-authors before submission to the Astronomy & Astrophysics journal. In §5.2, we present preliminary analysis on the gas-phase metallicity of ESO 400-43 , which we plan to publish in the format of a letter in the near future.

5.1 A 3D view on the stellar feedback from young star clusters in the Blue Compact Galaxy ESO 400-43

[1] Process nº 88887.837405/2023-00

Astronomy & Astrophysics manuscript no. output
July 26, 2024

A 3D view on the stellar feedback from young star clusters in the Blue Compact Galaxy ESO 400-43

A.E. Lassen[1,2], A. Adamo[2], A. Bik[2], R. Riffel[1], A.L. Chies-Santos[1], G. Östlin[2], P. Papaderos[3], and J. Cannon[4]

[1] Departamento de Astronomia, Instituto de Física, Universidade Federal do Rio Grande do Sul (UFRGS), Av. Bento Gonçalves, 9500, Porto Alegre, RS, Brazil
e-mail: augusto.lassen@ufrgs.br, augusto.lassen@gmail.com
[2] Department of Astronomy, The Oskar Klein Centre, Stockholm University, AlbaNova, SE-10691 Stockholm, Sweden
[3] Instituto de Astrofísica e Ciências do Espaço, Centro de Astrofísica da Universidade do Porto, Rua das Estrelas, 4150-762 Porto, Portugal
[4] Department of Physics & Astronomy, Macalester College, 1600 Grand Avenue, Saint Paul, MN 55105, USA

Received July 26, 2024; accepted March 16, 1997

ABSTRACT

Context. Local-Universe star-forming galaxies with metal-poor interstellar media (ISM) provide key laboratories to investigate star formation processes under unevolved chemical conditions and at spatial scales unfeasible for unlensed high-z star-forming galaxies. Blue compact galaxies (BCGs) offer favorable conditions to host elevated numbers of massive ($\log(M/M_\odot) > 5.0$) star clusters that inject mechanical (through strong stellar winds) and radiative energy into the ISM.
Aims. Using a combination of integral field spectroscopy from MUSE-AO and high-resolution imaging with HST, this work aims to investigate the stellar feedback from star clusters observed in ESO 400-43, a $z = 0.01965$ BCG with extreme ISM conditions.
Methods. From the strong optical emission lines observed in ESO 400-43, we determine spatially resolved properties of the ionized gas in the galaxy ISM, such as dust attenuation, electron temperature and density, degree of ionization and ionization mechanisms through emission-line diagnostic diagrams. The physical conditions of the ionized gas are compared to the properties of the star cluster population, derived using SED fitting with PROSPECTOR.
Results. The ionized gas morphology inspection reveals a pronounced low surface brightness loop extending ∼10 kpc towards the dwarf companion ESO 400-43 *b*. Irregular ionized gas kinematics suggest past merger events and galactic-scale outflows in the northwest region of the galaxy. Emission line maps highlight the role of the star clusters as the major ionization sources in ESO 400-43. About 5% of the star cluster population is young ($t < 5$ Myr) and massive, possibly hosting significant numbers of Wolf-Rayet (WR) stars. A hard ionizing field, traced by the nebular He II λ4686 emission line, spatially correlates with regions of higher concentration of young and massive star clusters. Spatially resolved emission line diagnostic diagrams revealed N-enriched gas surrounding regions with elevated SF activity and higher concentrations of young and massive star clusters, with possible fast radiative shocks propagating through the ISM of ESO 400-43.

Key words. keyword1 – keyword2 – keyword3 – keyword4

1. Introduction

In the hierarchical Λ Cold Dark Matter (ΛCDM) cosmological framework, low-mass dark matter halos are the first to form, and larger, more massive DM halos grow through successive mergers (White & Rees 1978; White & Frenk 1991; De Lucia & Blaizot 2007; Ishiyama 2014; Qu et al. 2017). Observations and semi-analytical models have already indicated the fundamental role played by $< 10^9\ M_\odot$ halos harbouring very metal-deficient stars in the reionization of the Universe (Choudhury & Ferrara 2006, 2007; Choudhury et al. 2008; Bouwens et al. 2012, 2015). Additional support for this scenario has been provided by recent James Webb Space Telescope (JWST) observations that revealed low-mass galaxies with efficient production of ionising photons (Asada et al. 2023; Simmonds et al. 2024; Atek et al. 2024). Given their low stellar masses and chemically unevolved interstellar medium (ISM), nearby metal-poor dwarf galaxies serve as unique laboratories for studying ISM properties, chemical enrichment, stellar feedback and star formation processes under conditions that resemble those expected for primitive galaxies with spatial resolution unfeasible for unlensed high-z galaxies (Tosi 2003; Motiño Flores et al. 2021; Annibali & Tosi 2022; Hunter et al. 2024).

Blue compact dwarf (BCD) galaxies are among the dwarf galaxies considered as local analogues of high-z star-forming galaxies. As their name suggests, BCDs are low-luminosity ($M_B \gtrsim -18$, Papaderos et al. 1996) blue galaxies with compact optical sizes (Searle & Sargent 1972; Loose & Thuan 1986; Papaderos et al. 2002). They are also characterized by a relatively high star formation rate (SFR), with their optical spectra presenting ongoing bursts of star formation traced by nebular emission lines on top of a much older stellar population (Kunth & Östlin 2000; Bergvall & Östlin 2002; Gil de Paz et al. 2003; Amorín et al. 2007). BCDs have high gas-fractions (Pustilnik et al. 2001; Filho et al. 2013; Amorín et al. 2016) and a chemically unevolved ISM, with a mean gas-phase metallicity $12 + \log(\mathrm{O/H}) \approx 8.1$ (Kunth & Östlin 2000; Papaderos et al. 2008). Even more extreme ISM conditions can be found in the extremely metal-deficient (XMD) galaxies, with $12 + \log(\mathrm{O/H}) \lesssim 7.7$ (Filho et al. 2015; Senchyna et al. 2019; Zou et al. 2024). The combination of strong emission lines that enable the characterization of their ISM with low gas-phase metallicities makes BCDs ideal labo-

Table 1. Summary of HST observations for ESO 400-43. The target was observed as part of the Hi-PEEC program (GO 14066) in the filters indicated by the first column. Zeropoints were calculated using SYNPHOT and aperture corrections were computed for apertures up to 0.8″. Values of magnitude limit are informed in the last column.

Filter	Camera	Exposure Time ($N_{\rm exp}$) [s]	Zeropoint [AB mag]	a_c [AB mag]	Magnitude Limit [AB mag]
F336W (U)	WFC3/UVIS	3620 (4)	24.720	−0.24	26.7
F438W (B)	WFC3/UVIS	1736 (2)	24.829	−0.27	27.3
F606W (V)	WFC3/UVIS	1117 (2)	26.070	−0.25	27.3
F665N (Hα)	WFC3/UVIS	1440 (2)	22.724	−0.27	27.9
F814W (I)	WFC3/UVIS	1800 (3)	25.102	−0.36	27.1

ratories for deepening our understanding of the star formation processes in unevolved systems. Stellar population synthesis and star cluster-based studies suggest that BCDs are currently experiencing rapid bursts of star formation, preceded by long periods of little star formation (SF) activity (Adamo et al. 2010; Zhao et al. 2011). Kinematical analyses of BCDs have revealed irregular velocity fields, suggesting that mergers and infalling gas clouds are the responsible for triggering the starbursts (Östlin et al. 2001; Moiseev et al. 2015).

The formation of massive ($\log(M/M_\odot) \gtrsim 5.0$) star clusters is favored by conditions observed in merging, interacting and starburst galaxies (Bastian et al. 2006; Whitmore et al. 2010, 2014; Adamo et al. 2020a). BCDs, for instance, have been observed to host considerable amounts of young and massive star clusters (Östlin et al. 2003; Adamo et al. 2010, 2011; Bik et al. 2018). The stellar feedback in star-forming galaxies is dominated mainly by the energetic radiative and mechanic outputs from the O stars that are released into the ISM. After a short period of time (3 Myr $\lesssim$ t $\lesssim$ 5 Myr Leitherer et al. 1999; Smith et al. 2002), O stars may evolve into Wolf-Rayet (WR) stars, a stage of stellar evolution when the outer layers are expelled due to strong stellar winds, exposing the inner stellar cores where the effective temperatures ($T_{\rm eff}$) can be as high as $\sim$ 100.000 K (Crowther 2007). The radiation released from WR stars into the ISM is very hard, and often transitions of He^+, with an ionisation potential of 54.4 eV, can be observed (Brinchmann et al. 2008). The powerful stellar winds produce broad emission features and inject mechanical energy into the ISM. Part of the nucleosynthesized material is expelled due to the strong stellar winds and plays a key role in the chemical enrichment of the ISM (López-Sánchez & Esteban 2010; Kobayashi & Ferrara 2024). After the short WR evolutionary stage, the massive stars die as supernovae, which also contribute significantly to the injection of mechanical energy into the ISM (Leitherer et al. 1999; Meynet & Maeder 2005).

In this paper, we use HST imaging data to constrain the physical properties of the star cluster population in the BCG ESO 400-43 and AO-assisted Integral Field Unit (IFU) spectroscopic data from the Multi-Unit Spectroscopic Explorer (MUSE) to determine the physical conditions of the ionized gas. We combine spectroscopy and multiband photometry to explore the stellar feedback driven by the star clusters into the ISM of ESO 400-43. In §2, we present the data used in this paper and describe the data reduction process. In §3, we describe the methods employed in the analysis, whose results are presented and briefly discussed in §4. We discuss the main results in §5, and finish the paper summarizing our findings in §6. Throughout this work, a WMAP9 cosmology (Planck Collaboration et al. 2014) and a Solar Oxygen abundance of log(O/H) + 12 = 8.69 (Asplund et al. 2009) are assumed.

2. Observations and data reduction

2.1. Spectroscopic IFU observations

In this paper we present the analysis of the Blue Compact Galaxy (BCG) ESO 400-43 (z = 0.01965 ± 0.00001, corresponding to a luminosity distance of approximately 85 Mpc. For more details on the redshift estimation we refer to §3.1) using data obtained with the integral field spectroscopy multi-unit spectroscopic explorer (MUSE, Bacon et al. 2010), mounted on the 8.2 m ESO Very Large Telescope (VLT) at Paranal, Chile, with the aid of the Adaptive Optics (AO) system (Program ID: 60.A-9191(A), PI: A. Bik) in the Wide-Field Mode (WFM). The target was observed during the night of September 17th, 2017, in $\sim$ 0.61h split into four exposures of 550s each, with two additional separate sky exposures with an exposure time of 150 seconds each. Exposures were taken in the O - S - O - O - S - O order (O = Object, S = Sky exposure). The nominal wavelength covers the spectral range of 4600 –9350 Å with mean spectral sampling of 1.25 Å over a 1 arcmin^2 field-of-view with an angular sampling of 0.2″. In the AO mode, the wavelength region 5755 –6010 Å is blocked to avoid contamination from the laser guide system. The resolving power ($R \equiv \Delta\lambda/\lambda$) of MUSE spectrograph varies from R ~1750 at 465 nm to R ~3750 at 930 nm.

The data was reduced using MUSE pipeline v2.8.7 (Weilbacher et al. 2020) within the ESO Recipe Execution Tool (EsoRex) environment (ESO CPL Development Team 2015). We start by creating the master bias and flat-field frames from the associated raw calibrations. A wavelength solution for each slice of the CCD is performed based on the computation of the Line Spread Function (LSF) of three arc lamps exposures (HgCd, Ne and Xe). A geometry table is used to map the location of the IFU slices in the FoV, and twilight flat exposures are combined to correct for illumination. A flux calibration solution is obtained by means of observing standard stars on the same night as the observations, and the sky continuum is measured from the separate sky exposures. The initial astrometric calibration is performed using the catalogs distributed with the pipeline. Additionally, a list of Raman line transitions distributed with the pipeline is used to correct for contamination from the scattered light from the laser guide system. In the post-processing stage, the flux calibration and sky subtraction are applied to the frames, respecting the aforementioned object-sky exposure order. The exposures are aligned using their relative individual shifts and combined to produce the final datacube.

To estimate the seeing of the combined exposure, we use the MUSE Python Data Analysis Framework (MPDAF, Bacon et al. 2016) Python package to fit the Field Spread Function (FSF), adopting a circular Moffat function with wavelength-dependent Moffat shape parameters (FWHM and β, Moffat 1969; Bacon et al. 2017). The FWHM varies from 1″ to 0.7″ across the nominal wavelength range, but throughout this work we adopt the

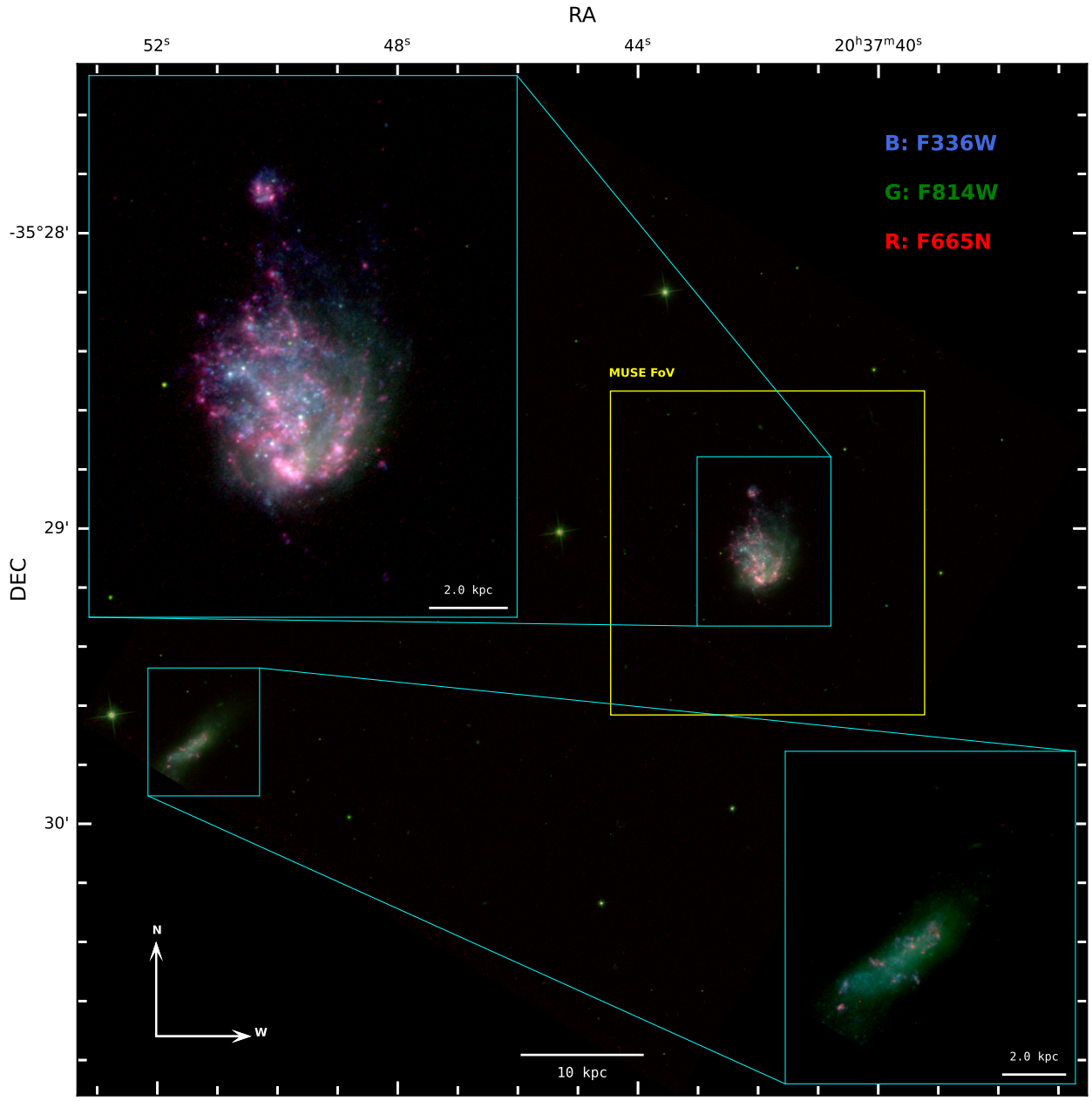

Fig. 1. Color-composite image of the HST Field-of-View (FoV), with the frames used for each RGB channel indicated on the top right. The MUSE footprint of the FoV is visualised by the yellow rectangle. The cyan rectangles show zoom-in figures of the BCD ESO 400-43 (top left) and its dwarf companion ESO 400-43b (bottom right), separated by a projected distance of ~ 70 kpc (Bergvall & Jorsater 1988).

value of 0.85″ , measured on the white-light image, as the Point-Spread Function (PSF) FWHM.

2.2. HST observations

To achieve the spatial scales necessary to study the star clusters in ESO 400-43, we use data from the Hubble Space Telescope (HST) in four broad-band filters (UBVI) corresponding to the Wide Field Camera 3 (WFC3) F336W, F438W, F606W and F814W filters, respectively, and in one narrow-band filter centered on Hα (F665N). ESO 400-43 was observed as part of the *Hubble imaging Probe of Extreme Environments and Clusters* program (HiPEEC, GO 14066 PI: A. Adamo; Adamo et al. 2020a). We summarize the HST/WFC3 data analysed in this work in Table 1, where we list the zeropoint AB magnitudes for each filter and aperture corrections calculated using the most recent tables of encircled energy distributions for WFC3 available in SYNPHOT Python package (STScI Development Team 2018). The aperture corrections listed on Table 1 were estimated for apertures up to 0.8″.

The FLC-calibrated single frames were downloaded from the MAST archive, and cosmic ray treatment was performed using LACosmic (van Dokkum 2001). The single frames were then aligned using the TweakReg module from DRIZZLEPAC Python package, using a GAIA DR3 (Gaia Collaboration et al. 2023) source catalog to obtain an absolute astrometric solution and register the World Coordinate System (WCS) of the individual exposures to a common reference frame. The single exposures for each filter were drizzled into a final science image using

DRIZZLEPAC with the native pixel scale of WFC3/UVIS detector (0.04″/px) and with North-up orientation. Assuming a WMAP9 cosmology (Planck Collaboration et al. 2014), the luminosity distance of ESO 400-43 is $d_L \approx 85$ Mpc, which corresponds to a physical resolution of of ∼16 pc/px for the HST spatial resolution. To obtain a more accurate WCS solution for the MUSE data, as well as to enable combined studies of the stellar population from which feedback originates and ionised gas properties in the galaxy, we matched the position of 7 point-like sources in the FoV with their positions in the final HST science frames.

3. Analysis methods

In this section, we describe the methods employed in the analysis. In §3.1, we detail the continuum subtraction through PPXF full spectral fitting. In §3.2, we show details on the Hα emission-line fitting procedure used to inspect the ionized gas in ESO 400-43, and in §3.3 we estimate the dust attenuation in the ISM of ESO 400-43 via Balmer decrement. In §3.4, we describe how electron temperature and density measurements were obtained, and in §3.5 we detail the construction of emission line maps to inspect the ionization in the ISM of ESO 400-43. The extraction of the radial spectra used later to calculate the ionized gas mass is presented in §3.6. In §3.7, we describe the extraction and aperture photometry analysis of the star clusters in ESO 400-43, and in §3.8 the SED fitting of the star cluster catalog.

3.1. Stellar continuum fitting

A proper treatment of the stellar emission continuum is essential to accurately estimate the flux of the nebular emission lines in the spectra of ESO 400-43, particularly for the Balmer recombination lines, whose profiles might be influenced by underlying absorption features if the contribution of young and intermediate stellar populations is significant (González Delgado & Leitherer 1999; González Delgado et al. 1999). To model the continuum with a high enough signal-to-noise ratio (SNR), we spatially bin the data using the Voronoi tessellation method (Cappellari & Copin 2003) with the Weighted Voronoi Tesselation (WVT) adaptation (Diehl & Statler 2006). The binning patterns are applied to achieve a SNR of 150 across the featureless continuum wavelength range of 5020 – 5060 Å , allowing a maximum of 60 spaxels per bin. The spectrum of each bin is corrected for foreground Galactic extinction using the dust maps from Schlegel et al. (1998) and adopting the CCM reddening law (Cardelli et al. 1989), resulting in corrections of $E(B-V) \approx 0.03$ mag at the position of ESO 400-43 on the sky.

To estimate the redshift of ESO 400-43, we extract an integrated spectrum using an aperture with a diameter of 20″ (∼8 kpc) that completely covers ESO 400-43 (considering white-light image). Single 1D Gaussian profiles are fitted to the strongest observed emission lines (Hα; Hβ; [O III] $\lambda\lambda$ 4959,5007; [S II] $\lambda\lambda$ 6717,31 and [N II] $\lambda\lambda$6548,83) to determine the center of each line in the observed frame. The final redshift value is estimated as the mean of the shifts in each line, resulting in $z = 0.01965 \pm 0.00001$. Before proceeding with the continuum fitting, the spectra are shifted to their rest-frame wavelength using the derived redshift.

We model the continuum emission using the spectral fitting code PPXF (Cappellari & Emsellem 2004; Cappellari 2017), which fits the input spectra implementing a convolution between templates of simple stellar populations (SSPs) with the line-of-sight velocity distribution (LOSVD):

$$G_{\rm mod}(x) = T(x) * \mathrm{LOSVD}(cx) \quad (1)$$

where $x \equiv \ln \lambda$ and c is the speed of light. In this work, we use the SSP models from Bruzual & Charlot (2003) as templates, limiting our fit to the wavelength range of 4510 – 7070 Å to avoid contamination from sky-subtraction residuals. The fit is performed in two steps: First, the spectral regions corresponding to the main emission lines and to the regions blocked by the laser are masked; in the second step, the fit is performed masking the 3σ deviant spectral pixels.

The best-fit continuum is obtained for each Voronoi bin. To re-scale the solution to the spaxel resolution, we adopt the simplifying assumption that the stellar populations at the spaxel level vary only by a scale factor compared to the bin solution. This scale factor is estimated from the median difference between the unmasked spectral pixels of each spaxel and its corresponding bin. For previous applications of this methodology, we refer to Della Bruna et al. (2020). To produce a "pure-gas" cube, we subtract the re-scaled solution from each spaxel corrected for foreground Galactic extinction wherever we have sufficient SNR to produce a reliable PPXF fit. In the outskirts, we use LSDCAT (Herenz & Wisotzki 2017) to subtract the continuum using a median filter with filter size of 150 Å.

3.2. Hα emission-line fitting for ionized gas kinematic analysis

To inspect the kinematics of the ionized gas described in §4.1, we apply a Voronoi binning with WVT adaptation to the Hα emission line to achieve a SNR≈10 across the pure-gas cube, allowing a maximum area of 400 arcsec^2 for individual bins. The spectrum of each bin is extracted, and the Hα emission line profile is fitted using single 1D Gaussian component with the IFSCUBE[1] Python package (Ruschel-Dutra et al. 2021). A 5th-order polynomial fit is used as the pseudo-continuum to account for continuum subtraction residuals. The fitted Gaussian profiles provide the velocity and velocity dispersion σ(Hα) of the emitting gas, where we correct the latter for instrumental broadening using the polynomial parameterization of the MUSE spectrograph Line Spread Function (LSF) described in Guérou et al. (2017)[2]. To maintain consistency throughout this work, the flux of Hα emission line is obtained by integration over the wavelength range 6556.0 – 6566.0Å with MPDAF. The uncertainties on the flux estimates are determined by MPDAF as the square root of the variance across the integrated wavelength range:

$$\delta F(\Delta\lambda) = \sqrt{\sum_{i=\lambda_i}^{\lambda_f} \sigma^2(f_i) \times \Delta\lambda^2} \quad (2)$$

where $\sigma^2(f_i)$ is the variance of the spectral pixels within the integrated wavelength range.

3.3. Extinction map

Reddening estimates and a reddening map are obtained by performing a Voronoi tessellation over the pure-gas cube, targeting a SNR of 25 in the Hβ emission line and allowing a maximum of 20 spaxels per bin (∼1 arcsec^2). We assume the CCM reddening

[1] https://ifscube.readthedocs.io/en/latest/

[2] $\sigma_{\rm inst}$ [Å] $= 5.866 \times 10^{-8}\lambda^2 - 9.187 \times 10^{-4}\lambda + 6.04$

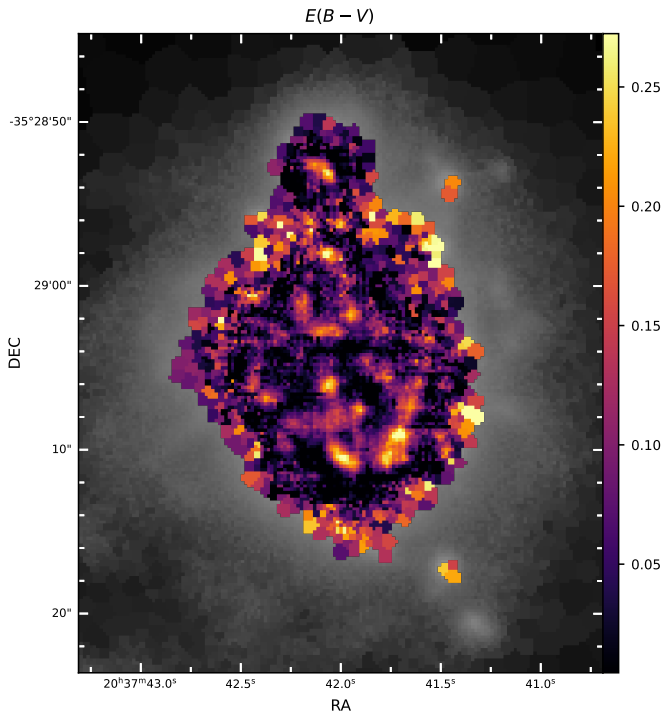

Fig. 2. Reddening map traced by the color excess $E(B-V)$ determined from the Balmer decrement. The binning pattern corresponds to Voronoi bins targeting a SNR = 25 in Hβ with a maximum of 20 spaxels per bin. The gray-scale background image corresponds to the Hα flux map.

law (Cardelli et al. 1989) with $R_V = 3.1$ and a theoretical Balmer decrement of $(\mathrm{H}\alpha/\mathrm{H}\beta)_{\mathrm{int}} = 2.863$, which corresponds to the case B recombination (i.e., a homogeneous dust screen model for an optically thick nebula) for an electron temperature and density of $T_e = 1 \times 10^4$ K and $N_e = 100\,\mathrm{cm}^{-3}$, respectively (Osterbrock & Ferland 2006). The color excess $E(B-V)$ is determined using the PYNEB Python package (Luridiana et al. 2015), where the fluxes of Hα and Hβ for each Voronoi bin are calculated by integrating the bin spectra in the ranges of 6556 – 6569 Å and 4855.5 – 4865.5 Å, respectively. The uncertainties on $E(B-V)$ are estimated by error propagation of the analytical expression:

$$\delta E(B-V) = \frac{1.086}{k(\lambda_{\mathrm{H}\beta}) - k(\lambda_{\mathrm{H}\alpha})} \sqrt{\left(\frac{\delta \mathrm{H}\alpha}{\mathrm{H}\alpha}\right)^2 + \left(\frac{\delta \mathrm{H}\beta}{\mathrm{H}\beta}\right)^2} \quad (3)$$

where the errors on Hα and Hβ flux estimates were calculated using the expression 2. In Fig. 2, we present the resulting extinction map. The errors calculated via equation 3 are observed to increase inside-out, ranging from relative errors of ∼2% in the innermost regions to ∼12% in the outskirts. The inner regions of the extinction map reveal compact areas with $A_V \approx 0.7$, which coincide with many bright clusters seen by HST, followed by regions where the extinction rapidly drops to zero.

3.4. Electron temperature and density

The electron temperature T_e can be determined using the emission line ratio between temperature-sensitive auroral and nebular transitions from the same ion species (Osterbrock & Ferland 2006). Some common line ratios used for T_e determination are [O III]$\lambda\lambda$4959, 5007/λ4363, [N II]$\lambda\lambda$6548, 83/λ5755, [S III]$\lambda\lambda$9069, 9532/λ6312, among others (Pérez-Montero 2017). The electron density N_e of a nebula, on the other hand, can be determined by doublets whose emission line ratios are sensitive to density variations across the density range typically spanned by nebulae (Osterbrock & Ferland 2006), with [S II]$\lambda\lambda$6716,31 as the most commonly used doublet.

In this work we employ PYNEB to estimate T_e and N_e in two independent steps. In the first step, we apply a Voronoi binning on the pure-gas cube targeting a SNR = 5 on the faint [S III]λ6312 line, allowing a maximum of 15 spaxels per bin. The continuum-subtracted spectrum of each bin is extracted, and at the NIR wavelengths, where a continuum modelling with pPXF was not performed, we merge the pure-gas spectrum with the median-filtered spectrum to include the [S III]λ9069 line. The de-reddened emission line fluxes of [S III]λ6312, [S II]$\lambda\lambda$6716,31 and [S III]λ9069 are obtained by integrating the spectra within 6308.5 – 6316.0 Å, 6710.5 – 6723.0 Å, 6726.0 – 6737.0 Å and 9064.0 – 9073.5 Å wavelength windows, respectively. The line ratios within this regions are used to determine T_e and N_e using the `getCrossTemDen` routine from PYNEB, which iteratively cross-converges the temperature and density values to obtain self-consistent results. Given that the complementary line [S III]λ9532 lies outside the spectral range covered by our MUSE observations, the theoretical collision strength I(9532 Å) = 2.44 × I(9069 Å) (Tayal & Gupta 1999) is assumed. In the second step, we extend our density estimates further out in the ISM of ESO 400-43, where measuring T_e is no longer possible due to the faintness of [S III]λ6312. In this case, the Voronoi binning is applied to the [S II]λ6731 line (the faintest of the doublet), targeting a SNR = 20 and allowing a maximum of 20 spaxels per bin. The process described above is repeated, but now the densities are estimated considering a fixed value of $T_e = 1.1 \times 10^4$ K.

3.5. Emission line maps

To map the ionization structure of the ISM in ESO 400-43 that is discussed in §4.5, we produce spatially resolved maps for the emission line ratios [O III]/[S II], [O III]/Hα and [N II]/Hα. The maps are produced from Voronoi binning patterns applied to the faintest line required for the calculation of each line ratio. The lines used for binning and the configuration of the binning patterns applied are listed on Table 2. For [N II]/Hα line ratio the transitions occur sufficiently close in the wavelength domain so that the reddening effects on the line ratio can be neglected, allowing the binning pattern to be applied directly to the pure-gas cubes. In contrast, for the [O III]/[S II] and [O III]/Hα line ratios, the binning pattern is applied to the reddening-corrected cube, produced using the methodology described in §3.3 and assuming $E(B-V) = 0$ in the outskirts where Hβ becomes too faint to provide reliable estimates of dust attenuation. In Table 2 we summarize the configurations of Voronoi binning patterns used in the sections §3.1 – §3.5.

3.6. Extraction of radial spectra

To estimate the mass of ionized gas in ESO 400-43 (see §4.3), we inspect the radial profiles of gas properties like T_e, N_e and L(Hα). To do this, we extract the mean spectrum from all spaxels in the pure-gas cube within a radius of 0.5″centered on the Hα emission peak. We repeat this extraction procedure using spatial masks that include only the spaxels within radial intervals of $[r; r+\Delta r]$ in steps of 0.5″. The extracted spectra are corrected for foreground Galactic extinction on-the-fly, and a reddening correction is performed following the techniques described in §3.3.

Table 2. Summary of the Voronoi binning patterns applied for each diagnostic, as indicated in the first column. The second and third columns list the ions and their corresponding lines used in each diagnostic. The bold lines represent the lines over which the binning pattern was applied, aiming for the SNR target described in the fourth column, estimated across the wavelength range specified in the sixth column. The fifth column shows the maximum physical area allowed for individual bins. The last two columns reference the figures and sections where the corresponding binning pattern is shown or used.

Diagnostic	Ions	Lines [Å]	$(SNR)_T$	Max. area (arcsec^2)	$\Delta\lambda$ [Å]	Figure	Section
Stellar continuum	–	–	150	2.4	5020.0 – 5060.0	–	§3.1
Kinematics of the ionised gas	H	**Hα**	10	400	6556.0 – 6566.0	5	§4.1
Extinction	H	Hα, **Hβ**	25	1.0	4855.5 – 4865.5	2	§3.3
Electron temperature	[S III]	**6312**, 9069	5	0.6	6308.5 – 6316.0	6	§3.4
Electron density	[S II]	6716, **6731**	20	0.8	6724.5 – 6736.0	6	§3.4
Ionization	[S II], [O III]	**6716+6731**, 5007	20	0.8	6709.0 – 6736.0	11	§3.5
	[O III], H	**5007**, Hα	10	16.0	5001.5 – 5010.5	11	§3.5
	[S II], H	**6716+6731**, Hα	20	0.8	6709.0 – 6736.0	11	§3.5
	[N II], H	**6548**, 6583, Hα	10	0.8	6543.0 – 6552.0	11	§3.5
BPT	[O III], H, [N II]	Hα, Hβ, 5007, **6583**	20	1.0	6577.5 – 6588.5	14,15	§4.7,4.8
	[O III], H, [S II]	Hα, Hβ, 5007, 6716, **6731**	20	1.0	6726.0 – 6735.0	14,15	§4.7,4.8
	[O III], H, [O I]	Hα, Hβ, 5007, **6300**	20	1.0	6294.5 – 6305.0	14,15	§4.7,4.8

As the radial annular layers move away from the center, larger portions of the sky are included in the apertures, increasing the background contribution to the mean radial spectra. Although a background subtraction was performed during the data reduction stage using separate sky exposures, apertures in empty regions of the FoV revealed a residual sky line at the exact position of [S II] λ6731 in the observed wavelength frame. If not treated, the intensity of this sky line can become of the order of [S II] λ6731 emission line itself in the outermost regions, artificially increasing the [S II] line ratio and hence the estimated electron density values. To mitigate this issue, we extract a representative sky spectrum from an empty corner of the pure-gas cube using the median of the spaxels within an aperture of radius 15 px (3.0″). This median sky spectrum is then subtracted from each individual spaxel within the annular apertures before calculating the mean radial spectra.

The effect of this residual sky line for increasing radii is illustrated in Fig. 3, where we plot the relative difference ($\equiv \sqrt{(f_1 - f_2)^2}/(f_1 + f_2)$) between the flux of [S II] λ6716 (blue line), [S II] λ6731 (black line), and the [S II] line ratio (gray dots) before and after subtracting the sky residual line. While the flux of [S II] λ6716 remains stable (with relative differences $\lesssim$2%) up to ∼8 kpc, the difference in the flux of [S II] λ6731 keeps rising until ∼6.5 kpc, where the annular apertures reach the northern star-forming region of ESO 400-43. At these locations, the signal is enhanced, and the contribution from the [S II] λ6731 emission line increases, but the sky residual rapidly dominates the integrated flux again, resulting in relative differences greater than 50% for $r > 8.0$ kpc. The radial contribution of this residual sky line on the [S II] line ratio used for density estimates approximately follows the radial behavior of the [S II] λ6731 flux. The red solid line highlights the threshold of 5% contribution from the sky residual line to the total flux.

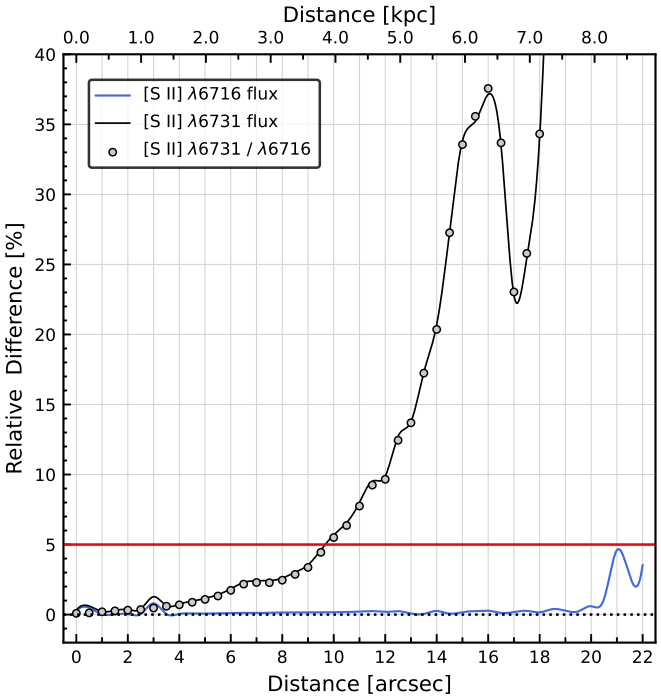

Fig. 3. Contribution from the sky residual line underlying the [S II] λ6731 emission line as a function of distance from the Hα emission peak. Radial spectra are extracted from the pure-gas cube using the mean of spaxels within concentric annuli spaced by 0.5″, with and without subtraction of a representative sky spectrum (see text). The flux of both [S II] emission lines is estimated for each spectrum in both cases, including their line ratio. The relative percentage difference is calculated as $L_{\rm diff} = \sqrt{(f_1 - f_2)^2}/(f_1 + f_2)$, with f_1 (f_2) as the quantities in the (un)subtracted spectra. While the flux of the [S II] λ6716 emission line (blue line) is basically unaffected by the background, for the [S II] λ6731 emission line (black line) and the the line ratio (gray dots), the background contribution increases for increasingly farther regions.

3.7. Star cluster extraction and photometry

In order to extract star cluster candidates, we start by performing a background subtraction on the HST F606W (V band) image with SExtractor (Bertin & Arnouts 1996; Barbary 2016) to enhance the detection of compact bright sources. We use a background mesh size of 28 pixels and allow the detection of sources with a minimum size of 5 contiguous pixels at least 4 times higher than the background RMS. The extraction results in a catalog of 805 sources that are visually inspected to minimize spurious detections and to include potentially blended or missed star clusters. After inspection, we estimate the centroid "center of mass" of each source within a square of 5 pixels width around each source and allow for a recentering of ≤1 pixel.

We perform aperture photometry on the candidate sources in all bands, using an aperture radius of 3 pixels. We estimate and subtract the local background using concentric annuli with inner and outer radii of 4 and 6 pixels, respectively. Given that some star clusters lie in bright crowded regions, we calculate the local sky level from the mode within the annular apertures to mitigate possible over-subtractions on the instrumental magnitude. The zero-point (ZP) AB magnitudes and aperture corrections up to 0.8″are calculated using the STSDAS STSYNPHOT Python package (STScI Development Team 2018) and are listed in Table 1. The error on the magnitude estimate is calculated as the sum in quadrature of the photometric error and an uncertainty of 0.05 mag on the ZP. For the final catalog, we impose a threshold of 0.4 mag in at least 3 broad bands for the magnitude error and perform a second visual inspection on a color-composite image to account for obvious detections that might have failed the minimum error criterion due to being located in crowded bright regions of the galaxy. The final catalogue contains 220 star clusters.

3.8. Star cluster SED fitting

With the photometry of the star clusters in one narrow band covering the observed-frame Hα emission (F665N) and four broad bands spanning the wavelength range from the NUV to NIR (F336W, F438W, F606W and F814W), we can model the Spectral Energy Distribution (SED) of each star cluster. For the SED fitting, we use the PROSPECTOR Python package (Johnson et al. 2021) with the Markov Chain Monte Carlo (MCMC) EMCEE sampler (Foreman-Mackey et al. 2013) to obtain the posterior distributions of the Flexible Stellar Population Synthesis (FSPS) models (Conroy et al. 2009; Conroy & Gunn 2010). To sample the posteriors, we employ 512 random walkers with burn-in steps of 16 and 32 walkers, supplemented by optimization of subsequent guesses given by a Levenberg-Marquardt least squares minimization. For the star formation history (SFH) model, we approximate the star clusters as Simple Stellar Populations (SSPs), i.e. a group of stars born at the same time and having the same initial element composition. We adopt a Chabrier (2003) stellar initial mass function (IMF) with 120 $M_\odot$ and 0.08 $M_\odot$ upper and lower mass cutoffs, respectively, and a Calzetti (2001) dust attenuation law.

In Table 3, we summarize the parameters included in our SED model, along with a brief description and whether they were kept free or fixed during the fit. Whenever a parameter is allowed to vary, a prior distribution and limiting values must be defined. For age and mass, we allowed uniform sampling within typical ranges spanned by young star clusters. For the optical depth τ_V, which is related to the dust attenuation, we use the statistics of the $E(B-V)$ values analyzed §3.3 to impose constraints on the prior distribution. Using information from previous analyses on the literature ($\bar{Z}_{\rm gas} = {}^1/_8\, Z_\odot$ Bergvall & Jorsater 1988; Bergvall & Östlin 2002), and preliminary results of gas-phase Oxygen abundances (Lassen et al., in prep.), we also imposed constraints on both the gas-phase metallicity, kept tied to $Z_\star$ during the fit, and the ionization parameter ($\log U$).

In Fig. 4, we present the SED fitting results for a single star cluster, the brightest one located in the region peaking in Hα emission as seen by MUSE. The upper panel shows the best-fit SED spectrum, with the estimated HST photometry in each band represented by the blue points, converted to flux density units. The transmission curves of the 5 filters are re-scaled and shown below the best-fit spectrum. The bottom panel presents

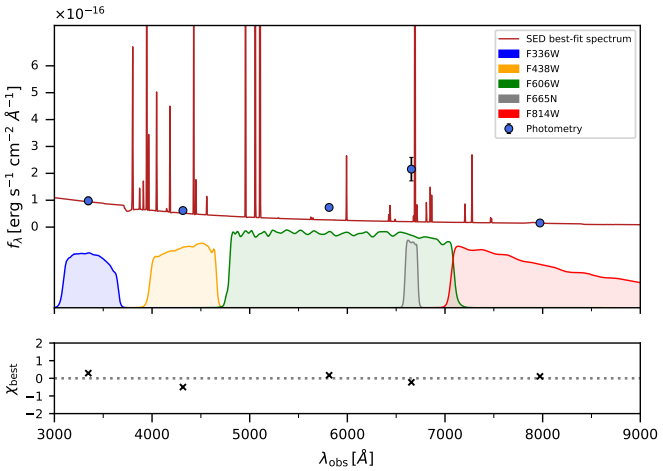

Fig. 4. SED best-fit spectrum (red line) for the cluster corresponding to the emission peaks of Hα and He II λ4686. Blue points represent the AB magnitudes derived from HST multiband photometry and converted to flux densities. The transmission curves of the HST filters used are presented below the spectrum, and the fitting residuals are presented in the bottom panel.

the best-fit residuals, where $\chi_{\rm best}$ is defined as the difference between the predicted and observed magnitudes, scaled to the estimated uncertainty of the observed values. The best-fit results for this cluster, including their uncertainties represented by the 84.1% and 15.9% distributions of the final chains of walkers, are listed in Table 4.

4. Results

In this section, we present the results of this work. In §4.1, we show the morphology of the ionized gas and maps of velocity and velocity dispersion. In §4.2, we present the distribution of electron temperature and density across the ISM of ESO 400-43, and in §4.3 we calculate the ionized gas mass. In §4.4, we show the properties of the star cluster population in the BCG. In §4.5 we map the ionization in ESO 400-43. From §4.6 to §4.8, we present the results regarding the presence of hard radiation field in ESO 400-43 and spatially resolved diagnostic diagrams to map the ionization mechanism.

4.1. Gas kinematics

In Figure 5 we present an Hα flux map (left panel) of ESO 400-43, showing that the ionized gas is detected almost across the entire 1 arcmin^2 MUSE FoV. A pronounced loop of low surface-brightness ionized gas is observed in the lower left corner of the FoV, extending towards its dwarf companion ESO 400-43*b*. This loop extends ~10 kpc in the southwest direction, within a previously reported low surface-brightness (μ_V ~28 mag arcsec^{-2}) optical bridge connecting the dwarf companions (Micheva et al. 2013). In the middle panel, we present the velocity map of Hα emission line, obtained through the following expression:

$$v_{\rm rot,H\alpha} = (v_{\rm obs,H\alpha} - v_{\rm sys})/\sin(i) \quad (4)$$

where i is the inclination angle, $v_{\rm sys}$ is the systemic velocity, and $v_{\rm obs,H\alpha}$ is the observed line profile velocity. The velocities in the middle panel were corrected for an inclination of $i \approx 55°$ (Östlin et al. 1999).

Table 3. Summary of SED fitting, including parameters kept fixed and free, their initial guesses and the adopted prior distributions and limits.

Parameter	Description	Free/Fixed (Ini. guess)	Prior
z	Redshift	Fixed (0.01965)	—
t	Age	Free (2.0 Myr)	Uniform: 1.0 Myr – 500.0 Myr
$\log(M_\star/M_\odot)$	Total stellar mass formed	Free (5.7)	Uniform: 3.7 − 6.7
$\log(Z_\star/Z_\odot)$	Stellar metallicity	Free (-0.5)	Clipped Normal: $\mu = -0.5$, $\sigma = 0.4$, min, max $= -1.0, 0.0$
$\tau_{\rm dust,V}$	Dust attenuation, represented by optical depth at the V band ($A_V = 1.086\,\tau_V$)	Free (0.3)	Clipped Normal: $\mu = 0.8$, $\sigma = 0.6$, min, max $= 0.0, 2.0$
$\log(Z_{\rm gas}/Z_\odot)$	Gas-phase metallicity	Tied to $Z_\star$	—
$\log U$	Ionisation parameter	Free (-2.6)	Uniform: -3.5 − -0.5
IMF	Initial Mass Function	Calzetti (2001)	—
SFH	Star Formation History model	Fixed (SSPs)	—

The velocity values span the range from +60 to -60 km s^{-1}, in fair agreement with previous velocity amplitudes derived using VLT/FORS2 long-slit spectroscopy (Östlin et al. 2004). While the left part of the galaxy is approaching the observer line-of-sight, a smaller central part is receding. In the central regions of the BCG, two structures intriguingly resemble a spinning pattern. The Hα line profile is narrower in the inner regions of ESO 400-43, with values ranging from 10 to 50 km s^{-1}. On the other hand, on the left side of the galaxy σ(Hα) reaches $\gtrsim 100$ km s^{-1}, where skewed and broader line profiles can be observed, indicating the presence of complex gas kinematics possibly driven by outflows.

4.2. Mapping T_e and N_e across the ISM of ESO 400-43

In Fig. 6 we present the maps of T_e (right panel) and N_e (left panel) for ESO 400-43. From the 4486 bins where a density value was estimated, 140 bins (∼3%) presented emission line ratios [S II] $I(6731/6716) \lesssim 0.68$, corresponding to the regime of low densities where [S II]$\lambda\lambda$6716,31 is no longer sensitive to density variations (Osterbrock & Ferland 2006). None of those bins are located in regions with SNR([S III] λ6312) > 5, being mostly located near the edges of the Voronoi binning pattern. To handle these spaxels in the N_e map, we perform a 2D Gaussian smoothing of the original N_e map to interpolate the problematic spaxels with valid neighbors. The interpolated values are then replaced at their corresponding locations to produce the map shown in the left panel of Fig. 6. This map reveals the inner structure of the galaxy, with density increases corresponding to the locations of the star clusters and with a density peak of $N_e \sim 300$ cm^{-3} in the bottom region of ESO400-43, which also corresponds to the peak of Hα emission.

As we approach the edges of the density map, one would expect a smooth decrease in density values. Instead, a noisy pattern is observed. Although the Voronoi tessellation method provides bin spectra with sufficiently high SNR to calculate consistent density values, the binning pattern for the production of N_e map was performed over the [S II] λ6731 emission line, the faintest of the [S II] doublet. This line is contaminated with a residual sky line (§3.6), thus in the outermost regions, its signal is artificially boosted, leading to the inclusion of noisy bins among the final Voronoi binning pattern. A significant improvement is observed in the density map after applying the sky subtraction detailed in §3.6, nonetheless an erratic pattern of density values is still observed at the edges, possibly caused by local background variations and/or noisy bins.

The median electron density across the galaxy is $N_e = 91^{+83}_{-52}$ cm^{-3}, where the errors represent the difference between the mean and the 84.1% and 15.9% quartiles of the density distribution. The electron temperature T_e reaches $\sim 1.1 \times 10^4$ K at the density peak, decreasing to 900 K in the eastern region of the galaxy. In the northern region, the temperature is systematically higher than in the rest of the galaxy, with $T_e > 1.2 \times 10^4$ K. The mean temperature across the regions highlighted in the right panel of Fig. 6 is $T_e = (1.1 \pm 0.1) \times 10^4$, whereas the mean temperatures in the "bulk" of the galaxy and on the northern region are $T_e = (1.1 \pm 0.1) \times 10^4$ and $T_e = (1.3 \pm 0.1) \times 10^4$, respectively.

4.3. Ionized gas mass

To estimate the mass of ionized gas in ESO 400-43, we use the radial spectra whose extraction procedure is detailed in §3.6. For each radial spectrum, we calculate the emission line fluxes of Hα, Hβ, [S III] $\lambda\lambda$6312,9069 and [S II] $\lambda\lambda$6716,31, which are corrected for dust attenuation using the Balmer decrement. These fluxes are used to produce the radial profiles presented in Fig. 7.

The values of F(Hα) are obtained by integrating over the wavelength range corresponding to the emission line, where the values in the upper panel of Fig. 7 correspond to the mean flux within each annular aperture. The flux drops almost monotonically, except for a bump around 7 kpc corresponding to the northern structure of ESO 400-43 (see Figs. 1 and 5). To mitigate possible effects of sky contamination in the nearby continuum of the [S II] $\lambda\lambda$6716,31 and [S III] λ9069 emission lines, we fit single 1D Gaussian components to these lines with IFSCUBE, including [S III] λ6312. The radial profiles of T_e and N_e presented in the second and third panels of Fig. 7, respectively, were obtained self-consistently using the procedure described in §3.4. Only temperature estimates for spectra with SNR([S III] λ6312) > 5 and SNR([S II] λ6731) > 5 are included. For spectra without temperature estimates, the density is calculated at a fixed temperature of 1.1×10^4 K. The uncertainties in the line fluxes obtained via Gaussian fitting were estimated through 500 MCMC iterations using the expression from Lenz & Ayres (1992) and Wesson (2016).

The yellow triangles in the third panel correspond to spectra with a contribution of >5% from the sky residual line. Even after the background subtraction highlighted in §3.6, these values still present increasingly larger density values for increasingly higher distances from the Hα emission peak. This could not be explained by the [S II] line ratios possibly falling below the density-sensibility threshold: The bottom panel of Fig. 7 also presents the radial profiles of the [S II] line ratios, highlighting the sensitivity threshold with the red dotted line. In the calculation of the ionized gas mass, we assume that for $r \geqslant 10''$(4 kpc) the density values obtained are unreliable, and thus $N_e = 10$ cm^{-3} is adopted

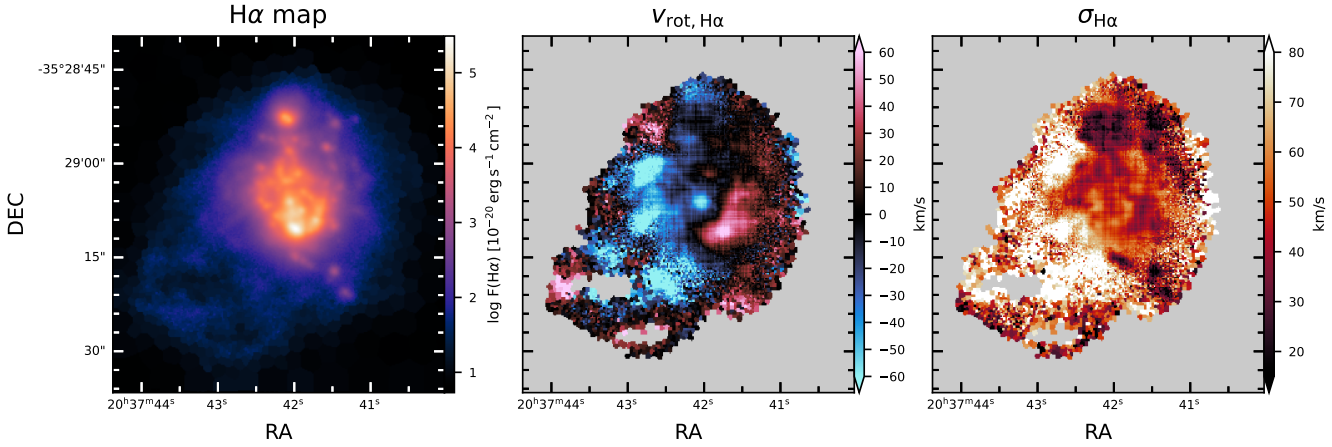

Fig. 5. Morphology and kinematics of the ionised gas in ESO 400-43. The maps were obtained from a Voronoi binning applied over the Hα emission line aiming a SNR = 10.*Left panel*: Hα flux map, where a loop of low surface brightness ionised gas extending towards the direction of the dwarf companion ESO 400-43*b* is observed. *Middle panel*: Velocity map for the ionised gas, showing the presence of a spinning structure in the center of the galaxy, as well as a large portion of emitting gas moving in the direction of the observer line-of-sight in the west and south-west regions. *Right panel*: Velocity dispersion map of the ionised gas traced by $\sigma_{\rm H\alpha}$. The values presented are corrected for the spectrograph instrumental broadening and were obtained considering a single Gaussian component.

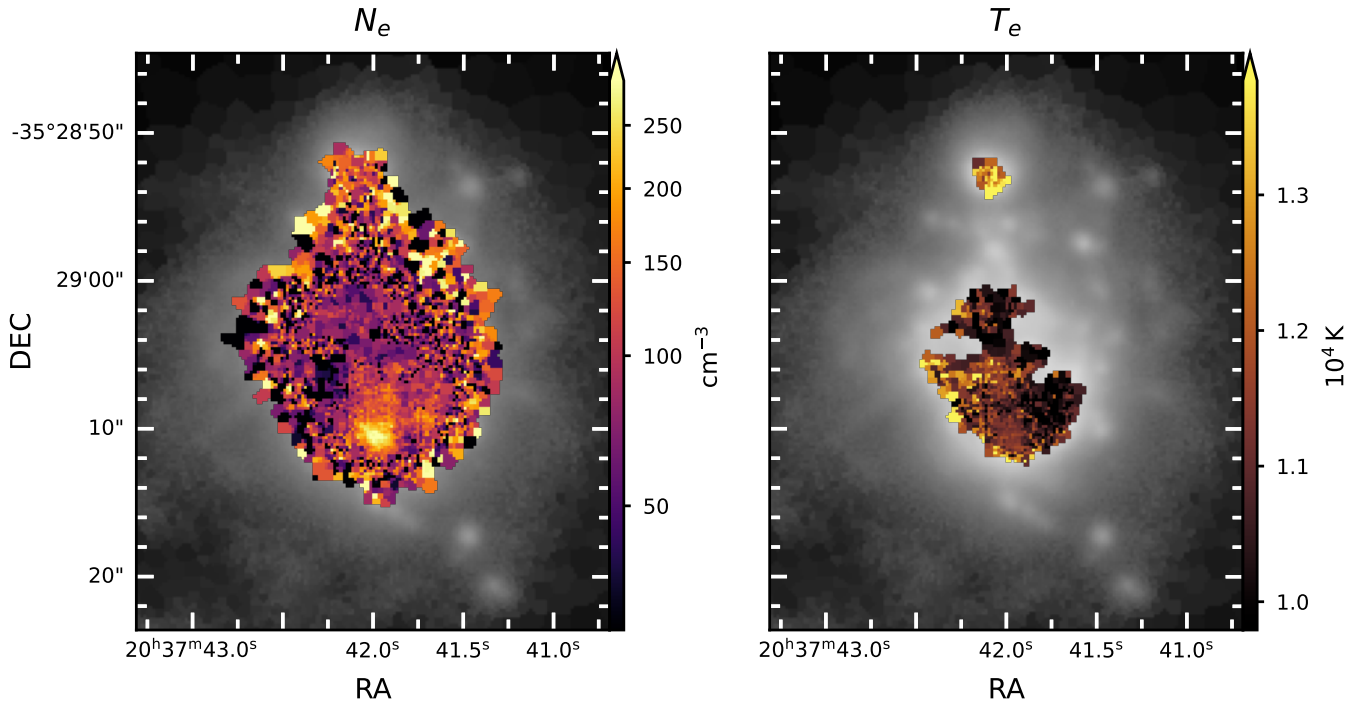

Fig. 6. Spatially resolved maps of electron density (left panel) and temperature (right panel) obtained with PYNEB. The former is obtained in a Voronoi binning map over [S II] λ6731 targeting a SNR = 20, whereas the latter is obtained in a Voronoi binning map over [S III] λ6312 targeting a SNR = 5. Bins with more than 20 and 15 spaxels per bin, respectively, are masked.

in this regime. The mass of ionised gas is calculated using the expression:

$$M_{\rm H\,II} = \frac{\mu\, m_{\rm H}}{h\, \nu_{\rm H\alpha}\, \alpha^{\rm eff}_{\rm H\alpha}} \times \frac{L_{\rm H\alpha,0}}{N_e} \quad (5)$$

where μ is the Hydrogen atomic weight (which we assume to be 1.0), $m_{\rm H}$ is the Hydrogen mass, h is the Planck constant, $\nu_{\rm H\alpha}$ is the frequency of the photons produced in the Hα transition, and $\alpha^{\rm eff}_{\rm H\alpha}$ is the Hα recombination coefficient assuming the case B recombination. For a temperature of $T_e = 1.1 \times 10^4$ K, $\alpha^{\rm eff}_{\rm H\alpha} = 1.069 \times 10^{-13}$ cm^{3}s^{-1} (Pequignot et al. 1991). For the estimate of the de-reddened $L_{\rm H\alpha,0}$, we assume a WMAP9 cosmology (Planck Collaboration et al. 2014) and use the radial flux of Hα shown in Fig. 7 multiplied by the area of the corresponding annuli. The total mass of ionized gas is calculated by summing the masses obtained from applying equation 5 consecutively in radial steps of 0.5″.

Under these assumptions, we obtain a value of $M_{\rm H\,II} = (4.011 \pm 0.007) \times 10^7\, M_\odot$ for the total ionized gas mass in

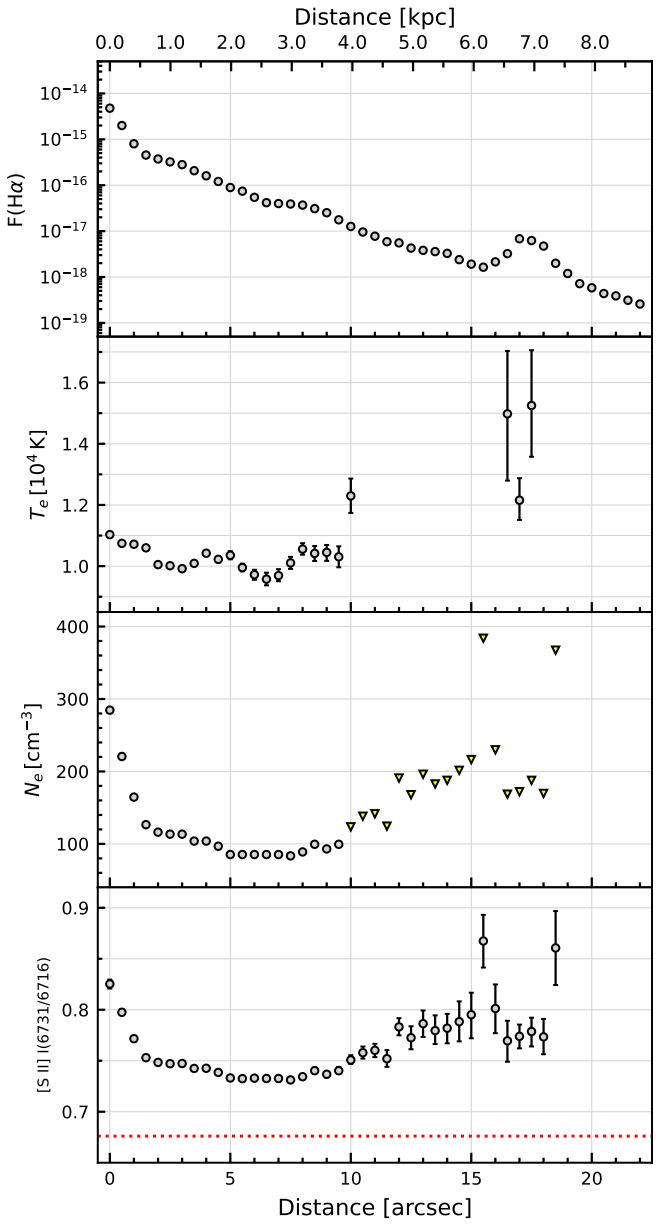

Fig. 7. Radial profiles in ESO 400-43, built from the mean of spaxels within concentric annuli spaced by 0.5″, centered at the Hα emission peak. The F(Hα) (upper panel) is obtained by integrating under the Hα emission line for the extracted mean radial spectra. Electron temperature and density are shown in the second and third panels, respectively, and were obtained through the techniques described in §3.4. Only estimates with SNR([S III] λ6312) > 5 and SNR([S II] λ6731) > 5 are shown. In the density profile, yellow triangles correspond to locations where a sky residual line underlying [S II] λ6731 contributes more than 5% to the [S II] line ratio shown in the bottom panel. The red dotted line corresponds to the low-density regime for which the [S II] line ratio becomes insensitive to density variations.

ESO 400-43. It is challenging to determine the real density uncertainties due to the aforementioned reasons, so the reported uncertainties on $M_{\rm H\,II}$ reflect the error propagation from the uncertainties of the redshift and F(Hα), representing a lower limit for the true uncertainty. Our estimate is about one order of magnitude lower than the $M_{\rm H\,II} = 5.5 \times 10^8\,M_\odot$ value reported by Östlin et al. (1999), however they adopted a fixed value of $N_e = 10\,{\rm cm}^{-3}$ and thus provided an upper limit for the ionized gas mass. Similarly, our estimate can be considered an upper limit since we use $N_e = 10\,{\rm cm}^{-3}$ for $r \geqslant 4$ kpc, while the density radial profile in Fig. 7 suggests the decline is smoother. Additionally, discrepancies between our estimated values could be also partially attributed to the derived values of F(Hα). Using Fabry-Perot interferometry with narrow-band interference filters Östlin et al. (1999) estimates $F(\mathrm{H}\alpha) = (2.4 \pm 0.7) \times 10^{-15}\,\mathrm{W/m^2}$, whereas our estimate results in $F(\mathrm{H}\alpha) = (1.061 \pm 0.001) \times 10^{-15}\,\mathrm{W/m^2}$.

4.4. Star cluster demographics

In this section, we present an overview of the star cluster properties across ESO 400-43 using the SED fitting results discussed in §3.8. The star cluster with the best-fit SED presented in Fig. 4 (Star cluster A hereafter) is both massive ($M_\star > 10^5\,M_\odot$) and very young ($t < 5$ Myr). In such massive and young star clusters, significant numbers of high-mass stars in advanced stellar evolutionary phases might be present. However, WR stars are often challenging to detect due to, for instance, continuum dilution that can mask He II emission (Buckalew et al. 2005; Bibby & Crowther 2010). This issue does not apply to the region where Star Cluster A is located, as discussed further in §4.6.

In Fig. 8 we present a gray-scale V band image of ESO 400-43 with the position of the star clusters overlaid. The clusters are color-coded according to age bins: Blue for clusters with $t \leqslant 5$ Myr, yellow for clusters with 5 Myr < t < 15 Myr and red for $t \geqslant 15$ Myr. Symbols indicate cluster masses: Circles are used for $M/M_\odot \leqslant 10^5$ and triangles for $M/M_\odot > 10^5$. This scheme reveals a higher distribution of young clusters in the bottom region and on the structure located to the right of Hα emission peak. Moving upward, older and intermediate-age star clusters start to dominate the distribution, although a few young star clusters are still observed. In the northernmost structure of the BCG, young star clusters are prevalent, consistent with the ionized gas morphology shown in Fig. 5. The concentration of star clusters decreases in the western regions, and the few star clusters observed are mainly old. The underlying white contours represent the He II λ 4686 emission levels (see §4.6 for contour definition). The contours show that regions with higher He II λ 4686 emission coincide with several young and massive star clusters, particularly at the peak of He II λ 4686, suggesting the presence of WR star clusters.

To explore the properties of individual star clusters and relate them to the gas properties derived from the IFU analysis, we select 6 star clusters shown in color-composite zoomed-in images in the right panel of Fig. 8. The black circles represent the 3 px apertures used to estimate the photometry, and the red dashed circles represent the inner and outer concentric annuli used for local background estimation. The white dashed aperture corresponds to the 0.85″MUSE PSF, over which we integrate to obtain the spectra for correlating with gas properties at the corresponding regions in the following sections. The regions are identified alphabetically, and their location within the galaxy is shown in the left panel of Fig. 8. Below we list the criteria adopted to select these regions:

- **A:** Brightest cluster in the region corresponding to the peak of He II λ 4686.
- **B:** Brightest cluster in the SF region located nearby cluster A. Also exhibits considerable He II λ 4686 emission levels.
- **C:** Brightest cluster in the northern structure of the BCD.
- **D:** Brightest star cluster located nearby the central spinning structure observed in v(Hα).

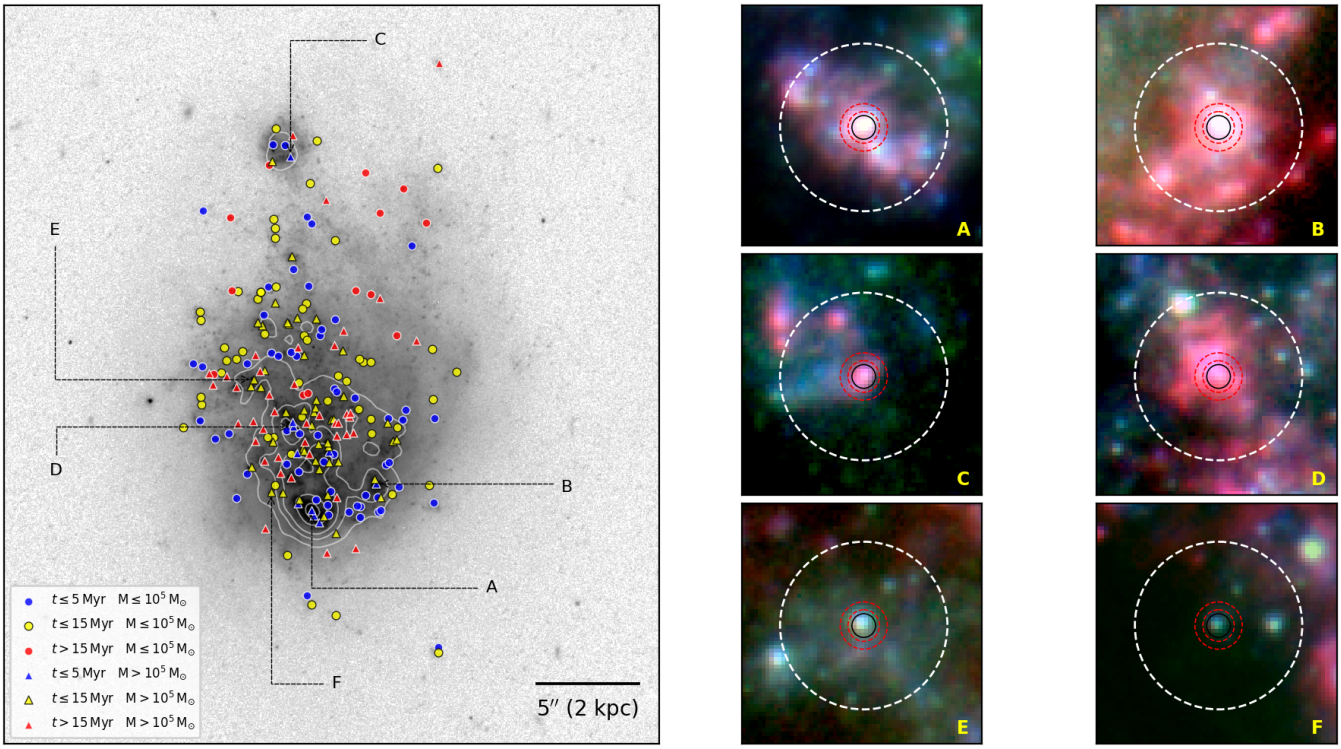

Fig. 8. *Left panel*: The 220 star cluster population overlaid in the grayscale V band image of ESO 400-43 used for extraction. The clusters are colour-coded according to bins of age, and the symbols (circle or triangles) represent bins of mass. The underlying contours represent the He II λ4686 emission, measured with MUSE (see §4.6). *Right panels*: Zoom-in colour-composite HST images of 6 star clusters selected for a closer inspection (see text). Their location in ESO 400-43 is highlighted by the labels in the left panel. The black and red circles represent the aperture used to estimate the photometry and the annuli used to estimate the local background, respectively. The white dashed circles represent the aperture with the MUSE PSF size used to extract approximated spectra of the 6 star clusters.

– **E:** Bright and massive intermediate-age star cluster located more distant from the emission peak, in a region with low signal of [S III] λ6312.
– **F:** Bright cluster located in the compact region of high [N II]/Hα shown in Fig. 11.

In Fig. 9 we present the age-mass diagram for the 220 star clusters analyzed. Recent bursts of star formation are indicated by regions of higher cluster density in the age-mass diagram, and from Fig. 9 at least 3 recent SF episodes at $t \approx 4$ Myr, $t \approx 10$ Myr and $t \approx 20$ Myr can be inferred. Several $M/M_\odot > 10^5$ star clusters are observed, with the high-mass end of the distribution being $M/M_\odot \approx 6.7 \times 10^6$. The selected clusters are marked in Fig. 9 as blue diamonds to highlight their positions in the diagram. Clusters A, B, C and F are part of the most recent burst, while clusters E and D were formed ~10 Myr ago.

In Table 4 we list the SED best-fit values obtained for the 6 selected clusters, where the reported uncertainties are estimated from the 84.1% and 15.9% quartiles of each parameter MCMC chain. The spectral properties reported in the table were obtained by applying the techniques described in §3.3 and §3.4 to the MUSE spectra integrated over an aperture with the size of the MUSE PSF (For a comparison of the size of the MUSE PSF with the size of the clusters, we refer to Fig. 8). The uncertainties on the spectral properties were determined using 500 MCMC iterations based on normal distributions over the emission line fluxes used. For the Star Formation Rate (SFR) estimate, we have applied the calibration from Kennicutt (1998) assuming a Chabrier (2003) IMF:

$$\log(\mathrm{SFR}\,[\mathrm{M_\odot\,yr^{-1}}]) = -41.34 + \log(\mathrm{L(H}\alpha)\,[\mathrm{erg\,s^{-1}}]) \quad (6)$$

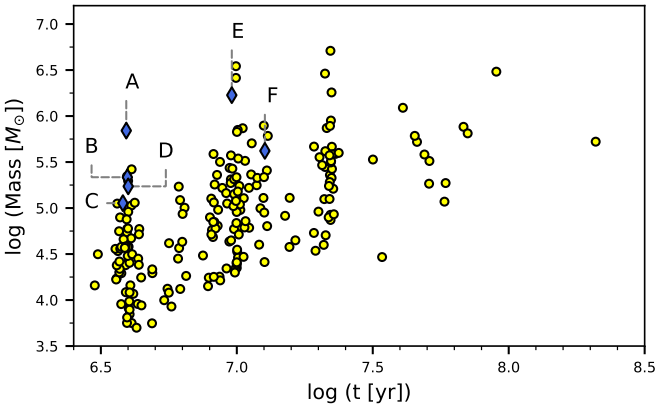

Fig. 9. Age-mass diagram for the star cluster population (yellow points). The 6 selected clusters are plot as blue diamonds and are indicated by the labels.

where we have estimated a luminosity distance of $d_L \approx 85$ Mpc, considering the aforementioned redshift of $z = 0.01965$ and a WMAP9 cosmology (Planck Collaboration et al. 2014) and used the de-reddened flux of Hα to calculate (L(Hα). We stress that the calibration from equation 6 represents an upper limit for the SFR in ESO 400-43, given that the Kennicutt (1998) calibration assumes Solar abundance, and re-calibrations for lower metallicities translate into small subtractions of the estimated SFR (Ly et al. 2016).

In Fig. 10 we show histograms for the derived SED best-fit values of age, mass, metallicity and color excess. For the two lat-

Table 4. SED best-fit properties and spectral properties of clusters

Cluster label	SED best-fit properties					Spectral properties			
	t [Myr]	$\log(M/M_\odot)$	$E(B-V)$	$Z/Z_\odot$	$\log U$	$E(B-V)$	N_e [cm^{-3}]	T_e [$\times 10^4$ K]	SFR [$M_\odot$ yr^{-1}]
A	$3.9^{+0.4}_{-1.7}$	$5.800^{+0.002}_{-0.003}$	$0.22^{+0.06}_{-0.02}$	$0.22^{+0.27}_{-0.07}$	$-1.0^{+0.7}_{-0.8}$	0.1792 ± 0.0008	261 ± 5	1.150 ± 0.003	0.864 ± 0.002
B	$3.9^{+0.3}_{-0.1}$	$5.280^{+0.004}_{-0.001}$	$0.16^{+0.05}_{-0.05}$	$0.4^{+0.4}_{-0.1}$	$-2.63^{+0.30}_{-0.04}$	0.191 ± 0.001	147 ± 7	1.002 ± 0.006	0.2443 ± 0.0007
C	$5.0^{+1.1}_{-0.4}$	$5.533^{+0.001}_{-0.002}$	$0.48^{+0.11}_{-0.04}$	$0.122^{+0.076}_{-0.009}$	$-2.5^{+0.0}_{-0.6}$	0.141 ± 0.002	151 ± 11	1.33 ± 0.01	0.0731 ± 0.0003
D	$4.0^{+0.3}_{-1.2}$	$4.733^{+0.015}_{-0.009}$	$0.00^{+0.03}_{-0.00}$	$0.3^{+0.2}_{-0.1}$	$-3.0^{+0.4}_{-0.4}$	0.142 ± 0.001	99 ± 7	1.206 ± 0.008	0.2214 ± 0.0006
E	$6.5^{+0.5}_{-0.4}$	$5.535^{+0.001}_{-0.001}$	$0.0^{+0.1}_{-0.0}$	$0.6^{+0.2}_{-0.2}$	$-2.49^{+0.13}_{-0.09}$	0.029 ± 0.002	85 ± 13	1.00 ± 0.03	0.0340 ± 0.0002
F	13.0^{+1}_{-4}	$5.533^{+0.001}_{-0.003}$	$0.08^{+0.14}_{-0.02}$	$0.6^{+0.3}_{-0.2}$	$-2.34^{+0.05}_{-0.39}$	0.035 ± 0.001	119 ± 9	1.13 ± 0.01	0.0963 ± 0.0003

ter properties, we also present the distribution of values considering the bins of age presented in Fig. 8 overlaid as blue, yellow and red histograms. The values of age used to determine each bin are shown in the top left histogram as dashed vertical green lines. 30% of the clusters have ages below 5 Myr, 45% have ages below 15 Myr but above 5 Myr, and, from the remaining 25% clusters older than 15 Myr, only 15% have ages higher than 50 Myr. The peak of the age distribution occurs at $t \sim 10$ Myr. In the case of the mass, 60% of the clusters lie in the mass interval $4.4 \leqslant \log(M/M_\odot) \leqslant 5.5$, with only 8 clusters (< 4%) more massive than $10^6\ M_\odot$. For the metallicity, more than 90% of the sample presents metallicities below $0.4\ Z_\odot$. Considering the bins of age, the intermediate-age category is the one presenting the highest occurrence of clusters with $Z/Z_\odot > 1/3$, followed by the young and old: 25%, 13% and 7%, respectively.

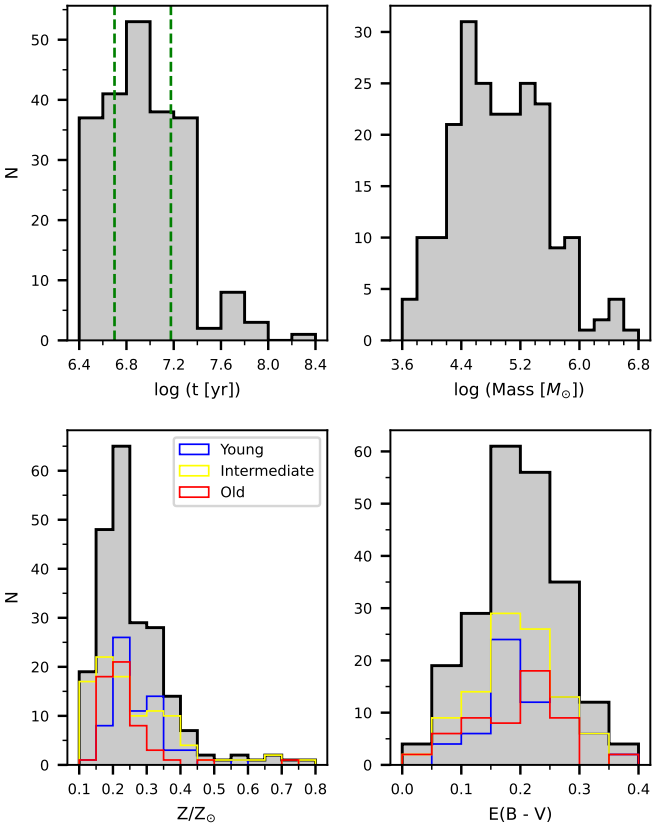

Fig. 10. Histograms for the distribution of SED best-fit parameters among the star cluster population. In the age histogram the vertical green dashed lines indicate the values of $t = 5$ Myr and $t = 15$ Myr used for the age bins. In the histograms of metallicity and reddening (bottom left and right panels) the histograms in bins of age are presented together with the full sample.

4.5. Mapping the ISM ionization state

In the emission-line maps [O III]/[S II], [O III]/Hα and Hα/[S II], bright compact structures with a high ionization degree become visible, corresponding to the positions of the brightest star clusters and thus indicating the ionized gas surrounding the young star clusters in ESO 400-43. In all three maps, the highest line ratios are located at the bottom region of the galaxy, coinciding with the peak of Hα emission (see Fig. 1). At this position, the line ratios reach levels approximately 6× higher than those in the ionized gas seen in [O III]/[S II] and Hα/[S II]. The strongest emission lines across the ISM of ESO 400-43 are Hα and [O III] λ5007, which allow us to probe the ionization degree further out and partially cover the low surface brightness ionized gas loop located at the southwest corner of the galaxy. The ionization decreases as we move away from central regions, with [O III]/H$\alpha < 0.75$ in the gas loop, while [O III]/H$\alpha > 1$ in the inner regions of the BCG. This trend is expected, given that O^{2+} requires more energetic photons for ionization compared to H^+, and as we move outward, we are also moving away from the ionizing sources (star clusters).

Using photoionization models to map the nebulae ionization structure with the optical depth in the Magellanic Clouds, Pellegrini et al. (2012) shows that high levels of [O III]/[S II] are correlated with optically thin nebular conditions, where the density-bounded condition favours the escape of Lyman Continuum (LyC) photons. Furthermore, observations of $z \lesssim 0.3$ LyC Emitters (LCEs) correlate the deficiency of [S II] in comparison to regular star-forming galaxies with LyC leakage (Wang et al. 2021). Given the lower ionization potential of S^+ compared to H^+, the [S II] emission arises slightly beyond the Strömgren sphere that defines a classical H II region and is suppressed in the presence of LyC leakage (Rivera-Thorsen et al. 2017; Wang et al. 2021; Komarova et al. 2024). As we move outwards in the ISM of ESO 400-43, the mean-free path of the ionizing photons increases and the nebulae become optically thick to the LyC photons (ionization bounded), when both [O III]/[S II] and Hα/[S II] decrease (Bik et al. 2018).

The map of [N II]/Hα is smaller in comparison to the other maps since [N II] λ6548 is fainter. In this map, it is also possible to observe two compact regions with [N II]/H$\alpha \lesssim 0.08$ that coincide with the position of high-ionization regions in the other maps. The northern structure of the galaxy also presents low values of [N II]/Hα, but it is more extended in comparison to the compact structures tracing the presence of the star clusters, sim-

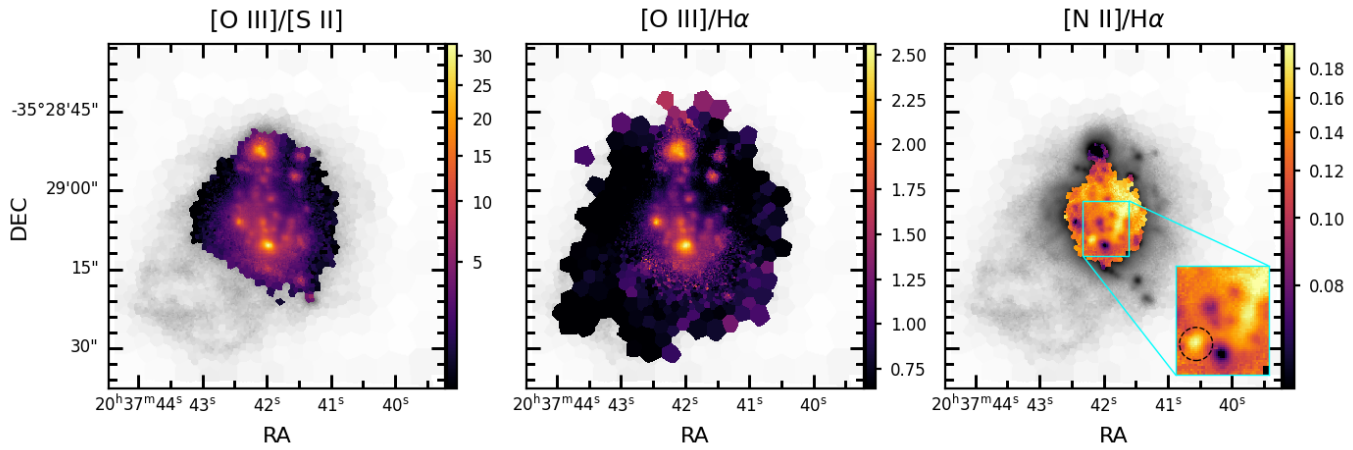

Fig. 11. Emission line maps of ESO 400-43, obtained via Voronoi binning patterns applied on the faintest line involved in line-ratio calculation. The maps show the entire MUSE FoV. *Left*: Map of [O III] λ5007 / [S II] $\lambda\lambda$6716,31, tracing the thickness of the nebulae for the escape of LyC photons. *Middle*: Map of [O III] λ5007 / Hα tracing the degree of ionisation in the BCD, which extends to the low-surface brightness loop of ionised gas. *Right*: [N II] $\lambda\lambda$6548,83 / Hα, tracing the N-enrichment in the ISM of the BCD. The zoom-in plot shows the region with the peak of Hα emission, highlighting the presence of a compact structure with high values of [N II] /Hα.

ilarly to what is observed in the other maps. The decrease of [N II]/Hα in the star-forming regions is consistent with ionization from UV photons produced by massive stars (Veilleux & Osterbrock 1987; Stasińska et al. 2006), and as the distance from the ionizing sources increases, this line ratio is expected to increase. Intriguingly, an extended region of [N II]/H$\alpha > 0.15$ is observed in the north-east region of the galaxy, as well as a compact region of [N II]/H$\alpha > 0.15$ located between the two aforementioned regions, tracing a pocket of N-enriched gas.

4.6. Inspecting He II λ4686 emission in ESO 400-43

To produce doubly ionized He atoms, very energetic photons ($h\nu \geqslant 54.4$ eV) are required, four times the energy needed to ionise an atom of Hydrogen. Therefore, transitions of He^+ are often used to trace the presence of hard radiation fields typically produced by sources like an Active Galactic Nucleus (AGN) (Tozzi et al. 2023) or Wolf-Rayet (WR) and Of-type stars (Schaerer 1996; Bergeron et al. 1997; Schaerer & Stasińska 1999; Brinchmann et al. 2008). Although this is the case of many dwarf galaxies in which the nebular emission line He II λ4686 is observed, the lack of WR features in several He II-emitting BCDs has also led to the proposition of fast radiative shocks as a possible responsible for this transition (e.g., Thuan & Izotov 2005; Kehrig et al. 2008; Herenz et al. 2017; Plat et al. 2019).

To inspect the hard ionisation field across ESO 400-43, we show the emission line map of the nebular He II λ4686 in Fig. 12, which is the strongest transition of the ion He^+ in the optical. The flux map is created by integrating the pure-gas datacube over the wavelength range of 4683 – 4689 Å. We smooth the spatially resolved flux map using the Integrated Nested Laplace Approximation (INLA[3], Rue et al. 2009) method, which takes into account spatial correlations between adjacent spaxels by using the inverse of the variance for weighting. For previous works using INLA to smooth astronomical images and spatially resolved maps, we refer to González-Gaitán et al. (2019) and Azevedo et al. (2023).

From Fig. 12 it is possible to observe significant emission of the nebular He II λ4686 in several locations, reaching a peak of $\sim 6\times10^{-18}$ ergs^{-1}cm^{-2} in the region corresponding to star cluster A. The contours, which are the same contours shown in Fig. 8, represent the mean He II λ4686 flux across the FoV (thus nearly the background level) + 3,5,10,15 and 20 times the background standard deviation. Combining this information from the IFU data with the star clusters SED fitting results shown in Fig. 8, it is possible to see that the intensity of He II emission increases in locations with a higher density of young and massive star clusters. The inset plot presents a zoom-in of the region peaking in He II emission and its surroundings. The black circle indicates the position of the PSF-sized aperture used to extract the spectrum of region A, which is also shown in Fig. 8.

Given that this spectrum encloses the peak of He II emission, we can use it to search for WR signatures. The most prominent WR signatures in the optical spectrum of star-forming regions are the broad emission features arising in the continuum around λ4686 Å and λ5808Å , known as the blue and red bumps, respectively. The former is a blend of emission lines from He II, N III and C III λ4650 in the case of Carbon rich WR stars (WC stars), which are broadened due to the strong stellar winds in WR stars (Liang et al. 2020). These lines are often faint, with the broad He II emission remaining as the most common signature for the presence of WR stars. The red bump is fainter, produced by the broad emission of C IV $\lambda\lambda$5801,12 from WC stars (Smith et al. 2016). In Fig. 13 we present the spectrum of the region around cluster A in a wavelength window around He II, where a broad feature underlying the nebular He II λ4686 emission is clearly observed. We use IFSCUBE to fit single Gaussians to the emission line profiles, except for He II λ4686, for which we adopt one narrow and one broad component. The individual components are presented in Fig. 13 as blue dashed lines, and the model spectrum is shown by the red solid line. The bottom panel presents the residuals of the fit. We find velocities of 111 ± 5 km s^{-1} and 131 ± 25 km s^{-1}, and velocity dispersions of 96 ± 4 km s^{-1} and 720 ± 35 km s^{-1} for the narrow and broad components, respectively. For the error estimate, we run the fit using 500 MCMC iterations.

[3] https://www.r-inla.org/home

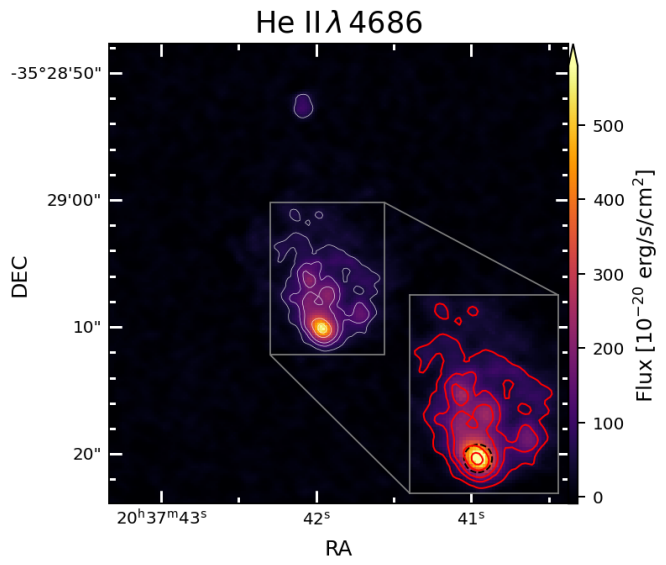

Fig. 12. Map of the nebular He II λ4686 emission line, obtained via integration in the wavelength range 4683 – 4689 Å across the pure-gas cube. The map is smoothed taking into account the flux correlation between neighbouring spaxels weighted by 1 / σ(He II λ4686) with the INLA R-package. The contours represent the background level + (3, 5, 10, 15, 20) × σ. The inset plot presents a zoom-in of ESO 400-43, where the black circle is the aperture with the size of the MUSE PSF centred in the position of star cluster A.

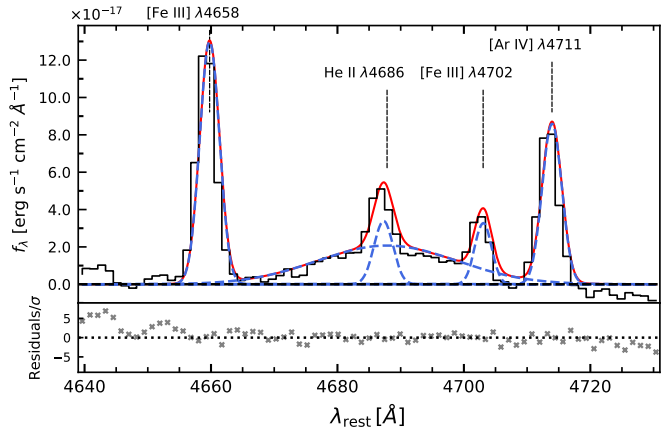

Fig. 13. Emission-line fitting of the spectrum corresponding to star cluster A in a wavelength window around He II λ4686. Besides the Fe^{+2} and Ar^{+3} lines indicated by the labels, a broad bump centred in λ = 4686 Å is observed and fitted, indicating the presence of WR stars in the location corresponding to the peak of He II λ4686 emission.

4.7. Emission line diagnostic diagrams

To investigate the sources of ionization in the ISM of ESO 400-43, we use the derived optical emission line fluxes in the BPT diagnostic diagrams (Baldwin et al. 1981; Veilleux & Osterbrock 1987). The locus occupied by each emission-line ratio in the BPT diagram results from the combination of several parameters that affect the ionization like gas-phase metallicity, electron density and hardness of the radiation field (Kewley et al. 2006; Stasińska et al. 2006; Cid Fernandes et al. 2011; Bik et al. 2018), and reflect the shape of the ionizing source SED. In this section, we present three different diagnostic diagrams ([N II], [S II], [O I]), and the procedure used to construct them is described below.

Meanwhile in all the diagrams the y-axis corresponds to the emission line ratio between [O III] $I(\lambda4959 + \lambda5007)$ and Hβ, the line ratios used in the x-axis vary between each diagram. We start by applying a Voronoi binning with the WVT adaptation over the pure-gas cube, aiming for a minimum SNR on the faintest emission line of each line ratio (We refer to Table 2 for details of the Voronoi binning patterns adopted for each diagram). The line fluxes are calculated by integrating over small wavelength windows around each line, which are used to calculate the line ratios. No reddening correction is performed, given that, by construction, the emission lines used in all the diagnostic diagrams are close enough in the spectral dimension, so that reddening effects can be neglected. We present the BPT diagrams in Fig. 14, where each point represents the line ratios calculated for a given bin. The bins are color-coded according to their Hα surface brightness (total Hα flux divided by their physical area).

We also present the delimiting lines from Kewley et al. (2001, black solid line), Kauffmann et al. (2003, black dashed line) and Stasińska et al. (2006, black dotted line). The Kewley et al. (2001) line was defined as the upper boundary in the diagnostic diagrams, provided by an extensive grid of photoionization models of H II regions with young star clusters as the ionizing sources, so regular star-forming regions cannot produce emission-line ratios above this line. The Kauffmann et al. (2003) line was defined empirically using a large galaxy sample from the Sloan Digital Sky Survey (SDSS) to separate Normal Star-Forming (NSF) galaxies from galaxies hosting an AGN. Similarly, using a large (∼20.000) sample of SDSS galaxy spectra, Stasińska et al. (2006) inspected the contamination of low-level nuclear activity in a NSF sample to define a more restrictive boundary to separate the "pure" SF envelope in the [N II] diagram, i.e. galaxies with no signs of ionizing sources other than OB stars.

From Fig. 14 it is possible to observe several points lying above the Stasińska et al. (2006) line and a few points lying above the Kewley et al. (2001) and Kauffmann et al. (2003) delimiting lines in the [N II] diagram. In the [S II] and [O I] diagrams, the points are virtually all above the lines delimiting the locus of the NSF envelope. Additionally, two branches of points can be observed in all the diagrams, being more pronounced in the [N II] diagram, where the second branch hosts the bins with higher $\log \Sigma_{H\alpha}$ values, thus it is associated to the regions with higher SF activity, although some bins with relatively elevated $\log \Sigma_{H\alpha}$ can be also found in the main branch. Furthermore, the direction of separation of the second branch in relation to the main one in the [N II] diagram is towards higher values of [N II] / Hα. Both pieces of information suggest that the recent episodes of star-formation might be releasing N-enriched material into the ISM. Kewley et al. (2006) predicts the increasing of [N II] / Hα and [O III] / Hβ in the presence of very hot O stars or WR stars.

An additional mechanism that can explain hard ionization fields is the presence of fast radiative shocks in the ISM (Allen et al. 2008). In Fig. 14, the grid of fast radiative shocks calculated with the MAPPINGS III code (Allen et al. 2008) is plotted over the bins. The grids presented consider shocks plus precursor for the low-density regime (N_e = 1 cm^{-3}) and a Large Magellanic Cloud (LMC) abundance. The dashed black lines correspond to curves of constant magnetic fields with the following intensities: $B\,(\mu G)$ = 1.0 × 10^{-4}, 2.0, 5.0, 10.0. The blue solid lines represent, in all the diagrams, curves of constant shock velocity. The three curves presented have velocities of 200, 250 and 300 km s^{-1}. Although several regions of our diagnostic diagrams co-

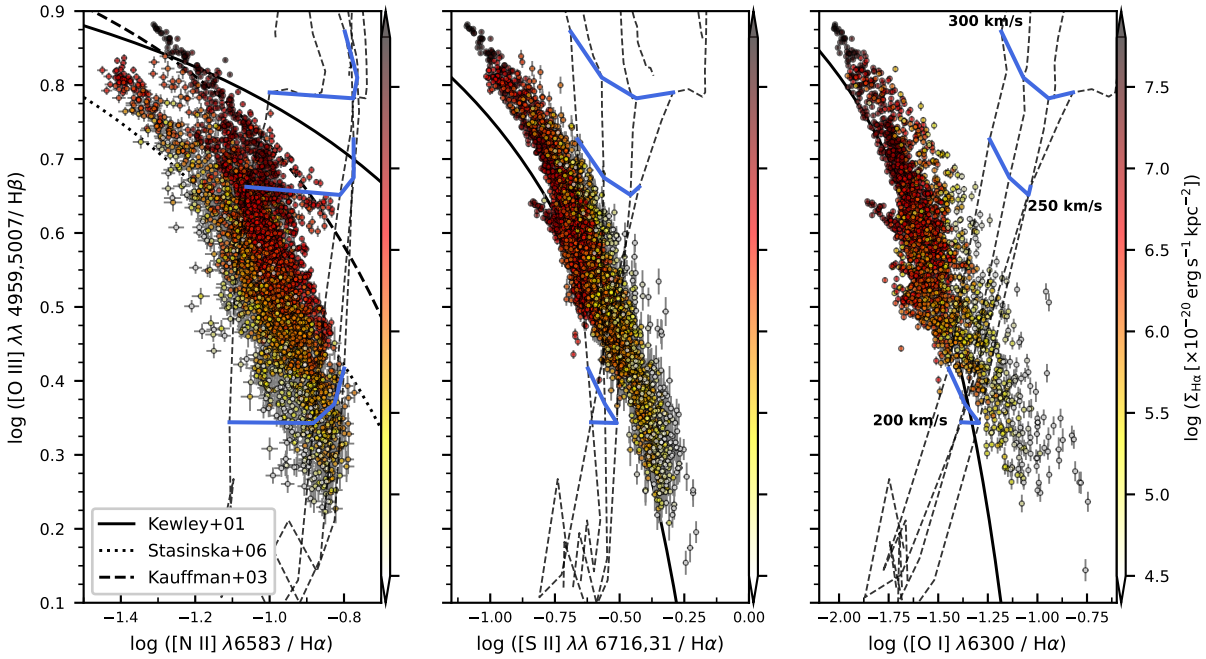

Fig. 14. BPT diagnostic diagrams for ESO 400-43. The points correspond to Voronoi bins, with the binning pattern aiming a threshold SNR over the faintest line of each diagram. The bins are color-coded according to the flux of Hα divided by the physical area of each bin. The black solid line corresponds to the Kewley et al. (2001) delimiting line in all diagrams. In the [N II] diagram the blacked dashed and dotted lines correspond to the Kauffmann et al. (2003) and Stasińska et al. (2006) delimiting lines, respectively. We overlay in each diagram the grids of fast radiative shocks from Allen et al. (2008) for a LMC abundance, where the black thin dashed lines represent lines of constant magnetic field intensity of $B\,(\mu G) = 1.0 \times 10^{-4}$, 2.0, 5.0, 10.0. The blue solid lines represent iso-velocity curves with $v\,(\mathrm{km\,s^{-1}}) = 200, 250, 300$.

incide with the grid positions, the presence of shocks can also be mimicked when dense columns of neutral and highly ionised gas in the observer line-of-sight are projected into two dimensions (Ercolano et al. 2012). The presence of highly ionised gas in ESO 400-43 is traced by the high ratios of [O III] / Hα observed in the emission line maps presented in Fig. 11, which extend much farther out in the ISM of ESO 400-43 than the region under analysis in our diagnostic diagrams. Neutral gas also seems to be present in considerable amounts in ESO 400-43, as previous observations in the 21-cm line indicate the presence of a $5 \times 10^9\ M_\odot$ slowly rotating H I halo. The presence of shocks in the ISM of ESO 400-43 and their location are investigated more in the following section.

4.8. Spatially resolved emission line diagnostic diagrams

In order to investigate the location of the bins in ESO 400-43, we present the spatially resolved BPT diagrams in Fig. 15. The diagrams used here are the same as in Fig. 14, but the bins are now color-coded according to criteria described below.

- **Red bins:** Bins above the Kewley et al. (2001) line in the [N II] diagram, indicating a source of hard ionizing photons.
- **Yellow bins:** In order to separate the two branches in the [N II] BPT diagram we added a small shift of 0.09 in the Stasińska et al. (2006) line, which is the black dotted line in Fig. 15. The points coloured in yellow are the ones belonging to the second branch in the [N II] diagram, tracing the N-enriched gas in ESO 400-43.
- **Blue bins:** Bins corresponding to locations of high [N II] / Hα (> 0.9; value chosen from emission-line map in Fig. 11) in ESO 400-43 that have, simultaneously, [O III] / Hβ high enough to lie above the shifted Stasińska et al. (2006) line.
- **Magenta bins:** Bins overlapping the grid of fast radiative shock models considering a LMC abundance in the [O I] diagram, where we extended the grids shown in Fig. 14 to include all available magnetic field intensities, i.e., $B\,(\mu G) = 1 \times 10^{-4}$, 1.0, 2.0, 4.0, 5.0, 10.0.
- **Green bins:** Bins that do not overlap the grid of fast radiative shock models in the O I diagram, but have higher [O I] / Hα and lower [O III] / Hβ in comparison to shock-ionized candidates, although also lying above the Kewley et al. (2001) line in the O I diagram.

The cyan points over-plotted in all diagrams correspond to the position of the spectra of the 6 clusters shown in Fig. 8, labelled according to the symbols. Additionally, we add the integrated spectrum of ESO 400-43, the same used to estimate the BCG redshift from the strongest emission lines.

All the bins colored according to the criteria in one diagram are mapped onto their original coordinates to be properly identified in other binning patterns. As expected, the position of the red points tracing the presence of hard ionization sources coincides with the location of the Hα and He II λ4686 emission peaks in ESO 400-43, the region around star cluster A. The fact that region A exhibits a WR signature (Fig. 13) indicates that WR stars are the main contributors to the hard radiation field in the ISM of ESO 400-43. The position of the hardly-ionized bins in the N-enriched branch aligns with previous findings that highlight the role of WR stars in the chemical enrichment of the ISM (López-Sánchez & Esteban 2010; Kumari et al. 2018; Kobayashi & Ferrara 2024; Rivera-Thorsen et al. 2024, among others). Moreover, the yellow points tracing the N-enriched branch in the [N II] diagram lie predominantly in

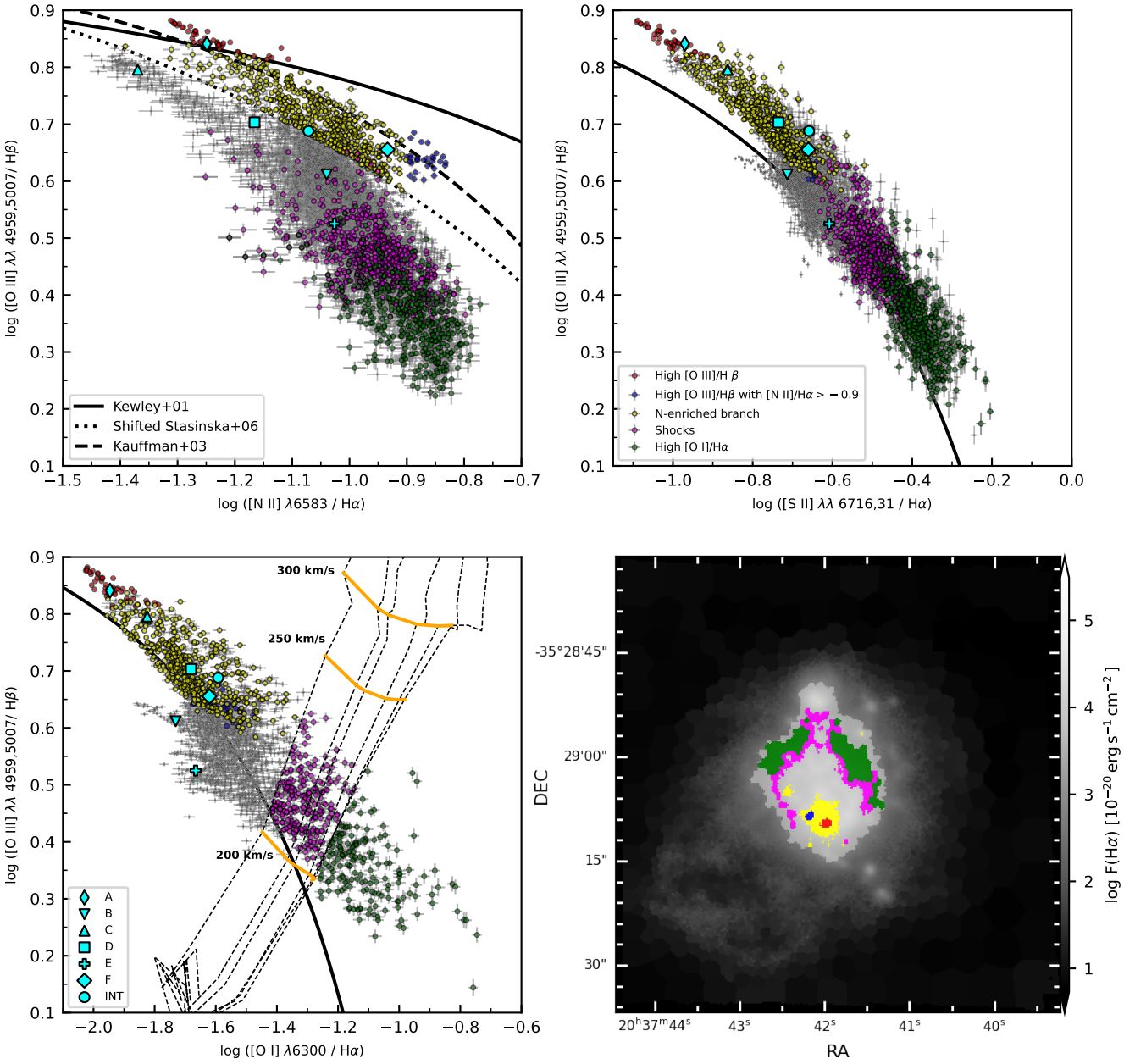

Fig. 15. Spatially resolved BPT diagrams for ESO 400-43. The delimiting lines are the same as in Fig. 14, except for the Stasińska et al. (2006) line, where we have applied a small shift of 0.09 to separate the main branch from the N-enriched branch in the [N II] diagram. The bins are colour-coded with criteria specified in the label on top right panel (see text). The position of the bins are represented by the colours scheme plotted upon the Hα image of ESO 400-43 in the bottom right panel. The cyan points correspond to the positions in the diagram of the 6 selected regions, including the position of the integrated spectrum of ESO 400-43. The grid of shocks presented in the [O I] is the same as in Fig. 14, except for the inclusion of the $B\,(\mu G) = 1.0, 4.0$ models.

the vicinity of region A, likely enriched by the nucleosynthetic products of WN stars ejected through strong stellar winds. The analysis of the gas-phase metallicity in ESO 400-43 is beyond the scope of this work, and will be addressed in a future paper (Lassen et al., in prep.).

The round structure with high [N II] / Hα is recovered by the criteria used to define the blue points, but not the trail of high [N II] / Hα observed in the zoom-in frame presented in Fig. 11. This indicates that, despite the possible presence of N-enriched material in the trail, it is less ionized than the round structure. The number of spaxels that make up the blue structure is fewer than the number of spaxels within an aperture with the size of the MUSE PSF (29 and 61 spaxels, respectively). Therefore, when we plot the spectra integrated around region F (The cyan diamond in Fig. 15), the spaxels with high values of [N II] Hα are averaged with the surrounding spaxels, sresulting in a spectrum slightly shifted to lower values of [N II] / Hα, as observed in Fig. 15. In the [S II] and [O I] diagrams, none of the branches separating from the main one (and lying below the delimiting line) correspond to the N-enriched branch seen in the [N II] diagram. Instead, these branches are associated with regions corresponding to star clusters B and E, which appear to behave more like "regular" star-forming regions.

The regions overlapping the grid of shock models in the [O I] diagram are located in the outskirts, similar to the green points. The existence of the latter could not be explained, for instance, by magnetic field values not covered by the Allen et al. (2008) models. For a given value of [O I] / Hα, increasing the intensity of the magnetic field would actually increase the ionization traced by [O III] / Hβ instead of decreasing it. On the other hand, the lower value of magnetic field used in the models displayed in Fig. 15 is already very low ($10^{-4}\,\mu G$).

5. Discussion

Using the optical emission line fluxes in ESO 400-43, we derived several properties of the ionized gas in the galaxy. By combining it with high-resolution imaging of ESO 400-43 provided by HST observations in four broadband and one narrowband filters, we inspected the stellar feedback from star clusters on the ISM of the BCG. This study offers a valuable view on the star formation processes in an ISM with extreme dynamic and gas-phase metallicity conditions.

5.1. The ionized gas in ESO 400-43

ESO 400-43 presents an extensive halo of ionized gas, occupying nearly the entire MUSE Fov. Using the radial Hα surface brightness profile, we estimated an ionized gas mass of $M_{\rm HII} \approx 4 \times 10^7\,M_\odot$. The inspection of the ionized gas morphology in Fig. 5 revealed the presence of a pronounced loop of low surface-brightness ionized gas. This loop is located within an even fainter optical bridge that connects the dwarf companions (Micheva et al. 2013). Unfortunately, the loop is faint and only Hα, Hβ and [O III] λ5007 emission lines can be observed, hindering deeper characterization of the gas physical conditions in the loop. Unlike the inner regions of the BCG, the intensity of [O III] λ5007 in the loop is lower than that of Hα, which becomes apparent in the [O III] / Hα emission line map from Fig. 11.

The velocity and velocity dispersion fields in the BCG are irregular, as can be observed from Fig. 5. In the inner regions of the BCG, the velocity dispersion presents lower values and reveals a complex and intriguing structure, but it reaches high values with complex gas dynamics on the west side of the galaxy, enclosing the region where the loop is found. Visual inspection of these regions shows complex Hα line profiles, which are broadened and also exhibit skewed line profiles, suggesting the presence of outflows and also gas motions in a preferential direction. The same does not occur on the east side of ESO 400-43. At the same time that the possible galactic-scale outflows in the outermost regions of the galaxy drive the broadening of Hα emission line, in inner galaxy regions with high SF activity (such as region A), we observed that the tails of the strong emission lines could not be efficiently modeled by single Gaussian components, indicating the necessity of at least a second component to describe the complex gas dynamics more accurately. This underlying broader component could be originated, for instance, by strong stellar winds. However, a detailed multi-component analysis of the gas in ESO 400-43 is beyond the scope of this work. The irregular pattern of the emitting gas is also reflected in the rotation velocity map of Hα in Fig. 5, where two spinning central structures are observed. Östlin et al. (1999) and Östlin et al. (2001) already reported the uncommon rapid decay of the rotation curves for this BCG, suggesting that gas infall likely caused by the interaction with ESO 400-43 *b* and/or a past merger with a smaller galaxy as the trigger of the starburst in ESO 400-43.

5.2. Massive star clusters as the sources of hard ionizing radiation

We have detected He II λ4686 emission across ESO 400-43. The intensity peak of He II λ4686 emission coincides with the Hα emission peak (see Fig. 12), decreasing in the regions with fewer star clusters and presenting a slight increase in the northern structure of ESO 400-43, where at least one $M/M_\odot > 10^5$ star cluster is found. In Fig. 8, this spatial correlation is visible, where the best-fit SED star cluster ages and masses are overlaid on an HST F606W (V band) image of ESO 400-43 with the contours of He II λ4686 emission. Using an aperture with the size of the PSF centered on the He II λ4686 emission peak, we have shown the presence of a broad feature ($720 \pm 35\,{\rm km\,s^{-1}}$) underlying He II λ4686 nebular emission, tracing WR stars. However, similar broad components are not detected in the northern regions of ESO 400-43, even when inspecting these locations with apertures $\sim$3$\times$ larger than the PSF. This is consistent with the distribution of massive star clusters in ESO 400-43, but even in these regions, the nebular He II λ4686 emission is still detected.

Hard ionization fields have been reported in several BCDs, with observed high-ionization emission lines from heavy elements in their spectra (Izotov & Thuan 1999; Fricke et al. 2001; Thuan & Izotov 2005; Izotov et al. 2007; Kehrig et al. 2015, , among many others). The hardness of the ionizing radiation is known to correlate with the galaxy gas-phase metallicity, with the intensity of the nebular He II λ4686 emission increasing for lower $Z_{\rm gas}$ values (Campbell et al. 1986; Guseva et al. 2000; Thuan & Izotov 2005). The origin of this nebular emission has been a subject of debate in the literature. Although WC stars were found to contribute significantly to the total He II emission in the $1/5\,Z_\odot \leqslant Z \leqslant Z_\odot$ metallicity regime (Gonzalez-Delgado et al. 1994; Schaerer 1996), a lack of WR signatures was reported in galaxies with nebular He II emission, when fast radiative shocks were proposed to be the responsible for the ionizing radiation (Kehrig et al. 2008; Monreal-Ibero et al. 2010; Neugent & Massey 2011; Izotov et al. 2012; Plat et al. 2019). Similarly, Herenz et al. (2017) found evidence of He II emission caused by shocks in a supershell structure in the extremely metal-poor compact starburst SBS 0335-52E.

Overlaying a grid of fast radiative shock models plus precursor from Allen et al. (2008) in the [O I] diagnostic diagram, we have observed several regions with ionization consistent with shocks with $200\,{\rm km\,s^{-1}} \lesssim v \lesssim 250\,{\rm km\,s^{-1}}$ located in the outermost regions of ESO 400-43 (see Fig. 15). However, we found He II emission, for instance, in the northern structure of the galaxy (traced by region C in the spatially resolved diagnostic diagram from Fig. 15) and in the central regions with several $5\,{\rm Myr} \leq t \leq 15\,{\rm Myr}$ clusters, regions not covered by the grid of shock models. We selected the grid considering shocks propagating in an ISM with LMC abundance (12 + log(O/H) = 8.35, Russell & Dopita 1992), but changing the models to lower abundances like the SMC abundance (12 + log(O/H) = 8.03, Russell & Dopita 1992) does not place the grids of shocks plus precursor on the location of region C, for instance, in the diagnostic diagrams. Although this ionization by shocks could be mimicked by columns of neutral gas (Ercolano et al. 2012, which is certainly present, as demonstrated by Bergvall & Jorsater (1988)), it is also important to mention that for low abundances, the available set of shock models from Allen et al. (2008) was calculated considering only $N_e = 1\,{\rm cm^{-3}}$ and shocks propagating in weakly ionized ISM (Izotov et al. 2012), conditions that are not representative of those observed in the ISM of ESO 400-43.

5.3. The star cluster population in ESO 400-43

The extraction procedure described in §3.7 resulted in a catalog of 220 star clusters in ESO 400-43. In §4.4 we presented the statistical properties of this star cluster population, obtained via SED fitting. The peak of the age distribution is ≈10 Myr, with ≈80% having ages less than 20 Myr. Given that the positions of the star clusters observed with high-resolution HST imaging coincide with the locations of ionized gas traced by Hα emission seen in MUSE-AO observations (which are sensitive to the short-lived OB stars; Kennicutt 1998), this age distribution provides consistent results. In the case of the mass distribution, about 60% of the clusters lie in the mass range of $4.4 \leqslant \log(M/M_\odot) \leqslant 5.5$, with the massive clusters ($> 10^5\ M_\odot$) representing ∼44% of the sample. If we consider the star clusters that are candidate to host significant numbers of WR stars, i.e. massive and young star clusters, these represent 5% of the cluster sample.

Using the SED best-fit values, we inspected the age-mass diagram for the cluster sample in ESO 400-43, finding evidence of three starburst events in the last 4, 10 and 20 Myr. This diagram shows clusters spanning a wide range of ages, from a few Myr to hundreds of Myr. Extended episodes of cluster formation have also been observed in other Hi-PEEC galaxies (Adamo et al. 2020a), possibly tracing the duration of the merging process. However, unlike these galaxies, we do not find clusters with ages greater than 200 Myr. Compared to the age-mass diagrams of the six Hi-PEEC galaxies in Adamo et al. (2020a), we find a slightly lower value for the highest mass-end of the distribution, as well as for other local Universe galaxies undergoing mergers (e.g., Linden et al. 2017; Mok et al. 2019). However, our highest mass-end of $\approx \log(M/M_\odot) = 6.7$ is similar to reported values of star cluster populations in M83 (Adamo et al. 2015) and in a sample of dwarf galaxies (Adamo et al. 2020b; Cook et al. 2023) from the Legacy Extragalactic Ultraviolet Survey (Calzetti et al. 2015, LEGUS).

6. Conclusions

In this work, we combined integral field spectroscopic data from MUSE-AO with high-resolution imaging from HST in four broadband (F336W, F438W, F606W and F814W) filters and one narrowband (F665N) filter to study the stellar feedback from star clusters on the ionized gas in the BCG ESO 400-43. Below, we summarize our findings:

1. **Kinematic analysis of ionized gas:** A kinematic analysis of the ionized gas in ESO 400-43 revealed an irregular velocity rotation pattern in the BCG, with the presence of a central spinning structure and with the amplitude of gas rotation in accordance with previously reported values. These findings align with the hypothesis raised by Östlin et al. (1999) and Östlin et al. (2001), where the erratic rotation curve of ESO 400-43 was attributed to gas infall, possibly caused by a past merger with a smaller galaxy. In the northwest region of the galaxy, the gas dynamics increase in complexity, with broadened and skewed Hα emission line profiles suggesting the presence of outflows.
2. **Ionized gas morphology:** The analysis of the ionized gas morphology revealed the presence of a pronounced loop of low surface-brightness ionized gas in the southwest corner of ESO 400-43, extending 10 kpc towards the direction of the dwarf companion ESO 400-43 *b* and within a previously reported low surface brightness optical bridge that connects the pair of galaxies (Micheva et al. 2013). From the emission line maps, it was possible to see that [O III] λ5007 / Hα < 1 in the loop, unlike the inner regions of ESO 400-43. Using radial profiles of nebular properties up to 22″from the Hα emission peak, we estimated an ionized gas mass of $(4.011 \pm 0.007) \times 10^7\ M_\odot$.
3. **ISM ionization degree:** We inspected the ionization degree across the ISM of ESO 400-43 using the emission line maps of [O III] / Hα, [O III] / [S II] and [N II] / Hα. For the first two emission line maps, bright and compact structures that are spatially correlated with the star clusters appeared, highlighting the role of the clusters as the major contributors to the ionization in the ISM of ESO 400-43. In the [N II] / Hα emission line map, the regions corresponding to the star clusters are correlated with drops of [N II] / Hα values. Additionally, we observed both a gas trail and a compact structure with high values of [N II] / Hα, where the latter possibly traces a pocket of N-enriched gas slightly offset from the Hα emission peak.
4. **Star cluster population in ESO 400-43:** We extracted a catalog of 220 star clusters in ESO 400-43, for which we performed a SED fitting with PROSPECTOR. We have found that 10 out of 220 (∼5%) star clusters are young ($t < 5$ Myr) and massive ($\log(M/M_\odot) > 5.0$), candidates for hosting significant numbers of WR stars. These clusters are located primarily in the bottom region of ESO 400-43 (coinciding with Hα and He II λ4686 emission peaks), with one massive young star cluster found in the northern star-forming structure. The star clusters are mainly metal-poor, with the peak of the metallicity distribution at $\sim$¼ $Z/Z_\odot$, corresponding to a gas-phase metallicity of 12 + log(O/H) ≈ 8.1. From the age-mass diagram of the star clusters, we observe a bursty SFH in the last ∼100 Myr, with three starbursts in the last 4 Myr, 10 Myr and 20 Myr.
5. **Hard ionizing radiation in ESO 400-43**: He II λ4686 emission was observed across the ISM of ESO 400-43, with increased intensity spatially correlating with increasing concentration of young and massive star clusters. This suggests that the hard ionizing radiation in the BCG might be caused by WR stars. We extracted an integrated spectrum of the region corresponding to both the peak of He II λ4686 emission and highest concentration of young and massive star clusters in ESO 400-43 using an aperture with the size of MUSE PSF, where two components were detected: A narrow ($\sigma = 96 \pm 4$ km s^{-1}) nebular He II λ4686 emission and a broad ($\sigma = 720 \pm 35$ km s^{-1}) component, a signature of WR stars that supports the aforementioned hypothesis. However, nebular He II emission is also found in regions devoid of these young and massive star clusters, where the broad component could not be detected even using apertures as large as 3× the PSF size. Although fast radiative shocks could be invoked to explain the hard ionization field in these regions, diagnostic diagrams suggest these are located only in the outermost regions of ESO 400-43. Nonetheless, tracing the presence of fast radiative shocks is challenging in ESO 400-43, as the models of Allen et al. (2008) might not be representative of such an extreme ISM.
6. **Emission line diagnostic diagrams:** We used the [N II], [S II] and [O I] diagnostic diagrams to inspect the ionization mechanism across ESO 400-43. In the [S II] and [O I] diagrams, virtually all the points lie above the Kewley et al. (2001) line that defines an upper boundary for ionization from OB stars. In the [N II] diagram, two branches clearly separate, indicating a region of N-enriched gas. In the BPT diagram color-coded according to the surface brightness of

Hα, it is possible to see that this N-enriched component is associated with regions of higher SF activity. We used a shifted version of the Stasińska et al. (2006) delimiting line to separate both branches and inspect their location within the ISM of ESO 400-43. This branch arises mainly from the surroundings of the region peaking in He II emission, which could be caused, for instance, by nucleosynthesized elements ejected from WR stars that enrich the surrounding ISM. Fast radiative shocks were also investigated using the grid of shock plus precursor models from Allen et al. (2008), assuming a LMC abundance. The regions overlapping the grid of shock models in the [O I] diagram corresponds to the outermost regions of ESO 400-43.

Acknowledgements. AEL acknowledges the support from Coordenação de Aperfeiçoamento de Pessoal de Nível Superior (CAPES) in the scope of the Program CAPES-PrInt, process number 88887.837405/2023-00 and CAPES-PROEX fellowship, process number 88887.513351/2020-00.

References

Adamo, A., Hollyhead, K., Messa, M., et al. 2020a, MNRAS, 499, 3267
Adamo, A., Kruijssen, J. M. D., Bastian, N., Silva-Villa, E., & Ryon, J. 2015, MNRAS, 452, 246
Adamo, A., Östlin, G., & Zackrisson, E. 2011, MNRAS, 417, 1904
Adamo, A., Östlin, G., Zackrisson, E., et al. 2010, MNRAS, 407, 870
Adamo, A., Zeidler, P., Kruijssen, J. M. D., et al. 2020b, Space Sci. Rev., 216, 69
Allen, M. G., Groves, B. A., Dopita, M. A., Sutherland, R. S., & Kewley, L. J. 2008, ApJS, 178, 20
Amorín, R., Muñoz-Tuñón, C., Aguerri, J. A. L., & Planesas, P. 2016, A&A, 588, A23
Amorín, R. O., Muñoz-Tuñón, C., Aguerri, J. A. L., Cairós, L. M., & Caon, N. 2007, A&A, 467, 541
Annibali, F. & Tosi, M. 2022, Nature Astronomy, 6, 48
Asada, Y., Sawicki, M., Desprez, G., et al. 2023, MNRAS, 523, L40
Asplund, M., Grevesse, N., Sauval, A. J., & Scott, P. 2009, ARA&A, 47, 481
Atek, H., Labbé, I., Furtak, L. J., et al. 2024, Nature, 626, 975
Azevedo, G. M., Chies-Santos, A. L., Riffel, R., et al. 2023, MNRAS, 523, 4680
Bacon, R., Accardo, M., Adjali, L., et al. 2010, Proc. SPIE, 7735, 773508
Bacon, R., Conseil, S., Mary, D., et al. 2017, A&A, 608, A1
Bacon, R., Piqueras, L., Conseil, S., Richard, J., & Shepherd, M. 2016, MPDAF: MUSE Python Data Analysis Framework, Astrophysics Source Code Library, record ascl:1611.003
Baldwin, J. A., Phillips, M. M., & Terlevich, R. 1981, PASP, 93, 5
Barbary, K. 2016, The Journal of Open Source Software, 1, 58
Bastian, N., Saglia, R. P., Goudfrooij, P., et al. 2006, A&A, 448, 881
Bergeron, P., Ruiz, M. T., & Leggett, S. K. 1997, ApJS, 108, 339
Bergvall, N. & Jorsater, S. 1988, Nature, 331, 589
Bergvall, N. & Östlin, G. 2002, A&A, 390, 891
Bertin, E. & Arnouts, S. 1996, A&AS, 117, 393
Bibby, J. L. & Crowther, P. A. 2010, MNRAS, 405, 2737
Bik, A., Östlin, G., Menacho, V., et al. 2018, A&A, 619, A131
Bouwens, R. J., Illingworth, G. D., Oesch, P. A., et al. 2015, ApJ, 811, 140
Bouwens, R. J., Illingworth, G. D., Oesch, P. A., et al. 2012, ApJ, 752, L5
Brinchmann, J., Kunth, D., & Durret, F. 2008, A&A, 485, 657
Bruzual, G. & Charlot, S. 2003, MNRAS, 344, 1000
Buckalew, B. A., Kobulnicky, H. A., & Dufour, R. J. 2005, ApJS, 157, 30
Calzetti, D. 2001, PASP, 113, 1449
Calzetti, D., Lee, J. C., Sabbi, E., et al. 2015, AJ, 149, 51
Campbell, A., Terlevich, R., & Melnick, J. 1986, MNRAS, 223, 811
Cappellari, M. 2017, MNRAS, 466, 798
Cappellari, M. & Copin, Y. 2003, MNRAS, 342, 345
Cappellari, M. & Emsellem, E. 2004, PASP, 116, 138
Cardelli, J. A., Clayton, G. C., & Mathis, J. S. 1989, ApJ, 345, 245
Chabrier, G. 2003, PASP, 115, 763
Choudhury, T. R. & Ferrara, A. 2006, MNRAS, 371, L55
Choudhury, T. R. & Ferrara, A. 2007, MNRAS, 380, L6
Choudhury, T. R., Ferrara, A., & Gallerani, S. 2008, MNRAS, 385, L58
Cid Fernandes, R., Stasińska, G., Mateus, A., & Vale Asari, N. 2011, MNRAS, 413, 1687
Conroy, C. & Gunn, J. E. 2010, ApJ, 712, 833
Conroy, C., Gunn, J. E., & White, M. 2009, ApJ, 699, 486
Cook, D. O., Lee, J. C., Adamo, A., et al. 2023, MNRAS, 519, 3749
Crowther, P. A. 2007, ARA&A, 45, 177
De Lucia, G. & Blaizot, J. 2007, MNRAS, 375, 2
Della Bruna, L., Adamo, A., Bik, A., et al. 2020, A&A, 635, A134
Diehl, S. & Statler, T. S. 2006, MNRAS, 368, 497
Ercolano, B., Dale, J. E., Gritschneder, M., & Westmoquette, M. 2012, MNRAS, 420, 141
ESO CPL Development Team. 2015, EsoRex: ESO Recipe Execution Tool, Astrophysics Source Code Library, record ascl:1504.003
Filho, M. E., Sánchez Almeida, J., Muñoz-Tuñón, C., et al. 2015, ApJ, 802, 82
Filho, M. E., Winkel, B., Sánchez Almeida, J., et al. 2013, A&A, 558, A18
Foreman-Mackey, D., Hogg, D. W., Lang, D., & Goodman, J. 2013, PASP, 125, 306
Fricke, K. J., Izotov, Y. I., Papaderos, P., Guseva, N. G., & Thuan, T. X. 2001, AJ, 121, 169
Gaia Collaboration, Vallenari, A., Brown, A. G. A., et al. 2023, A&A, 674, A1
Gil de Paz, A., Madore, B. F., & Pevunova, O. 2003, ApJS, 147, 29
González Delgado, R. M. & Leitherer, C. 1999, ApJS, 125, 479
González Delgado, R. M., Leitherer, C., & Heckman, T. M. 1999, ApJS, 125, 489
Gonzalez-Delgado, R. M., Perez, E., Tenorio-Tagle, G., et al. 1994, ApJ, 437, 239
González-Gaitán, S., de Souza, R. S., Krone-Martins, A., et al. 2019, MNRAS, 482, 3880
Guérou, A., Krajnović, D., Epinat, B., et al. 2017, A&A, 608, A5
Guseva, N. G., Izotov, Y. I., & Thuan, T. X. 2000, ApJ, 531, 776
Herenz, E. C., Hayes, M., Papaderos, P., et al. 2017, A&A, 606, L11
Herenz, E. C. & Wisotzki, L. 2017, A&A, 602, A111
Hunter, D. A., Elmegreen, B. G., & Madden, S. C. 2024, arXiv e-prints, arXiv:2402.17004
Ishiyama, T. 2014, ApJ, 788, 27
Izotov, Y. I. & Thuan, T. X. 1999, ApJ, 511, 639
Izotov, Y. I., Thuan, T. X., & Guseva, N. G. 2007, ApJ, 671, 1297
Izotov, Y. I., Thuan, T. X., & Privon, G. 2012, MNRAS, 427, 1229
Johnson, B. D., Leja, J., Conroy, C., & Speagle, J. S. 2021, ApJS, 254, 22
Kauffmann, G., Heckman, T. M., Tremonti, C., et al. 2003, MNRAS, 346, 1055
Kehrig, C., Vílchez, J. M., Pérez-Montero, E., et al. 2015, ApJ, 801, L28
Kehrig, C., Vílchez, J. M., Sánchez, S. F., et al. 2008, A&A, 477, 813
Kennicutt, R. C. J. 1998, ARA&A, 36, 189
Kewley, L. J., Dopita, M. A., Sutherland, R. S., Heisler, C. A., & Trevena, J. 2001, ApJ, 556, 121
Kewley, L. J., Groves, B., Kauffmann, G., & Heckman, T. 2006, MNRAS, 372, 961
Kobayashi, C. & Ferrara, A. 2024, ApJ, 962, L6
Komarova, L., Oey, M. S., Hernandez, S., et al. 2024, arXiv e-prints, arXiv:2404.01435
Kumari, N., James, B. L., Irwin, M. J., Amorín, R., & Pérez-Montero, E. 2018, MNRAS, 476, 3793
Kunth, D. & Östlin, G. 2000, A&A Rev., 10, 1
Leitherer, C., Schaerer, D., Goldader, J. D., et al. 1999, ApJS, 123, 3
Lenz, D. D. & Ayres, T. R. 1992, PASP, 104, 1104
Liang, F.-H., Li, C., Li, N., et al. 2020, ApJ, 896, 121
Linden, S. T., Evans, A. S., Rich, J., et al. 2017, ApJ, 843, 91
Loose, H. H. & Thuan, T. X. 1986, in Star-forming Dwarf Galaxies and Related Objects, 73–88
López-Sánchez, Á. R. & Esteban, C. 2010, A&A, 517, A85
Luridiana, V., Morisset, C., & Shaw, R. A. 2015, A&A, 573, A42
Ly, C., Malkan, M. A., Rigby, J. R., & Nagao, T. 2016, ApJ, 828, 67
Meynet, G. & Maeder, A. 2005, A&A, 429, 581
Micheva, G., Östlin, G., Bergvall, N., et al. 2013, MNRAS, 431, 102
Moffat, A. F. J. 1969, A&A, 3, 455
Moiseev, A. V., Tikhonov, A. V., & Klypin, A. 2015, MNRAS, 449, 3568
Mok, A., Chandar, R., & Fall, S. M. 2019, ApJ, 872, 93
Monreal-Ibero, A., Vílchez, J. M., Walsh, J. R., & Muñoz-Tuñón, C. 2010, A&A, 517, A27
Motiño Flores, S. M., Wiklind, T., & Eufrasio, R. T. 2021, ApJ, 921, 130
Neugent, K. F. & Massey, P. 2011, ApJ, 733, 123
Osterbrock, D. E. & Ferland, G. J. 2006, Astrophysics of gaseous nebulae and active galactic nuclei (University Science Books)
Östlin, G., Amram, P., Bergvall, N., et al. 2001, A&A, 374, 800
Östlin, G., Amram, P., Masegosa, J., Bergvall, N., & Boulesteix, J. 1999, A&AS, 137, 419
Östlin, G., Cumming, R. J., Amram, P., et al. 2004, A&A, 419, L43
Östlin, G., Zackrisson, E., Bergvall, N., & Rönnback, J. 2003, A&A, 408, 887
Papaderos, P., Guseva, N. G., Izotov, Y. I., & Fricke, K. J. 2008, A&A, 491, 113
Papaderos, P., Izotov, Y. I., Thuan, T. X., et al. 2002, A&A, 393, 461
Papaderos, P., Loose, H. H., Thuan, T. X., & Fricke, K. J. 1996, A&AS, 120, 207
Pellegrini, E. W., Oey, M. S., Winkler, P. F., et al. 2012, ApJ, 755, 40
Pequignot, D., Petitjean, P., & Boisson, C. 1991, A&A, 251, 680
Pérez-Montero, E. 2017, PASP, 129, 043001
Planck Collaboration, Ade, P. A. R., Aghanim, N., et al. 2014, A&A, 571, A16
Plat, A., Charlot, S., Bruzual, G., et al. 2019, MNRAS, 490, 978

Pustilnik, S. A., Brinks, E., Thuan, T. X., Lipovetsky, V. A., & Izotov, Y. I. 2001, AJ, 121, 1413
Qu, Y., Helly, J. C., Bower, R. G., et al. 2017, MNRAS, 464, 1659
Rivera-Thorsen, T. E., Chisholm, J., Welch, B., et al. 2024, arXiv e-prints, arXiv:2404.08884
Rivera-Thorsen, T. E., Östlin, G., Hayes, M., & Puschnig, J. 2017, ApJ, 837, 29
Rue, H., Martino, S., & Chopin, N. 2009, Journal of the Royal Statistical Society Series B: Statistical Methodology, 71, 319
Ruschel-Dutra, D., Storchi-Bergmann, T., Schnorr-Müller, A., et al. 2021, MNRAS, 507, 74
Russell, S. C. & Dopita, M. A. 1992, ApJ, 384, 508
Schaerer, D. 1996, ApJ, 467, L17
Schaerer, D. & Stasińska, G. 1999, A&A, 345, L17
Schlegel, D. J., Finkbeiner, D. P., & Davis, M. 1998, ApJ, 500, 525
Searle, L. & Sargent, W. L. W. 1972, ApJ, 173, 25
Senchyna, P., Stark, D. P., Chevallard, J., et al. 2019, MNRAS, 488, 3492
Simmonds, C., Tacchella, S., Hainline, K., et al. 2024, MNRAS, 527, 6139
Smith, L. J., Crowther, P. A., Calzetti, D., & Sidoli, F. 2016, ApJ, 823, 38
Smith, L. J., Norris, R. P. F., & Crowther, P. A. 2002, MNRAS, 337, 1309
Stasińska, G., Cid Fernandes, R., Mateus, A., Sodré, L., & Asari, N. V. 2006, MNRAS, 371, 972
STScI Development Team. 2018, synphot: Synthetic photometry using Astropy, Astrophysics Source Code Library, record ascl:1811.001
Tayal, S. S. & Gupta, G. P. 1999, ApJ, 526, 544
Thuan, T. X. & Izotov, Y. I. 2005, ApJS, 161, 240
Tosi, M. 2003, Ap&SS, 284, 651
Tozzi, G., Maiolino, R., Cresci, G., et al. 2023, MNRAS, 521, 1264
van Dokkum, P. G. 2001, PASP, 113, 1420
Veilleux, S. & Osterbrock, D. E. 1987, ApJS, 63, 295
Wang, B., Heckman, T. M., Amorín, R., et al. 2021, ApJ, 916, 3
Weilbacher, P. M., Palsa, R., Streicher, O., et al. 2020, A&A, 641, A28
Wesson, R. 2016, MNRAS, 456, 3774
White, S. D. M. & Frenk, C. S. 1991, ApJ, 379, 52
White, S. D. M. & Rees, M. J. 1978, MNRAS, 183, 341
Whitmore, B. C., Brogan, C., Chandar, R., et al. 2014, ApJ, 795, 156
Whitmore, B. C., Chandar, R., Schweizer, F., et al. 2010, AJ, 140, 75
Zhao, Y., Gu, Q., & Gao, Y. 2011, AJ, 141, 68
Zou, H., Sui, J., Saintonge, A., et al. 2024, ApJ, 961, 173

Appendix A: SED results for the 6 selected star clusters

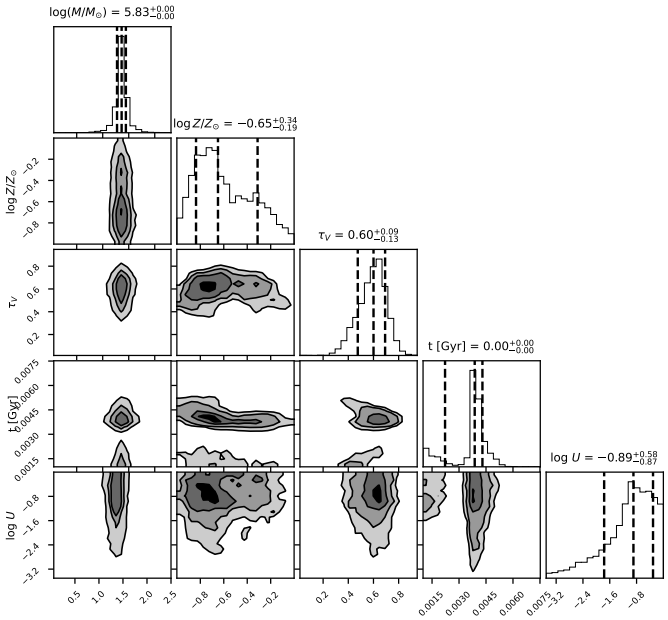

Fig. A.1. SED distribution of posteriors for star cluster A, highlighting the 15.9%, 50% and 84.1% quartiles. The best-fit spectrum is shown in Fig. 4.

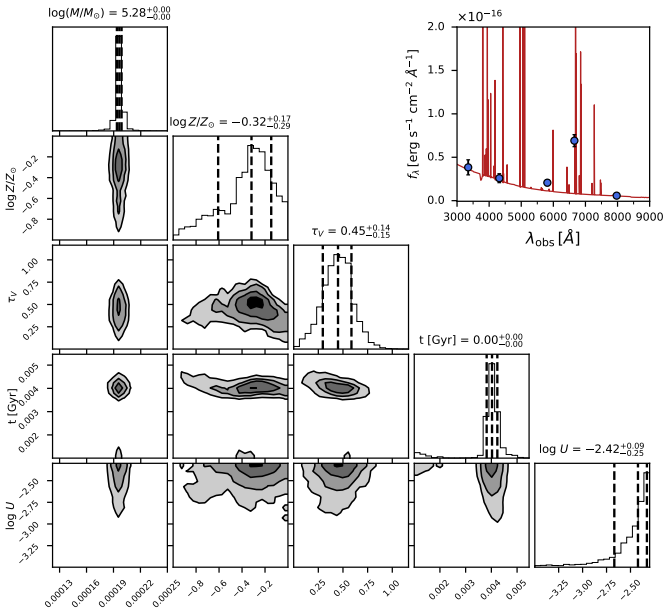

Fig. A.2. SED best-fit for star cluster B, and the 15.9%, 50% and 84.1% quartiles of the posteriors.

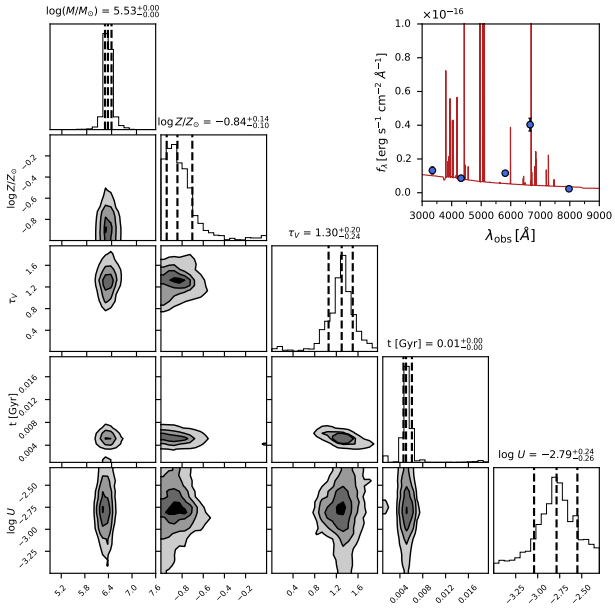

Fig. A.3. SED best-fit for star cluster C, and the 15.9%, 50% and 84.1% quartiles of the posteriors.

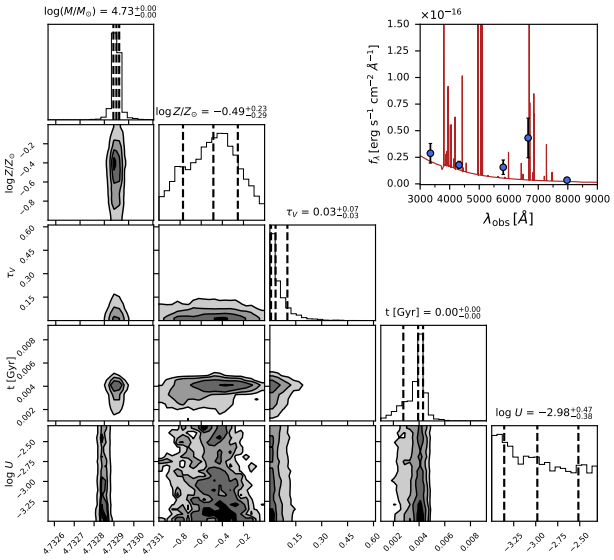

Fig. A.4. SED best-fit for star cluster D, and the 15.9%, 50% and 84.1% quartiles of the posteriors.

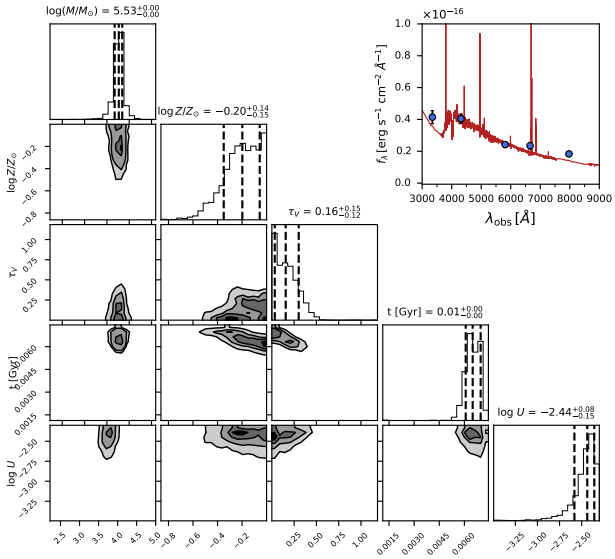

Fig. A.5. SED best-fit for star cluster E, and the 15.9%, 50% and 84.1% quartiles of the posteriors.

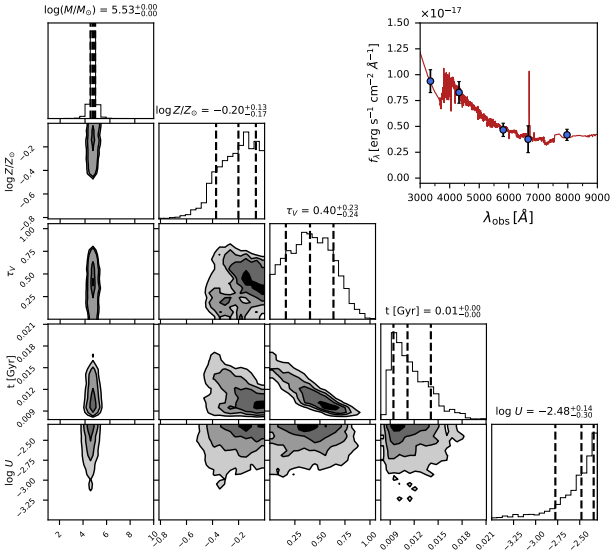

Fig. A.6. SED best-fit for star cluster F, and the 15.9%, 50% and 84.1% quartiles of the posteriors.

5.2 Gas-phase metallicity in ESO 400-43

Here, we detail a preliminary analysis related to the gas-phase metallicity in the ISM of ESO 400-43 . To apply the T_e–based method discussed in §3.4.1, we need at least one auroral emission line from a set that is sensitive to T_e variations across the galaxy ISM. Considering the most common emission line set used to apply the direct method in the optical (which are listed in equations 3.16 – 3.18), [O III] λ4363 is outside the wavelength range covered by MUSE spectrograph and [N II] λ5755 is within the spectral region blocked due to the laser guide system contamination. Fortunately, [S III] λ6312 is detected in the innermost regions of ESO 400-43 and therefore is used to estimate the gas-phase metallicity. However, this auroral emission line is very faint and can be detected at sufficient SNR level only in a few regions of ESO 400-43 . To illustrate the coverage of [S III] λ6312 across ESO 400-43 , the reader can check the T_e map in Fig. 6 of §5.1.

Thus, besides estimating the metallicity in these inner galaxy regions, part of the ongoing analysis also consists in finding reliable metallicity estimates in the outskirts of the galaxy, where the direct method is not applicable. For this, we are currently investigating the use of both strong-line calibrations and the photoionization-based code H II - χ - MISTRY v5.3 (Pérez-Montero, 2014; Pérez-Montero et al., 2021). In the case of the latter, we divide the ISM into three zones:

i) The zone in which [S III] λ6312 emission line can be detected with SNR $\geqslant$ 5, allowing gas-phase metallicities to be estimated using the direct method. This emission line is very weak, so this zone corresponds to the regions of ESO 400-43 presenting the highest SNR values.

ii) The zone in which the [O II] $\lambda\lambda$7319,7330 doublet can be detected with a minimum SNR of 20. This doublet is important when using H II - χ - MISTRY in the absence of [S III] λ6312 because the transitions of O^+ ion offer observational information on the relative abundance O^+/H^+. The latter is usually measured from the [O II] $\lambda\lambda$3726,29 doublet (see Equation §3.26), which is outside the wavelength range covered by the MUSE IFS. In this case, H II - χ - MISTRY relies on the relation proposed by Kniazev et al. (2003), shown in Equation 3.29.

iii) The outermost zone among the three, defined by the region with the [N II] λ6583 emission line detected at a minimum SNR level of 20. In this outermost region, H II - χ - MISTRY relies on the empirical grids shown in Fig. 28, requiring the minimum emission line set that includes Hβ, [O III] λ5007, [S II] $\lambda\lambda$6717,31 and [N II] λ6583.

To illustrate the three-zone sketch described above, we refer to Fig. 30. These zones are created using the Voronoi binning algorithm (Cappellari; Copin, 2003) with

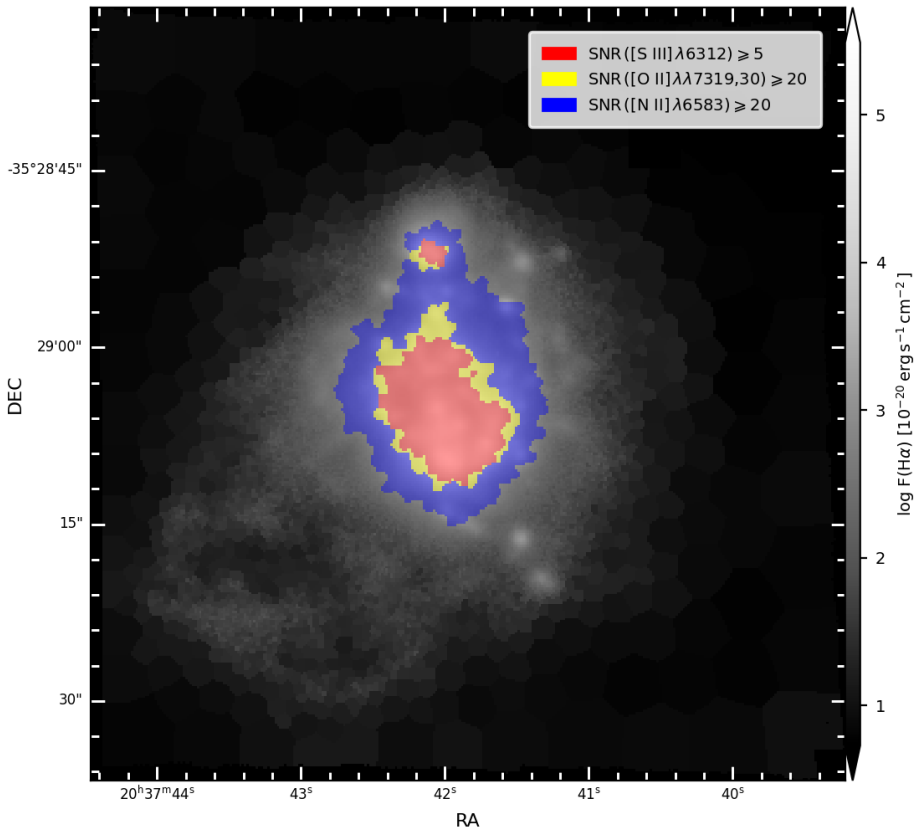

Figure 30 – Scheme illustrating the three-zone sketch used to analyze the gas-phase metallicity in ESO 400-43 with H II - χ - MISTRY. The red region corresponds to the extension of the binning pattern over [S III] λ6312 emission line aiming for a SNR = 5. The same for the yellow and blue regions, except that in these cases the binning pattern was applied over [O II] $\lambda\lambda$7319,30 and [N II] λ6583, respectively, aiming a SNR = 20. The background gray-scale image corresponds to the Hα flux map over the entire MUSE FoV.

the Weighted Voronoi Tessellation (WVT) proposed by Diehl and Statler (2006), applied over the emission lines [S III] λ6312, [O II] $\lambda\lambda$7319,7330 and [N II] λ6583 targeting a SNR of 5, 20 and 20, respectively. The extension and location of these binning patterns are shown overlaid on a Hα flux map (gray) in Fig. 30, with zones labeled. We extract the spectra from the cells defined by each binning pattern and measure the emission line fluxes by integrating over the line in the pure-gas cube, similarly to what has been done in §5.1. H II - χ - MISTRY requires de-reddened input emission line fluxes, so during the extraction procedure we correct the spectra for foreground Galactic extinction and for dust attenuation with the Balmer decrement assuming the CCM (Cardelli; Clayton; Mathis, 1989) reddening law. We also used the grid restrictions considering the case of Extreme Emission Line Galaxies (EELGs) from Pérez-Montero et al. (2021), with the ionizing SED corresponding to a BPASS (Eldridge et al., 2017) instantaneous burst model with $t = 1$ Myr.

Since H II - χ - MISTRY will be used in the zones where the direct method cannot be applied, we can perform a sanity check by comparing H II - χ - MISTRY metallicity predictions with the values derived through the direct method. The comparisons are shown in Fig. 31 for O/H and N/O. The O/H gas-phase abundance is estimated from Equation 3.22, with relative O^+/H^+ and O^{2+}/H^+ abundances given by equations 3.29 and 3.25, respectively. As the He II λ4686 emission line is detected in many of the regions within the [S III] zone, we considered taking into account the presence of the O^{3+} ion in the ICF determination (see Equation 3.23). However, when inspecting the bin corresponding to the highest He II $\lambda4686/H\beta$ value, we found a difference of only 0.1 dex in the metallicity when this ICF is used. Since this is below the typical associated uncertainties, we have adopted the simplifying assumption of $\mathrm{ICF}(O^+ + O^{2+}) \approx 1$ for all bins. In the case of Nitrogen, we first calculate N^+/H^+ using the $\mathrm{ICF}(N^+)$ prescriptions from Izotov et al. (2006), and then calculate N/O via the expression $N^+/O^+ = (N^+/H^+)/(O^+/H^+)$. Finally, we adopt the nebular structure sketch from Garnett (1992), which was discussed in §3.4.1. In this sketch, T_e measurements derived from the transitions of S^{2+} correspond to the intermediate ISM excitation layer (Garnett, 1992; Pérez-Montero, 2017), whereas the temperatures used for the determination of O^+/H^+ and O^{2+}/H^+ abundances correspond to the low and high ionization nebular regions, respectively. To circumvent this, we have used the T_e–T_e relations from Rogers et al. (2021):

$$T_e\,[\mathrm{O\,II}] \approx T_e\,[\mathrm{N\,II}] = 0.68(\pm0.03) \times T_e\,[\mathrm{S\,III}] + 0.28(\pm0.02) \tag{5.1}$$

$$T_e\,[\mathrm{O\,III}] = 0.63(\pm0.07) \times T_e\,[\mathrm{S\,III}] + 0.36(\pm0.06) \tag{5.2}$$

In Fig. 31 we can see that H II - χ - MISTRY returns metallicities that agree with the T_e–derived values within ±0.2 dex for both O/H and N/O. A large spread in the observed metallicity values is also noticeable, with Z_{gas} ranging from $12 + \log(\mathrm{O/H}) = 7.7$ ($\approx 0.1\,Z_\odot$) and $12 + \log(\mathrm{O/H}) = 8.7$ ($\approx Z_\odot$).

Before including strong-line calibrations in the discussion, we will first inspect the behavior of the N/O vs. O/H relation within the [S III] zone using the T_e–derived metallicities, as the resulting relation can define which indices we should adopt (see §3.4.2 and §4.2). The N/O vs. O/H relation obtained via the direct method is shown in the left panel of Fig. 32. Surprisingly, instead of the expected positive slope that arises from the secondary N production in the ISM (see Figures 26 and 27), a negative slope is observed. Using a linear function of the type $y(x) = ax+b$, we fit the mean trend using the metallicity values in bins of 0.1 dex (gray circles), obtaining $\log(\mathrm{N/O}) = -0.618\times[12+\log(\mathrm{O/H})]+3.894$ as the best fit (blue solid line). The cyan square represents the luminosity-weighted means of O/H and N/O, resulting in $12 + \log(\mathrm{O/H}) = 8.26$ and $\log(\mathrm{N/O}) = -1.21$. The trend observed in the N/O vs. O/H relation clearly deviates from the relation used to calibrate N-based indices with Z_{gas}, severely undermining the reliability of these metallicity estimates.

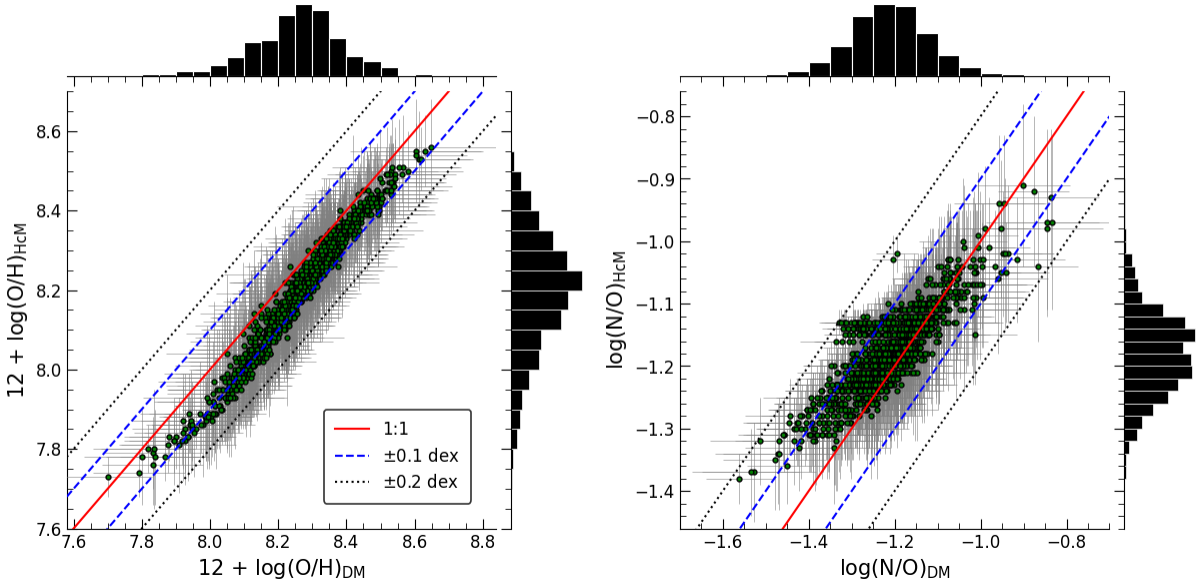

Figure 31 – Comparison between metallicity values (O/H and N/O) obtained through the direct method and H II - χ - MISTRY metallicity predictions in the [S III] zone. The red solid line represents the identity, with ±0.1 dex and ±0.2 dex deviations represented by the blue dashed and black dotted lines, respectively. The histograms show each metallicity distributions.

Fortunately, as argued in §3.4.2, indices based on other strong emission lines can be also used to investigate the metallicity behavior in the [O II] and [N II] zones[2]. With this in mind, we can use the indices O_3S_2 and N_2S_2 (Equations 3.38 and 3.31) to inspect the indirect N/O vs. O/H relation, which is shown in the right panel of Fig. 32.

In Fig. 32, the diamonds correspond to T_e–based estimates, while circles correspond to strong-line calibration estimations. The red points in both panels indicate bins that are located within the [S III] zone, while yellow points correspond to bins located in the [O II]+[N II] zones. Once again, a negative slope is observed, with a best-fit relation of $\log(\mathrm{N/O}) = -0.596 \times [12 + \log(\mathrm{O/H})] + 3.672$, which is slightly less steep than the best fit obtained only from T_e–based metallicity estimates. The luminosity-weighted metallicities are 12 + log(O/H) = 8.44 and log(N/O) = -1.36. However, the points in the right panel clearly do not fit into a linear relation as well as the points in the left panel. There are even two branches of points emerging in this relation, resembling the N-enriched branch observed in the [N II] diagnostic diagram presented in §5.1. Additionally, we kept the same range for the x and y axis in both panels to reinforce how the cloud of points in the right panel is shrunk compared to the T_e–based estimates. The shrinking happens in the direction of lower N/O values and higher O/H values. From Fig. 33 a question that arises is if the adopted strong-line calibrations are deriving the abundances as expected.

In the spirit of the comparison between T_e–based and H II - χ - MISTRY estimates

[2] Actually, we do not need to distinguish between both zones in the case of metallicity values estimated from strong-line calibration, since, different from estimates using H II - χ - MISTRY, the addition of the [O II] doublet adds no extra information.

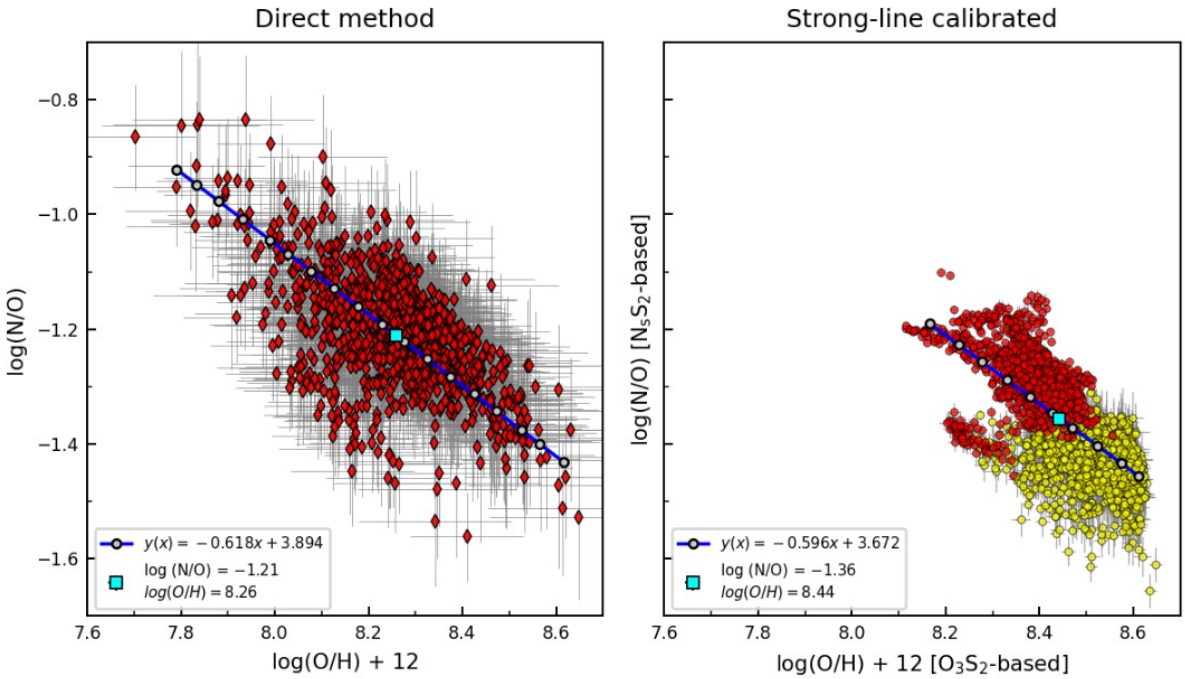

Figure 32 – N/O vs. O/H relation obtained through the direct method (Left panel) and strong-line calibrations (Right panel) based on the N_2S_2 and O_3S_2 indices. Red diamonds correspond to T_e–based metallicity values in the [S III] zone, whereas circles correspond to metallicity estimates from strong-line calibrations, with red corresponding to the [S III] zone and yellow corresponding to bins located in the [O II]+[N II] zones. Gray circles stand for the median values in metallicity bins of 0.1 dex that were used to fit a linear relation, with best fit shown as a blue solid line in both panels. The resulting coefficients are shown in the label, as well as the luminosity-weighted O/H and N/O values, whose location in the diagrams is shown as a cyan square.

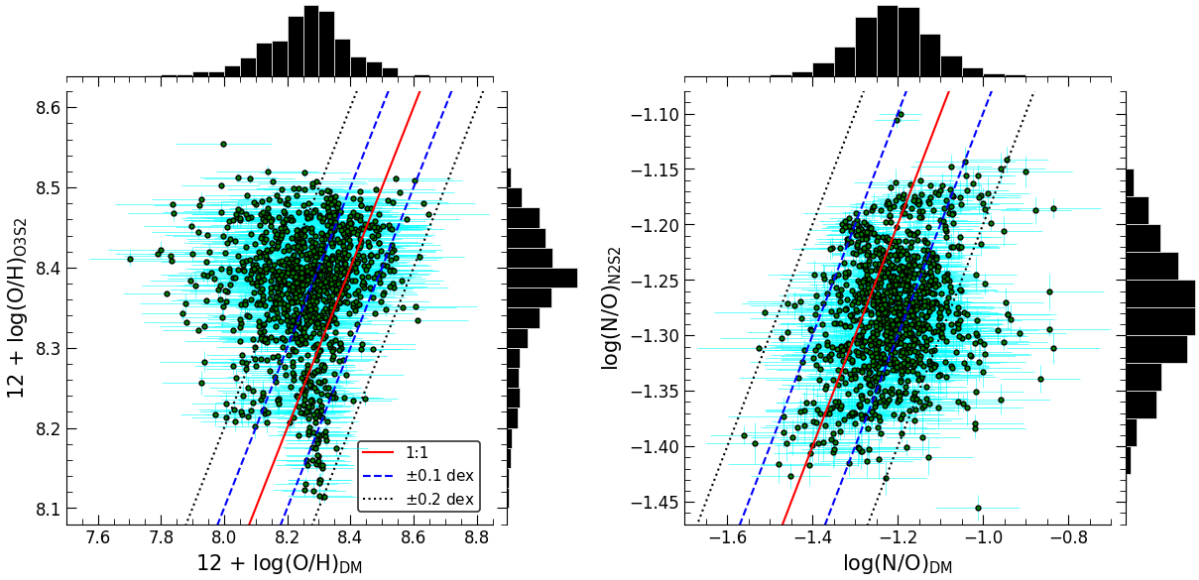

Figure 33 – Same as in Fig. 31, but now we are comparing metallicity values obtained through strong-line calibrations with the T_e–based values.

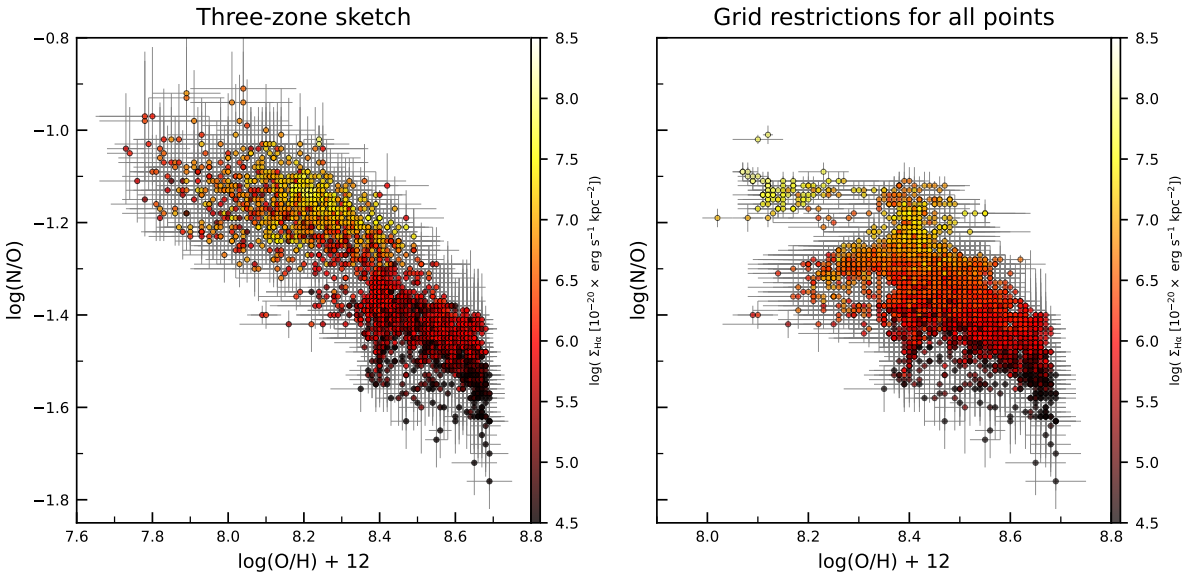

Figure 34 – N/O vs. O/H relation using H II - χ - MISTRY. In the left panel, we run H II - χ - MISTRY using three different grids, one for each of the zones presented in Fig. 30. In the right panel we use the same grid for all points, giving as input the minimum set of emission line fluxes, when H II - χ - MISTRY uses empirical grids of log U vs. log (O/H) and log (N/O) vs. log (O/H) with restrictions based on the space of parameters covered by a sample of EELGs. In both figures a negative slope is observed. The bins are color-coded according to their surface Hα flux ($\Sigma_{H\alpha}$), with an emerging anti-correlation between gas-phase metallicity and SFR.

shown in Fig. 31, we repeat the procedure now for indirect estimates within the [S III] zone, which is presented in Fig. 33. In this relation, it is possible to observe that, although the majority of the points still lie within ±0.2 dex from the identity relation, the indirect abundance determinations are systematically overestimating O and N, which is exactly the "shrinking" effect observed in Fig. 32. One possible cause for these overestimations, which are not observed in the case shown in Fig. 31, is the residual sky line underlying [S II] λ6731 emission line (see §5.1): The artificial boost caused by the sky contamination in the flux of [S II] can result in a decrease of both S-based indices O_3S_2 and N_2S_2, which, given their calibrations with metallicity (Curti et al., 2020b; Pérez-Montero et al., 2021, Equations 3.38 and 3.31), would translate into higher O/H and N/O values.

The metallicity calibrations based on N and S indices will hardly work in the case of ESO 400-43. While N-based indices suffer from the intrinsic assumption of a positive slope in the N/O vs. O/H relation caused by secondary N production, S-based indices will struggle to estimate the metallicity in the outskirts of the galaxy (exactly where we need the calibrations to operate) due to the residual background contamination that is hard to eliminate. Thus, we will have to rely on H II - χ - MISTRY for the metallicity estimates on the outskirts of the galaxy, as photoionization-based codes do not need to assume any prior shape for the N/O vs. O/H (Pérez-Montero, 2014; Vale Asari et al., 2016; Kumari et al., 2018). The N/O vs. O/H relation obtained using H II - χ - MISTRY is shown in Fig. 34.

In the left panel of Fig. 34, we have used the three zones shown in Fig. 30 and

run H II - χ - MISTRY using separate grids for each zone. To increase the grid definition, we allowed for interpolation at the cost of additional computational time. The points in Fig. 34 are color-coded according to the surface density Hα flux, a tracer of recent SFR activity. We avoid color coding the points directly for SFR level due to the metallicity dependence of the calibration between SFR and $Q_{\rm H}$ (Kennicutt, 1998a; Ly et al., 2016; Kumari et al., 2018, see also §3.6). Another reason to use $\Sigma_{\rm H\alpha}$ is that larger bins might have integrated Hα fluxes comparable to individual spaxels in the inner regions, which prevents misleading interpretations. Intriguingly, the points exhibit an anti-correlation between SFR and metallicity, suggesting that recent star formation bursts were likely triggered by the infall of metal-poor gas (Sánchez Almeida et al., 2014; Kumari et al., 2018; del Valle-Espinosa et al., 2023, among many others). Similarly to what has been observed in Fig. 32, in Fig. 34 we also note a puzzling large spread in the estimated metallicities, spanning ∼1 dex. Further investigation is necessary to understand such spread, but one possible explanation is that the starburst was initiated by a merger between ESO 400-43 and a smaller, less metal-rich galaxy. This hypothesis aligns with previous suggestions raised by Östlin et al. (1999), Östlin et al. (2001) and could explain the highly irregular gas rotation pattern observed in §5.1, which is decoupled from the stellar body, which follows the expected solid body rotation curve (Östlin et al., 2001).

At first glance, the presence of two segregated clouds of points in the left panel may also seem intriguing. However, this segregation arises from the fact that this plot mixes points calculated using three different grids. To test this hypothesis, we run H II - χ - MISTRY for all zones providing only the minimum set of emission lines (Hβ, [O III] λ5007, [S II] $\lambda\lambda$6717,31 and [N II] λ6583). In this case, the code relies on the empirical restricted grids shown in Fig. 28. In the right panel it is apparent that the segregation is significantly alleviated, but the points with highest SFR values (corresponding to those where the T_e method is applicable) also shift towards lower values of N/O and O/H. We believe this occurs because of the limitations on the grids from Pérez-Montero et al. (2021) shown in Fig. 28: For 12 + log(O/H) < 8.5, the grid restricts the values of N/O to log(N/O) < -1.0. However, as seen in Fig. 32, N/O in ESO 400-43 can reach values as high as log(N/O) ≈ −0.8. Even though the grid restrictions in Pérez-Montero et al. (2021) were designed for EELGs, the ISM conditions in the most intense starburst regions of ESO 400-43 seem to be even more extreme than those found in EELGs.

As stated at the beginning of this section, these are preliminary results that shall be investigated and discussed in more depth in the near future.

6 Conclusions

In this chapter, we summarize our main findings, dedicating a section to each galaxy. We conclude by proposing ideas that could potentially inspire future follow-up studies of this work.

6.1 SDSS J020536-081424

We have serendipitously found a $z = 0.04025$ irregular emission line source (SDSS J020536-081424) close, in projected distance, to the Early-Type Galaxy Mrk 1172. Using stellar population fitting with STARLIGHT, we determined a stellar mass of $\sim 3 \times 10^9\ M_\odot$ for SDSS J020536-081424 , consistent with typical masses of dwarf galaxies (Lelli, 2022). While the stellar emission of the Early-Type Galaxy is dominated by old stellar populations with $\log t > 10$, SDSS J020536-081424 presented two stellar populations with ages $8.0 \lesssim \log t \lesssim 8.5$ and $t \approx 1\,\mathrm{Gyr}$. A posterior self-consistent stellar population fitting with FADO using larger apertures, when the signal of the continuum is enhanced, revealed the presence of an underlying older stellar component with $t > 2\,\mathrm{Gyr}$ (§4.2).

Using the stellar velocity field of Mrk 1172 and the rotation of the ionized gas in the dwarf, we fit a kinematic model assuming gas orbiting in the plane of a disk, finding an alignment of the line of the nodes, which is interpreted as a sign of interaction between the galaxy pair. Intriguingly, SDSS J020536-081424 exhibits several kpc-sized clumps when observed in Hα. Using Hα velocity-sliced maps, we have shown that the clumps reside in the rotating gas, with morphology resembling a disk undergoing tidal disruption.

Simulations indicate that interactions might reduce the momentum of metal-poor gas in the Intergalactic Medium and/or Circumgalactic Medium, channeling large amounts of gas into the galaxy Interstellar Medium (Muratov et al., 2015; del Valle-Espinosa et al., 2023). Accretion of cold gas is hard to detect directly due to the faint absorption features and low densities of the gas (Sánchez Almeida et al., 2014), but indirect evidence is provided by off-center star-forming regions with increased Star Formation Rates and associated localized drops in the gas-phase metallicity, observed for star-forming dwarf galaxies (Sánchez Almeida et al., 2014; del Valle-Espinosa et al., 2023), tadpole galaxies in the local Universe (Sánchez Almeida et al., 2013) and at $z \gtrsim 2$ (Elmegreen et al., 2007; Elmegreen; Elmegreen, 2010), several spiral galaxies within MaNGA survey (Sánchez-Menguiano et al., 2019; Hwang et al., 2019) and in extremely metal-poor star-forming galaxies (Papaderos et al., 2008; Filho et al., 2013). For detailed reviews on the processes related to the accretion of cold gas, we refer to Tumlinson, Peeples and Werk (2017) and Fox and Davé (2017). In cases where metal-poor gas fuels star formation, an anti-correlation

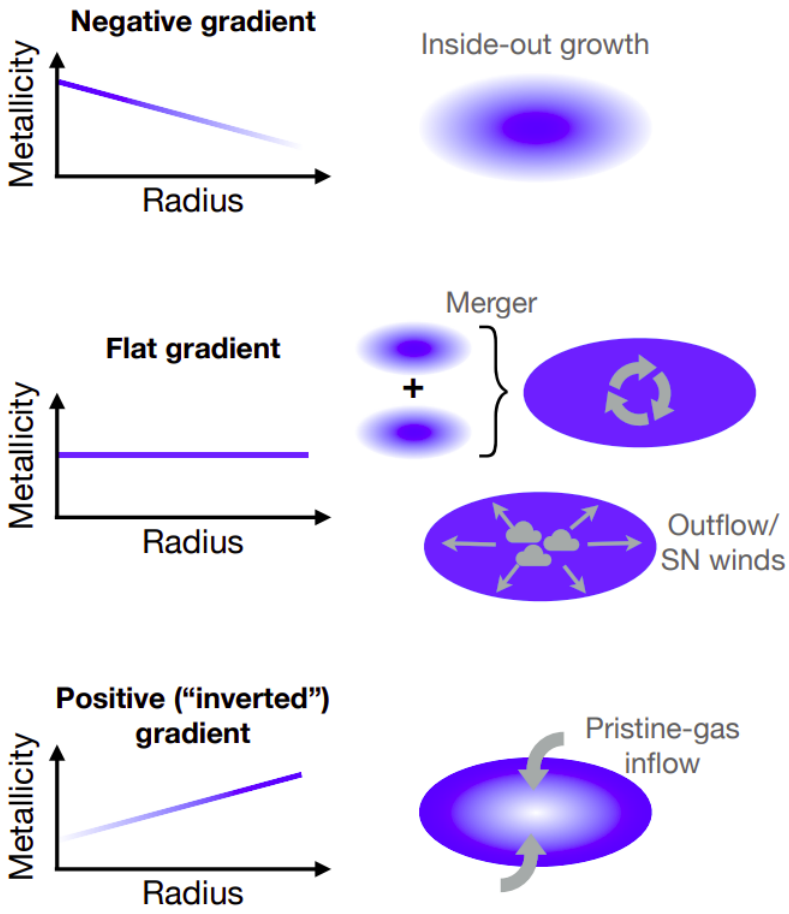

Figure 35 – Illustration of the metallicity gradients produced by different mechanisms. Negative trends (top) represent a classical inside-out growth, with older and chemically evolved stellar populations occupying central galaxy regions (e.g. bulge). Flat gradients (middle) are usually observed in the presence of galactic-scale efficient mechanisms that can redistribute the gas, such as mergers, SN winds and accretion of previously enriched gas expelled from the ISM due to powerful outflows. Inverted metallicity gradient are typically observed in the case of accretion of metal-poor gas. Credit: Venturi et al. (2024).

between gas-phase metallicity and Star Formation Rate is expected to be observed at spaxel resolution (Sánchez Almeida et al., 2018). Accretion of metal-poor gas has been found to be a common driver of star formation and galaxy growth at $z \sim 3$ galaxies, and since the flow of cold gas triggers new episodes of star-formation, an "inverted" metallicity gradient is observed (Cresci et al., 2010; Curti et al., 2020a, see Fig. 35).

With this in mind we inspected this scenario for SDSS J020536-081424 (§4.2), finding a flat relation instead. Although we do not show metallicity radial plots in §4.2, re-arranging the x-axis from SFR to radial distance would hardly change the tight metallicity distribution around the mean. We do not discard the scenario of metal-poor gas accretion as the trigger of clump formation in SDSS J020536-081424 . At $z \approx 0.04$ we are severely limited by spatial resolution, and the metal-poor gas supposedly linked to the younger stellar populations could be simply diluted with the surrounding chemically evolved gas.

Flat metallicity gradients are common among low-mass irregular galaxies (Kobulnicky; Skillman, 1997; van Zee; Haynes, 2006; Matteucci, 2012), with homogeneous distributions of both N and O found in dwarf irregulars (Croxall et al., 2009; Haurberg; Rosenberg; Salzer, 2013) and blue compact dwarfs (Lagos et al., 2014) at spatial scales of $\sim$1 kpc (Bresolin, 2019). Moreover, recent low-resolution JWST/NIRSpec spatially resolved analysis of three $6 \lesssim z \lesssim 8$ galaxies with masses $7.6 \lesssim \log(M/M_{\odot}) \lesssim 9.3$ found evidence of flat metallicity gradients (Venturi et al., 2024). Several mechanisms can produce flat gradients, such as galaxy mergers and interactions (Kewley et al., 2010; Bresolin; Kennicutt; Ryan-Weber, 2012; Torres-Flores et al., 2014), but also alternative large-scale processes able to efficiently mix and redistribute the gas within the ISM. For instance, enriched material can be expelled due to strong Supernova (SN) winds and outflows (Tenorio-Tagle, 1996; Legrand et al., 2000), accretion of previously enriched gas that has been expelled due to intense stellar feedback (Gibson et al., 2013; Ma et al., 2017; Venturi et al., 2024), or, as indicated by simulations, due metal mixing resulting from turbulence driven by gravitational instabilities (Petit et al., 2015).

Hα channel maps and $v_{\mathrm{H}\alpha}$ provide evidence for a possible disk in SDSS J020536-081424 , with the clumps located at this rotating component. Further investigation is required to claim for the existence of a disk, as an alternative hypothesis is that the gas started to rotate in response to the stellar velocity field of Mrk 1172 as SDSS J020536-081424 increasingly approached the ETG. However, the observation of clumps residing in the rotating component led us to suggest they have been formed *in situ* through Violent Disk Instability (see §1.6). Given that clumpy star formation was common among disk galaxies around the Cosmic Noon, with clumpy morphologies in the Local Universe being restricted mainly to low-mass galaxies (see references in §1.6), we believe that SDSS J020536-081424 represents an unique system to study the triggers of clumpy star formation with a spatial resolution that is unfeasible for unlensed $z \approx 2$ star-forming galaxies.

6.2 ESO 400-43

ESO 400-43 is a $z = 0.01965$ Blue Compact Galaxy that exhibits several star clusters in its Interstellar Medium and has a dwarf companion (ESO 400-43*b*) located $\sim$50 kpc in projected distance. Using Hubble Space Telescope multiband photometry, we have estimated the properties of the star cluster population in ESO 400-43 through Spectral Energy Distribution fitting with PROSPECTOR. We have found a total of 220 star clusters, with ages $6.4 \lesssim \log(t\,[\mathrm{yr}]) \lesssim 8.4$ and masses $3.6 \lesssim \log(M/M_{\odot}) \lesssim 6.8$. Approximately 5% of the star cluster population is young ($t < 5$ Myr) and massive ($\log(M/M_{\odot}) > 5.0$), possibly hosting significant numbers of massive stars. These clusters are predominantly located in the regions of ESO 400-43 with higher fluxes of Hα and He II λ4686. The metallicity

distribution of the clusters peaks around 12 + log(O/H) ≈ 8.1. The age-mass diagram of the star clusters indicate a bursty Star Formation History in ESO 400-43 with three starbursts in the last 4 Myr, 10 Myr and 20 Myr.

We have identified He II λ4686 emission across the Interstellar Medium of ESO 400-43 , with increasing intensity correlated with regions showing higher concentration of young and massive star clusters, suggesting that this hard ionization field might be caused by Wolf-Rayet stars. Using an aperture with the size of the Point Spread Function centered on the peak of He II emission, we observed the presence of a broad component, tracing the presence of Wolf-Rayet stars. However, nebular He II emission is also found in regions devoid of young and massive star clusters, which could be caused by fast radiative shocks.

We inspected the ionization mechanism across the Interstellar Medium of ESO 400-43 using the [N II], [S II] and [O I] spatially resolved emission line diagnostic diagrams. In the [S II] and [O I] diagrams, virtually all bins lie above the upper boundary defined by the Kewley et al. (2001) delimiting line. In the [N II] diagram, two separated branches clearly emerge, suggesting the presence of a region of N-enriched gas. Inspecting the regions of ESO 400-43 corresponding to this N-enriched branch, we observe that they are located in the surroundings of the region peaking in He II emission. Combined with the gas-phase metallicity analysis, we conclude that the N enrichment in the Interstellar Medium of ESO 400-43 is likely caused by nucleosynthesized elements ejected from Wolf-Rayet stars. Elevated values of N/O have been recently reported for high-z galaxies observed with James Webb Space Telescope, such as the $z = 10.6$ GN-z11 galaxy (Bunker et al., 2023), stacked spectra of $z \gtrsim 6$ strong emission line sources (Topping et al., 2024), a $z \sim 8$ galaxy with metal-poor gas-phase metallicities but with super-solar N/O ratios (Marques-Chaves et al., 2024), and the $z = 2.37$ gravitationally lensed Sunburst Arc (Vink, 2023; Rivera-Thorsen et al., 2024). In the case of the latter, a value of log(N/O) = -0.74±0.09 is found, about 0.8 dex higher than typical values of H II regions spanning similar gas-phase metallicity values (Rivera-Thorsen et al., 2024). Both chemical evolution models (Kobayashi; Ferrara, 2024) and detections of broad components in He II λ4686 and C IV λ5808 in N-enriched high-z galaxies (Rivera-Thorsen et al., 2024; Welch et al., 2024) have led some authors to suggest Wolf-Rayet and supermassive stars as the dominant source of chemical enrichment in their Interstellar Medium (Charbonnel et al., 2023; Nagele; Umeda, 2023; Senchyna et al., 2024; Welch et al., 2024; Yanagisawa et al., 2024).

The feedback from young star clusters in ESO 400-43 plays an important role in the chemical evolution of the galaxy Interstellar Medium, and ESO 400-43 represents a very interesting case of study to deepen our understanding on the star formation and chemical evolution processes at extreme Interstellar Medium conditions resembling those expected for high-z galaxies.

6.3 Future prospects

With respect to SDSS J020536-081424 , we believe that hydrodynamical simulations represent a natural path to continue investigating the triggers of clumpy star formation. In preliminary simulations conducted by our collaborator Dr. Rubens Machado, it was possible to reproduce realistic orbits for the dwarf, but the simulations could not achieve integrated Star Formation Rate values as high as the observed SFR $= 0.7\,M_{\odot}\,\mathrm{yr}^{-1}$. This might indicate the necessity of a recent past merger between two low-mass galaxies in the simulations to reach the measured SFR level in SDSS J020536-081424 . Additionally, the simulations can help us understand in more detail the role played by the interaction with the ETG in the formation of the clumps. If these clumps were formed from gravitational instabilities in the disk, could the instabilities have been caused by some compression on the disk during the stage of alignment with the stellar motion in the ETG? If that is the case, are the timescales for clump formation related to its increasing proximity with the ETG? Moreover, what is the fate of these clumps? Will they dissolve and form a pseudo-bulge or is SDSS J020536-081424 going to be accreted by Mrk 1172 before that? Hydrodynamical simulations represent powerful tools to try answering such questions.

With respect to ESO 400-43 , we intend to proceed with the analysis presented in §5.2 and publish it as a letter in the Astronomy & Astrophysics journal. We are particularly intrigued by the few spaxels lying above the Kewley et al. (2001) upper boundary in the [N II] diagram (see 5.1), corresponding to the He II emission peak. With the metallicities correctly estimated, one possibility is to use He II/Hβ vs. 12 + log(O/H) proposed by Shirazi and Brinchmann (2012) to distinguish between hard ionization from WR stars and AGN. As mentioned in §2.1, it is known that the stellar body of ESO 400-43 is decoupled from the gas, thus we have particular interest in exploring the galaxy stellar kinematics in the detail MUSE is able to provide. For this, the plan is to use the Ca triplet, which must be carefully separated from the nearby Paschen emission lines. Additionally, we have observed skewed Hα line profiles in the outskirts of the galaxy, indicating the presence of outflows, but broadened emission lines are also observed in the innermost galaxy regions, possibly indicating powerful stellar winds. We have particular interest in performing a multi-component analysis of the Interstellar Medium in ESO 400-43 to determine the physical and chemical properties derived from the broad component, e.g., could it be that when we separate the broad component arising from stellar winds in the N-enriched region, the resulting narrow components would move in the [N II] diagnostic diagram, from the N-enriched branch to the location corresponding to the main branch? We are also collaborators in a MeerKAT proposal submitted very recently, and if accepted, we will participate in the subsequent project relating galaxy properties derived in the optical with those derived from the neutral gas.

Finally, in September 1st I will assume a postdoctoral research position at the

Istituto Nazionale di Astrofisica (INAF) – Osservatoria di Padova, where the main project is related to the effect of the environment on the unwinding of spiral arms. Although unwinding spiral arms are typically associated with interacting galaxies (Pettitt; Tasker; Wadsley, 2016; Pettitt et al., 2017), a recent analysis of a sub-sample of 11 stripped galaxies from GASP[1] (GAs Stripping Phenomena in galaxies with MUSE) proposed that ram-pressure stripping alone is able to induce unwinding structures (Bellhouse et al., 2021), offering observational support for earlier predictions from hydrodynamical simulations (Schulz; Struck, 2001; Steinhauser; Schindler; Springel, 2016). The main project consists of a spatially resolved analysis of a galaxy sample exhibiting unwinding features in 6 local galaxy clusters recently observed with MUSE (P.I.: Vulcani). The research aims to determine how often unwinding spiral arms can be produced by either ram-pressure stripping or tidal interactions alone, and how often these features arise from a combination of both processes.

[1] https://web.oapd.inaf.it/gasp/

Bibliography

Adamo, A. et al. The First Billion Years, According to JWST. *arXiv e-prints*, p. arXiv:2405.21054, maio 2024. Cited in page 34.

Adamo, A. et al. Bound star clusters observed in a lensed galaxy 460 Myr after the Big Bang. *Nature*, v. 632, n. 8025, p. 513–516, ago. 2024. Cited in page 26.

Adamo, A. et al. Star cluster formation in the most extreme environments: insights from the HiPEEC survey. *Monthly Notices of the Royal Astronomical Society*, v. 499, n. 3, p. 3267–3294, dez. 2020. Cited 2 times in pages 25 and 47.

Adamo, A. et al. Probing the role of the galactic environment in the formation of stellar clusters, using M83 as a test bench. *Monthly Notices of the Royal Astronomical Society*, v. 452, n. 1, p. 246–260, set. 2015. Cited in page 25.

Adamo, A.; Östlin, G.; Zackrisson, E. Probing cluster formation under extreme conditions: massive star clusters in blue compact galaxies. *Monthly Notices of the Royal Astronomical Society*, v. 417, n. 3, p. 1904–1912, nov. 2011. Cited 2 times in pages 25 and 27.

Adamo, A. et al. Super star clusters in Haro 11: properties of a very young starburst and evidence for a near-infrared flux excess. *Monthly Notices of the Royal Astronomical Society*, v. 407, n. 2, p. 870–890, set. 2010. Cited 2 times in pages 25 and 26.

Adamo, A. et al. The ages and metallicities of the globular clusters in the Sparkler. *Monthly Notices of the Royal Astronomical Society*, v. 525, n. 1, p. L6–L10, out. 2023. Cited in page 26.

Adamo, A. et al. Star Clusters Near and Far; Tracing Star Formation Across Cosmic Time. *Space Science Reviews*, v. 216, n. 4, p. 69, jun. 2020. Cited 2 times in pages 26 and 27.

Adams, D. et al. Galaxy Zoo: Clump Scout: Surveying the Local Universe for Giant Star-forming Clumps. *Astrophysical Journal*, v. 931, n. 1, p. 16, maio 2022. Cited 2 times in pages 30 and 32.

Agertz, O. et al. Large-scale galactic turbulence: can self-gravity drive the observed H I velocity dispersions? *Monthly Notices of the Royal Astronomical Society*, v. 392, n. 1, p. 294–308, jan. 2009. Cited 2 times in pages 30 and 32.

Ahn, C. P. et al. The Ninth Data Release of the Sloan Digital Sky Survey: First Spectroscopic Data from the SDSS-III Baryon Oscillation Spectroscopic Survey. *Astrophysical Journal, Supplement*, v. 203, n. 2, p. 21, dez. 2012. Cited in page 36.

Akhlaghi, M.; Ichikawa, T. Noise-based Detection and Segmentation of Nebulous Objects. *Astrophysical Journal, Supplement*, v. 220, n. 1, p. 1, set. 2015. Cited in page 49.

Alam, S. et al. The Eleventh and Twelfth Data Releases of the Sloan Digital Sky Survey: Final Data from SDSS-III. *Astrophysical Journal, Supplement*, v. 219, n. 1, p. 12, jul. 2015. Cited in page 46.

Albán, M.; Wylezalek, D. Classifying the full SDSS-IV MaNGA Survey using optical diagnostic diagrams: Presentation of AGN catalogs in flexible apertures. *Astronomy and Astrophysics*, v. 674, p. A85, jun. 2023. Cited in page 75.

Allard, F.; Homeier, D.; Freytag, B. *Model Atmospheres From Very Low Mass Stars to Brown Dwarfs. 16th Cambridge Workshop on Cool Stars, Stellar Systems, and the Sun.* Seattle: Astronomical Society of the Pacific Conference Series, 2011. v. 448. Cited in page 54.

Allen, M. G. et al. The MAPPINGS III Library of Fast Radiative Shock Models. *Astrophysical Journal, Supplement*, v. 178, n. 1, p. 20–55, set. 2008. Cited in page 74.

Alloin, D. et al. Nitrogen and oxygen abundances in galaxies. *Astronomy and Astrophysics*, v. 78, p. 200–216, set. 1979. Cited in page 68.

Alongi, M. et al. Evolutionary sequences of stellar models with semiconvection and convective overshoot. I. $Z = 0.008$. *Astronomy and Astrophysics Supplement Series*, v. 97, p. 851–871, mar. 1993. Cited in page 78.

Amorín, R. et al. The host in blue compact galaxies.. Structural properties and scaling relations. *Astronomy and Astrophysics*, v. 501, n. 1, p. 75–88, jul. 2009. Cited in page 18.

Amorín, R. et al. Extreme emission-line galaxies out to $z \sim 1$ in zCOSMOS. I. Sample and characterization of global properties. *Astronomy and Astrophysics*, v. 578, p. A105, jun. 2015. Cited in page 18.

Amorín, R. et al. Complex Gas Kinematics in Compact, Rapidly Assembling Star-forming Galaxies. *Astrophysical Journal, Letters*, v. 754, n. 2, p. L22, ago. 2012. Cited in page 70.

Amorín, R. O. et al. The stellar host in blue compact dwarf galaxies. The need for a two-dimensional fit. *Astronomy and Astrophysics*, v. 467, n. 2, p. 541–558, maio 2007. Cited in page 18.

Anders, P. et al. Star cluster formation and evolution in the dwarf starburst galaxy NGC 1569. *Monthly Notices of the Royal Astronomical Society*, v. 347, n. 1, p. 17–28, jan. 2004. Cited in page 26.

Anders, P.; Fritze-v. Alvensleben, U. Spectral and photometric evolution of young stellar populations: The impact of gaseous emission at various metallicities. *Astronomy and Astrophysics*, v. 401, p. 1063–1070, abr. 2003. Cited in page 74.

Andrews, B. H.; Martini, P. The Mass-Metallicity Relation with the Direct Method on Stacked Spectra of SDSS Galaxies. *Astrophysical Journal*, v. 765, n. 2, p. 140, mar. 2013. Cited 2 times in pages 21 and 22.

Annibali, F.; Tosi, M. Chemical and stellar properties of star-forming dwarf galaxies. *Nature Astronomy*, v. 6, p. 48–58, jan. 2022. Cited 4 times in pages 16, 17, 20, and 33.

Annibali, F. et al. The Cluster Population of the Irregular Galaxy NGC 4449 as Seen by the Hubble Advanced Camera for Surveys. *Astronomical Journal*, v. 142, n. 4, p. 129, out. 2011. Cited in page 26.

Annibali, F. et al. Young Stellar Populations and Star Clusters in NGC 1705. *Astronomical Journal*, v. 138, n. 1, p. 169–183, jul. 2009. Cited in page 26.

Armah, M. et al. Chemical abundances in Seyfert galaxies - VII. Direct abundance determination of neon based on optical and infrared emission lines. *Monthly Notices of the Royal Astronomical Society*, v. 508, n. 1, p. 371–391, nov. 2021. Cited in page 65.

Ashman, K. M.; Zepf, S. E. *Globular Cluster Systems*. Cambridge: Cambridge University Press, 1998. Cited in page 26.

Asplund, M.; Amarsi, A. M.; Grevesse, N. The chemical make-up of the Sun: A 2020 vision. *Astronomy and Astrophysics*, v. 653, p. A141, set. 2021. Cited in page 70.

Asplund, M. et al. The Chemical Composition of the Sun. *Annual Review of Astronomy and Astrophysics*, v. 47, n. 1, p. 481–522, set. 2009. Cited 2 times in pages 20 and 70.

Atek, H. et al. Most of the photons that reionized the Universe came from dwarf galaxies. *Nature*, v. 626, n. 8001, p. 975–978, fev. 2024. Cited in page 17.

Atek, H. et al. Are Ultra-faint Galaxies at z = 6-8 Responsible for Cosmic Reionization? Combined Constraints from the Hubble Frontier Fields Clusters and Parallels. *Astrophysical Journal*, v. 814, n. 1, p. 69, nov. 2015. Cited in page 16.

Bacon, R. et al. *MPDAF: MUSE Python Data Analysis Framework*. 2016. Astrophysics Source Code Library. Record ascl:1611.003. Available at: <https://ascl.net/1611.003>. Cited in page 50.

Baldwin, J. A.; Phillips, M. M.; Terlevich, R. Classification parameters for the emission-line spectra of extragalactic objects. *Publications of the ASP*, v. 93, p. 5–19, fev. 1981. Cited in page 75.

Barro, G. et al. Extremely Red Galaxies at z = 5–9 with MIRI and NIRSpec: Dusty Galaxies or Obscured Active Galactic Nuclei? *Astrophysical Journal*, v. 963, n. 2, p. 128, mar. 2024. Cited in page 34.

Bassett, R. et al. DYNAMO - II. Coupled stellar and ionized-gas kinematics in two low-redshift clumpy discs. *Monthly Notices of the Royal Astronomical Society*, v. 442, n. 4, p. 3206–3221, ago. 2014. Cited in page 30.

Bastian, N. On the star formation rate - brightest cluster relation: estimating the peak star formation rate in post-merger galaxies. *Monthly Notices of the Royal Astronomical Society*, v. 390, n. 2, p. 759–768, out. 2008. Cited in page 27.

Bastian, N.; Goodwin, S. P. Evidence for the strong effect of gas removal on the internal dynamics of young stellar clusters. *Monthly Notices of the Royal Astronomical Society*, v. 369, n. 1, p. L9–L13, jun. 2006. Cited in page 25.

Belfiore, F. et al. SDSS IV MaNGA - spatially resolved diagnostic diagrams: a proof that many galaxies are LIERs. *Monthly Notices of the Royal Astronomical Society*, v. 461, n. 3, p. 3111–3134, set. 2016. Cited in page 74.

Bellhouse, C. et al. GASP XXIX - unwinding the arms of spiral galaxies via ram-pressure stripping. *Monthly Notices of the Royal Astronomical Society*, v. 500, n. 1, p. 1285–1312, jan. 2021. Cited in page 150.

Bellocchi, E. et al. Uncertainties in gas kinematics arising from stellar continuum modeling in integral field spectroscopy data: the case of NGC 2906 observed with VLT/MUSE. *Astronomy and Astrophysics*, v. 625, p. A83, maio 2019. Cited in page 58.

Berendzen, R.; Hart, R.; Seeley, D. *Man discovers the galaxies*. New York: McGraw-Hill, 1976. Cited in page 15.

Berg, D. A. et al. CHAOS IV: Gas-phase Abundance Trends from the First Four CHAOS Galaxies. *Astrophysical Journal*, v. 893, n. 2, p. 96, abr. 2020. Cited in page 67.

Berg, D. A. et al. Direct Oxygen Abundances for Low-luminosity LVL Galaxies. *Astrophysical Journal*, v. 754, n. 2, p. 98, ago. 2012. Cited in page 69.

Bergvall, N. *Dwarf Galaxies: Keys to Galaxy Formation and Evolution. Star Forming Dwarf Galaxies*. Heidelberg: Astrophysics and Space Science Proceedings, Springer, 2012. v. 28. Cited in page 33.

Bergvall, N.; Jorsater, S. ESO400-G43, a forming galaxy? *Nature*, v. 331, n. 6157, p. 589–591, fev. 1988. Cited 2 times in pages 37 and 38.

Bergvall, N.; Östlin, G. Massive (?) starburst hosts of blue compact galaxies (BCGs). Optical/near-IR observations of 4 BCGs and their companions. *Astronomy and Astrophysics*, v. 390, p. 891–915, ago. 2002. Cited 2 times in pages 18 and 38.

Bertin, E. *Automatic Astrometric and Photometric Calibration with SCAMP*. San Francisco: Astronomical Society of the Pacific Conference Series, 2006. v. 351. 112 p. Cited in page 46.

Bertin, E. *SWarp: Resampling and Co-adding FITS Images Together*. 2010. Astrophysics Source Code Library. Record ascl:1010.068. Available at: <https://ascl.net/1010.068>. Cited in page 47.

Bertoldo-Coêlho, M. et al. SMARTY: The MILES moderate resolution near-infrared stellar library. *Monthly Notices of the Royal Astronomical Society*, v. 530, n. 4, p. 3651–3668, jun. 2024. Cited in page 54.

Biémont, E.; Frémat, Y.; Quinet, P. Ionization Potentials of Atoms and Ions from Lithium to Tin (Z = 50). *Atomic Data and Nuclear Data Tables*, v. 71, p. 117, jan. 1999. Cited in page 65.

Bigiel, F. et al. The Star Formation Law in Nearby Galaxies on Sub-Kpc Scales. *Astronomical Journal*, v. 136, n. 6, p. 2846–2871, dez. 2008. Cited in page 26.

Bik, A. et al. Super star cluster feedback driving ionization, shocks and outflows in the halo of the nearby starburst ESO 338-IG04. *Astronomy and Astrophysics*, v. 619, p. A131, nov. 2018. Cited 2 times in pages 25 and 32.

Binette, L. et al. Photoionization in elliptical galaxies by old stars. *Astronomy and Astrophysics*, v. 292, p. 13–19, dez. 1994. Cited in page 74.

Binggeli, B.; Sandage, A.; Tarenghi, M. Studies of the Virgo Cluster. I. Photometry of 109 galaxies near the cluster center to serve as standards. *Astronomical Journal*, v. 89, p. 64–82, jan. 1984. Cited in page 18.

Binggeli, B.; Tarenghi, M.; Sandage, A. The abundance and morphological segregation of dwarf galaxies in the field. *Astronomy and Astrophysics*, v. 228, p. 42–60, fev. 1990. Cited in page 17.

Binney, J.; Tremaine, S. *Galactic Dynamics: Second Edition*. New Jersey: Princeton University Press, 2008. Cited 2 times in pages 30 and 31.

Bouché, N. et al. Signatures of Cool Gas Fueling a Star-Forming Galaxy at Redshift 2.3. *Science*, v. 341, n. 6141, p. 50–53, jul. 2013. Cited in page 32.

Bournaud, F.; Elmegreen, B. G.; Elmegreen, D. M. Rapid Formation of Exponential Disks and Bulges at High Redshift from the Dynamical Evolution of Clump-Cluster and Chain Galaxies. *Astrophysical Journal*, v. 670, n. 1, p. 237–248, nov. 2007. Cited in page 32.

Bournaud, F. et al. The Long Lives of Giant Clumps and the Birth of Outflows in Gas-rich Galaxies at High Redshift. *Astrophysical Journal*, v. 780, n. 1, p. 57, jan. 2014. Cited in page 30.

Bouwens, R. J. et al. Lower-luminosity Galaxies Could Reionize the Universe: Very Steep Faint-end Slopes to the UV Luminosity Functions at $z \geq 5 - 8$ from the HUDF09 WFC3/IR Observations. *Astrophysical Journal, Letters*, v. 752, n. 1, p. L5, jun. 2012. Cited 2 times in pages 16 and 29.

Bouwens, R. J. et al. UV-continuum Slopes at $z \sim$ 4-7 from the HUDF09+ERS+CANDELS Observations: Discovery of a Well-defined UV Color-Magnitude Relationship for $z \geq 4$ Star-forming Galaxies. *Astrophysical Journal*, v. 754, n. 2, p. 83, ago. 2012. Cited in page 29.

Bouwens, R. J. et al. Reionization After Planck: The Derived Growth of the Cosmic Ionizing Emissivity Now Matches the Growth of the Galaxy UV Luminosity Density. *Astrophysical Journal*, v. 811, n. 2, p. 140, out. 2015. Cited in page 16.

Boylan-Kolchin, M. Stress testing ΛCDM with high-redshift galaxy candidates. *Nature Astronomy*, v. 7, p. 731–735, jun. 2023. Cited in page 34.

Boylan-Kolchin, M.; Bullock, J. S.; Kaplinghat, M. Too big to fail? The puzzling darkness of massive Milky Way subhaloes. *Monthly Notices of the Royal Astronomical Society*, v. 415, n. 1, p. L40–L44, jul. 2011. Cited in page 33.

Boylan-Kolchin, M.; Bullock, J. S.; Kaplinghat, M. The Milky Way's bright satellites as an apparent failure of ΛCDM. *Monthly Notices of the Royal Astronomical Society*, v. 422, n. 2, p. 1203–1218, maio 2012. Cited in page 33.

Bradford, J. D.; Geha, M. C.; Blanton, M. R. A Study in Blue: The Baryon Content of Isolated Low-mass Galaxies. *Astrophysical Journal*, v. 809, n. 2, p. 146, ago. 2015. Cited in page 32.

Bresolin, F. Metallicity gradients in small and nearby spiral galaxies. *Monthly Notices of the Royal Astronomical Society*, v. 488, n. 3, p. 3826–3843, set. 2019. Cited in page 147.

Bresolin, F.; Kennicutt, R. C.; Ryan-Weber, E. Gas Metallicities in the Extended Disks of NGC 1512 and NGC 3621. Chemical Signatures of Metal Mixing or Enriched Gas Accretion? *Astrophysical Journal*, v. 750, n. 2, p. 122, maio 2012. Cited in page 147.

Bresolin, F.; Kennicutt, R. C. J.; Stetson, P. B. An HST Study of OB Associations and Star Clusters in M101. *Astronomical Journal*, v. 112, p. 1009, set. 1996. Cited in page 26.

Bressan, A. et al. Evolutionary Sequences of Stellar Models with New Radiative Opacities. II. $Z = 0.02$. *Astronomy and Astrophysics Supplement Series*, v. 100, p. 647, set. 1993. Cited in page 78.

Brinchmann, J. et al. The physical properties of star-forming galaxies in the low-redshift Universe. *Monthly Notices of the Royal Astronomical Society*, v. 351, n. 4, p. 1151–1179, jul. 2004. Cited in page 18.

Brooks, A. M. et al. The Origin and Evolution of the Mass-Metallicity Relationship for Galaxies: Results from Cosmological N-Body Simulations. *Astrophysical Journal, Letters*, v. 655, n. 1, p. L17–L20, jan. 2007. Cited 2 times in pages 21 and 22.

Bruzual, G.; Charlot, S. Stellar population synthesis at the resolution of 2003. *Monthly Notices of the Royal Astronomical Society*, v. 344, n. 4, p. 1000–1028, out. 2003. Cited in page 58.

Bundy, K. et al. Overview of the SDSS-IV MaNGA Survey: Mapping nearby Galaxies at Apache Point Observatory. *Astrophysical Journal*, v. 798, n. 1, p. 7, jan. 2015. Cited in page 23.

Bunker, A. J. et al. JADES NIRSpec Spectroscopy of GN-z11: Lyman-α emission and possible enhanced nitrogen abundance in a z = 10.60 luminous galaxy. *Astronomy and Astrophysics*, v. 677, p. A88, set. 2023. Cited in page 148.

Burkert, A. et al. High-redshift Star-forming Galaxies: Angular Momentum and Baryon Fraction, Turbulent Pressure Effects, and the Origin of Turbulence. *Astrophysical Journal*, v. 725, n. 2, p. 2324–2332, dez. 2010. Cited in page 30.

Byler, N. et al. Nebular Continuum and Line Emission in Stellar Population Synthesis Models. *Astrophysical Journal*, v. 840, n. 1, p. 44, maio 2017. Cited in page 57.

Calabrò, A. et al. Characterization of star-forming dwarf galaxies at $0.1 \lesssim z \lesssim 0.9$ in VUDS: probing the low-mass end of the mass-metallicity relation. *Astronomy and Astrophysics*, v. 601, p. A95, maio 2017. Cited 2 times in pages 17 and 18.

Caldwell, R.; Kamionkowski, M. Cosmology: Dark matter and dark energy. *Nature*, v. 458, n. 7238, p. 587–589, abr. 2009. Cited in page 15.

Calura, F. et al. The evolution of the mass-metallicity relation in galaxies of different morphological types. *Astronomy and Astrophysics*, v. 504, n. 2, p. 373–388, set. 2009. Cited in page 22.

Calzetti, D. *Star Formation Rate Indicators*. Cambridge: Cambridge University Press, 2013. 419 p. Cited in page 77.

Campbell, A.; Terlevich, R.; Melnick, J. The stellar populations and evolution of H II galaxies - I. High signal-to-noise optical spectroscopy. *Monthly Notices of the Royal Astronomical Society*, v. 223, p. 811–825, dez. 1986. Cited in page 67.

Cantiello, M.; Brocato, E.; Blakeslee, J. P. The star cluster population of the spiral galaxy NGC 3370. *Astronomy and Astrophysics*, v. 503, n. 1, p. 87–101, ago. 2009. Cited in page 26.

Cappellari, M. Improving the full spectrum fitting method: accurate convolution with Gauss-Hermite functions. *Monthly Notices of the Royal Astronomical Society*, v. 466, n. 1, p. 798–811, abr. 2017. Cited 2 times in pages 23 and 56.

Cappellari, M. Full spectrum fitting with photometry in PPXF: stellar population versus dynamical masses, non-parametric star formation history and metallicity for 3200 LEGA-C galaxies at redshift $z \approx 0.8$. *Monthly Notices of the Royal Astronomical Society*, v. 526, p. 3273–3300, 2023. Cited in page 56.

Cappellari, M.; Copin, Y. Adaptive spatial binning of integral-field spectroscopic data using Voronoi tessellations. *Monthly Notices of the Royal Astronomical Society*, v. 342, n. 2, p. 345–354, jun. 2003. Cited in page 138.

Cappellari, M.; Emsellem, E. Parametric Recovery of Line-of-Sight Velocity Distributions from Absorption-Line Spectra of Galaxies via Penalized Likelihood. *Publications of the ASP*, v. 116, n. 816, p. 138–147, fev. 2004. Cited 2 times in pages 23 and 56.

Cardelli, J. A.; Clayton, G. C.; Mathis, J. S. The Relationship between Infrared, Optical, and Ultraviolet Extinction. *Astrophysical Journal*, v. 345, p. 245, out. 1989. Cited 2 times in pages 60 and 139.

Cardoso, L. S. M.; Gomes, J. M.; Papaderos, P. Self-consistent population spectral synthesis with FADO. I. The importance of nebular emission in modelling star-forming galaxies. *Astronomy and Astrophysics*, v. 622, p. A56, fev. 2019. Cited in page 57.

Carnall, A. C. et al. A first look at the SMACS0723 JWST ERO: spectroscopic redshifts, stellar masses, and star-formation histories. *Monthly Notices of the Royal Astronomical Society*, v. 518, n. 1, p. L45–L50, jan. 2023. Cited in page 34.

Carrasco, E. R. et al. *Results from the commissioning of the Gemini South Adaptive Optics Imager (GSAOI) at Gemini South Observatory*. Bellingham, Washington (USA): Society of Photo-Optical Instrumentation Engineers (SPIE), 2012. v. 8447. 84470N p. Cited 4 times in pages 43, 44, 45, and 46.

Carroll, B. W.; Ostlie, D. A. *An introduction to modern astrophysics, Second Edition*. Cambridge: Cambridge University Press, 2017. Cited in page 59.

Casamiquela, L. et al. Differential abundances of open clusters and their tidal tails: Chemical tagging and chemical homogeneity. *Astronomy and Astrophysics*, v. 635, p. A8, mar. 2020. Cited in page 20.

Castellanos, M.; Díaz, A. I.; Terlevich, E. A comprehensive study of reported high-metallicity giant H II regions - I. Detailed abundance analysis. *Monthly Notices of the Royal Astronomical Society*, v. 329, n. 2, p. 315–335, jan. 2002. Cited in page 67.

Cava, A. et al. The nature of giant clumps in distant galaxies probed by the anatomy of the cosmic snake. *Nature Astronomy*, v. 2, p. 76–82, nov. 2018. Cited 3 times in pages 28, 30, and 32.

Ceverino, D.; Dekel, A.; Bournaud, F. High-redshift clumpy discs and bulges in cosmological simulations. *Monthly Notices of the Royal Astronomical Society*, v. 404, n. 4, p. 2151–2169, jun. 2010. Cited in page 32.

Ceverino, D. et al. Gas inflow and metallicity drops in star-forming galaxies. *Monthly Notices of the Royal Astronomical Society*, v. 457, n. 3, p. 2605–2612, abr. 2016. Cited 2 times in pages 21 and 23.

Chabrier, G. Galactic Stellar and Substellar Initial Mass Function. *Publications of the ASP*, v. 115, n. 809, p. 763–795, jul. 2003. Cited 2 times in pages 72 and 77.

Chandar, R. et al. The Fraction of Stars That Form in Clusters in Different Galaxies. *Astrophysical Journal*, v. 849, n. 2, p. 128, nov. 2017. Cited in page 26.

Charbonnel, C. et al. N-enhancement in GN-z11: First evidence for supermassive stars nucleosynthesis in proto-globular clusters-like conditions at high redshift? *Astronomy and Astrophysics*, v. 673, p. L7, maio 2023. Cited in page 148.

Chevance, M. et al. The Life and Times of Giant Molecular Clouds. In: *Protostars and Planets VII*. Seattle: Astronomical Society of the Pacific Conference Series, 2023. v. 534, p. 1. Cited in page 25.

Chies-Santos, A. L. et al. An optical/NIR survey of globular clusters in early-type galaxies. I. Introduction and data reduction procedures. *Astronomy and Astrophysics*, v. 525, p. A19, jan. 2011. Cited in page 27.

Chiosi, C.; Maeder, A. The evolution of massive stars with mass loss. *Annual Review of Astronomy and Astrophysics*, v. 24, p. 329–375, jan. 1986. Cited in page 54.

Chisholm, J. et al. Scaling Relations Between Warm Galactic Outflows and Their Host Galaxies. *Astrophysical Journal*, v. 811, n. 2, p. 149, out. 2015. Cited in page 21.

Choi, E. et al. The Role of Black Hole Feedback on Size and Structural Evolution in Massive Galaxies. *Astrophysical Journal*, v. 866, n. 2, p. 91, out. 2018. Cited in page 18.

Choudhury, T. R.; Ferrara, A. Updating reionization scenarios after recent data. *Monthly Notices of the Royal Astronomical Society*, v. 371, n. 1, p. L55–L59, set. 2006. Cited in page 16.

Choudhury, T. R.; Ferrara, A. Searching for the reionization sources. *Monthly Notices of the Royal Astronomical Society*, v. 380, n. 1, p. L6–L10, set. 2007. Cited in page 16.

Choudhury, T. R.; Ferrara, A.; Gallerani, S. On the minimum mass of reionization sources. *Monthly Notices of the Royal Astronomical Society*, v. 385, n. 1, p. L58–L62, mar. 2008. Cited in page 16.

Christensen, C. R. et al. Tracing Outflowing Metals in Simulations of Dwarf and Spiral Galaxies. *Astrophysical Journal*, v. 867, n. 2, p. 142, nov. 2018. Cited in page 22.

Christian, C. A.; Schommer, R. A. BVI Photometry of Star Clusters in M33. *Astronomical Journal*, v. 95, p. 704, mar. 1988. Cited in page 26.

Chu, Y.-H.; Kennicutt, R. C. J. Kinematic Structure of the 30 Doradus Giant H II Region. *Astrophysical Journal*, v. 425, p. 720, abr. 1994. Cited in page 27.

Cid Fernandes, R. On tests of full spectral fitting algorithms. *Monthly Notices of the Royal Astronomical Society*, v. 480, n. 4, p. 4480–4488, nov. 2018. Cited in page 58.

Cid Fernandes, R. et al. The star formation history of Seyfert 2 nuclei. *Monthly Notices of the Royal Astronomical Society*, v. 355, n. 1, p. 273–296, nov. 2004. Cited in page 74.

Cid Fernandes, R. et al. Semi-empirical analysis of Sloan Digital Sky Survey galaxies - I. Spectral synthesis method. *Monthly Notices of the Royal Astronomical Society*, v. 358, n. 2, p. 363–378, abr. 2005. Cited in page 55.

Cid Fernandes, R. et al. A comprehensive classification of galaxies in the Sloan Digital Sky Survey: how to tell true from fake AGN? *Monthly Notices of the Royal Astronomical Society*, v. 413, n. 3, p. 1687–1699, maio 2011. Cited 2 times in pages 74 and 75.

Claeyssens, A. et al. Star formation at the smallest scales: a JWST study of the clump populations in SMACS0723. *Monthly Notices of the Royal Astronomical Society*, v. 520, n. 2, p. 2180–2203, abr. 2023. Cited 2 times in pages 26 and 32.

Coelho, P. et al. A library of high resolution synthetic stellar spectra from 300 nm to 1.8 μm with solar and α-enhanced composition. *Astronomy and Astrophysics*, v. 443, n. 2, p. 735–746, nov. 2005. Cited in page 54.

Coelho, P. R. T. A new library of theoretical stellar spectra with scaled-solar and α-enhanced mixtures. *Monthly Notices of the Royal Astronomical Society*, v. 440, n. 2, p. 1027–1043, maio 2014. Cited in page 54.

Coelho, P. R. T.; Bruzual, G.; Charlot, S. To use or not to use synthetic stellar spectra in population synthesis models? *Monthly Notices of the Royal Astronomical Society*, v. 491, n. 2, p. 2025–2042, jan. 2020. Cited in page 54.

Conroy, C. Modeling the Panchromatic Spectral Energy Distributions of Galaxies. *Annual Review of Astronomy and Astrophysics*, v. 51, n. 1, p. 393–455, ago. 2013. Cited 2 times in pages 53 and 54.

Conroy, C.; Gunn, J. E.; White, M. The Propagation of Uncertainties in Stellar Population Synthesis Modeling. I. The Relevance of Uncertain Aspects of Stellar Evolution and the Initial Mass Function to the Derived Physical Properties of Galaxies. *Astrophysical Journal*, v. 699, n. 1, p. 486–506, jul. 2009. Cited in page 53.

Conselice, C. J.; Bershady, M. A.; Jangren, A. The Asymmetry of Galaxies: Physical Morphology for Nearby and High-Redshift Galaxies. *Astrophysical Journal*, v. 529, n. 2, p. 886–910, fev. 2000. Cited in page 28.

Cortese, L.; Catinella, B.; Smith, R. The Dawes Review 9: The role of cold gas stripping on the star formation quenching of satellite galaxies. *Publications of the Astronomical Society of Australia*, v. 38, p. e035, ago. 2021. Cited in page 21.

Cowie, L. L.; Hu, E. M.; Songaila, A. Faintest Galaxy Morphologies From HST WFPC2 Imaging of the Hawaii Survey Fields. *Astronomical Journal*, v. 110, p. 1576, out. 1995. Cited in page 28.

Cresci, G. et al. Gas accretion as the origin of chemical abundance gradients in distant galaxies. *Nature*, v. 467, n. 7317, p. 811–813, out. 2010. Cited in page 146.

Croxall, K. V. et al. CHAOS III: Gas-phase Abundances in NGC 5457. *Astrophysical Journal*, v. 830, n. 1, p. 4, out. 2016. Cited in page 67.

Croxall, K. V. et al. Chemical Abundances of Seven Irregular and Three Tidal Dwarf Galaxies in the M81 Group. *Astrophysical Journal*, v. 705, n. 1, p. 723–738, nov. 2009. Cited in page 147.

Cucciati, O. et al. The star formation rate density and dust attenuation evolution over 12 Gyr with the VVDS surveys. *Astronomy and Astrophysics*, v. 539, p. A31, mar. 2012. Cited in page 29.

Curti, M. et al. New fully empirical calibrations of strong-line metallicity indicators in star-forming galaxies. *Monthly Notices of the Royal Astronomical Society*, v. 465, n. 2, p. 1384–1400, fev. 2017. Cited 2 times in pages 68 and 70.

Curti, M. et al. The KLEVER Survey: spatially resolved metallicity maps and gradients in a sample of $1.2 < z < 2.5$ lensed galaxies. *Monthly Notices of the Royal Astronomical Society*, v. 492, n. 1, p. 821–842, fev. 2020. Cited in page 146.

Curti, M. et al. The mass-metallicity and the fundamental metallicity relation revisited on a fully T_e-based abundance scale for galaxies. *Monthly Notices of the Royal Astronomical Society*, v. 491, n. 1, p. 944–964, jan. 2020. Cited 3 times in pages 68, 70, and 143.

Daddi, E. et al. Very High Gas Fractions and Extended Gas Reservoirs in $z = 1.5$ Disk Galaxies. *Astrophysical Journal*, v. 713, n. 1, p. 686–707, abr. 2010. Cited in page 28.

Daddi, E. et al. Multiwavelength Study of Massive Galaxies at $z \sim 2$. I. Star Formation and Galaxy Growth. *Astrophysical Journal*, v. 670, n. 1, p. 156–172, nov. 2007. Cited in page 18.

Dahlen, T. et al. Evolution of the Luminosity Function, Star Formation Rate, Morphology, and Size of Star-forming Galaxies Selected at Rest-Frame 1500 and 2800 Å. *Astrophysical Journal*, v. 654, n. 1, p. 172–185, jan. 2007. Cited in page 29.

Danieli, S.; van Dokkum, P. Revisiting the Size-Luminosity Relation in the Era of Ultra Diffuse Galaxies. *Astrophysical Journal*, v. 875, n. 2, p. 155, abr. 2019. Cited in page 18.

Davé, R.; Finlator, K.; Oppenheimer, B. D. Galaxy evolution in cosmological simulations with outflows - II. Metallicities and gas fractions. *Monthly Notices of the Royal Astronomical Society*, v. 416, n. 2, p. 1354–1376, set. 2011. Cited in page 23.

De Lucia, G.; Blaizot, J. The hierarchical formation of the brightest cluster galaxies. *Monthly Notices of the Royal Astronomical Society*, v. 375, n. 1, p. 2–14, fev. 2007. Cited in page 16.

de Rossi, M. E.; Tissera, P. B.; Scannapieco, C. Clues for the origin of the fundamental metallicity relations - I. The hierarchical building up of the structure. *Monthly Notices of the Royal Astronomical Society*, v. 374, n. 1, p. 323–336, jan. 2007. Cited in page 22.

De Silva, G. M. et al. Chemical Homogeneity in the Hyades. *Astronomical Journal*, v. 131, n. 1, p. 455–460, jan. 2006. Cited in page 20.

Dekel, A. et al. Cold streams in early massive hot haloes as the main mode of galaxy formation. *Nature*, v. 457, n. 7228, p. 451–454, jan. 2009. Cited in page 30.

Dekel, A. et al. Clump survival and migration in VDI galaxies: an analytical model versus simulations and observations. *Monthly Notices of the Royal Astronomical Society*, v. 511, n. 1, p. 316–340, mar. 2022. Cited in page 32.

Dekel, A.; Sari, R.; Ceverino, D. Formation of Massive Galaxies at High Redshift: Cold Streams, Clumpy Disks, and Compact Spheroids. *Astrophysical Journal*, v. 703, n. 1, p. 785–801, set. 2009. Cited 2 times in pages 28 and 30.

del Valle-Espinosa, M. G. et al. Spatially resolved chemodynamics of the starburst dwarf galaxy CGCG 007-025: evidence for recent accretion of metal-poor gas. *Monthly Notices of the Royal Astronomical Society*, v. 522, n. 2, p. 2089–2104, jun. 2023. Cited 4 times in pages 21, 70, 144, and 145.

Desprez, G. et al. ΛCDM not dead yet: massive high-z Balmer break galaxies are less common than previously reported. *Monthly Notices of the Royal Astronomical Society*, v. 530, n. 3, p. 2935–2952, maio 2024. Cited in page 34.

Dessauges-Zavadsky, M. et al. Molecular clouds in the Cosmic Snake normal star-forming galaxy 8 billion years ago. *Nature Astronomy*, v. 3, p. 1115–1121, set. 2019. Cited in page 32.

Dessauges-Zavadsky, M. et al. On the Stellar Masses of Giant Clumps in Distant Star-forming Galaxies. *Astrophysical Journal, Letters*, v. 836, n. 2, p. L22, fev. 2017. Cited in page 30.

Dey, A. et al. Overview of the DESI Legacy Imaging Surveys. *Astronomical Journal*, v. 157, n. 5, p. 168, maio 2019. Cited 2 times in pages 36 and 37.

Dias, B. et al. Age and metallicity of star clusters in the Small Magellanic Cloud from integrated spectroscopy. *Astronomy and Astrophysics*, v. 520, p. A85, set. 2010. Cited in page 58.

Diehl, S.; Statler, T. S. Adaptive binning of X-ray data with weighted Voronoi tessellations. *Monthly Notices of the Royal Astronomical Society*, v. 368, n. 2, p. 497–510, maio 2006. Cited in page 139.

Dopita, M. A. et al. Chemical abundances in high-redshift galaxies: a powerful new emission line diagnostic. *Astrophysics and Space Science*, v. 361, p. 61, fev. 2016. Cited 4 times in pages 68, 69, 70, and 71.

Drinkwater, M. J. et al. The WiggleZ Dark Energy Survey: survey design and first data release. *Monthly Notices of the Royal Astronomical Society*, v. 401, n. 3, p. 1429–1452, jan. 2010. Cited in page 31.

Efstathiou, G. Suppressing the formation of dwarf galaxies via photoionization. *Monthly Notices of the Royal Astronomical Society*, v. 256, n. 2, p. 43P–47P, maio 1992. Cited in page 18.

Eldridge, J. J.; Stanway, E. R. New Insights into the Evolution of Massive Stars and Their Effects on Our Understanding of Early Galaxies. *Annual Review of Astronomy and Astrophysics*, v. 60, p. 455–494, ago. 2022. Cited 2 times in pages 53 and 54.

Eldridge, J. J. et al. Binary Population and Spectral Synthesis Version 2.1: Construction, Observational Verification, and New Results. *Publications of the Astronomical Society of Australia*, v. 34, p. e058, nov. 2017. Cited 2 times in pages 72 and 139.

Ellison, S. L. et al. Clues to the Origin of the Mass-Metallicity Relation: Dependence on Star Formation Rate and Galaxy Size. *Astrophysical Journal, Letters*, v. 672, n. 2, p. L107, jan. 2008. Cited in page 22.

Elmegreen, B. G. Star Formation in a Crossing Time. *Astrophysical Journal*, v. 530, n. 1, p. 277–281, fev. 2000. Cited in page 25.

Elmegreen, B. G. Two Thresholds for Globular Cluster Formation and the Common Occurrence of Massive Clusters in the Early Universe. *Astrophysical Journal*, v. 869, n. 2, p. 119, dez. 2018. Cited in page 24.

Elmegreen, B. G.; Elmegreen, D. M. Tadpole Galaxies in the Hubble Ultra Deep Field. *Astrophysical Journal*, v. 722, n. 2, p. 1895–1907, out. 2010. Cited in page 145.

Elmegreen, B. G. et al. Massive Clumps in Local Galaxies: Comparisons with High-redshift Clumps. *Astrophysical Journal*, v. 774, n. 1, p. 86, set. 2013. Cited in page 30.

Elmegreen, D. M. et al. Resolved Galaxies in the Hubble Ultra Deep Field: Star Formation in Disks at High Redshift. *Astrophysical Journal*, v. 658, n. 2, p. 763–777, abr. 2007. Cited 2 times in pages 30 and 145.

Elmegreen, D. M. et al. Galaxy Morphologies in the Hubble Ultra Deep Field: Dominance of Linear Structures at the Detection Limit. *Astrophysical Journal*, v. 631, n. 1, p. 85–100, set. 2005. Cited in page 28.

Elmegreen, D. M. et al. Galaxy Morphologies in the Hubble Ultra Deep Field: Dominance of Linear Structures at the Detection Limit. *Astrophysical Journal*, v. 631, n. 1, p. 85–100, set. 2005. Cited in page 28.

Erben, T. et al. GaBoDS: The Garching-Bonn Deep Survey. IV. Methods for the image reduction of multi-chip cameras demonstrated on data from the ESO Wide-Field Imager. *Astronomische Nachrichten*, v. 326, n. 6, p. 432–464, jul. 2005. Cited in page 44.

Eriksson, K. B. S.; Pettersson, J. E. New Measurements in the Spectrum of the Neutral Nitrogen Atom. *Physica Scripta*, v. 3, n. 5, p. 211–217, maio 1971. Cited in page 65.

Escala, A.; Larson, R. B. Stability of Galactic Gas Disks and the Formation of Massive Clusters. *Astrophysical Journal, Letters*, v. 685, n. 1, p. L31, set. 2008. Cited in page 30.

ESO CPL Development Team. *EsoRex: ESO Recipe Execution Tool*. 2015. Astrophysics Source Code Library. Record ascl:1504.003. Available at: <https://ascl.net/1504.003>. Cited in page 41.

Euclid Collaboration et al. Euclid preparation. VII. Forecast validation for Euclid cosmological probes. *Astronomy and Astrophysics*, v. 642, p. A191, out. 2020. Cited in page 15.

Fagotto, F. et al. Evolutionary sequences of stellar models with new radiative opacities. III. $Z = 0.0004$ and $Z = 0.05$. *Astronomy and Astrophysics Supplement Series*, v. 104, p. 365–376, abr. 1994. Cited in page 78.

Fagotto, F. et al. Evolutionary sequences of stellar models with new radiative opacities. IV. $Z = 0.004$ and $Z = 0.008$. *Astronomy and Astrophysics Supplement Series*, v. 105, p. 29–38, maio 1994. Cited in page 78.

Fall, S. M.; Efstathiou, G. Formation and rotation of disc galaxies with haloes. *Monthly Notices of the Royal Astronomical Society*, v. 193, p. 189–206, out. 1980. Cited in page 18.

Fensch, J.; Bournaud, F. The role of gas fraction and feedback in the stability and evolution of galactic discs: implications for cosmological galaxy formation models. *Monthly Notices of the Royal Astronomical Society*, v. 505, n. 3, p. 3579–3589, ago. 2021. Cited in page 32.

Ferguson, H. C.; Binggeli, B. Dwarf elliptical galaxies. *Astronomy and Astrophysics Review*, v. 6, n. 1-2, p. 67–122, nov. 1994. Cited in page 17.

Ferland, G. J. et al. The 2013 Release of Cloudy. *Revista Mexicana de Astronomia y Astrofisica*, v. 49, p. 137–163, abr. 2013. Cited in page 72.

Filho, M. E. et al. Extremely Metal-poor Galaxies: The Environment. *Astrophysical Journal*, v. 802, n. 2, p. 82, abr. 2015. Cited in page 20.

Filho, M. E. et al. Extremely metal-poor galaxies: The H I content. *Astronomy and Astrophysics*, v. 558, p. A18, out. 2013. Cited in page 145.

Finkelstein, S. L. et al. The Evolution of the Galaxy Rest-frame Ultraviolet Luminosity Function over the First Two Billion Years. *Astrophysical Journal*, v. 810, n. 1, p. 71, set. 2015. Cited in page 16.

Finlator, K.; Davé, R. The origin of the galaxy mass-metallicity relation and implications for galactic outflows. *Monthly Notices of the Royal Astronomical Society*, v. 385, n. 4, p. 2181–2204, abr. 2008. Cited 2 times in pages 21 and 22.

Fisher, D. B. et al. Connecting Clump Sizes in Turbulent Disk Galaxies to Instability Theory. *Astrophysical Journal, Letters*, v. 839, n. 1, p. L5, abr. 2017. Cited 3 times in pages 30, 32, and 33.

Fisher, D. B. et al. DYNAMO-HST survey: clumps in nearby massive turbulent discs and the effects of clump clustering on kiloparsec scale measurements of clumps. *Monthly Notices of the Royal Astronomical Society*, v. 464, n. 1, p. 491–507, jan. 2017. Cited 3 times in pages 28, 32, and 33.

Fitzpatrick, E. L. Correcting for the Effects of Interstellar Extinction. *Publications of the ASP*, v. 111, n. 755, p. 63–75, jan. 1999. Cited in page 60.

Förster Schreiber, N. M. et al. The SINS Survey: SINFONI Integral Field Spectroscopy of $z \sim 2$ Star-forming Galaxies. *Astrophysical Journal*, v. 706, n. 2, p. 1364–1428, dez. 2009. Cited in page 30.

Förster Schreiber, N. M. et al. Constraints on the Assembly and Dynamics of Galaxies. II. Properties of Kiloparsec-scale Clumps in Rest-frame Optical Emission of z ∼2 Star-forming Galaxies. *Astrophysical Journal*, v. 739, n. 1, p. 45, set. 2011. Cited in page 32.

Förster Schreiber, N. M.; Wuyts, S. Star-Forming Galaxies at Cosmic Noon. *Annual Review of Astronomy and Astrophysics*, v. 58, p. 661–725, ago. 2020. Cited in page 28.

Fox, A.; Davé, R. *Gas Accretion onto Galaxies*. Heidelberg: Springer, 2017. v. 430. Cited in page 145.

Gaia Collaboration et al. Gaia Data Release 3. Summary of the content and survey properties. *Astronomy and Astrophysics*, v. 674, p. A1, jun. 2023. Cited in page 48.

Gallart, C. et al. The ACS LCID Project: On the Origin of Dwarf Galaxy Types—A Manifestation of the Halo Assembly Bias? *Astrophysical Journal, Letters*, v. 811, n. 2, p. L18, out. 2015. Cited in page 18.

Garnett, D. R. Nitrogen in Irregular Galaxies. *Astrophysical Journal*, v. 363, p. 142, nov. 1990. Cited in page 70.

Garnett, D. R. Electron Temperature Variations and the Measurement of Nebular Abundances. *Astronomical Journal*, v. 103, p. 1330, abr. 1992. Cited 3 times in pages 63, 67, and 140.

Geha, M. et al. A Stellar Mass Threshold for Quenching of Field Galaxies. *Astrophysical Journal*, v. 757, n. 1, p. 85, set. 2012. Cited in page 17.

Genzel, R. et al. From Rings to Bulges: Evidence for Rapid Secular Galaxy Evolution at $z \sim 2$ from Integral Field Spectroscopy in the SINS Survey. *Astrophysical Journal*, v. 687, n. 1, p. 59–77, nov. 2008. Cited in page 32.

Genzel, R. et al. The Sins Survey of $z \sim 2$ Galaxy Kinematics: Properties of the Giant Star-forming Clumps. *Astrophysical Journal*, v. 733, n. 2, p. 101, jun. 2011. Cited 2 times in pages 28 and 31.

Gibson, B. K. et al. Constraining sub-grid physics with high-redshift spatially-resolved metallicity distributions. *Astronomy and Astrophysics*, v. 554, p. A47, jun. 2013. Cited in page 147.

Gieles, M. et al. Star cluster disruption by giant molecular clouds. *Monthly Notices of the Royal Astronomical Society*, v. 371, n. 2, p. 793–804, set. 2006. Cited in page 24.

Girardi, L. et al. Evolutionary sequences of stellar models with new radiative opacities. VI. $Z = 0.0001$. *Astronomy and Astrophysics Supplement Series*, v. 117, p. 113–125, maio 1996. Cited in page 78.

Glazebrook, K. et al. A massive galaxy that formed its stars at z ≈ 11. *Nature*, v. 628, n. 8007, p. 277–281, abr. 2024. Cited in page 34.

Goldbaum, N. J.; Krumholz, M. R.; Forbes, J. C. Mass Transport and Turbulence in Gravitationally Unstable Disk Galaxies. II: The Effects of Star Formation Feedback. *Astrophysical Journal*, v. 827, n. 1, p. 28, ago. 2016. Cited in page 32.

Gomes, J. M.; Papaderos, P. Fitting Analysis using Differential evolution Optimization (FADO):. Spectral population synthesis through genetic optimization under self-consistency boundary conditions. *Astronomy and Astrophysics*, v. 603, p. A63, jul. 2017. Cited in page 57.

González Delgado, R. M.; Leitherer, C. Synthetic Spectra of H Balmer and He I Absorption Lines. I. Stellar Library. *Astrophysical Journal, Supplement*, v. 125, n. 2, p. 479–488, dez. 1999. Cited in page 57.

González Delgado, R. M.; Leitherer, C.; Heckman, T. M. Synthetic Spectra of H Balmer and He I Absorption Lines. II. Evolutionary Synthesis Models for Starburst and Poststarburst Galaxies. *Astrophysical Journal, Supplement*, v. 125, n. 2, p. 489–509, dez. 1999. Cited in page 57.

Gonzalez, R. C.; Woods, R. E. *Digital image processing*. Boston: Addison-Wesley, 1992. Cited in page 48.

Goodwin, S. P. Residual gas expulsion from young globular clusters. *Monthly Notices of the Royal Astronomical Society*, v. 284, n. 4, p. 785–802, fev. 1997. Cited in page 25.

Gordon, K. D. et al. A Quantitative Comparison of the Small Magellanic Cloud, Large Magellanic Cloud, and Milky Way Ultraviolet to Near-Infrared Extinction Curves. *Astrophysical Journal*, v. 594, n. 1, p. 279–293, set. 2003. Cited in page 60.

Gouliermis, D. A. Unbound Young Stellar Systems: Star Formation on the Loose. *Publications of the ASP*, v. 130, n. 989, p. 072001, jul. 2018. Cited in page 25.

Green, A. W. et al. DYNAMO - I. A sample of Hα-luminous galaxies with resolved kinematics. *Monthly Notices of the Royal Astronomical Society*, v. 437, n. 2, p. 1070–1095, jan. 2014. Cited in page 32.

Gruppioni, C. et al. The Herschel PEP/HerMES luminosity function - I. Probing the evolution of PACS selected Galaxies to $z \approx 4$. *Monthly Notices of the Royal Astronomical Society*, v. 432, n. 1, p. 23–52, jun. 2013. Cited in page 29.

Guérou, A. et al. The MUSE Hubble Ultra Deep Field Survey. V. Spatially resolved stellar kinematics of galaxies at redshift $0.2 \lesssim z \lesssim 0.8$. *Astronomy and Astrophysics*, v. 608, p. A5, nov. 2017. Cited in page 56.

Gunn, J. E.; Gott J. R., I. On the Infall of Matter Into Clusters of Galaxies and Some Effects on Their Evolution. *Astrophysical Journal*, v. 176, p. 1, ago. 1972. Cited in page 21.

Guo, Y. et al. Clumpy Galaxies in CANDELS. I. The Definition of UV Clumps and the Fraction of Clumpy Galaxies at $0.5 < z < 3$. *Astrophysical Journal*, v. 800, n. 1, p. 39, fev. 2015. Cited in page 30.

Guo, Y. et al. Multi-wavelength View of Kiloparsec-scale Clumps in Star-forming Galaxies at $z \sim 2$. *Astrophysical Journal*, v. 757, n. 2, p. 120, out. 2012. Cited in page 30.

Guo, Y. et al. Clumpy Galaxies in CANDELS. II. Physical Properties of UV-bright Clumps at $0.5 \leq z < 3$. *Astrophysical Journal*, v. 853, n. 2, p. 108, fev. 2018. Cited in page 28.

Guo, Y. et al. The Bursty Star Formation Histories of Low-mass Galaxies at $0.4 < z < 1$ Revealed by Star Formation Rates Measured From Hβ and FUV. *Astrophysical Journal*, v. 833, n. 1, p. 37, dez. 2016. Cited in page 17.

Gurzadyan, G. A. *The Physics and Dynamics of Planetary Nebulae*. Heidelberg: Springer, 1997. Cited in page 57.

Guseva, N. G. et al. New candidates for extremely metal-poor emission-line galaxies in the SDSS/BOSS DR10. *Astronomy and Astrophysics*, v. 579, p. A11, jul. 2015. Cited in page 20.

Halpern, J. P.; Steiner, J. E. Low ionization active galactic nuclei : X-ray or shock heated? *Astrophysical Journal, Letters*, v. 269, p. L37–L41, jun. 1983. Cited in page 74.

Harvey, T. et al. EPOCHS IV: SED Modelling Assumptions and their impact on the Stellar Mass Function at $6.5 < z < 13.5$ using PEARLS and public JWST observations. *arXiv e-prints*, p. arXiv:2403.03908, mar. 2024. Cited in page 34.

Haurberg, N. C.; Rosenberg, J.; Salzer, J. J. Metal Abundances of 12 Dwarf Irregulars from the ADBS Survey. *Astrophysical Journal*, v. 765, n. 1, p. 66, mar. 2013. Cited in page 147.

Hayward, C. C.; Hopkins, P. F. How stellar feedback simultaneously regulates star formation and drives outflows. *Monthly Notices of the Royal Astronomical Society*, v. 465, n. 2, p. 1682–1698, fev. 2017. Cited 2 times in pages 22 and 32.

Heckman, T. M. An Optical and Radio Survey of the Nuclei of Bright Galaxies - Activity in the Normal Galactic Nuclei. *Astronomy and Astrophysics*, v. 87, p. 152, jul. 1980. Cited in page 74.

Henry, R. B. C.; Edmunds, M. G.; Köppen, J. On the Cosmic Origins of Carbon and Nitrogen. *Astrophysical Journal*, v. 541, n. 2, p. 660–674, out. 2000. Cited 2 times in pages 70 and 71.

Hirschauer, A. S. et al. ALFALFA Discovery of the Most Metal-poor Gas-rich Galaxy Known: AGC 198691. *Astrophysical Journal*, v. 822, n. 2, p. 108, maio 2016. Cited in page 20.

Ho, L. C. LINERs as low-luminosity active galactic nuclei. *Advances in Space Research*, v. 23, n. 5-6, p. 813–822, jan. 1999. Cited in page 74.

Hoffmann, S. L. et al. *New Drizzlepac Handbook Version 2.0 Released In Hdox: Updated Documentation For HST Image Analysis*. Washington, DC: American Astronomical Society, 2021. v. 53. 216.02 p. Cited in page 48.

Hopkins, P. F.; Kereš, D.; Murray, N. Accretion does not drive the turbulence in galactic discs. *Monthly Notices of the Royal Astronomical Society*, v. 432, n. 4, p. 2639–2646, jul. 2013. Cited in page 30.

Hopkins, P. F. et al. Galaxies on FIRE (Feedback In Realistic Environments): stellar feedback explains cosmologically inefficient star formation. *Monthly Notices of the Royal Astronomical Society*, v. 445, n. 1, p. 581–603, nov. 2014. Cited in page 17.

Huertas-Company, M. et al. Galaxy morphology from $z \sim 6$ through the lens of JWST. *Astronomy and Astrophysics*, v. 685, p. A48, maio 2024. Cited in page 28.

Hwang, H.-C. et al. Anomalously Low-metallicity Regions in MaNGA Star-forming Galaxies: Accretion Caught in Action? *Astrophysical Journal*, v. 872, n. 2, p. 144, fev. 2019. Cited in page 145.

Ishiyama, T. Hierarchical Formation of Dark Matter Halos and the Free Streaming Scale. *Astrophysical Journal*, v. 788, n. 1, p. 27, jun. 2014. Cited in page 16.

Israelian, G. et al. Galactic evolution of nitrogen. *Astronomy and Astrophysics*, v. 421, p. 649–658, jul. 2004. Cited in page 71.

Izotov, Y. I. et al. Low-redshift compact star-forming galaxies as analogues of high-redshift star-forming galaxies. *Astronomy and Astrophysics*, v. 646, p. A138, fev. 2021. Cited in page 33.

Izotov, Y. I.; Guseva, N. G.; Thuan, T. X. Green Pea Galaxies and Cohorts: Luminous Compact Emission-line Galaxies in the Sloan Digital Sky Survey. *Astrophysical Journal*, v. 728, n. 2, p. 161, fev. 2011. Cited 2 times in pages 57 and 58.

Izotov, Y. I. et al. Abundance patterns in the low-metallicity emission-line galaxies from the Early Data Release of the Sloan Digital Sky Survey. *Astronomy and Astrophysics*, v. 415, p. 87–94, fev. 2004. Cited in page 66.

Izotov, Y. I. et al. The chemical composition of metal-poor emission-line galaxies in the Data Release 3 of the Sloan Digital Sky Survey. *Astronomy and Astrophysics*, v. 448, n. 3, p. 955–970, mar. 2006. Cited 4 times in pages 65, 66, 67, and 140.

Izotov, Y. I.; Thuan, T. X. Heavy-Element Abundances in Blue Compact Galaxies. *Astrophysical Journal*, v. 511, n. 2, p. 639–659, fev. 1999. Cited in page 69.

Izotov, Y. I.; Thuan, T. X.; Guseva, N. G. Hunting for extremely metal-poor emission-line galaxies in the Sloan Digital Sky Survey: MMT and 3.5 m APO observations. *Astronomy and Astrophysics*, v. 546, p. A122, out. 2012. Cited in page 20.

Izotov, Y. I. et al. J0811+4730: the most metal-poor star-forming dwarf galaxy known. *Monthly Notices of the Royal Astronomical Society*, v. 473, n. 2, p. 1956–1966, jan. 2018. Cited in page 20.

Jaskot, A. E.; Ravindranath, S. Photoionization Models for the Semi-forbidden C III] 1909 Emission in Star-forming Galaxies. *Astrophysical Journal*, v. 833, n. 2, p. 136, dez. 2016. Cited in page 73.

Johnson, J. W. et al. Dwarf galaxy archaeology from chemical abundances and star-formation histories. *Monthly Notices of the Royal Astronomical Society*, v. 526, n. 4, p. 5084–5109, dez. 2023. Cited in page 20.

Jones, D. H. et al. The 6dF Galaxy Survey: final redshift release (DR3) and southern large-scale structures. *Monthly Notices of the Royal Astronomical Society*, v. 399, n. 2, p. 683–698, out. 2009. Cited in page 37.

Kakkad, D. et al. Spatially resolved electron density in the narrow line region of $z < 0.02$ radio AGNs. *Astronomy and Astrophysics*, v. 618, p. A6, out. 2018. Cited 2 times in pages 62 and 63.

Karachentsev, I. D. et al. A Catalog of Neighboring Galaxies. *Astronomical Journal*, v. 127, n. 4, p. 2031–2068, abr. 2004. Cited in page 17.

Karachentsev, I. D.; Makarov, D. I.; Kaisina, E. I. Updated Nearby Galaxy Catalog. *Astronomical Journal*, v. 145, n. 4, p. 101, abr. 2013. Cited in page 17.

Kauffmann, G. et al. The host galaxies of active galactic nuclei. *Monthly Notices of the Royal Astronomical Society*, v. 346, n. 4, p. 1055–1077, dez. 2003. Cited 2 times in pages 75 and 76.

Keel, W. C. et al. AGN photoionization of gas in companion galaxies as a probe of AGN radiation in time and direction. *Monthly Notices of the Royal Astronomical Society*, v. 483, n. 4, p. 4847–4865, mar. 2019. Cited in page 74.

Keenan, F. P. et al. Nebular and Auroral Emission Lines of [Ar IV] in the Optical Spectra of Planetary Nebulae. *Astrophysical Journal*, v. 487, n. 1, p. 457–462, set. 1997. Cited in page 61.

Kehrig, C. et al. Uncovering multiple Wolf-Rayet star clusters and the ionized ISM in Mrk 178: the closest metal-poor Wolf-Rayet H II galaxy. *Monthly Notices of the Royal Astronomical Society*, v. 432, n. 4, p. 2731–2745, jul. 2013. Cited in page 69.

Kennicutt, R. C.; Evans, N. J. Star Formation in the Milky Way and Nearby Galaxies. *Annual Review of Astronomy and Astrophysics*, v. 50, p. 531–608, set. 2012. Cited in page 24.

Kennicutt, R. C. J. Star Formation in Galaxies Along the Hubble Sequence. *Annual Review of Astronomy and Astrophysics*, v. 36, p. 189–232, jan. 1998. Cited 3 times in pages 28, 77, and 144.

Kennicutt, R. C. J. The Global Schmidt Law in Star-forming Galaxies. *Astrophysical Journal*, v. 498, n. 2, p. 541–552, maio 1998. Cited in page 26.

Kennicutt R. C., J.; Kent, S. M. A survey of H-alpha emission in normal galaxies. *Astronomical Journal*, v. 88, p. 1094–1107, ago. 1983. Cited in page 77.

Kennicutt R. C., J.; Tamblyn, P.; Congdon, C. E. Past and Future Star Formation in Disk Galaxies. *Astrophysical Journal*, v. 435, p. 22, nov. 1994. Cited in page 77.

Kewley, L. J. et al. Theoretical Evolution of Optical Strong Lines across Cosmic Time. *Astrophysical Journal*, v. 774, n. 2, p. 100, set. 2013. Cited in page 73.

Kewley, L. J. et al. Theoretical Modeling of Starburst Galaxies. *Astrophysical Journal*, v. 556, n. 1, p. 121–140, jul. 2001. Cited 4 times in pages 75, 76, 148, and 149.

Kewley, L. J. et al. The host galaxies and classification of active galactic nuclei. *Monthly Notices of the Royal Astronomical Society*, v. 372, n. 3, p. 961–976, nov. 2006. Cited 3 times in pages 74, 75, and 76.

Kewley, L. J. et al. Metallicity Gradients and Gas Flows in Galaxy Pairs. *Astrophysical Journal, Letters*, v. 721, n. 1, p. L48–L52, set. 2010. Cited 2 times in pages 70 and 147.

Kirby, E. N. et al. The Universal Stellar Mass-Stellar Metallicity Relation for Dwarf Galaxies. *Astrophysical Journal*, v. 779, n. 2, p. 102, dez. 2013. Cited in page 20.

Klessen, R. S. et al. Quiescent and Coherent Cores from Gravoturbulent Fragmentation. *Astrophysical Journal*, v. 620, n. 2, p. 786–794, fev. 2005. Cited in page 25.

Klypin, A. et al. Where Are the Missing Galactic Satellites? *Astrophysical Journal*, v. 522, n. 1, p. 82–92, set. 1999. Cited in page 33.

Kniazev, A. Y. et al. Discovery of Eight New Extremely Metal Poor Galaxies in the Sloan Digital Sky Survey. *Astrophysical Journal, Letters*, v. 593, n. 2, p. L73–L76, ago. 2003. Cited 3 times in pages 20, 68, and 138.

Knowles, A. T. et al. sMILES SSPs: a library of semi-empirical MILES stellar population models with variable [α/Fe] abundances. *Monthly Notices of the Royal Astronomical Society*, v. 523, n. 3, p. 3450–3470, ago. 2023. Cited in page 54.

Kobayashi, C.; Ferrara, A. Rapid Chemical Enrichment by Intermittent Star Formation in GN-z11. *Astrophysical Journal, Letters*, v. 962, n. 1, p. L6, fev. 2024. Cited 2 times in pages 20 and 148.

Kobulnicky, H. A.; Skillman, E. D. Elemental Abundance Variations and Chemical Enrichment from Massive Stars in Starbursts. II. NGC 1569. *Astrophysical Journal*, v. 489, n. 2, p. 636–655, nov. 1997. Cited 2 times in pages 70 and 147.

Komatsu, E. et al. Seven-year Wilkinson Microwave Anisotropy Probe (WMAP) Observations: Cosmological Interpretation. *Astrophysical Journal, Supplement*, v. 192, n. 2, p. 18, fev. 2011. Cited in page 16.

Kormendy, J. Brightness distributions in compact and normal galaxies. II. Structure parameters of the spheroidal component. *Astrophysical Journal*, v. 218, p. 333–346, dez. 1977. Cited in page 18.

Kormendy, J. Families of ellipsoidal stellar systems and the formation of dwarf elliptical galaxies. *Astrophysical Journal*, v. 295, p. 73–79, ago. 1985. Cited in page 18.

Koski, A. T. Spectrophotometry of Seyfert 2 galaxies and narrow-line radio galaxies. *Astrophysical Journal*, v. 223, p. 56–73, jul. 1978. Cited in page 74.

Kovač, K.; Oosterloo, T. A.; van der Hulst, J. M. A blind H I survey in the Canes Venatici region. *Monthly Notices of the Royal Astronomical Society*, v. 400, n. 2, p. 743–765, dez. 2009. Cited in page 17.

Kreckel, K. et al. A physically motivated "charge-exchange method" for measuring electron temperatures within H II regions. *Astronomy and Astrophysics*, v. 667, p. A16, nov. 2022. Cited in page 65.

Krueger, H.; Fritze-v. Alvensleben, U.; Loose, H. H. Optical and near infrared spectral energy distributions. of blue compact galaxies from evolutionary synthesis. *Astronomy and Astrophysics*, v. 303, p. 41, nov. 1995. Cited in page 57.

Kruijssen, J. M. D. On the fraction of star formation occurring in bound stellar clusters. *Monthly Notices of the Royal Astronomical Society*, v. 426, n. 4, p. 3008–3040, nov. 2012. Cited in page 26.

Krumholz, M. R.; McKee, C. F. How do bound star clusters form? *Monthly Notices of the Royal Astronomical Society*, v. 494, n. 1, p. 624–641, maio 2020. Cited in page 25.

Ku, H. Notes on the use of propagation of error formulas. *Journal of Research of the National Bureau of Standards: Engineering and Instrumentation*, National Bureau of Standards, v. 70C, p. 263, out. 1966. Cited in page 198.

Kumari, N. et al. O/H-N/O: the curious case of NGC 4670. *Monthly Notices of the Royal Astronomical Society*, v. 476, n. 3, p. 3793–3815, maio 2018. Cited 5 times in pages 67, 70, 73, 143, and 144.

Kumari, N. et al. Metallicity calibrations for diffuse ionized gas and low-ionization emission regions. *Monthly Notices of the Royal Astronomical Society*, v. 485, n. 1, p. 367–381, maio 2019. Cited in page 68.

Kunth, D.; Maurogordato, S.; Vigroux, L. CCD observations of blue compact galaxies : a mixed bag of morphological types. *Astronomy and Astrophysics*, v. 204, p. 10–20, out. 1988. Cited in page 18.

Kunth, D.; Östlin, G. The most metal-poor galaxies. *Astronomy and Astrophysics Review*, v. 10, p. 1–79, jan. 2000. Cited 2 times in pages 20 and 33.

Kurucz, R. L. Model atmospheres for G, F, A, B, and O stars. *Astrophysical Journal, Supplement*, v. 40, p. 1–340, maio 1979. Cited in page 54.

Kurucz, R. L. *Model Atmospheres for Population Synthesis*. Cambridge: Cambridge University Press – Proceedings of the International Astronomical Union, 1992. v. 149. 225 p. Cited in page 54.

Kurucz, R. L. Including all the lines. *Canadian Journal of Physics*, v. 89, p. 417–428, abr. 2011. Cited in page 54.

Labbé, I. et al. A population of red candidate massive galaxies 600 Myr after the Big Bang. *Nature*, v. 616, n. 7956, p. 266–269, abr. 2023. Cited in page 34.

Lacerda, E. A. D. et al. Diffuse ionized gas in galaxies across the Hubble sequence at the CALIFA resolution. *Monthly Notices of the Royal Astronomical Society*, v. 474, n. 3, p. 3727–3739, mar. 2018. Cited in page 74.

Lada, C. J.; Lada, E. A. Embedded Clusters in Molecular Clouds. *Annual Review of Astronomy and Astrophysics*, v. 41, p. 57–115, jan. 2003. Cited 2 times in pages 25 and 26.

Lagos, P. et al. On the properties of the interstellar medium in extremely metal-poor blue compact dwarf galaxies. GMOS-IFU spectroscopy and SDSS photometry of the double-knot galaxy HS 2236+1344. *Astronomy and Astrophysics*, v. 569, p. A110, set. 2014. Cited in page 147.

Lanz, T.; Hubeny, I. A Grid of Non-LTE Line-blanketed Model Atmospheres of O-Type Stars. *Astrophysical Journal, Supplement*, v. 146, n. 2, p. 417–441, jun. 2003. Cited in page 55.

Laor, A. A Note on the Viability of Gaseous Ionization in Active Galaxies by Fast Shocks. *Astrophysical Journal, Letters*, v. 496, n. 2, p. L71–L74, abr. 1998. Cited in page 74.

Lara-López, M. A. et al. A fundamental plane for field star-forming galaxies. *Astronomy and Astrophysics*, v. 521, p. L53, out. 2010. Cited in page 23.

Larsen, S. S. The Luminosity Function of Star Clusters in Spiral Galaxies. *Astronomical Journal*, v. 124, n. 3, p. 1393–1409, set. 2002. Cited in page 27.

Larsen, S. S. The mass function of young star clusters in spiral galaxies. *Astronomy and Astrophysics*, v. 494, n. 2, p. 539–551, fev. 2009. Cited in page 25.

Larsen, S. S.; Richtler, T. Young massive star clusters in nearby galaxies . I. Identification and general properties of the cluster systems. *Astronomy and Astrophysics*, v. 345, p. 59–72, maio 1999. Cited 2 times in pages 25 and 26.

Larson, R. B. Turbulence and star formation in molecular clouds. *Monthly Notices of the Royal Astronomical Society*, v. 194, p. 809–826, mar. 1981. Cited in page 25.

Lassen, A. E. et al. The metal-poor dwarf irregular galaxy candidate next to Mrk 1172. *Monthly Notices of the Royal Astronomical Society*, v. 506, n. 3, p. 3527–3539, set. 2021. Cited in page 36.

Le Borgne, J. F. et al. STELIB: A library of stellar spectra at $R \sim 2000$. *Astronomy and Astrophysics*, v. 402, p. 433–442, maio 2003. Cited in page 58.

Legrand, F. et al. A continuous low star formation rate in IZw 18? *Astronomy and Astrophysics*, v. 355, p. 891–899, mar. 2000. Cited in page 147.

Leitherer, C.; Robert, C.; Heckman, T. M. Atlas of Synthetic Ultraviolet Spectra of Massive Star Populations. *Astrophysical Journal, Supplement*, v. 99, p. 173, jul. 1995. Cited in page 77.

Lelli, F. Gas dynamics in dwarf galaxies as testbeds for dark matter and galaxy evolution. *Nature Astronomy*, v. 6, p. 35–47, jan. 2022. Cited 2 times in pages 17 and 145.

Lequeux, J. et al. Chemical Composition and Evolution of Irregular and Blue Compact Galaxies. *Astronomy and Astrophysics*, v. 80, p. 155, dez. 1979. Cited 2 times in pages 21 and 22.

Levenberg, K. A method for the solution of certain non-linear problems in least squares. *Quarterly of applied mathematics*, v. 2, n. 2, p. 164–168, 1944. Cited in page 50.

Lilly, S. J. et al. The Canada-France Redshift Survey: The Luminosity Density and Star Formation History of the Universe to z approximately 1. *Astrophysical Journal, Letters*, v. 460, p. L1, mar. 1996. Cited 2 times in pages 28 and 29.

Lind, K.; Bergemann, M.; Asplund, M. Non-LTE line formation of Fe in late-type stars - II. 1D spectroscopic stellar parameters. *Monthly Notices of the Royal Astronomical Society*, v. 427, n. 1, p. 50–60, nov. 2012. Cited in page 55.

Liu, F. et al. The chemical compositions of solar twins in the open cluster M67. *Monthly Notices of the Royal Astronomical Society*, v. 463, n. 1, p. 696–704, nov. 2016. Cited in page 20.

Livermore, R. C. et al. Resolved spectroscopy of gravitationally lensed galaxies: global dynamics and star-forming clumps on ∼100 pc scales at $1 < z < 4$. *Monthly Notices of the Royal Astronomical Society*, v. 450, n. 2, p. 1812–1835, jun. 2015. Cited in page 30.

Looser, T. J. et al. The stellar Fundamental Metallicity Relation: The correlation between stellar mass, star-formation rate and stellar metallicity. *Monthly Notices of the Royal Astronomical Society*, jun. 2024. Cited 2 times in pages 23 and 24.

López-Sánchez, Á. R. et al. Eliminating error in the chemical abundance scale for extragalactic H II regions. *Monthly Notices of the Royal Astronomical Society*, v. 426, n. 4, p. 2630–2651, nov. 2012. Cited in page 67.

López-Sánchez, Á. R.; Esteban, C. Massive star formation in Wolf-Rayet galaxies. IV. Colours, chemical-composition analysis and metallicity-luminosity relations. *Astronomy and Astrophysics*, v. 517, p. A85, jul. 2010. Cited 2 times in pages 20 and 70.

López-Sánchez, Á. R. et al. Ionized gas in the XUV disc of the NGC 1512/1510 system. *Monthly Notices of the Royal Astronomical Society*, v. 450, n. 4, p. 3381–3409, jul. 2015. Cited in page 61.

López-Sanjuan, C. et al. The dominant role of mergers in the size evolution of massive early-type galaxies since $z \sim 1$. *Astronomy and Astrophysics*, v. 548, p. A7, dez. 2012. Cited in page 18.

Lotz, J. M. et al. The Major and Minor Galaxy Merger Rates at $z < 1.5$. *Astrophysical Journal*, v. 742, n. 2, p. 103, dez. 2011. Cited 2 times in pages 28 and 29.

Lovell, C. C. et al. Extreme value statistics of the halo and stellar mass distributions at high redshift: are JWST results in tension with ΛCDM? *Monthly Notices of the Royal Astronomical Society*, v. 518, n. 2, p. 2511–2520, jan. 2023. Cited in page 34.

Luridiana, V.; Morisset, C.; Shaw, R. A. PyNeb: a new tool for analyzing emission lines. I. Code description and validation of results. *Astronomy and Astrophysics*, v. 573, p. A42, jan. 2015. Cited 2 times in pages 63 and 65.

Ly, C. et al. The Metal Abundances across Cosmic Time (MACT) Survey. I. Optical Spectroscopy in the Subaru Deep Field. *Astrophysical Journal, Supplement*, v. 226, n. 1, p. 5, set. 2016. Cited 3 times in pages 77, 78, and 144.

Ma, X. et al. Why do high-redshift galaxies show diverse gas-phase metallicity gradients? *Monthly Notices of the Royal Astronomical Society*, v. 466, n. 4, p. 4780–4794, abr. 2017. Cited in page 147.

Madau, P.; Dickinson, M. Cosmic Star-Formation History. *Annual Review of Astronomy and Astrophysics*, v. 52, p. 415–486, ago. 2014. Cited 2 times in pages 28 and 29.

Madau, P. et al. High-redshift galaxies in the Hubble Deep Field: colour selection and star formation history to $z \sim 4$. *Monthly Notices of the Royal Astronomical Society*, v. 283, n. 4, p. 1388–1404, dez. 1996. Cited 2 times in pages 28 and 29.

Madau, P.; Haardt, F. Cosmic Reionization after Planck: Could Quasars Do It All? *Astrophysical Journal, Letters*, v. 813, n. 1, p. L8, nov. 2015. Cited in page 17.

Madau, P.; Pozzetti, L.; Dickinson, M. The Star Formation History of Field Galaxies. *Astrophysical Journal*, v. 498, n. 1, p. 106–116, maio 1998. Cited in page 77.

Magic, Z. et al. The Stagger-grid: A grid of 3D stellar atmosphere models. II. Horizontal and temporal averaging and spectral line formation. *Astronomy and Astrophysics*, v. 560, p. A8, dez. 2013. Cited in page 55.

Magnelli, B. et al. Evolution of the dusty infrared luminosity function from $z = 0$ to $z = 2.3$ using observations from Spitzer. *Astronomy and Astrophysics*, v. 528, p. A35, abr. 2011. Cited in page 29.

Magnelli, B. et al. The deepest Herschel-PACS far-infrared survey: number counts and infrared luminosity functions from combined PEP/GOODS-H observations. *Astronomy and Astrophysics*, v. 553, p. A132, maio 2013. Cited in page 29.

Magrini, L. et al. Scaling relations of metallicity, stellar mass and star formation rate in metal-poor starbursts - II. Theoretical models. *Monthly Notices of the Royal Astronomical Society*, v. 427, n. 2, p. 1075–1088, dez. 2012. Cited in page 22.

Maiolino, R.; Mannucci, F. De re metallica: the cosmic chemical evolution of galaxies. *Astronomy and Astrophysics Review*, v. 27, n. 1, p. 3, fev. 2019. Cited 5 times in pages 22, 23, 68, 70, and 73.

Mandelker, N. et al. The population of giant clumps in simulated high-z galaxies: in situ and ex situ migration and survival. *Monthly Notices of the Royal Astronomical Society*, v. 443, n. 4, p. 3675–3702, out. 2014. Cited in page 30.

Mannucci, F. et al. A fundamental relation between mass, star formation rate and metallicity in local and high-redshift galaxies. *Monthly Notices of the Royal Astronomical Society*, v. 408, n. 4, p. 2115–2127, nov. 2010. Cited in page 23.

Marasco, A.; Fraternali, F.; Binney, J. J. Supernova-driven gas accretion in the Milky Way. *Monthly Notices of the Royal Astronomical Society*, v. 419, n. 2, p. 1107–1120, jan. 2012. Cited 2 times in pages 21 and 70.

Maraston, C. Evolutionary population synthesis: models, analysis of the ingredients and application to high-z galaxies. *Monthly Notices of the Royal Astronomical Society*, v. 362, n. 3, p. 799–825, set. 2005. Cited in page 54.

Marino, R. A. et al. The O_3N_2 and N_2 abundance indicators revisited: improved calibrations based on CALIFA and T_e-based literature data. *Astronomy and Astrophysics*, v. 559, p. A114, nov. 2013. Cited 4 times in pages 68, 69, 72, and 73.

Marquardt, D. W. An algorithm for least-squares estimation of nonlinear parameters. *Journal of the society for Industrial and Applied Mathematics*, SIAM, v. 11, p. 431–441, 1963. Cited in page 50.

Marques-Chaves, R. et al. Extreme N-emitters at high redshift: Possible signatures of supermassive stars and globular cluster or black hole formation in action. *Astronomy and Astrophysics*, v. 681, p. A30, jan. 2024. Cited in page 148.

Martin, D. C. et al. The Galaxy Evolution Explorer: A Space Ultraviolet Survey Mission. *Astrophysical Journal, Letters*, v. 619, n. 1, p. L1–L6, jan. 2005. Cited in page 36.

Martins, L. P.; Coelho, P. Testing the accuracy of synthetic stellar libraries. *Monthly Notices of the Royal Astronomical Society*, v. 381, n. 4, p. 1329–1346, nov. 2007. Cited in page 55.

Martins, L. P. et al. A high-resolution stellar library for evolutionary population synthesis. *Monthly Notices of the Royal Astronomical Society*, v. 358, n. 1, p. 49–65, mar. 2005. Cited in page 54.

Mashchenko, S.; Wadsley, J.; Couchman, H. M. P. Stellar Feedback in Dwarf Galaxy Formation. *Science*, v. 319, n. 5860, p. 174, jan. 2008. Cited in page 21.

Mateo, M. L. Dwarf Galaxies of the Local Group. *Annual Review of Astronomy and Astrophysics*, v. 36, p. 435–506, jan. 1998. Cited in page 20.

Matteucci, F. Abundance ratios in ellipticals and galaxy formation. *Astronomy and Astrophysics*, v. 288, p. 57–64, ago. 1994. Cited 2 times in pages 21 and 22.

Matteucci, F. *Chemical Evolution of Galaxies*. Berlin: Springer Nature, 2012. Cited 2 times in pages 20 and 147.

McConnachie, A. W. The Observed Properties of Dwarf Galaxies in and around the Local Group. *Astronomical Journal*, v. 144, n. 1, p. 4, jul. 2012. Cited in page 18.

McGregor, P. et al. *Ground-based Instrumentation for Astronomy: Gemini South Adaptive Optics Imager (GSAOI)*. Bellingham, Washington (USA): Society of Photo-Optical Instrumentation Engineers (SPIE), 2004. v. 5492. 1033-1044 p. Cited 2 times in pages 43 and 44.

Messa, M. et al. The young star cluster population of M51 with LEGUS - I. A comprehensive study of cluster formation and evolution. *Monthly Notices of the Royal Astronomical Society*, v. 473, n. 1, p. 996–1018, jan. 2018. Cited in page 25.

Messa, M. et al. Star-forming clumps in the Lyman Alpha Reference Sample of galaxies - I. Photometric analysis and clumpiness. *Monthly Notices of the Royal Astronomical Society*, v. 487, n. 3, p. 4238–4260, ago. 2019. Cited 4 times in pages 27, 28, 32, and 33.

Meynet, G.; Maeder, A. Stellar evolution with rotation. XI. Wolf-Rayet star populations at different metallicities. *Astronomy and Astrophysics*, v. 429, p. 581–598, jan. 2005. Cited in page 69.

Micheva, G. et al. Deep multiband surface photometry on a sample of 24 blue compact galaxies - I. *Monthly Notices of the Royal Astronomical Society*, v. 431, n. 1, p. 102–144, maio 2013. Cited 2 times in pages 38 and 39.

Miller, B. W. The Star Formation Histories of Sculptor Group Dwarf Galaxies. I. Current Star Formation Rates and Oxygen Abundances. *Astronomical Journal*, v. 112, p. 991, set. 1996. Cited in page 20.

Miller, B. W.; Hodge, P. Spectroscopy of H II Regions in M81 Group Dwarf Galaxies. *Astrophysical Journal*, v. 458, p. 467, fev. 1996. Cited in page 20.

Mitra, S.; Choudhury, T. R.; Ferrara, A. Cosmic reionization after Planck II: contribution from quasars. *Monthly Notices of the Royal Astronomical Society*, v. 473, n. 1, p. 1416–1425, jan. 2018. Cited in page 17.

Mo, H.; van den Bosch, F. C.; White, S. *Galaxy Formation and Evolution*. Cambridge: Cambridge University Press, 2010. Cited 2 times in pages 16 and 74.

Mo, H. J.; Mao, S.; White, S. D. M. The formation of galactic discs. *Monthly Notices of the Royal Astronomical Society*, v. 295, n. 2, p. 319–336, abr. 1998. Cited in page 18.

Moffat, A. F. J. A Theoretical Investigation of Focal Stellar Images in the Photographic Emulsion and Application to Photographic Photometry. *Astronomy and Astrophysics*, v. 3, p. 455, dez. 1969. Cited in page 49.

Mohr, P. J.; Taylor, B. N. CODATA recommended values of the fundamental physical constants: 2002. *Reviews of Modern Physics*, American Physical Society, v. 77, p. 1–107, Mar 2005. Available at: <https://link.aps.org/doi/10.1103/RevModPhys.77.1>. Cited in page 65.

Mollá, M.; García-Vargas, M. L.; Bressan, A. PopStar I: evolutionary synthesis model description. *Monthly Notices of the Royal Astronomical Society*, v. 398, n. 1, p. 451–470, 08 2009. ISSN 0035-8711. Available at: <https://doi.org/10.1111/j.1365-2966.2009.15160.x>. Cited 2 times in pages 57 and 72.

Mollá, M. et al. The nitrogen-to-oxygen evolution in galaxies: the role of the star formation rate. *Monthly Notices of the Royal Astronomical Society*, v. 372, n. 3, p. 1069–1080, nov. 2006. Cited in page 70.

Momcheva, I. G. et al. Nebular Attenuation in Hα-selected Star-forming Galaxies at $z = 0.8$ from the NewHα Survey. *Astronomical Journal*, v. 145, n. 2, p. 47, fev. 2013. Cited in page 61.

Moore, B. et al. Dark Matter Substructure within Galactic Halos. *Astrophysical Journal, Letters*, v. 524, n. 1, p. L19–L22, out. 1999. Cited in page 33.

Moore, C. E. Selected tables of atomic spectra-a atomic energy levels-b multiplet tables: O I data derived from the analyses of optical spectra. U.S. Government printing office, 1976. Cited in page 65.

Mouhcine, M. et al. Simulating the mass-metallicity relation from z $\sim$ 1. *Astronomy and Astrophysics*, v. 486, n. 3, p. 711–720, ago. 2008. Cited in page 22.

Mowla, L. et al. The Sparkler: Evolved High-redshift Globular Cluster Candidates Captured by JWST. *Astrophysical Journal, Letters*, v. 937, n. 2, p. L35, out. 2022. Cited in page 26.

Muratov, A. L. et al. Gusty, gaseous flows of FIRE: galactic winds in cosmological simulations with explicit stellar feedback. *Monthly Notices of the Royal Astronomical Society*, v. 454, n. 3, p. 2691–2713, dez. 2015. Cited in page 145.

Nagele, C.; Umeda, H. Multiple Channels for Nitrogen Pollution by Metal-enriched Supermassive Stars and Implications for GN-z11. *Astrophysical Journal, Letters*, v. 949, n. 1, p. L16, maio 2023. Cited in page 148.

Nakajima, K.; Ouchi, M. Ionization state of inter-stellar medium in galaxies: evolution, SFR-M_*-Z dependence, and ionizing photon escape. *Monthly Notices of the Royal Astronomical Society*, v. 442, n. 1, p. 900–916, jul. 2014. Cited in page 73.

Neichel, B. et al. Gemini multiconjugate adaptive optics system review - II. Commissioning, operation and overall performance. *Monthly Notices of the Royal Astronomical Society*, v. 440, n. 2, p. 1002–1019, maio 2014. Cited in page 43.

Newville, M. et al. *lmfit/lmfit-py: 1.3.1*. Zenodo, 2024. Available at: <https://zenodo.org/records/11813>. Cited in page 50.

Nicholls, D. C.; Kewley, L. J.; Sutherland, R. S. Estimating Electron Temperatures in Ionized Nebulae: The Direct Method and its Limitations. *Publications of the ASP*, v. 132, n. 1009, p. 033001, mar. 2020. Cited in page 61.

Nicholls, D. C. et al. Abundance scaling in stars, nebulae and galaxies. *Monthly Notices of the Royal Astronomical Society*, v. 466, n. 4, p. 4403–4422, abr. 2017. Cited in page 71.

Nieva, M. F.; Przybilla, N. Present-day cosmic abundances. A comprehensive study of nearby early B-type stars and implications for stellar and Galactic evolution and interstellar dust models. *Astronomy and Astrophysics*, v. 539, p. A143, mar. 2012. Cited in page 71.

Noeske, K. G. et al. New insights to the photometric structure of Blue Compact Dwarf Galaxies from deep near-infrared studies. II. The sample of northern BCDs. *Astronomy and Astrophysics*, v. 429, p. 115–127, jan. 2005. Cited in page 18.

Noeske, K. G. et al. Star Formation in AEGIS Field Galaxies since $z = 1.1$: The Dominance of Gradually Declining Star Formation, and the Main Sequence of Star-forming Galaxies. *Astrophysical Journal, Letters*, v. 660, n. 1, p. L43–L46, maio 2007. Cited in page 18.

Noguchi, M. Early Evolution of Disk Galaxies: Formation of Bulges in Clumpy Young Galactic Disks. *Astrophysical Journal*, v. 514, n. 1, p. 77–95, mar. 1999. Cited in page 30.

Oesch, P. A. et al. Structure and Morphologies of $z \sim 7 - 8$ Galaxies from Ultra-deep WFC3/IR Imaging of the Hubble Ultra-deep Field. *Astrophysical Journal, Letters*, v. 709, n. 1, p. L21–L25, jan. 2010. Cited in page 18.

Oklopčić, A. et al. Giant clumps in the FIRE simulations: a case study of a massive high-redshift galaxy. *Monthly Notices of the Royal Astronomical Society*, v. 465, n. 1, p. 952–969, fev. 2017. Cited in page 32.

Osterbrock, D. E.; Ferland, G. J. *Astrophysics of gaseous nebulae and active galactic nuclei*. New York: University Science Books, 2006. Cited 6 times in pages 57, 60, 61, 62, 64, and 65.

Östlin, G. et al. Dynamics of blue compact galaxies, as revealed by their Hα velocity fields. II. Mass models and the starburst triggering mechanism. *Astronomy and Astrophysics*, v. 374, p. 800–823, ago. 2001. Cited 3 times in pages 37, 38, and 144.

Östlin, G. et al. Dynamics of blue compact galaxies, as revealed by their Hα velocity fields. I. The data, velocity fields and rotation curves. *Astronomy and Astrophysics Supplement Series*, v. 137, p. 419–444, jun. 1999. Cited 2 times in pages 38 and 144.

Östlin, G.; Bergvall, N.; Roennback, J. Globular clusters in the blue compact galaxy ESO 338-IG04 (Tololo 1924-416), as tracers of the star formation history. Results from HST/WFPC2 observations. *Astronomy and Astrophysics*, v. 335, p. 85–112, jul. 1998. Cited in page 26.

Östlin, G. et al. Stellar dynamics of blue compact galaxies. I. Decoupled star-gas kinematics in ESO 400-G43. *Astronomy and Astrophysics*, v. 419, p. L43–L47, maio 2004. Cited in page 38.

Östlin, G. et al. The temporal and spatial evolution of the starburst in ESO 338-IG04 as probed by its star clusters. *Astronomy and Astrophysics*, v. 408, p. 887–903, set. 2003. Cited 2 times in pages 25 and 26.

Ouchi, M. et al. Large Area Survey for $z = 7$ Galaxies in SDF and GOODS-N: Implications for Galaxy Formation and Cosmic Reionization. *Astrophysical Journal*, v. 706, n. 2, p. 1136–1151, dez. 2009. Cited in page 16.

Pacheco, T. A. et al. A Grid of Synthetic Spectra for Subdwarfs: Non-LTE Line-blanketed Atmosphere Models. *Astrophysical Journal, Supplement*, v. 256, n. 2, p. 41, out. 2021. Cited in page 55.

Padoan, P. et al. Supernova Driving. I. The Origin of Molecular Cloud Turbulence. *Astrophysical Journal*, v. 822, n. 1, p. 11, maio 2016. Cited in page 25.

Pagel, B. E. J. et al. The primordial helium abundance from observations of extragalactic H II regions. *Monthly Notices of the Royal Astronomical Society*, v. 255, p. 325–345, mar. 1992. Cited in page 67.

Pandya, V. et al. Galaxies Going Bananas: Inferring the 3D Geometry of High-redshift Galaxies with JWST-CEERS. *Astrophysical Journal*, v. 963, n. 1, p. 54, mar. 2024. Cited in page 28.

Papaderos, P. et al. Extremely metal-poor star-forming galaxies. New detections and general morphological and photometric properties. *Astronomy and Astrophysics*, v. 491, n. 1, p. 113–129, nov. 2008. Cited 2 times in pages 20 and 145.

Papaderos, P. et al. Optical structure and star formation in blue compact dwarf galaxies. I. Observations and profile decomposition. *Astronomy and Astrophysics Supplement Series*, v. 120, p. 207–228, dez. 1996. Cited in page 18.

Peebles, P. J. E. *The large-scale structure of the universe*. New Jersey: Princeton University Press, 1980. Cited in page 16.

Peimbert, M. Temperature Determinations of H II Regions. *Astrophysical Journal*, v. 150, p. 825, dez. 1967. Cited in page 65.

Peimbert, M.; Costero, R. Chemical Abundances in Galactic H II Regions. *Boletin de los Observatorios Tonantzintla y Tacubaya*, v. 5, p. 3–22, maio 1969. Cited in page 65.

Pérez-Montero, E. Deriving model-based T_e-consistent chemical abundances in ionized gaseous nebulae. *Monthly Notices of the Royal Astronomical Society*, v. 441, n. 3, p. 2663–2675, jul. 2014. Cited 4 times in pages 72, 73, 138, and 143.

Pérez-Montero, E. Ionized Gaseous Nebulae Abundance Determination from the Direct Method. *Publications of the ASP*, v. 129, n. 974, p. 043001, abr. 2017. Cited 6 times in pages 61, 63, 65, 66, 67, and 140.

Pérez-Montero, E. et al. Extreme emission-line galaxies in SDSS - I. Empirical and model-based calibrations of chemical abundances. *Monthly Notices of the Royal Astronomical Society*, v. 504, n. 1, p. 1237–1252, jun. 2021. Cited 6 times in pages 70, 73, 138, 139, 143, and 144.

Pérez-Montero, E.; Contini, T. The impact of the nitrogen-to-oxygen ratio on ionized nebula diagnostics based on [N II] emission lines. *Monthly Notices of the Royal Astronomical Society*, v. 398, n. 2, p. 949–960, set. 2009. Cited 3 times in pages 68, 70, and 71.

Pérez-Montero, E. et al. The dependence of oxygen and nitrogen abundances on stellar mass from the CALIFA survey. *Astronomy and Astrophysics*, v. 595, p. A62, out. 2016. Cited in page 72.

Pérez-Montero, E. et al. Are Wolf-Rayet Stars Able to Pollute the Interstellar Medium of Galaxies? Results from Integral Field Spectroscopy. *Advances in Astronomy*, v. 2013, p. 837392, jan. 2013. Cited in page 69.

Pérez-Montero, E. et al. The softness diagram for MaNGA star-forming regions: diffuse ionized gas contamination or local HOLMES predominance? *Astronomy and Astrophysics*, v. 669, p. A88, jan. 2023. Cited in page 75.

Petit, A. C. et al. Mixing and transport of metals by gravitational instability-driven turbulence in galactic discs. *Monthly Notices of the Royal Astronomical Society*, v. 449, n. 3, p. 2588–2597, maio 2015. Cited 2 times in pages 70 and 147.

Pettini, M.; Pagel, B. E. J. [O III]/[N II] as an abundance indicator at high redshift. *Monthly Notices of the Royal Astronomical Society*, v. 348, n. 3, p. L59–L63, mar. 2004. Cited in page 68.

Pettini, M. et al. C, N, O abundances in the most metal-poor damped Lyman alpha systems. *Monthly Notices of the Royal Astronomical Society*, v. 385, n. 4, p. 2011–2024, abr. 2008. Cited in page 70.

Pettitt, A. R.; Tasker, E. J.; Wadsley, J. W. Gas and stellar spiral structures in tidally perturbed disc galaxies. *Monthly Notices of the Royal Astronomical Society*, v. 458, n. 4, p. 3990–4007, jun. 2016. Cited in page 150.

Pettitt, A. R. et al. Star formation and ISM morphology in tidally induced spiral structures. *Monthly Notices of the Royal Astronomical Society*, v. 468, n. 4, p. 4189–4204, jul. 2017. Cited in page 150.

Pilyugin, L. S. et al. On the electron temperatures in high-metallicity H II regions. *Monthly Notices of the Royal Astronomical Society*, v. 398, n. 1, p. 485–496, set. 2009. Cited in page 67.

Pipino, A.; Calura, F.; Matteucci, F. The two regimes of the cosmic sSFR evolution are due to spheroids and discs. *Monthly Notices of the Royal Astronomical Society*, v. 432, n. 3, p. 2541–2548, jul. 2013. Cited in page 22.

Planck Collaboration et al. Planck 2013 results. XVI. Cosmological parameters. *Astronomy and Astrophysics*, v. 571, p. A16, nov. 2014. Cited 2 times in pages 36 and 37.

Planck Collaboration et al. Planck 2015 results. XIV. Dark energy and modified gravity. *Astronomy and Astrophysics*, v. 594, p. A14, set. 2016. Cited in page 15.

Poggianti, B. M. et al. GASP XXIII: A Jellyfish Galaxy as an Astrophysical Laboratory of the Baryonic Cycle. *Astrophysical Journal*, v. 887, n. 2, p. 155, dez. 2019. Cited in page 21.

Polyachenko, V. L.; Polyachenko, E. V.; Strel'Nikov, A. V. Stability criteria for gaseous self-gravitating disks. *Astronomy Letters*, v. 23, n. 4, p. 483–491, jul. 1997. Cited in page 32.

Pottasch, S. R.; Bernard-Salas, J.; Roellig, T. L. Abundances of planetary nebula NGC 2392. *Astronomy and Astrophysics*, v. 481, n. 2, p. 393–400, abr. 2008. Cited in page 65.

Pustilnik, S. A.; Martin, J. M. H I study of extremely metal-deficient dwarf galaxies. I. The Nançay radio telescope observations of twenty-two objects. *Astronomy and Astrophysics*, v. 464, n. 3, p. 859–869, mar. 2007. Cited in page 20.

Putman, M. E. et al. The Gas Content and Stripping of Local Group Dwarf Galaxies. *Astrophysical Journal*, v. 913, n. 1, p. 53, maio 2021. Cited in page 17.

Qi, Y. et al. Stellar proper motions in the outskirts of classical dwarf spheroidal galaxies with Gaia EDR3. *Monthly Notices of the Royal Astronomical Society*, v. 512, n. 4, p. 5601–5619, jun. 2022. Cited in page 19.

Raman, C. V.; Krishnan, K. S. A New Type of Secondary Radiation. *Nature*, v. 121, n. 3048, p. 501–502, mar. 1928. Cited in page 43.

Rasmussen, J.; Ponman, T. J.; Mulchaey, J. S. Gas stripping in galaxy groups - the case of the starburst spiral NGC 2276. *Monthly Notices of the Royal Astronomical Society*, v. 370, n. 1, p. 453–467, jul. 2006. Cited in page 21.

Rathborne, J. M. et al. Molecular Clouds and Clumps in the Boston University-Five College Radio Astronomy Observatory Galactic Ring Survey. *Astrophysical Journal, Supplement*, v. 182, n. 1, p. 131–142, maio 2009. Cited in page 25.

Reddy, N. A.; Steidel, C. C. A Steep Faint-End Slope of the UV Luminosity Function at $z \sim 2 - 3$: Implications for the Global Stellar Mass Density and Star Formation in Low-Mass Halos. *Astrophysical Journal*, v. 692, n. 1, p. 778–803, fev. 2009. Cited in page 29.

Reines, A. E. et al. The Importance of Nebular Continuum and Line Emission in Observations of Young Massive Star Clusters. *Astrophysical Journal*, v. 708, n. 1, p. 26–37, jan. 2010. Cited in page 57.

Renzini, A.; Fusi Pecci, F. Tests of evolutionary sequences using color-magnitude diagrams of globular clusters. *Annual Review of Astronomy and Astrophysics*, v. 26, p. 199–244, jan. 1988. Cited in page 54.

Revaz, Y. The compactness of ultra-faint dwarf galaxies: A new challenge? *Astronomy and Astrophysics*, v. 679, p. A2, nov. 2023. Cited 2 times in pages 18 and 19.

Revaz, Y.; Jablonka, P. Pushing back the limits: detailed properties of dwarf galaxies in a ΛCDM universe. *Astronomy and Astrophysics*, v. 616, p. A96, ago. 2018. Cited 2 times in pages 21 and 33.

Ribeiro, B. et al. The VIMOS Ultra-Deep Survey: A major merger origin for the high fraction of galaxies at $2 < z < 6$ with two bright clumps. *Astronomy and Astrophysics*, v. 608, p. A16, nov. 2017. Cited in page 30.

Riffel, R. et al. Observational constraints on the stellar recycled gas in active galactic nuclei feeding. *Monthly Notices of the Royal Astronomical Society*, v. 531, n. 1, p. 554–574, jun. 2024. Cited in page 74.

Riffel, R. et al. Mapping the stellar population and gas excitation of MaNGA galaxies with MEGACUBES. Results for AGN versus control sample. *Monthly Notices of the Royal Astronomical Society*, v. 524, n. 4, p. 5640–5657, out. 2023. Cited in page 75.

Riffel, R. et al. Probing the near-infrared stellar population of Seyfert galaxies. *Monthly Notices of the Royal Astronomical Society*, v. 400, n. 1, p. 273–290, nov. 2009. Cited in page 74.

Rigaut, F. et al. Gemini multiconjugate adaptive optics system review - I. Design, trade-offs and integration. *Monthly Notices of the Royal Astronomical Society*, v. 437, n. 3, p. 2361–2375, jan. 2014. Cited in page 43.

Rigby, A. J. et al. CHIMPS: physical properties of molecular clumps across the inner Galaxy. *Astronomy and Astrophysics*, v. 632, p. A58, dez. 2019. Cited 2 times in pages 24 and 25.

Rivera-Thorsen, T. E. et al. The Sunburst Arc with JWST: Detection of Wolf-Rayet stars injecting nitrogen into a low-metallicity, $z = 2.37$ proto-globular cluster leaking ionizing photons. *arXiv e-prints*, p. arXiv:2404.08884, abr. 2024. Cited 2 times in pages 20 and 148.

Robertson, B. E. Galaxy Formation and Reionization: Key Unknowns and Expected Breakthroughs by the James Webb Space Telescope. *Annual Review of Astronomy and Astrophysics*, v. 60, p. 121–158, ago. 2022. Cited in page 17.

Robotham, A. S. G.; Driver, S. P. The GALEX-SDSS NUV and FUV flux density and local star formation rate. *Monthly Notices of the Royal Astronomical Society*, v. 413, n. 4, p. 2570–2582, jun. 2011. Cited in page 29.

Rogers, N. S. J. et al. CHAOS. VI. Direct Abundances in NGC 2403. *Astrophysical Journal*, v. 915, n. 1, p. 21, jul. 2021. Cited 2 times in pages 67 and 140.

Roman-Duval, J. et al. Physical Properties and Galactic Distribution of Molecular Clouds Identified in the Galactic Ring Survey. *Astrophysical Journal*, v. 723, n. 1, p. 492–507, nov. 2010. Cited in page 25.

Roman-Oliveira, F. V. et al. OMEGA-OSIRIS mapping of emission-line galaxies in A901/2-V. The rich population of jellyfish galaxies in the multicluster system Abell 901/2. *Monthly Notices of the Royal Astronomical Society*, v. 484, n. 1, p. 892–905, mar. 2019. Cited in page 21.

Rybicki, G. B.; Lightman, A. P. *Radiative Processes in Astrophysics*. Weinheim: Wiley-VCH Publishers Inc., 1986. Cited in page 57.

Ryden, B. *Introduction to cosmology*. Cambridge: Cambridge University Press, 2003. Cited 2 times in pages 15 and 16.

Sabbadin, F.; Minello, S.; Bianchini, A. Sharpless 176: a large, nearby planetary nebula. *Astronomy and Astrophysics*, v. 60, p. 147–149, ago. 1977. Cited in page 68.

Sales, L. V.; Wetzel, A.; Fattahi, A. Baryonic solutions and challenges for cosmological models of dwarf galaxies. *Nature Astronomy*, v. 6, p. 897–910, jun. 2022. Cited in page 33.

Salpeter, E. E. The Luminosity Function and Stellar Evolution. *Astrophysical Journal*, v. 121, p. 161, jan. 1955. Cited in page 77.

Sánchez Almeida, J. et al. Automatic Unsupervised Classification of All Sloan Digital Sky Survey Data Release 7 Galaxy Spectra. *Astrophysical Journal*, v. 714, n. 1, p. 487–504, maio 2010. Cited in page 73.

Sánchez Almeida, J. et al. Local anticorrelation between star formation rate and gas-phase metallicity in disc galaxies. *Monthly Notices of the Royal Astronomical Society*, v. 476, n. 4, p. 4765–4781, jun. 2018. Cited in page 146.

Sánchez Almeida, J. et al. Star formation sustained by gas accretion. *Astronomy and Astrophysics Review*, v. 22, p. 71, jul. 2014. Cited in page 145.

Sánchez Almeida, J. et al. Localized Starbursts in Dwarf Galaxies Produced by the Impact of Low-metallicity Cosmic Gas Clouds. *Astrophysical Journal, Letters*, v. 810, n. 2, p. L15, set. 2015. Cited in page 21.

Sánchez Almeida, J. et al. Metallicity Inhomogeneities in Local Star-forming Galaxies as a Sign of Recent Metal-poor Gas Accretion. *Astrophysical Journal*, v. 783, n. 1, p. 45, mar. 2014. Cited 3 times in pages 21, 144, and 145.

Sánchez Almeida, J. et al. Local Tadpole Galaxies: Dynamics and Metallicity. *Astrophysical Journal*, v. 767, n. 1, p. 74, abr. 2013. Cited in page 145.

Sánchez-Blázquez, P. et al. Medium-resolution Isaac Newton Telescope library of empirical spectra. *Monthly Notices of the Royal Astronomical Society*, v. 371, n. 2, p. 703–718, set. 2006. Cited in page 54.

Sánchez-Menguiano, L. et al. Characterizing the Local Relation between Star Formation Rate and Gas-phase Metallicity in MaNGA Spiral Galaxies. *Astrophysical Journal*, v. 882, n. 1, p. 9, set. 2019. Cited in page 145.

Sánchez, S. F. Spatially Resolved Spectroscopic Properties of Low-Redshift Star-Forming Galaxies. *Annual Review of Astronomy and Astrophysics*, v. 58, p. 99–155, ago. 2020. Cited in page 75.

Sánchez, S. F. et al. CALIFA, the Calar Alto Legacy Integral Field Area survey. I. Survey presentation. *Astronomy and Astrophysics*, v. 538, p. A8, fev. 2012. Cited in page 69.

Sanders, D. B. et al. The IRAS Revised Bright Galaxy Sample. *Astronomical Journal*, v. 126, n. 4, p. 1607–1664, out. 2003. Cited in page 29.

Sanders, R. L. et al. The MOSDEF Survey: The Evolution of the Mass-Metallicity Relation from $z = 0$ to $z \sim 3.3$. *Astrophysical Journal*, v. 914, n. 1, p. 19, jun. 2021. Cited in page 68.

Sargent, W. L. W.; Searle, L. Isolated Extragalactic H II Regions. *Astrophysical Journal, Letters*, v. 162, p. L155, dez. 1970. Cited in page 18.

Sarzi, M. et al. The SAURON project - XVI. On the sources of ionization for the gas in elliptical and lenticular galaxies. *Monthly Notices of the Royal Astronomical Society*, v. 402, n. 4, p. 2187–2210, mar. 2010. Cited in page 74.

Savage, B. D.; Mathis, J. S. Observed properties of interstellar dust. *Annual Review of Astronomy and Astrophysics*, v. 17, p. 73–111, jan. 1979. Cited in page 60.

Schenker, M. A. et al. The UV Luminosity Function of Star-forming Galaxies via Dropout Selection at Redshifts $z \sim 7$ and 8 from the 2012 Ultra Deep Field Campaign. *Astrophysical Journal*, v. 768, n. 2, p. 196, maio 2013. Cited in page 29.

Schiminovich, D. et al. The GALEX-VVDS Measurement of the Evolution of the Far-Ultraviolet Luminosity Density and the Cosmic Star Formation Rate. *Astrophysical Journal, Letters*, v. 619, n. 1, p. L47–L50, jan. 2005. Cited in page 29.

Schirmer, M. THELI: Convenient Reduction of Optical, Near-infrared, and Mid-infrared Imaging Data. *Astrophysical Journal, Supplement*, v. 209, n. 2, p. 21, dez. 2013. Cited 3 times in pages 44, 46, and 47.

Schlafly, E. F.; Finkbeiner, D. P. Measuring Reddening with Sloan Digital Sky Survey Stellar Spectra and Recalibrating SFD. *Astrophysical Journal*, v. 737, n. 2, p. 103, ago. 2011. Cited in page 58.

Schlegel, D. J.; Finkbeiner, D. P.; Davis, M. Maps of Dust Infrared Emission for Use in Estimation of Reddening and Cosmic Microwave Background Radiation Foregrounds. *Astrophysical Journal*, v. 500, n. 2, p. 525–553, jun. 1998. Cited 2 times in pages 58 and 59.

Schruba, A.; Bialy, S.; Sternberg, A. The Metallicity Dependence of the H I Shielding Layers in Nearby Galaxies. *Astrophysical Journal*, v. 862, n. 2, p. 110, ago. 2018. Cited in page 25.

Schruba, A.; Kruijssen, J. M. D.; Leroy, A. K. How Galactic Environment Affects the Dynamical State of Molecular Clouds and Their Star Formation Efficiency. *Astrophysical Journal*, v. 883, n. 1, p. 2, set. 2019. Cited in page 25.

Schulz, S.; Struck, C. Multi stage three-dimensional sweeping and annealing of disc galaxies in clusters. *Monthly Notices of the Royal Astronomical Society*, v. 328, n. 1, p. 185–202, nov. 2001. Cited in page 150.

Searle, L.; Sargent, W. L. W. Inferences from the Composition of Two Dwarf Blue Galaxies. *Astrophysical Journal*, v. 173, p. 25, abr. 1972. Cited in page 20.

Senchyna, P. et al. GN-z11 in Context: Possible Signatures of Globular Cluster Precursors at Redshift 10. *Astrophysical Journal*, v. 966, n. 1, p. 92, maio 2024. Cited in page 148.

Serenelli, A. et al. Weighing stars from birth to death: mass determination methods across the HRD. *Astronomy and Astrophysics Review*, v. 29, n. 1, p. 4, dez. 2021. Cited in page 53.

Sestito, F. et al. The extended 'stellar halo' of the Ursa Minor dwarf galaxy. *Monthly Notices of the Royal Astronomical Society*, v. 525, n. 2, p. 2875–2890, out. 2023. Cited in page 19.

Setton, D. J. et al. UNCOVER NIRSpec/PRISM Spectroscopy Unveils Evidence of Early Core Formation in a Massive, Centrally Dusty Quiescent Galaxy at $z_{spec} = 3.97$. *arXiv e-prints*, p. arXiv:2402.05664, fev. 2024. Cited in page 34.

Shapley, H.; Curtis, H. D. The Scale of the Universe. *Bulletin of the National Research Council*, v. 2, n. 11, p. 171–217, maio 1921. Cited in page 15.

Sharov, A. S.; Novikov, I. D. *Edwin Hubble, The Discoverer of the Big Bang Universe*. Cambridge: Cambridge University Press, 1993. Cited in page 15.

Shen, S. et al. The Baryon Cycle of Dwarf Galaxies: Dark, Bursty, Gas-rich Polluters. *Astrophysical Journal*, v. 792, n. 2, p. 99, set. 2014. Cited in page 33.

Shibuya, T. et al. Morphologies of ∼190,000 Galaxies at $z = 0 - 10$ Revealed with HST Legacy Data. II. Evolution of Clumpy Galaxies. *Astrophysical Journal*, v. 821, n. 2, p. 72, abr. 2016. Cited 3 times in pages 28, 29, and 33.

Shirazi, M.; Brinchmann, J. Strongly star forming galaxies in the local Universe with nebular He II λ4686 emission. *Monthly Notices of the Royal Astronomical Society*, v. 421, n. 2, p. 1043–1063, abr. 2012. Cited 2 times in pages 75 and 149.

Silich, S.; Tenorio-Tagle, G. Gas expulsion versus gas retention: what process dominates in young massive clusters? *Monthly Notices of the Royal Astronomical Society*, v. 465, n. 2, p. 1375–1383, fev. 2017. Cited in page 21.

Silich, S.; Tenorio-Tagle, G. Gas expulsion versus gas retention in young stellar clusters-II. Effects of cooling and mass segregation. *Monthly Notices of the Royal Astronomical Society*, v. 478, n. 4, p. 5112–5122, ago. 2018. Cited in page 21.

Simmonds, C. et al. Low-mass bursty galaxies in JADES efficiently produce ionizing photons and could represent the main drivers of reionization. *Monthly Notices of the Royal Astronomical Society*, v. 527, n. 3, p. 6139–6157, jan. 2024. Cited in page 17.

Simon, J. D. The Faintest Dwarf Galaxies. *Annual Review of Astronomy and Astrophysics*, v. 57, p. 375–415, ago. 2019. Cited 2 times in pages 18 and 19.

Singh, R. et al. The nature of LINER galaxies:. Ubiquitous hot old stars and rare accreting black holes. *Astronomy and Astrophysics*, v. 558, p. A43, out. 2013. Cited in page 74.

Somerville, R. S.; Primack, J. R.; Faber, S. M. The nature of high-redshift galaxies. *Monthly Notices of the Royal Astronomical Society*, v. 320, n. 4, p. 504–528, fev. 2001. Cited in page 30.

Soto, E. et al. Physical Properties of Sub-galactic Clumps at $0.5 \leq z \leq 1.5$ in the UVUDF. *Astrophysical Journal*, v. 837, n. 1, p. 6, mar. 2017. Cited in page 28.

Soto, K. T. et al. ZAP - enhanced PCA sky subtraction for integral field spectroscopy. *Monthly Notices of the Royal Astronomical Society*, v. 458, n. 3, p. 3210–3220, maio 2016. Cited in page 43.

Spite, M. et al. First stars VI - Abundances of C, N, O, Li, and mixing in extremely metal-poor giants. Galactic evolution of the light elements. *Astronomy and Astrophysics*, v. 430, p. 655–668, fev. 2005. Cited in page 71.

Stanway, E. R.; Eldridge, J. J. Re-evaluating old stellar populations. *Monthly Notices of the Royal Astronomical Society*, v. 479, n. 1, p. 75–93, set. 2018. Cited in page 72.

Stasińska, G. A grid of model H II regions for extragalactic studies. *Astronomy and Astrophysics Supplement Series*, v. 83, p. 501, jun. 1990. Cited in page 66.

Stasińska, G. et al. Semi-empirical analysis of Sloan Digital Sky Survey galaxies - III. How to distinguish AGN hosts. *Monthly Notices of the Royal Astronomical Society*, v. 371, n. 2, p. 972–982, set. 2006. Cited in page 76.

Stasińska, G. et al. Can retired galaxies mimic active galaxies? Clues from the Sloan Digital Sky Survey. *Monthly Notices of the Royal Astronomical Society*, v. 391, n. 1, p. L29–L33, nov. 2008. Cited in page 74.

Staveley-Smith, L.; Davies, R. D.; Kinman, T. D. H I and optical obseravations of dwarf galaxies. *Monthly Notices of the Royal Astronomical Society*, v. 258, p. 334–346, set. 1992. Cited in page 17.

Steinhauser, D.; Schindler, S.; Springel, V. Simulations of ram-pressure stripping in galaxy-cluster interactions. *Astronomy and Astrophysics*, v. 591, p. A51, jun. 2016. Cited in page 150.

Stetson, P. B. DAOPHOT: A Computer Program for Crowded-Field Stellar Photometry. *Publications of the ASP*, v. 99, p. 191, mar. 1987. Cited in page 48.

Storchi-Bergmann, T.; Calzetti, D.; Kinney, A. L. Ultraviolet to Near-Infrared Spectral Distributions of Star-forming Galaxies: Metallicity and Age Effects. *Astrophysical Journal*, v. 429, p. 572, jul. 1994. Cited in page 68.

Strigari, L. E. Galactic searches for dark matter. *Physics Reports*, v. 531, n. 1, p. 1–88, out. 2013. Cited in page 53.

STScI CPL Development Team. *SYNPHOT: Synthetic photometry using Astropy*. 2018. Astrophysics Source Code Library. Record ascl:1811.001. Available at: <https://ascl.net/1811.001>. Cited in page 47.

Tacconi, L. J. et al. Phibss: Molecular Gas Content and Scaling Relations in $z \sim 1 - 3$ Massive, Main-sequence Star-forming Galaxies. *Astrophysical Journal*, v. 768, n. 1, p. 74, maio 2013. Cited in page 28.

Taibi, S. et al. Stellar metallicity gradients of Local Group dwarf galaxies. *Astronomy and Astrophysics*, v. 665, p. A92, set. 2022. Cited in page 20.

Takeuchi, T. T.; Yoshikawa, K.; Ishii, T. T. The Luminosity Function of IRAS Point Source Catalog Redshift Survey Galaxies. *Astrophysical Journal, Letters*, v. 587, n. 2, p. L89–L92, abr. 2003. Cited in page 29.

Tamburello, V. et al. A lower fragmentation mass scale in high-redshift galaxies and its implications on giant clumps: a systematic numerical study. *Monthly Notices of the Royal Astronomical Society*, v. 453, n. 3, p. 2490–2514, nov. 2015. Cited in page 30.

Tamburello, V. et al. Clumpy galaxies seen in Hα: inflated observed clump properties due to limited spatial resolution and sensitivity. *Monthly Notices of the Royal Astronomical Society*, v. 468, n. 4, p. 4792–4800, jul. 2017. Cited in page 30.

Tau, E. A.; Vivas, A. K.; Martínez-Vázquez, C. E. Extended Stellar Populations in Ultrafaint Dwarf Galaxies. *Astronomical Journal*, v. 167, n. 2, p. 57, fev. 2024. Cited in page 19.

Tayal, S. S.; Zatsarinny, O. Breit-Pauli Transition Probabilities and Electron Excitation Collision Strengths for Singly Ionized Sulfur. *Astrophysical Journal, Supplement*, v. 188, n. 1, p. 32–45, maio 2010. Cited in page 63.

Telles, J. E. *The structure and environment of H II galaxies*. Tese (Doutorado) — University of Cambridge, UK, jan. 1995. Cited in page 18.

Tenorio-Tagle, G. Interstellar Matter Hydrodynamics and the Dispersal and Mixing of Heavy Elements. *Astronomical Journal*, v. 111, p. 1641, abr. 1996. Cited in page 147.

Thornton, J. et al. The mass profiles of dwarf galaxies from Dark Energy Survey lensing. *arXiv e-prints*, p. arXiv:2311.14659, nov. 2023. Cited in page 17.

Tinsley, B. M. Evolution of the Stars and Gas in Galaxies. *Fundamentals of Cosmic Physics*, v. 5, p. 287–388, jan. 1980. Cited in page 53.

Tissera, P. B.; De Rossi, M. E.; Scannapieco, C. Fingerprints of the hierarchical building-up of the structure on the mass-metallicity relation. *Monthly Notices of the Royal Astronomical Society*, v. 364, n. 341, p. L38–L41, nov. 2005. Cited 2 times in pages 21 and 22.

Tolstoy, E.; Hill, V.; Tosi, M. Star-Formation Histories, Abundances, and Kinematics of Dwarf Galaxies in the Local Group. *Annual Review of Astronomy and Astrophysics*, v. 47, n. 1, p. 371–425, set. 2009. Cited in page 18.

Toomre, A. On the gravitational stability of a disk of stars. *Astrophysical Journal*, v. 139, p. 1217–1238, maio 1964. Cited in page 30.

Topping, M. W. et al. Metal-poor star formation at $z > 6$ with JWST: new insight into hard radiation fields and nitrogen enrichment on 20 pc scales. *Monthly Notices of the Royal Astronomical Society*, v. 529, n. 4, p. 3301–3322, abr. 2024. Cited in page 148.

Torres-Flores, S. et al. Star-forming regions and the metallicity gradients in the tidal tails: the case of NGC 92. *Monthly Notices of the Royal Astronomical Society*, v. 438, n. 2, p. 1894–1908, fev. 2014. Cited in page 147.

Torres-Peimbert, S.; Peimbert, M. Photoelectric photometry and physical conditions of planetary nebulae. *Revista Mexicana de Astronomia y Astrofisica*, v. 2, p. 181–207, ago. 1977. Cited in page 65.

Torrey, P. et al. Similar star formation rate and metallicity variability time-scales drive the fundamental metallicity relation. *Monthly Notices of the Royal Astronomical Society*, v. 477, n. 1, p. L16–L20, jun. 2018. Cited in page 23.

Tosi, M. Understanding dwarf galaxies as galactic building blocks. *Astrophysics and Space Science*, v. 284, n. 2, p. 651–660, abr. 2003. Cited in page 33.

Tremonti, C. A. et al. The Origin of the Mass-Metallicity Relation: Insights from 53,000 Star-forming Galaxies in the Sloan Digital Sky Survey. *Astrophysical Journal*, v. 613, n. 2, p. 898–913, out. 2004. Cited 3 times in pages 21, 22, and 23.

Trujillo, I. et al. The effects of seeing on Sérsic profiles - II. The Moffat PSF. *Monthly Notices of the Royal Astronomical Society*, v. 328, n. 3, p. 977–985, dez. 2001. Cited in page 49.

Trujillo, I. et al. The Luminosity-Size and Mass-Size Relations of Galaxies out to $z \sim 3$. *Astrophysical Journal*, v. 604, n. 2, p. 521–533, abr. 2004. Cited in page 18.

Trussler, J. et al. Both starvation and outflows drive galaxy quenching. *Monthly Notices of the Royal Astronomical Society*, v. 491, n. 4, p. 5406–5434, fev. 2020. Cited in page 24.

Tumlinson, J.; Peeples, M. S.; Werk, J. K. The Circumgalactic Medium. *Annual Review of Astronomy and Astrophysics*, v. 55, n. 1, p. 389–432, ago. 2017. Cited in page 145.

Väisänen, P. et al. Adaptive optics imaging and optical spectroscopy of a multiple merger in a luminous infrared galaxy. *Monthly Notices of the Royal Astronomical Society*, v. 384, n. 3, p. 886–906, mar. 2008. Cited in page 26.

Vale Asari, N. et al. Diffuse ionized gas and its effects on nebular metallicity estimates of star-forming galaxies. *Monthly Notices of the Royal Astronomical Society*, v. 489, n. 4, p. 4721–4733, nov. 2019. Cited in page 74.

Vale Asari, N. et al. BOND: Bayesian Oxygen and Nitrogen abundance Determinations in giant H II regions using strong and semistrong lines. *Monthly Notices of the Royal Astronomical Society*, v. 460, n. 2, p. 1739–1757, ago. 2016. Cited in page 143.

van den Bergh, S. et al. A Morphological Catalog of Galaxies in the Hubble deep Field. *Astronomical Journal*, v. 112, p. 359, ago. 1996. Cited in page 28.

van Dokkum, P. G. Cosmic-Ray Rejection by Laplacian Edge Detection. *Publications of the ASP*, v. 113, n. 789, p. 1420–1427, nov. 2001. Cited in page 48.

van Donkelaar, F.; Agertz, O.; Renaud, F. From giant clumps to clouds - II. The emergence of thick disc kinematics from the conditions of star formation in high redshift gas rich galaxies. *Monthly Notices of the Royal Astronomical Society*, v. 512, n. 3, p. 3806–3814, maio 2022. Cited in page 32.

van Zee, L.; Haynes, M. P. Oxygen and Nitrogen in Isolated Dwarf Irregular Galaxies. *Astrophysical Journal*, v. 636, n. 1, p. 214–239, jan. 2006. Cited in page 147.

Vazdekis, A. et al. Evolutionary stellar population synthesis with MILES - II. Scaled-solar and α-enhanced models. *Monthly Notices of the Royal Astronomical Society*, v. 449, n. 2, p. 1177–1214, maio 2015. Cited in page 54.

Vazdekis, A. et al. Evolutionary stellar population synthesis with MILES - I. The base models and a new line index system. *Monthly Notices of the Royal Astronomical Society*, v. 404, n. 4, p. 1639–1671, jun. 2010. Cited in page 54.

Venturi, G. et al. Gas-phase metallicity gradients in galaxies at $z \sim 6 - 8$. *arXiv e-prints*, p. arXiv:2403.03977, mar. 2024. Cited 2 times in pages 146 and 147.

Verbeke, R. et al. Gaseous infall triggering starbursts in simulated dwarf galaxies. *Monthly Notices of the Royal Astronomical Society*, v. 442, n. 2, p. 1830–1843, ago. 2014. Cited in page 23.

Viironen, K. et al. The S2N2 metallicity calibrator and the abundance gradient of M33. *Monthly Notices of the Royal Astronomical Society*, v. 381, n. 4, p. 1719–1726, nov. 2007. Cited in page 68.

Villaume, A. et al. The Extended IRTF Spectral Library: Expanded Coverage in Metallicity, Temperature, and Surface Gravity. *Astrophysical Journal, Supplement*, v. 230, n. 2, p. 23, jun. 2017. Cited in page 54.

Vincenzo, F. et al. Nitrogen and oxygen abundances in the Local Universe. *Monthly Notices of the Royal Astronomical Society*, v. 458, n. 4, p. 3466–3477, jun. 2016. Cited in page 70.

Vink, J. S. Very massive stars and nitrogen-emitting galaxies. *Astronomy and Astrophysics*, v. 679, p. L9, nov. 2023. Cited in page 148.

Vivas, A. K.; Martínez-Vázquez, C.; Walker, A. R. Gaia RR Lyrae Stars in Nearby Ultra-faint Dwarf Satellite Galaxies. *Astrophysical Journal, Supplement*, v. 247, n. 1, p. 35, mar. 2020. Cited in page 19.

Vollmer, B. et al. Ram Pressure Stripping and Galaxy Orbits: The Case of the Virgo Cluster. *Astrophysical Journal*, v. 561, n. 2, p. 708–726, nov. 2001. Cited in page 21.

Vulcani, B. et al. GASP XXIV. The History of Abruptly Quenched Galaxies in Clusters. *Astrophysical Journal*, v. 892, n. 2, p. 146, abr. 2020. Cited 2 times in pages 18 and 21.

Vulcani, B. et al. Enhanced Star Formation in Both Disks and Ram-pressure-stripped Tails of GASP Jellyfish Galaxies. *Astrophysical Journal, Letters*, v. 866, n. 2, p. L25, out. 2018. Cited in page 21.

Wade, R. A. et al. A two-color photometric system for the near infrared. *Publications of the ASP*, v. 91, p. 35–40, fev. 1979. Cited in page 37.

Wechsler, R. H.; Tinker, J. L. The Connection Between Galaxies and Their Dark Matter Halos. *Annual Review of Astronomy and Astrophysics*, v. 56, p. 435–487, set. 2018. Cited in page 18.

Weibel, A. et al. Galaxy build-up in the first 1.5 Gyr of cosmic history: insights from the stellar mass function at $z \sim 4 - 9$ from JWST NIRCam observations. *Monthly Notices of the Royal Astronomical Society*, v. 533, n. 2, p. 1808–1838, set. 2024. Cited in page 34.

Weilbacher, P. M. et al. The data processing pipeline for the MUSE instrument. *Astronomy and Astrophysics*, v. 641, p. A28, set. 2020. Cited in page 41.

Welch, B. et al. The Sunburst Arc with JWST: III. An Abundance of Direct Chemical Abundances. *arXiv e-prints*, p. arXiv:2405.06631, maio 2024. Cited in page 148.

Werk, J. K. et al. Metal Transport to the Gaseous Outskirts of Galaxies. *Astrophysical Journal*, v. 735, n. 2, p. 71, jul. 2011. Cited in page 21.

White, S. D. M.; Frenk, C. S. Galaxy Formation through Hierarchical Clustering. *Astrophysical Journal*, v. 379, p. 52, set. 1991. Cited in page 16.

White, S. D. M.; Rees, M. J. Core condensation in heavy halos: a two-stage theory for galaxy formation and clustering. *Monthly Notices of the Royal Astronomical Society*, v. 183, p. 341–358, maio 1978. Cited in page 16.

Whitmore, B. C. et al. ALMA Observations of the Antennae Galaxies. I. A New Window on a Prototypical Merger. *Astrophysical Journal*, v. 795, n. 2, p. 156, nov. 2014. Cited in page 25.

Whitmore, B. C. et al. The Antennae Galaxies (NGC 4038/4039) Revisited: Advanced Camera for Surveys and NICMOS Observations of a Prototypical Merger. *Astronomical Journal*, v. 140, n. 1, p. 75–109, jul. 2010. Cited in page 25.

Whitmore, B. C.; Schweizer, F. Hubble Space Telescope Observations of Young Star Clusters in NGC 4038/4039, "The Antennae" Galaxies. *Astronomical Journal*, v. 109, p. 960, mar. 1995. Cited in page 26.

Wilson, C. D. et al. Two Populations of Young Massive Star Clusters in Arp 220. *Astrophysical Journal*, v. 641, n. 2, p. 763–772, abr. 2006. Cited in page 26.

Wisnioski, E. et al. The KMOS^{3D} Survey: Design, First Results, and the Evolution of Galaxy Kinematics from $0.7 \leq z \leq 2.7$. *Astrophysical Journal*, v. 799, n. 2, p. 209, fev. 2015. Cited in page 30.

Wisnioski, E. et al. Scaling relations of star-forming regions: from kpc-sized clumps to H II regions. *Monthly Notices of the Royal Astronomical Society*, v. 422, n. 4, p. 3339–3355, jun. 2012. Cited 3 times in pages 28, 31, and 32.

Woo, J. et al. Stellar populations with optical spectra: deep learning versus popular spectrum fitting codes. *Monthly Notices of the Royal Astronomical Society*, v. 530, n. 4, p. 4260–4276, jun. 2024. Cited in page 58.

Wyder, T. K. et al. The Ultraviolet Galaxy Luminosity Function in the Local Universe from GALEX Data. *Astrophysical Journal, Letters*, v. 619, n. 1, p. L15–L18, jan. 2005. Cited in page 29.

Xiao, M. et al. Massive Optically Dark Galaxies Unveiled by JWST Challenge Galaxy Formation Models. *arXiv e-prints*, p. arXiv:2309.02492, set. 2023. Cited in page 34.

Yan, R.; Blanton, M. R. The Nature of LINER-like Emission in Red Galaxies. *Astrophysical Journal*, v. 747, n. 1, p. 61, mar. 2012. Cited in page 74.

Yanagisawa, H. et al. Strong He I Emission Lines in High N/O Galaxies at $z \sim 6$ Identified in JWST Spectra: High He/H Abundance Ratios or High Electron Densities? *arXiv e-prints*, p. arXiv:2405.01823, maio 2024. Cited in page 148.

Yang, L. et al. The size-luminosity relation of lensed galaxies at $z \sim 6 - 9$ in the Hubble Frontier Fields. *Monthly Notices of the Royal Astronomical Society*, v. 514, n. 1, p. 1148–1161, jul. 2022. Cited in page 18.

Yerokhin, V. A.; Shabaev, V. M. Lamb Shift of n = 1 and n = 2 States of Hydrogen-like Atoms, $1 \leq Z \leq 110$. *Journal of Physical and Chemical Reference Data*, v. 44, n. 3, p. 033103, set. 2015. Cited in page 65.

York, D. G. et al. The Sloan Digital Sky Survey: Technical Summary. *Astronomical Journal*, v. 120, n. 3, p. 1579–1587, set. 2000. Cited 2 times in pages 36 and 74.

Zanella, A. et al. An extremely young massive clump forming by gravitational collapse in a primordial galaxy. *Nature*, v. 521, n. 7550, p. 54–56, maio 2015. Cited in page 32.

Zanella, A. et al. A contribution of star-forming clumps and accreting satellites to the mass assembly of $z \sim 2$ galaxies. *Monthly Notices of the Royal Astronomical Society*, v. 489, n. 2, p. 2792–2818, out. 2019. Cited in page 30.

Zhang, H.-X. et al. The Blue Compact Dwarf Galaxy VCC 848 Formed by Dwarf-Dwarf Merging. *Astrophysical Journal, Letters*, v. 891, n. 1, p. L23, mar. 2020. Cited in page 26.

APPENDIX A – Co-authorships during the PhD

Here I list the papers I have participated during my PhD and my individual contribution to the work.

Title:	Spatially resolved self-consistent spectral modelling of jellyfish galaxies from MUSE with FADO: Trends with mass and stripping intensity
Year:	2023
Authors:	G.M. Azevedo, A.L. Chies-Santos, R. Riffel, J.M. Gomes, **A.E. Lassen**, J.P.V. Benedetti, R.S. de Souza, Q. Xu.
Journal:	Monthly Notices of the Royal Astronomical Society
DOI:	**10.1093/mnras/stad1641**
Contribution:	I have participated on regular meetings with the main authors to discuss scientific results and helped in the application of analysis methodologies related to ionized gas properties.

Title:	Bound star clusters observed in a lensed galaxy 460 Myr after the Big Bang
Year:	2024
Authors:	A. Adamo, L.D. Bradley, E. Vanzella, A. Claeyssens, B. Welch, J.M. Diego, G. Mahler, M. Oguri, K. Sharon, Abdurro'uf, T.Y. Hsiao, M. Messa, **A.E. Lassen**, E. Zackrisson, G. Brammer, D. Coe, V. Kokorev, M. Ricotti, A. Zitrin, S. Fujimoto, A.K. Inoue, T. Resseguier, J.R. Rigby, Y. Jiménez-Teja, A.R. Windhorst, T. Hashimoto, Y. Tamura.
Journal:	Nature
DOI:	**10.1038/s41586-024-07703-7**
Contribution:	I performed the SED fitting for the high-z star clusters assuming a SSP SFH model with PROSPECTOR to compare it with SED fitting properties derived by other collaborators using other SFH assumptions and/or BAGPIPES. The results were discussed with the paper first author.

Title:	Extragalactic globular cluster near-infrared spectroscopy. I) Integrated near-infrared spectra of Centaurus A/NGC 5128
Year:	2024
Authors:	L.G. Dahmer-Hahn, A.L. Chies-Santos, E. Eftekhari, E. Zanatta, R. Riffel, A. Vazdekis, A. Villaume, M.A. Beasley, **A.E. Lassen**.
Journal:	Astronomy and Astrophysics; Publication scheduled for V.690
DOI:	**10.1051/0004-6361/202449570**
Contribution:	I estimated the magnitudes of 21 extragalactic globular clusters in Centaurus A using aperture photometry of NIR-VISTA public data in the J and K_s bands.

APPENDIX B – Press Release

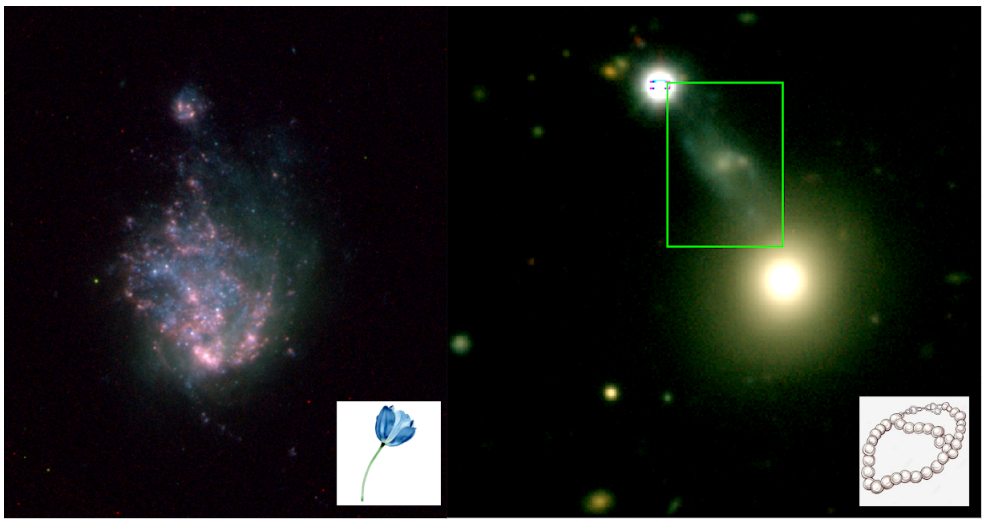

Figura 1: Nesse trabalho, apresentamos um estudo detalhado sobre a formação estelar e a composiçãao química de duas galáxias anãs próximas: ESO 400-43 (Relembrando uma tulipa, à esquerda na figura) e SDSS J0205-0814 (relembrando um colar de pérolas, dentro do retângulo amarelo à direita). No centro da imagem, sua companheira maior e mais massiva, Mrk 1172. O objeto brilhante no topo é uma estrela catalogada.

Tese de doutorado estuda duas galáxias anãs, análogas às galáxias dos primórdios do Universo: O "colar de pérolas" e a "tulipa"

Segundo o modelo cosmológico padrão, as primeiros estruturas de matéria escura tinham baixas massas, indicando um Universo primordial cheio de pequenas galáxias. Entender como essas galáxias formaram estrelas e elementos químicos, e como evoluíram até as galáxias que vemos hoje, é um dos principais objetivos da astrofísica moderna, impulsionando o lançamento do telescópio espacial James Webb (JWST).

Os metais (em astronomia utiliza-se o termo metal para elementos mais pesados que o Hélio) em uma galáxia estão diretamente ligados à evolução estelar, pois esses elementos formam-se através da fusão nuclear dentro das estrelas. As galáxias no Universo primordial passaram por seus primeiros episódios de formação estelar, resultando em gás pobre em metais. Uma característica peculiar de galáxias distantes, quando observadas no ultravioleta, é a presença de "caroços" gigantes, chamados *clumps*, especialmente cerca de 2 bilhões de anos após o Big Bang, um período conhecido como "meio-dia cósmico". Esses clumps são raramente observados em galáxias próximas. Galáxias anãs frequentemente apresentam baixa metalicidade, muito gás e, às vezes, até mesmo *clumps*. Essas características fazem dessas galáxias anãs laboratórios ideais para estudar a formação estelar e a evolução química em condições semelhantes às de galáxias distantes, mas em escalas espaciais muito maiores.

Nesse trabalho, apresentamos um estudo detalhado sobre a formação estelar e a composição química de duas galáxias anãs próximas: ESO 400-43 (à esquerda na Fig. 1), com o formato parecido com o de uma tulipa, e SDSS J0205-0814 (dentro do retângulo amarelo à direita na Fig. 1), com o formato parecido ao de um colar de pérolas. Ambas são pobres em metais e possuem características únicas que nos permitem investigar em detalhes os gatilhos para a formação de *clumps* gigantes, assim como a evolução química em ambientes de baixa metalicidade. Utilizamos dados do Very Large Telescope (VLT) Multi Unit Spectroscopic Explorer (MUSE) e imagens do telescópio espacial Hubble para essa análise.

No colar de pérolas, observamos vários *clumps* gigantes (as pérolas do colar) e evidências de uma componente de gás em rotação, possivelmente um disco. Confirmamos a interação gravitacional entre o colar de pérolas e Mrk 1172 (a galáxia no centro do painel da direita na Fig. 1) ao observar um alinhamento entre o movimento do gás na anã e das estrelas em Mrk 1172. Esses *clumps* estão na componente em rotação, sugerindo que se formaram pelo colapso do gás em regiões do disco com alta instabilidade gravitacional, fenômeno amplamente observado para galáxias distantes com *clumps*. O meio interestelar do colar de pérolas é quimicamente homogêneo, indicando um processo de mistura ou redistribuição de gás em grande escala, como re-acreção de gás previamente enriquecido ou fusões. Recentemente, distribuições homogêneas de metalicidade foram reportadas para galáxias distantes observadas com o JWST.

Na tulipa observamos vários aglomerados estelares, resultando na aparência "granulosa" vista na Fig. 1. Esses aglomerados injetam energia no gás através de explosões de supernovas e ventos estelares. Detectamos estrelas massivas em estágios avançados de evolução (estrelas Wolf-Rayet), que enriquecem a galáxia ao ejetar o material processado no interior dessas estrelas. Encontramos um padrão incomum para o enriquecimento de Nitrogênio nessa galáxia, semelhante ao de algumas galáxias distantes surpreendentemente ricas em metais recentemente observadas pelo JWST. Uma das explicações propostas baseia-se no papel fundamental das estrelas Wolf-Rayet no enriquecimento do meio interestelar, similar ao que observamos nan tulipa.

APPENDIX C – HST Point Spread Functions for other filters

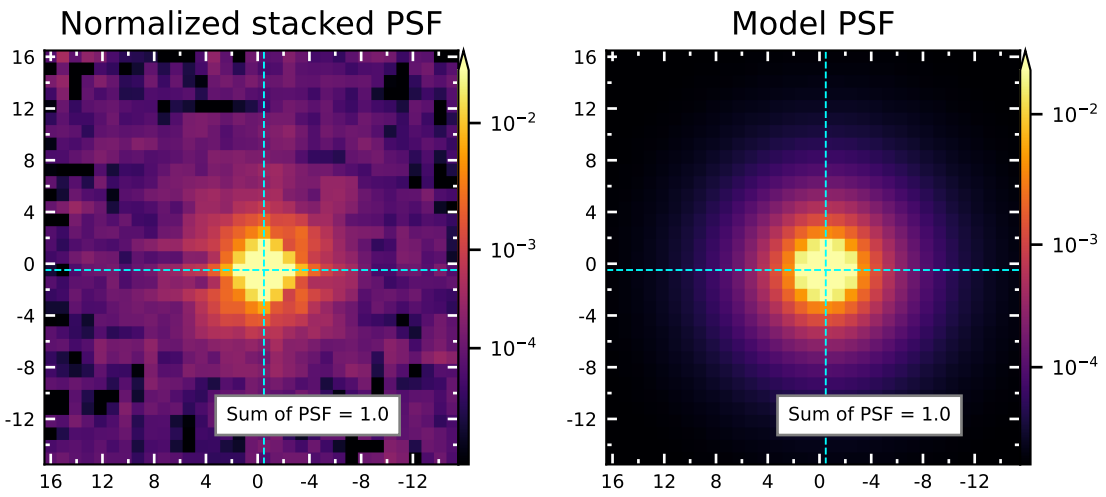

Figure 36 – Same as Fig. 16, but now for WFC3/UVIS F336W band.

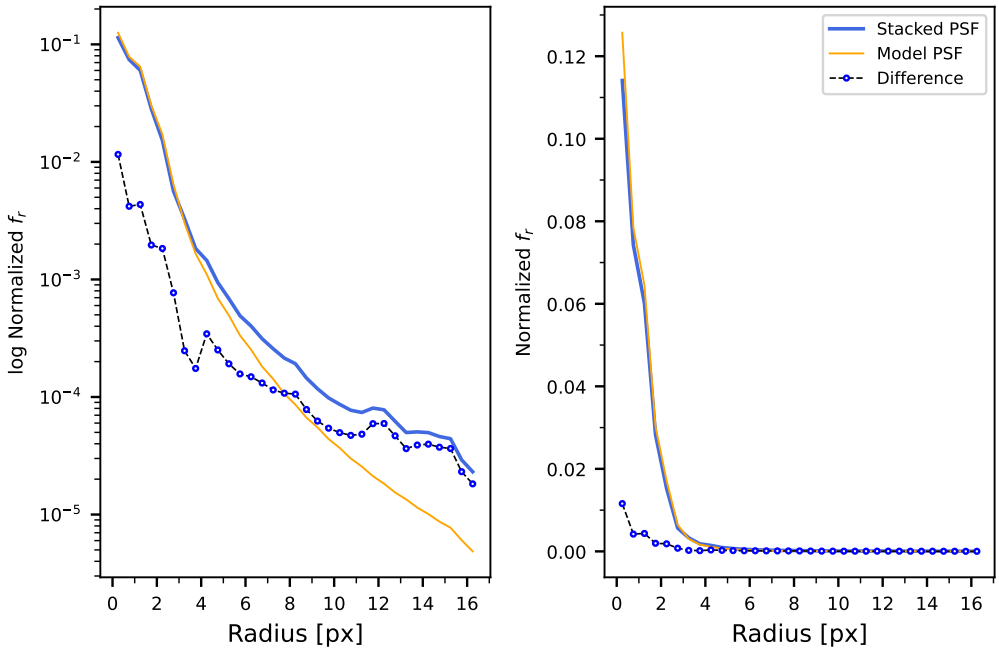

Figure 37 – Same as Fig. 17, but now for WFC3/UVIS F336W band.

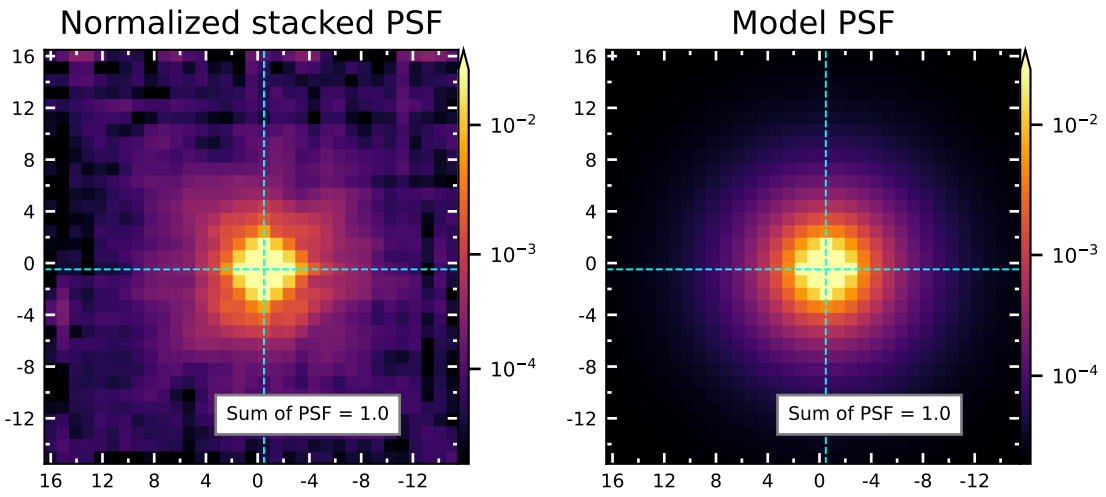

Figure 38 – Same as Fig. 16, but now for WFC3/UVIS F438W band.

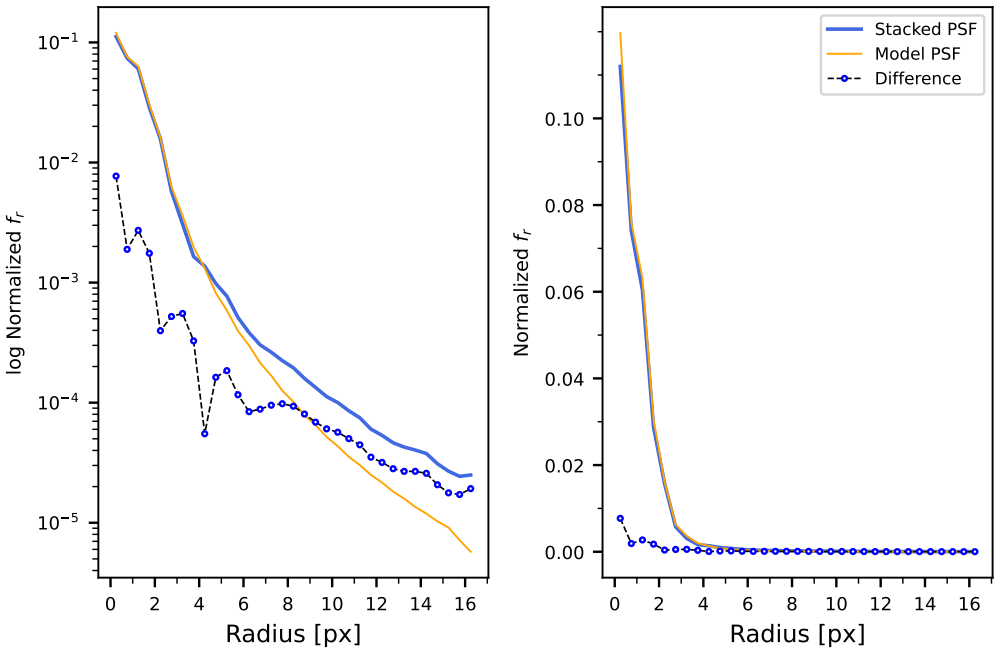

Figure 39 – Same as Fig. 17, but now for WFC3/UVIS F438W band.

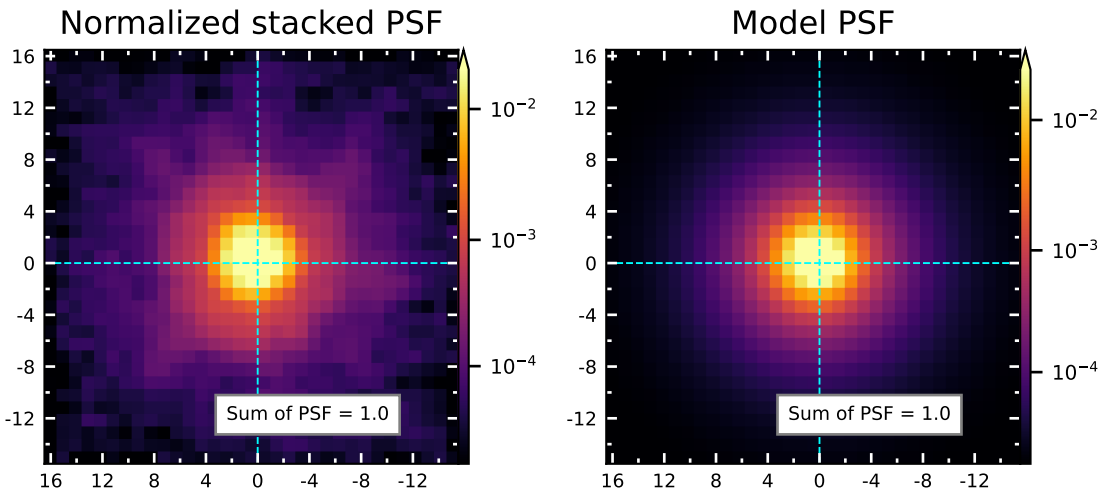

Figure 40 – Same as Fig. 16, but now for WFC3/UVIS F606W band.

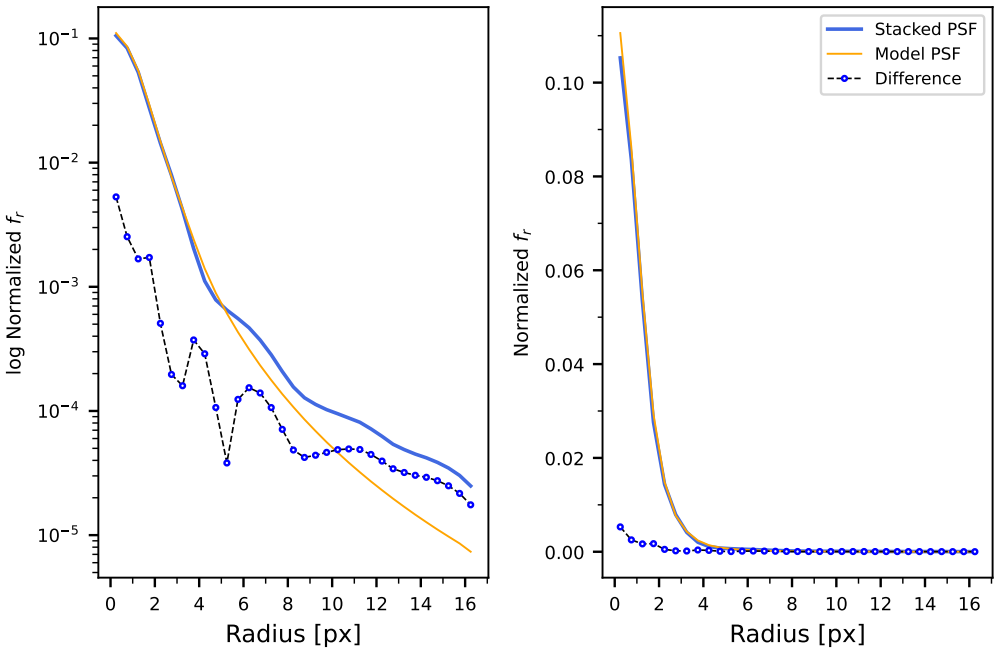

Figure 41 – Same as Fig. 17, but now for WFC3/UVIS F606W band.

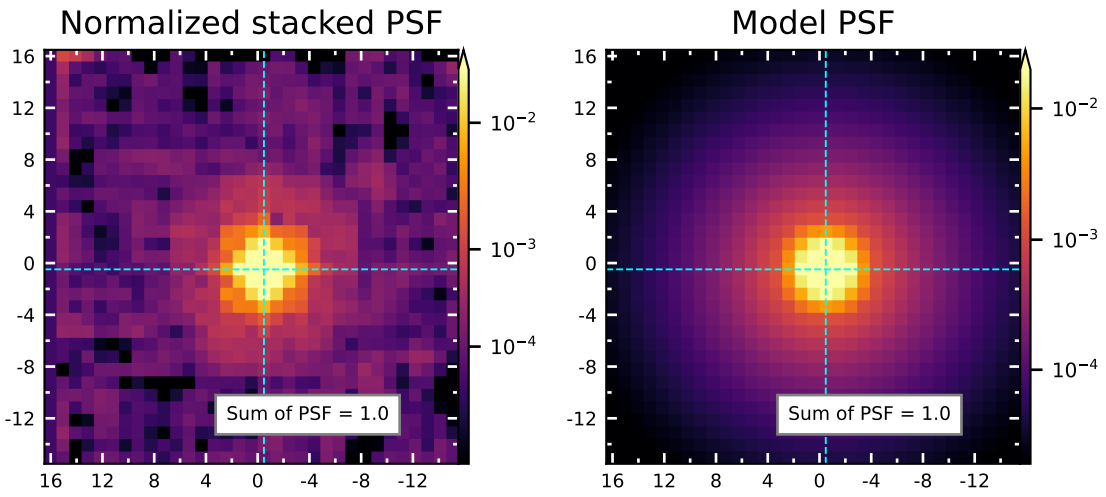

Figure 42 – Same as Fig. 16, but now for WFC3/UVIS F665N band.

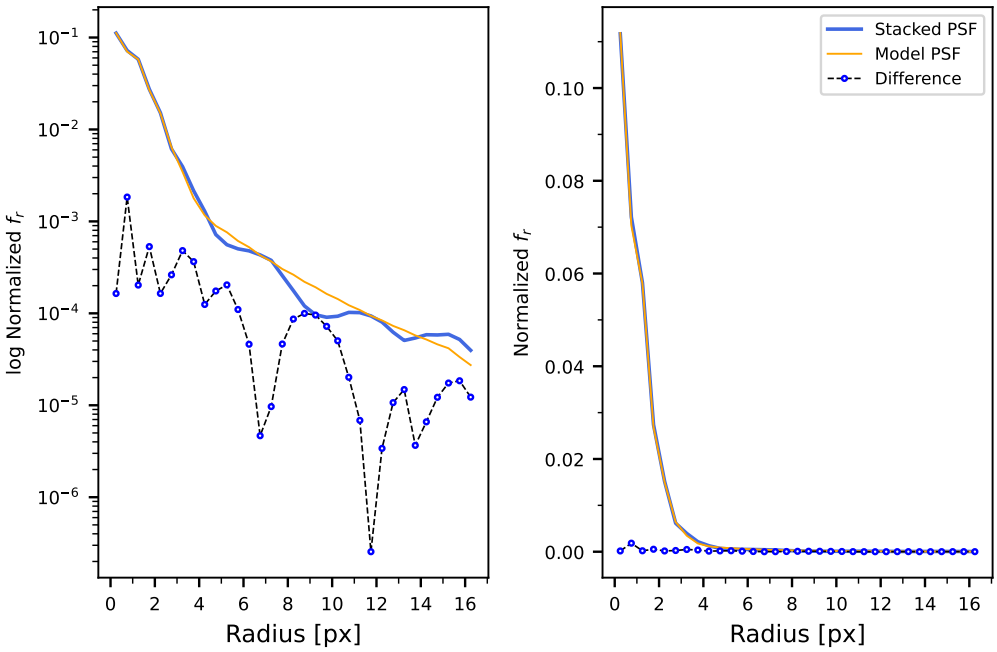

Figure 43 – Same as Fig. 17, but now for WFC3/UVIS F665N band.

APPENDIX D – Error propagation of the color excess analytical expression

We start from Equation 3.13:

$$E_{(B-V)} = \frac{2.5}{k(\lambda_{\mathrm{H}\beta}) - k(\lambda_{\mathrm{H}\alpha})} \log_{10}\left[\frac{(\mathrm{H}\alpha/\mathrm{H}\beta)_{\mathrm{obs}}}{(\mathrm{H}\alpha/\mathrm{H}\beta)_{\mathrm{int}}}\right]$$

We simplify the expression to the functional form:

$$f(x_1, x_2) = A \times \log_{10}\left(B \times \frac{x_1}{x_2}\right) \tag{D.1}$$

where $A \equiv 2.5/[k(\lambda_{\mathrm{H}\beta}) - k(\lambda_{\mathrm{H}\alpha})]$ and $B \equiv (\mathrm{H}\beta/\mathrm{H}\alpha)_{\mathrm{int}}$ are treated as constants. x_1 and x_2 are the observed Hα and Hβ fluxes, respectively, with uncertainties δx_1 and δx_2. Neglecting correlations and assuming independent variables, the error propagation of $f(x_1, x_2)$ can be obtained via the expression (Ku, 1966):

$$\delta f = \sqrt{\left(\frac{\partial f}{\partial x_1}\right)^2 (\delta x_1)^2 + \left(\frac{\partial f}{\partial x_2}\right)^2 (\delta x_2)^2} \tag{D.2}$$

The partial derivatives are:

$$\begin{aligned}
\frac{\partial f}{\partial x_j} &= A \times \frac{\partial}{\partial x_j}\left[\log_{10}\left(B \times \frac{x_1}{x_2}\right)\right] \\
&= A \times \frac{\partial}{\partial x_j}(\cancel{\log_{10} B} + \log_{10} x_1 - \log_{10} x_2) \\
&= A \times \left[\frac{\partial(\log_{10} x_1)}{\partial x_j} - \frac{\partial(\log_{10} x_2)}{\partial x_j}\right]
\end{aligned}$$

which leads to:

$$\frac{\partial f}{\partial x_1} = A \times \frac{\partial(\log_{10} x_1)}{\partial x_1} = \frac{A}{x_1 \ln 10} \tag{D.3}$$

$$\frac{\partial f}{\partial x_2} = -A \times \frac{\partial(\log_{10} x_2)}{\partial x_2} = \frac{-A}{x_2 \ln 10} \tag{D.4}$$

Replacing equations D.3 and D.4 into equation D.2, we have:

$$\begin{aligned}\delta f =& \sqrt{\frac{A^2\,\delta x_1^2}{x_1^2\,(\ln 10)^2} + \frac{A^2\,\delta x_2^2}{x_2^2\,(\ln 10)^2}} \\ =& \sqrt{\frac{A^2}{(\ln 10)^2} \times \sum_{j=1}^{2} \left(\frac{\delta x_j}{x_j}\right)^2} \\ =& \frac{A}{\ln 10} \times \sqrt{\sum_{j=1}^{2} \left(\frac{\delta x_j}{x_j}\right)^2}\end{aligned}$$

Replacing the variables, the expression above becomes:

$$\delta E_{(B-V)} = \frac{2.5}{\ln 10 \times [k(\lambda_{\mathrm{H}\beta}) - k(\lambda_{\mathrm{H}\alpha})]} \times \sqrt{\left(\frac{\delta \mathrm{H}\alpha}{\mathrm{H}\alpha}\right)^2 + \left(\frac{\delta \mathrm{H}\beta}{\mathrm{H}\beta}\right)^2} \tag{D.5}$$

which is exactly the equation 3.14 if we simplify $2.5/\ln(10) \approx 1.086$.